METHODOLOGY OF CITRATE-BASED BIOMATERIAL DEVELOPMENT AND APPLICATION

by

M. RICHARD TRAN

Presented to the Faculty of the Graduate School of
The University of Texas at Arlington in Partial Fulfillment
of the Requirements
for the Degree of

DOCTOR OF PHILOSOPHY

THE UNIVERSITY OF TEXAS AT ARLINGTON
December 2011

ACKNOWLEDGEMENTS

It is my pleasure to acknowledge the professors, colleagues, family and friends who have made this work possible. I would like to gratefully and sincerely thank Jian Yang for his guidance, contributions, patience, and most importantly, his friendship to make my Ph.D. experience productive, stimulating, and rewarding. He provided me vast opportunities, which challenged me not only to grow as a researcher, but also as an instructor, leader, and independent thinker. I will always remember “Chem-Is-Try,” and it has been an honor to be your first Ph.D. student. For everything you’ve done for me, I thank you. For this dissertation, I would also like to thank my committee members: Kristine Guleserian, Lei Shi, and Kytai Nguyen for their time, interest, and helpful comments, which have helped one of the biggest goals of my life come to fruition. Special thanks goes to Liping Tang, who served as my committee member, graduate advisor, and professor. His Tissue Engineering course was the catalyst for my research interests, and motivated me to further pursue research in biomaterial and scaffold design. Without his guidance, I would not be where I am today. To the faculty of the Bioengineering Department, thank you for your open doors and minds. It has been a pleasure to know you as a student, and I look forward to one day knowing you as a peer.

The members of the Yang research group have contributed immensely to my personal and professional time at The University of Texas at Arlington. The group has been a source of productive collaboration, friendship, and fun times. I am especially grateful for the help provided by Aleksey Kolasnikov and Ibrahim Qattan who constantly went above and beyond their regular research duties, and assisted me with all the tedious and difficult lab maintenance projects. Words cannot express how thankful I am to have “go-to-guys” I can count on no matter what the situation, and the friendship we have developed will definitely last a lifetime. I would also like to thank the Bioengineering Department staff for assisting me with the administrative tasks

necessary for completing my doctoral work. In particular, I would like to thank Cindy Bradfield for her help with the countless amounts of required paperwork, and for answering all my random questions. Our Texas Rangers discussions were always a pleasant relief from the monotony of a typical research day and reminded that there is a life outside of the lab.

I would also like to take this time to thank my family and close friends who were paramount in shaping my beliefs, character, and integrity. I owe the deepest gratitude to my parents, Hao and Nghiep Tran, who have always supported my decisions, even if they did not agree with them. Although they were never able to offer me advice in regards to college life or graduate work, they instilled in me the values of hard work, determination, self-discipline, and sacrifice. I would not have been able to pursue my dreams without their love, support, and the sacrifices they made throughout the many years of my education. Finally, I will always be indebted to my brother, Ronald, and friends, Bryan, Jeff, John, and Phuong, for always standing behind me in times of great difficulty in both my personal and professional lives. Thank you for always believing in me, and for tolerating my high levels of stress when school, lab, and life pushed me to the limits. Your encouragement, support, and faith in me are what ultimately gave me the strength to make all of this work possible.

This work was supported in part by American Heart Association Beginning Grant-in-Aid award (to J.Y.), award R21EB009795 from the National Institute of Biomedical Imaging and Bioengineering (NIBIB) (to J.Y.) and NIH R01 GM074021 (to L.T).

November 11, 2011

ABSTRACT

METHODOLOGY OF CITRATE-BASED
BIOMATERIAL DEVELOPMENT
AND APPLICATION

M. Richard Tran, PhD

The University of Texas at Arlington, 2011

Supervising Professor: Jian Yang

Biomaterials play central roles in modern strategies of regenerative medicine and tissue engineering. Attempts to find tissue-engineered solutions to cure various injuries or diseases have led to an enormous increase in the number of polymeric biomaterials over the past decade. The breadth of new materials arises from the multiplicity of anatomical locations, cell types, and mode of application, which all place application-specific requirements on the biomaterial. Unfortunately, many of the currently available biodegradable polymers are limited in their versatility to meet the wide range of requirements for tissue engineering. Therefore, a methodology of biomaterial development, which is able to address a broad spectrum of requirements, would be beneficial to the biomaterial field.

This work presents a methodology of citrate-based biomaterial design and application to meet the multifaceted needs of tissue engineering. We hypothesize that 1) citric acid, a non-toxic metabolic product of the body (Krebs Cycle), can be exploited as a universal multifunctional monomer and reacted with various diols to produce a new class of soft biodegradable elastomers with the flexibility to tune the material properties of the resulting

material to meet a wide range of requirements; 2) the newly developed citrate-based polymers can be used as platform biomaterials for the design of novel tissue engineering scaffolding; and 3) microengineering approaches in the form thin scaffold sheets, microchannels, and a new porogen design can be used to generate complex cell-cell and cell-microenvironment interactions to mimic tissue complexity and architecture.

To test these hypotheses, we first developed a methodology of citrate-based biomaterial development through the synthesis and characterization of a family of *in situ* crosslinkable and urethane-doped elastomers, which are synthesized using simple, cost-effective strategies and offer a variety methods to tailor the material properties to meet the needs of a particular application. Next, we introduced a new porogen generation technique, and showed the potential application of the newly developed materials through the fabrication and characterization of scaffold sheets, multiphasic small diameter vascular grafts, and multichanneled nerve guides. Finally, the *in vivo* applications of citrate-based materials are exemplified through the evaluation of peripheral nerve regeneration using multichanneled guides and the ability to assist in injection-based endoscopic mucosal resection therapy.

The results presented in this work show that citric acid can be utilized as a cornerstone in the development of novel biodegradable materials, and combined with microengineering approaches to produce the next generation of tissue engineering scaffolding. These enabling new biomaterials and scaffolding strategies should address many of the existing challenges in tissue engineering and advance the field as a whole.

TABLE OF CONTENTS

LIST OF ILLUSTRATIONS

LIST OF TABLES

CHAPTER 1

INTRODUCTION

1.1 Importance of Biomaterials

The development of novel biomaterials offers unique opportunities to tackle unmet clinical problems. Biomaterials are critical components of biomedical devices, and play central roles in modern strategies of regenerative medicine and tissue engineering, where cell-seeded constructs are designed to replace damaged or diseased tissues [1-3]. Biomaterials define a three-dimensional (3D) space for neo-tissue formation, regulate cell differentiation and phenotype, facilitate the localization and delivery of cells/bioactive factors, and elicit biological and mechanical functions of the native extracellular matrix (ECM) for proper tissue structure and function [4-7]. The importance of biomaterials has been previously demonstrated by the limited success of tissue engineering approaches, which circumvent the use of biomaterial substrates. In the absence of a cell-adhesion substrate, the direct injection of cell suspensions resulted in a lack of control over cell localization and survival due to the anchorage-dependent nature of many cell types [8, 9]. Therefore, by recreating the necessary biophysical and biochemical milieus to enhance the biological potentials of regenerative medicine, biomaterials have become an important aspect of regenerative medicine with the potential to solve today's medical problems.

1.2 Biodegradable Elastomers

As many of the tissues in the body are soft (low modulus) and elastic (high elongation at break) (**Table 1.1**), it is important that the implanted biomaterials match the mechanical properties of the tissues they intend to regenerate. A mismatch in mechanical compliance

between the implant and host tissue interface causes inflammation and scar tissue formation, which ultimately leads to improper tissue in growth, limited vascularization, and failure of the implant [10, 11]. Poly (L-lactide) (PLA), poly (glycolide) (PGA), and their copolymers (PLGA) are widely used in U.S. Food and Drug Administration (FDA) approved medical devices [12, 13], but their hydrophobic and stiff nature often compromises their success in soft tissue engineering applications [14-16]. As a result, many groups have focused on the synthesis, characterization, and application of materials with a wide range of biodegradable and elastomeric properties [17-20].

Table 1.1 Mechanical Properties of Soft Tissues

Tissue	**Tensile Strength (MPa)**	**Modulus (MPa)**	**Elongation at Break (%)**
Ulnar Peripheral Nerve	9.8 – 21.6	–	8 – 21
Human Bladder	0.27 ± 0.14	0.25 ± 0.18	0.69 ± 0.17
Human Coronary Artery	1.4 – 11.14	–	–
Bovine Elastin	–	1.1	–
Smooth Muscle Relaxed	–	0.006	300
Human ACL	24 – 112	–	–
Human Cartilage	3.7 – 10.5	–	–
Porcine Lung	–	0.005	–

Biodegradable elastomers are advantageous in that they can sustain and recover from multiple deformations without causing irritation to the surrounding tissue in a mechanically demanding environment [21-23]. Another advantage of an elastomeric scaffold is their ability to be used with mechanical conditioning regimens to promote improved tissue formation. By gradually transferring stress from the degrading synthetic matrix to the newly forming tissue, scaffolds with applied cyclic mechanical strains have been shown to increase collagen and elastin production in vascular smooth muscle cells [24, 25]. Numerous biodegradable elastomers have been developed for tissue engineering, and have found widespread use in the engineering of blood vessels, heart valves, nerves, cartilage, skin, bladder, and bone [26-32].

1.3 Existing Biodegradable Elastomers

As defined by the American Society for Testing and Materials (ASTM), an elastomer or bioelastomer is a substance with a glass transition temperature (T_g) lower than body temperature, an initial modulus in the range of 0.1 – 20 MPa, and the ability to recover to at least 1.25 times its original length following an applied stress of 1.5 times its original length for a 1 minute time period [33]. The use of elastomers in medical applications originates back to the beginning of the rubber industry, and since then, numerous materials have played a major role in advancement of medical technology. The following sections provide a brief review of the major classifications of existing biodegradable elastomers for tissue engineering applications.

1.3.1. Polyurethanes

Polyurethanes are segmented block co-polymers consisting of a combination of soft (macrodiols) and hard segments (diisocyanate and chain extender). Typically, the macrodiol is composed of difunctional polyester or polyether segments with low molecular weight diols or diamines used as a chain extender. This segmented architecture is responsible for the unique mechanical properties of polyurethanes, whereby the partially crystallized hard segments act as virtual crosslinks to give polyurethanes their high tensile strength and elasticity.

Polyurethanes are a class of polymers which have been extensively used as biomedical materials since the 1960's [34]. In addition to good biocompatibility, their controllable and diverse mechanical properties make them ideal biomaterials [35]. The typical applications of polyurethanes in medicine over the past years have included pacemaker leads, catheters, artificial heart prostheses, and coatings for silicone breast implants, which require that the implanted material remain stable inside the body for long periods of time. Subsequently, all traditional polyurethanes have been designed to be biostable and not degrade easily *in vivo* [34, 36].

By using polyether soft segments, a more hydrolytically stable material was produced, which increased the stability of the polymer in a long-term *in vivo* setting. However, the

polyether soft segments proved to be more susceptible to oxidation, which lead to unwanted degradation of the material, and the release of carcinogenic compounds due to the toxic precursors used during synthesis. For example, toluene diisocyanate is one of the most commonly used diisocyanates in the synthesis of biostable polyurethanes, and upon degradation of the urethane bonds, it results in the formation of toluene diamine, which has been shown to be carcinogenic. The effect of oxidation and subsequent degradation of the polyether–urethanes has led to the development of oxidation and hydrolysis resistant polycarbonate based polyurethanes.

Due to these complications, the interest in more biocompatible, hydrolytically unstable polyester based urethanes has increased over the last decade. Currently, the primary degradable polyurethanes used as a biomaterial in tissue engineering include polyester–urethanes, polyether–urethanes, and polyester–ether urethanes. Alternatively, hydrolytically labile bonds may be introduced in the hard segment to control the degradation rate of the polyurethane to suit a particular application [37-39], and faster degradation rates can also be obtained by making the polyurethane degradable, both hydrolytically and enzymatically [40]. The different types of biodegradable polyurethanes are discussed in the following sections.

1.3.1.1 Polyester–urethanes

Polyester–urethane is a term used to describe polyurethanes composed of polyester based soft segments. Different polyesters such as poly (L–Lactide) (PLA), poly (ε–caprolactone) (PCL), poly (vinyl alcohol) (PVA), and poly (glycolic acid) (PGA) have been used by various researchers for the synthesis of polyester–urethanes with a variety of unique properties.

For example, poly (ε–caprolactone) (PCL)–diols have been used by various researchers to synthesize polyester–urethanes with a wide range of properties. Different polyester–urethanes can be obtained by varying the molecular weight of the PCL–diol, the ratio of hard and soft segments, and the properties of monomers used in the synthesis [37]. The low glass transition temperature of PCL (T_g -60 °C) allows the polymer to be in an amorphous or

semi-crystalline state at normal body temperature, and is partially responsible for the strength and elasticity of the PCL based polyurethanes. The molecular weight of the PCL used for synthesis affects the mechanical properties of the resulting polyurethane. With all other parameters remaining the same, many researchers have noted a trend of increasing initial modulus and tensile strength when higher molecular weight PCL is used as the diol [37, 38, 41]. This phenomenon has been attributed to increasing phase separation leading to greater crystallinity of the higher molecular weight PCL soft segments. A wide range of mechanical properties were also obtained by replacing the PCL soft segment with a PCL–PLA co-polymer segment [42]. By varying the PLA to PCL content of the co-polymer, the properties of the polyurethane could be varied from a very stiff, inelastic polymer to a soft, elastic elastomer.

Other factors that affect the mechanical properties of the materials include the choice of diisocyanate and chain extender. Skarja *et al.* synthesized two different PCL–urethanes using both hexamethylene diisocyanate (HDI) and lysine diisocyanate (LDI) [37, 38]. The greater reactivity of the HDI resulted in higher molecular weight polyurethanes compared to those synthesized with LDI. When low soft segment molecular weights were used, the HDI based polyurethanes displayed a greater degree of phase separation when compared to the polyurethanes synthesized using LDI. The greater degree of phase separation displayed better tensile properties when compared to the LDI based polyurethanes due to the better packing of the hard segments. This phenomenon was illustrated in more recent work [43]. However, the effect of the diisocyanate on the mechanical properties of the polyurethane was not significant when higher soft segment molecular weights were used during synthesis.

The chain extender used during the synthesis is another means of modifying the mechanical properties of the polyurethane. Chain extenders are usually low molecular weight difunctional polyamines, polyfunctional polyamines, or polydiols, which are used to increase the molecular weight of the polyurethane. In addition to incorporating ester bonds in the soft segment, the incorporation of the appropriate chain extenders containing hydrolytically labile

ester linkages is a technique that has been exploited by researchers to increase polyurethane degradation rates [37, 38, 43, 44]. Furthermore, researchers have also synthesized amino acid based chain extenders, which are susceptible to enzymatic degradation [40, 45, 46]. These amino acid based chain extenders in combination with non-toxic diisocyanates such as LDI are expected to result in non-toxic and more biocompatible hard segment degradation products. The effect of the chain extender on mechanical properties mainly depends on the structure and the reactivity of the chain extender used. Chain extenders with pendant side chains may impede hard segment packing as opposed to aliphatic chain extenders, thereby resulting in inferior mechanical properties [41].

Tatai *et al.* demonstrated the effect of the reactivity of chain extender on the final properties of the polyurethane. Less reactive chain extenders resulted in polyurethanes with lower molecular weights and reduced mechanical properties when compared to polyurethanes synthesized using more reactive chain extenders. Different chain extenders have also been used to specifically tune the mechanical properties of polyurethanes. Due to the use of aliphatic diisocyanates, the biodegradable polyurethanes lack the stiffness of those made with aromatic diisocyanates. In order to overcome this drawback, Hirt *et al.* introduced poly (hydroxybutyric acid)–co–(hydroxyvaleric acid) (PHB/PV) as a chain extender into a polyurethane with PCL–diethylene glycol–PCL triblock soft segments using LDI as the diisocyanate [47]. The PHB/PV chain extender crystallized quickly to form glassy domains thereby causing better aggregation of the hard domains. The hard segment aggregation increased the phase segregation, which resulted in stiffer and stronger polyurethanes.

1.3.1.2 Poly (ester–ether) urethanes

Although the incorporation of ester bonds in the soft segment has been shown to create a more hydrolytically unstable biomaterial, the degradation rate of the polyurethane was still found to be slow. This was primarily due to the fact that the soft segment aliphatic polyesters such as PGA, PLA, and PCL were inherently very hydrophobic. It was hypothesized that the

incorporation of more hydrophilic macrodiols such as poly (ethylene glycol) (PEG) in the soft segment would increase the hydrophilicity of the polyurethanes, and accelerate hydrolytic degradation after implantation.

For example, triblock co-polymers of PCL–PEG–PCL were first used by Cohn *et al.* for the synthesis of faster degrading polyurethanes [48]. Further developments were made by Guan *et al.* who synthesized poly (ester–ether) urethanes using the PCL–PEG–PCL triblock co-polymer as a soft segment, a hard segment comprising of 1,4–butane diisocyanate, and putrescine as the chain extender [49]. By varying the ratio of PCL and PEG in the soft segment, the studies showed that the mechanical properties of the polyurethane could be improved by reducing the lengths of the PEG segments, and increasing the length of the PCL segments, which increased the degree of crystallinity to improve the mechanical properties of the polyurethane.

Ciardelli *et al.* also observed a similar phenomenon. The higher molecular weight of the triblock was able to increase the degree of soft segment crystallinity due to reduced interruption by the hard segments [44]. The effect of different ratios of the hydrophobic PCL and hydrophilic PEG on the overall hydrophilicity of the polyurethane has also been studied in detail [50]. A further increase in the degradation rates can be achieved by using hydrolytically and enzymatically labile chain extenders like phenylalanine diester in the hard segment of polyurethanes with PCL–PEG–PCL soft segments [37].

Polyurethane materials have also been used for cardiac reconstruction for congenital heart defects. Guan *et al*. designed a polyester urethane (PEU) based on 1,4–butane diisocyanate, PCL, and putrescine which could be fabricated into highly porous scaffolds using a thermal induced phase separation technique [51]. These biodegradable PEU scaffolds were implanted in the heart of adult rats in which a surgical defect had been introduced. The PEU scaffolds were found to permit greater cellular infiltration with minimal inflammation [52]. These PEU scaffolds were also fabricated into tubular constructs to evaluate their effectiveness as

vascular grafts. The tubular scaffolds were evenly seeded with mouse derived smooth muscle cells using a rotational vacuum seeding technique, and displayed burst pressure and suture retention values which closely matched that of native arteries [53]. In addition to vascular engineering, biodegradable polyurethanes based on methylene diphenyl diisocyanate (MDI) as the diisocyanate component have also been used as scaffold materials for ligament tissue engineering. PHB/PV based polyurethanes have also been investigated as bioresorbable nerve guide materials [54]. The nerve guides fabricated form these polyurethanes were degradable and supported nerve regeneration with reduced inflammatory response.

1.3.2. Polycarbonates

Polycarbonates are a family of block co-polymers, which are characterized by the presence of a carbonate bond in the backbone of the polymer chain. To date, the two major classes of biodegradable polycarbonates that have been extensively studied for biomedical applications are the co-polymers of poly (1,3–trimethylene carbonate), and tyrosine derived polycarbonates. The latter family of materials has a glass transition temperature ranging from 52–90 °C, making it a rigid material at room and body temperature. Since the scope of this discussion is limited to elastomeric materials, tyrosine derived polycarbonates have been omitted.

Poly (1,3–trimethylene carbonates) (PTMC) are an amorphous polymer, which was first synthesized by Zhu *et al.* through a bulk ring open polymerization of 1,3–trimethylene carbonate in the presence of catalysts [55]. PTMC were found to be rubbery materials at room temperature, and displayed low glass transition temperatures ranging from -26 °C to -15 °C. Further properties of PTMC are covered in Table 1.2.

Table 1.2 Thermal and Mechanical Properties of PTMC Co-polymers

		Thermal Properties		Mechanical Properties		
Polymer Name	**MW (Da)**	**Tg (°)**	**Tm (°)**	**Modulus (MPa)**	**Peak Stress (MPa)**	**Break Strain (%)**
Low MW PTMC	42,100	-15	-	2.94	0.49	160
High MW PTMC	324,000	-19	-	6	12	830
DLLA 21 TCM 79[a]	358,000	-9	-	5	2	270
DLLA 80 TCM 20[a]	718,000	33	-	1900	46	7
DLLA 50 TCM 50[a]	644,000	11	-	16	10	570
CL 23 TCM 77[a]	246,000	-25	-	3.9	0.8	103
CL 75 TCM 25[a]	183,000	-55	5.7	4.6	0.1	236
CL 90 TCM 10[a]	184,000	-22	49.9	252	40	906

[a] Denotes the mol % of each monomer in the co-polymer

In addition to moderate elastomeric properties, the utility of homopolymeric PTMC as a temporary implant material was hampered by its slow degradation. Over a 30-week period, the PTMC samples displayed a mass loss of only 9%. However, subcutaneously implanted PTMC samples were rapidly degraded *in vivo*, and the implanted samples beyond a 3-week period could not be detected macroscopically, which was attributed to hydrolytic and enzymatic cleavage of the carbonate bonds [56]. Co-polymerization with other polymers, primarily degradable polyesters like poly (D, L-lactide) (PDLLA) and PCL, has been employed to improve the degradability and the mechanical properties of polycarbonates [56-60].

The potential of these co-polymers as scaffolds for heart tissue engineering and synthetic nerve guides for nerve regeneration have also been evaluated [59-61]. It was also found that high molecular weight PTMC were very flexible and tough due to the excellent ultimate stress and strain characteristics. These mechanical properties were attributed to strain induced crystallization of the polymeric network upon application of high deforming stress. This phenomenon has also been studied extensively elsewhere [62].

1.3.2.1 Poly (D, L Lactide–co–1,3–trimethylene carbonate)

To tune the mechanical properties of the resulting polycarbonate, various researchers have controlled the molecular weight of the material using co-polymers of amorphous poly (D, L–lactide) and PTMC [58, 63, 64]. In all cases, the co-polymer synthesis was carried out through a bulk ring open polymerization of the different monomer ratios with stannous octoate

as the catalyst. High molecular weight poly (PDLLA–co–PTMC) co-polymers were obtained by varying the reaction conditions to reduce the degree of transesterification. The low molecular weight co-polymers were synthesized using 1,3–trimethylene carbonate with a T_g value of -26 °C [55, 64]. As expected, the co-polymerization was able to produce co-polymers, which had properties that were intermediate to those of the PDLLA and PTMC homopolymers. The T_g temperatures of the co-polymers ranged from -16 – 56 °C depending on the percentage of lactide units in the chain. Co-polymers with a greater lactide percentage had higher glass transition temperatures, and were generally stiffer. The mechanical properties of the various polymers ranged from weak elastomers to stiff and rigid materials. PTMC–PDLLA co-polymers with a higher PTMC content exhibited high elongation at break (600 – 800%), but were weak (tensile strength ≤ 2 MPa) and underwent irreversible deformations upon extension. A higher PDLLA content resulted in polymers with strong tensile strengths (28 – 33 MPa), but were brittle with low elongations at break (6 – 7%) [58].

Intermediate co-polymers containing similar molar percentages of both PTMC and PDLLA exhibited good elastomeric behavior. For example, a co-polymer containing equal molar percentages of PDLLA and PTMC (1:1 molar ratio) displayed a tensile strength of 10 MPa and an elongation up to 570%. The dependence of mechanical properties on the polymer molecular weight was also evident. The higher molecular weight co-polymers displayed better mechanical properties than their low molecular weight counterparts [58, 63]. All the co-polymers were found to be hydrophobic because of the hydrophobicity of the starting monomers, and the *in vitro* degradation was influenced by the percentage of the monomeric constituents. For example, the polymers with a higher PTMC content underwent surface degradation, while the higher lactide containing polymers underwent bulk degradation [64].

Pego *et al.* conducted a detailed investigation of the degradation behavior of these co-polymers over a 111–week period. During this study, the group examined the effect of the monomer composition on the *in vitro* degradation profiles. The effect of degradation on the

thermal and mechanical properties of the various co-polymers was also examined [65]. Even though PDLLA contained a higher number of ester bonds, the co-polymers showed faster degradation rates compared to PDLLA alone. This phenomenon was attributed to the lower T_g of the co-polymers when compared to PDLLA, which made the chains more mobile. The added mobility increased water uptake, and allowed the ester bonds to be more accessible in the co-polymers. The loss of mechanical properties, mass loss, and water uptake could all be co-related to the loss of molecular weight of the polymers as the hydrolytic scission of their chains progressed over the evaluation period.

The co-polymers containing a high percentage of PTMC were not resorbed over the evaluation period, and co-polymers with higher PDLLA contents were resorbed within 11 months. An extensive year-long study was also conducted by Pego *et al.* to evaluate the degradation profile of these polycarbonates *in vivo* [56]. It was determined that the polymers degraded faster under the influence of the physiological environment, as opposed to the long *in vitro* degradation times. This was caused by the enzymatic degradation of the carbonate moieties similar to that reported earlier [55]. To further support the theory of enzymatic breakdown of the carbonate bond, poly TMC was totally resorbed within 3 weeks *in vivo*, while a negligible mass loss was shown over a 2 year period *in vitro*.

PTMC–PDLLA co-polymer films were seeded with rat cardiomyocytes to determine their suitability for cardiac applications. Seeded cardiomyocytes adhered and proliferated very well on the PTMC–PDLLA films [59, 61]. Porous scaffolds made from PTMC and PDLLA co-polymers were prepared by a compression molding of the salt–polymer precipitate, and followed by salt leaching. Although the PTMC–PDLLA co-polymer films showed good cardiomyocytes growth, no cell culture results on PTMC–PDLLA co-polymer scaffolds have been reported [59, 66].

1.3.2.2 Poly (ε–caprolactone–co–1,3–trimethylene carbonate)

As mentioned previously, co-polymerizations were found to be a suitable method to modulate the degradation rates of elastomeric polymers based on PTMC. PDLLA was employed as a co-monomer to increase the degradation rate of the produced elastomers. However, for certain tissues repair applications such as synthetic nerve guides, it is more desirable to use an elastic material, which has a slower degradation rate. Pego *et al.* hypothesized that the co-polymerization of ε–caprolactone (PCL), a semicrystalline polyester which degrades very slowly, and 1,3–trimethylene carbonate could yield a co-polymer, which could degrade slower than the PTMC–PDLLA co-polymers while retaining their elasticity over a longer time period [57]. High molecular weight (M_n > 100,000) poly (caprolactone–co–trimethylene carbonate) (PCL-PTMC) co-polymers were synthesized through a ring open polymerization of the co-monomers in the presence of stannous octoate as a catalyst.

The glass transition temperatures of the co-polymers varied from -15 °C to -60 °C, depending on the molar percentage of each co-monomer in the melt. Co-polymers with higher caprolactone content had lower T_g values. As the caprolactone content increased, the co-polymers ranged from amorphous to semi-crystalline in nature. As observed with the PTMC–PDLLA co-polymers, increasing the molar percentage of PTMC in the material produced weak polymers with a low tolerance to deformation. Both *in vitro* and *in vivo* degradation studies were conducted to understand the mechanism of degradation of the co-polymers obtained [56, 67]. From the *in vitro* results, it was found that the PCL–PTMC based co-polymers degraded much slower than the PTMC–PDLLA based co-polymers [65]. The semicrystalline samples with a high PCL content did not undergo any dimensional changes over a two–year period. In contrast, the amorphous samples with higher PTMC content degraded more rapidly and showed reduced dimensions. The hydrolysis rate *in vitro* was a function of the PCL content in the co-polymer. Higher hydrolysis rates and subsequently higher water uptake and mass loss were detected in

the polymers with higher ester content. Even in the *in vivo* study, the PCL–PTMC co-polymers degraded slower when compared to the PTMC–PDLLA co-polymers [56].

Apart from material characterization, the adhesion and proliferation of human Schwann cells on these co-polymers has been studied to determine their suitability as artificial nerve guides [59, 60]. Human Schwann cells (HSCs) were seeded on PTMC and PCL–PTMC co-polymers coated with fibronectin to evaluate the suitability of these elastomers as nerve guide materials. These materials are ideal for fabrication of nerve guides because of their long degradation rates, which are well suited to the long regeneration time of neural tissue. The number of primary HSCs which attached to the coated polymers was similar to the number of cells seeded on a control gelatin film [60]. In addition, *in vivo* studies have shown that PCL–PTMC co-polymers can be effective nerve guides in the regeneration of autonomous neural tissue [68].

1.3.3. Polyesters

Polyesters are the most widespread category of polymers used in biomedical applications. The ester bond is important because it allows for degradation through hydrolytic cleavage in the presence of water. Unlike enzymatic degradation, this form of degradation is advantageous because of the minimal site–to–site and patient–to–patient variations. Polyesters that possess elastic properties to meet the requirements for soft tissue engineering are shown in Table 1.3. The following section will focus on the polyester elastomers that have been used in the field of soft tissue engineering.

Table 1.3 Mechanical Properties of Polyester Elastomers in Recent Research

	Mechanical Properties		
Polymer Name	**Young's Modulus (MPa)**	**Break Strain (%)**	**Tensile Strength (MPa)**
PHB	2500	3	36
P4HB	70	1000	50
PGS	0.056–1.2	40–448	0.2–0.5
PGSA	0.048–1.37	47–170	0.54–0.5
POC	1.85–13.98	117–502	2.93–11.15
PEC	0.25–1.91	140–1505	0.51–1.51
PPSC	0.6–1.23	226–432	0.87–2.12

1.3.3.1 Polyhydroxyalkanoates (PHAs)

In the early 1920's, it was discovered that the bacteria *bacillus megaterium* was capable of producing a unique chemical, poly (3–hydroxybutyrate) (PHB), which is the most common polymer among the polyester class. Since then, more than 150 different monomer combinations have been used in the formation of different polymers within the PHA family [69]. Four different pathways have been revealed for the synthesis of PHA through the process of biosynthesis, which has been mentioned in detail elsewhere [70]. Due to advancements in the field of genetic engineering, researchers have also used plants as the production house for PHB-related polymers [71].

Several groups have also reported the chemical synthesis of poly (3–hydroxyalkanoates) (P (3HB)) through the process of a ring opening of β–butyrolactone (BL) in the presence of aluminum, zinc, and tin based catalysts [72-74]. However, these reactions did not yield high molecular weight polymers. To overcome this limitation, Hori *et al.* utilized the distannoxane complexes as an excellent catalyst for the ring-opening polymerization of (*R*)–b–butyrolactone ((*R*)–BL) and BL to produce P [(*R*)–3HB] and P (3HB) of high molecular weights and in high yields [75]. By using different combinations of various monomers, researchers have successfully produced PHAs with a wide range of mechanical properties and degradation profiles. For example, poly (3–hydroxybutyrate) is a stiff polymer with a Young's Modulus of 2500 MPa and 3% elongation at break, whereas poly (4–hydroxybutyrate) is an elastic polymer with a Young's Modulus of 70 MPa and 1000% elongation at break. In terms of their biocompatibility, PHA elastomers are biosynthetic polymers and require serious consideration on their purity [76].

In the early 1990's, Akhtar *et al.* reported a prolonged acute inflammatory response and severe chronic inflammatory response from PHA films implanted *in vivo*. William *et al.* proposed the idea of using a depyrogenation technique through the use of an oxidizing agent that resulted in the reduction in the amount of endotoxins used during synthesis. In addition, William and co-

workers also understood the problems associated with the use of solvents while extracting the polymer. The group found that a material with higher purity could be obtained if the polymer was extracted with hexane or acetone instead of the traditional chlorinated solvents. In order to support their study, the research group performed *in vivo* tests by placing several different types of implants such as microspheres, tubes, and pellets subcutaneously in mice. The histological results revealed the formation of a thin fibroblast capsule (four to six cell layers), and the absence of macrophages at the implant sites [76] when non-chlorinated solvents were utilized.

Medical device companies have extensively investigated P4HB due to its potential as scaffold material for engineering various tissues. For example, Tepha Inc. is evaluating this member of the PHA family in order to meet all the standards set by the US Food and Drug Administration (FDA). In two independent studies lead by Stock and co-workers, it has been demonstrated that this elastomer is a potential candidate for engineering heart valves and for blood vessel augmentation [77, 78].

1.3.3.2 Poly (glycerol–sebacate) (PGS)

In the late 1990's, Nagata and co-workers reported their work on the synthesis and characterization of polyester based on sebacic acid and glycerol. By reacting glycerol and sebacic acid, they achieved their goal in creating an environmentally friendly plastic that can be degraded by soil bacteria [79]. PGS is synthesized through a polycondensation reaction, which produces degradable ester bonds throughout the polymer backbone to solve any degradation issues. However, material property challenges still remained due to the non-elastic nature of the polymer. In 2002, Wang *et al.* realized that the monomers of this polymer are biocompatible, which opened the door for its use in biomedical applications [80]. After further study of the synthesis procedure and chemical structure, Wang and co-workers realized that Nagata *et al.* were using a 2:3 molar ratio of glycerol and sebacic acid in the reaction, which resulted in the total consumption of all the available functional groups. In contrast, Wang *et al.* divided the reaction into two steps to preserve functional groups for later processing. Thus, a 1:1 molar ratio

of glycerol and sebacic acid was used to first obtain a linear pre-polymer. This initial step preserved the pendant hydroxyl groups in the PGS pre-polymer, which was later used to form an elastic three-dimensional crosslinked network through ester bond formation [80]. Through this novel idea, a new trend of initial pre-polymer formation followed by post-polymerization was introduced to produce scaffolding materials with improved functionality in the field of soft tissue engineering.

PGS is a soft (Young's Modulus of 0.282 ± 0.025 MPa) and elastic (elongation at break of 267 ± 59.4%) material that has potential for engineering tissue such as arteries, veins, and nerves [32, 80]. A study led by Sundback *et al.* utilizing PGS for neural reconstruction, showed the potential of PGS as a scaffolding material with a desirable biocompatibility [32]. The study also proved that a normal morphology and acceptable growth rate of Schwann cells could be obtained when compared to PLGA, which is widely used in neural reconstruction. In a study led by Chen and co-workers, the mechanical properties of PGS were evaluated by varying the degree of crosslinking in order to match the mechanical properties of myocardial tissues. They further demonstrated that PGS is bioresorbable through hydrolysis and enzymatic degradation. The degradation rate of PGS can be fine tuned in order to meet the requirement for the construction of heart patches [67].

1.3.3.3 Poly (glycerol sebacate) acrylate (PGSA)

In 2007, Nijst *et al.* created a photocurable elastomeric polymer based on the previously made PGS to rapidly crosslink and circumvent the harsh post-polymerization crosslinking of the previous material. The group incorporated vinyl functional groups into the polymer backbone by acrylating the available hydroxyl groups of the PGS pre-polymer with acryloyl chloride. Due to the presence of these vinyl groups, the polymer achieved a 3D crosslinked network structure through a free radical crosslinking mechanism using ultraviolet light, which eliminated the long and harsh post polymerization conditions used during the original PGS synthesis. This increased polymer's potential to encapsulate cells or temperature–sensitive biomolecules [3]. It

was also reported that the mechanical properties of polymer could be tuned according to the degree of acrylation (Table 1). Furthermore, co-polymerizing the polymer with PEG diacrylate (PEGDA) was also shown to modulate the mechanical properties of the polymer [3]. The prime interest of developing PGSA was to proliferate and differentiate stem cells into the desired tissue by encapsulating them in the porous matrix of the polymer. Interestingly, human embryonic stem cells (hESCs) encapsulated in the polymer matrix and allowed to grow for seven days showed a colonial organization expressing the Ki67 protein and all three germ layers [71].

1.3.3.4 Poly ((1,2–propanediol–sebacate)–citrate) (PPSC)

After realizing the outstanding work of the previous groups, Lei *et al.* proposed synthesizing an oligomer terminated with an alcohol from the monomers sebacic acid and 1,2–propanediol. In addition to further linking these oligomers, citric acid was incorporated to fine-tune the mechanical and degradation properties. The elastomer produced showed desirable mechanical properties with low water retention and a rapid degradation profile. However, biocompatibility tests and application oriented studies of this elastomer are not yet reported [81].

1.3.3.5 Poly (1,8–octanediol malate) (POM)

A recent study by Wan *et al.*, proposed a thermoset elastomer based on 1,8–octanediol and maleic acid utilizing a polycondensation reaction between the carboxylic acid and alcohol. This elastomer displayed tensile strengths of 7.32 ± 0.63 to 25.6 ± 1.42 MPa, compressive Young's Modulus of 0.12 ± 0.02 to 0.25 ± 0.01 KPa, and an elongation at break of less than 15%. However, no permanent deformation was reported after 500-press loading and release cycles with 30% maximum strain. The POM elastomer showed a linear degradation profile in PBS at 37 °C, where the majority of mass loss (up to 90 %) was reported by week 13. The study was targeted for the regeneration Annulus Fibrosus (AF). POM not only shows good AF cell growth, but also cell penetration into the scaffold. However, in order to support significant cell growth, POM required more than 2 days crosslinking at 120 °C under vacuum (2 Pa) [82].

1.4 Citrate-Based Polyester Elastomers

1.4.1. Citric Acid as a Cornerstone of Biomaterial Development

Among the polyester family of materials, citrate-based polyester elastomers have been shown to offer a wide range of controllable mechanical and degradation profiles along with surface affinities towards many cell types [83-85]. This new class of biomaterials is all synthesized with non-toxic monomers using simple and cost effective procedures. Citric acid has been historically known as a commercially important compound in the chemical, food and beverage, cleaning, and cosmetics industries [86, 87]. However, recent research in the field of biomaterials has exploited the benefits of citric acid in the development of biodegradable materials for tissue engineering [20, 88], drug delivery [89, 90], bioimaging [85], and gene delivery [91].

Citric acid is a nontoxic, FDA approved, readily available, inexpensive, and robust multifunctional monomer that can provide valuable pendant functionality to give citrate-based materials biomaterials their unique advantages over existing materials. Citric acid is mainly used to provide degradable ester-crosslink formation, but also allows for strong hydrogen bonding, fluorescent properties, balanced hydrophobicity, and enhanced hemocompatibility [87, 92, 93]. Sodium citrate, a salt form of citric acid, is often used in hospitals as an anticoagulant, and the calcium-chelating properties that allow its use as an anticoagulant may be implicated in the synthesis of materials with reduced thrombogenicity [84]. Furthermore, citrate moieties may play an important biological role in the materials for bone tissue engineering as citrate makes up 5.5% by weight of the organic portion of bone, and recent reports have shown the role of citric acid in regulating the thickness of hydroxyapatite nanocrystals within a collagen matrix [94]. Due to these multiple benefits, citric acid has now established itself as an important cornerstone in the development of novel biomaterials with unique properties over existing materials. The following sections provide a brief review of the recently developed citrate-based biodegradable elastomers.

1.4.2. Existing Citrate-Based Polyester Elastomers

1.4.2.1 Poly (diol citrates) (PDC)

In 2004, Yang *et al.* synthesized the first citrate-based elastomer, poly (diol citrates) (PDC), via a convenient and cost effective polycondensation reaction [84]. As seen in Figure 1.1, citric acid was used as a multifunctional monomer to react with different aliphatic diols ranging from 3-16 carbon chain lengths in a 1:1 molar ratio at 140 °C under mechanical stirring to form a pre-polymer, which could be further post-polymerized into crosslinked polyester networks under various polycondensation conditions [95]. The resulting material has been shown to cover a wide range of mechanical properties, degradation profiles, and surface energies, which are all important in controlling the biological response to an implanted material [95].

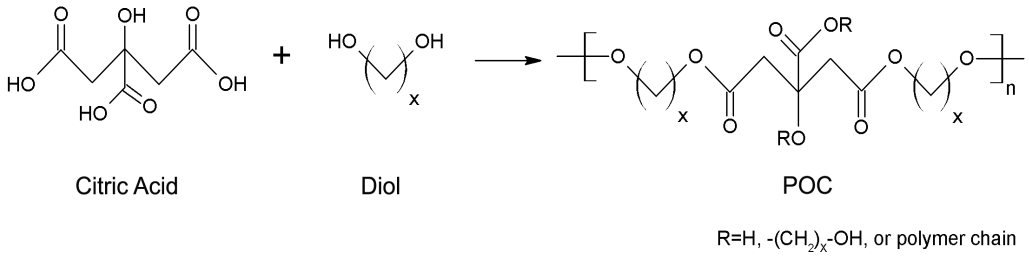

Figure 1.1 Poly (diol citrate) Synthesis Schematic

By controlling the post-polymerization temperature and time, the elastomer's mechanical properties and degradation rates can be tuned to fit a wide range of tissue engineering applications. An increase in post-polymerization temperature and time resulted in a network with increased mechanical properties due to the increased crosslinking densities. The reported range of mechanical properties for this family of elastomers meet the specific needs for the engineering of various soft tissues including cartilage, blood vessels, and bladders. The preliminary biocompatibility evaluations showed that PDC supported the attachment and proliferation of human aortic smooth muscle cells and endothelial cells without any surface modifications [84]. Histological analysis of poly (1,8-octanediol) (POC) films (a representative

PDC) subcutaneously implanted in Sprague-Dawley rats confirmed the material biocompatibility. After 4 months of implantation, the inflammatory response and thickness of the fibrous capsule was smaller than the reported values of commonly used biodegradable polymers, poly (D, L-lactic-co-glycolide) (PLGA) [84, 95].

Since the mechanical properties of this new family of elastomers could be tuned to fit the needs of vascular tissue engineering, Yang *et al.* reported on the fabrication of a novel biphasic scaffold for small diameter blood tissue engineering (**Figure 1.2**) [88]. These scaffolds consisted of a non-porous lumen and porous outer phase. The non-porous phase was designed to provide a continuous surface for the adhesion and proliferation of endothelial cells while maintaining the strength and elasticity of the construct. The outer porous phase was designed to facilitate the three-dimensional growth of smooth muscle cells. Burst pressures for this type of scaffold were as high as 2800 mmHg, which are similar to that of the native small diameter arteries [88]. The overall results suggest that PDC biphasic scaffold designs can be a viable strategy towards the engineering of small diameter blood vessels.

Figure 1.2 Poly (diol citrate) Vascular Graft

1.4.2.2 Poly (diol citrate) Composites

Previous studies have shown that adding a second component to the elastomeric phase of the polymer can enhance the mechanical properties of an elastomer. Webb *et al.* have

demonstrated that the strength and stiffness of PDC can be increased without losing the material's elasticity by introducing a biodegradable polymeric nanophase into the network. This is the first report on the creation of a nanocomposite composed of a biodegradable micro- and nanophase. The nanoparticles/nanostructure act as additional crosslink points to reinforce the polymer's network chains to increase the mechanical properties of the resulting material. When PLLA or PLGA were incorporated as the nanophase into the PDC network, the tensile strength and modulus increased from 1.51 ± 0.08 to 3.54 ± 0.35 MPa and 1.59 ± 0.13 to 17.73 ± 1.99 MPa, respectively, when compared to PDC controls. Due to the enhanced mechanical properties and biocompatibility of the composite, the elastomer network has been targeted for applications including tissue patches and the engineering of cartilage and ligaments where increased strength is required.

PDC composites with hydroxyapatite (HA) have also been developed for bone tissue engineering. HA is a bioceramic that is naturally present in bone, and has been shown to improve the osteoconductivity of polymers [96]. In 2006, Qiu *et al.* was the first group to produce a bioceramic-elastomer composite based upon HA and PDC, which showed mechanical properties comparable to native bone. The bioactive ceramic component was able to be incorporated up to 65% of the entire composite weight, which is more than previous material could incorporate, and maximized the osteointegration while maintaining the elastomer's degradability [83]. The elastomer composite successfully induced surface mineralization after 15 days of incubation in simulated body fluid (SBF), and displayed favorable primary human osteoblast cell adhesion *in vitro* with no chronic inflammation after implantation in rabbits. Composites implanted into rat medial femoral condyle appeared to be well integrated with the surrounding cartilage along with mineralized chondrocytes located immediately adjacent to the implant, which suggests normal bone remodeling. The composites also showed good processability in the ability to be machined and molded into bone screws for bone fixation applications [83].

1.4.2.3 Poly (xylitol-co-citrate) (PXC)

Bruggeman and coworkers first reported a polymer based on xylitol and citric acid referred to as poly (xylitol-co-citrate) **(**PXC) [1]. The rationale behind this design was to create a biologically relevant water-soluble pre-polymer using non-toxic FDA approved monomers endogenous to the human metabolic system. PXC was synthesized by reacting xylitol with citric acid at 150 °C and 40 mTorr for 1 – 12 hours. By using citric acid as a multifunctional monomer, PXC is able to form a randomly crosslinked network resulting in a polymer with elastic behavior. The pendant functionalities of xylitol were further modified with an acrylate group donated by methacrylic anhydride (**Figure 1.3**). It was claimed that through the use of xylitol, a metabolic intermediate in the mammalian carbohydrate, and citric acid, PXC should display good biocompatibility.

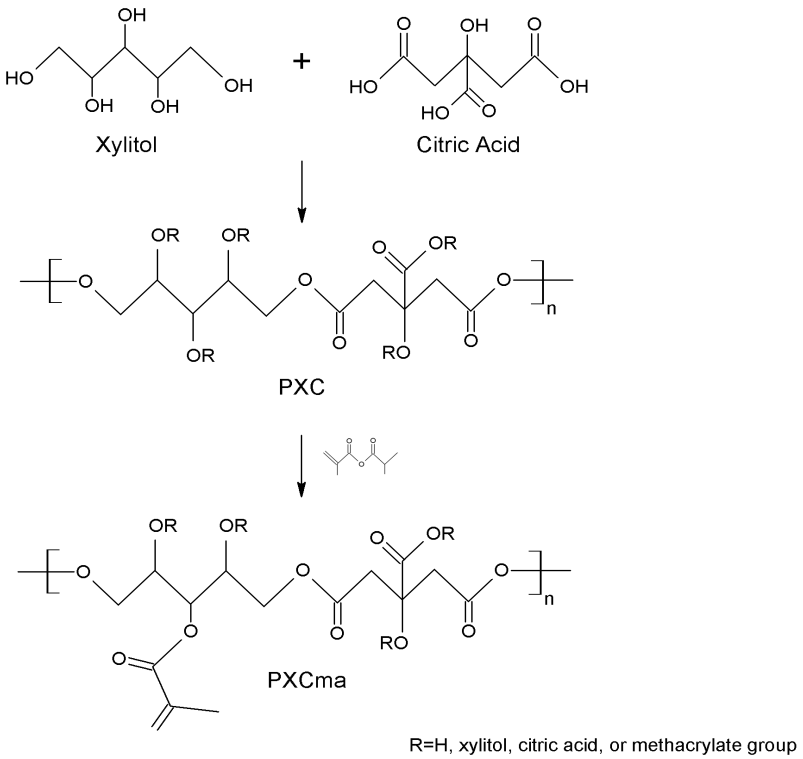

Figure 1.3 Poly (xylitol-co-citrate) Synthesis Schematic

PXC displayed a compressive modulus of 5.84 ± 1.15 KPa with a maximum compressive strain of 79.9 ± 5.6%. During the cyclic testing of this material, minimum hysteresis was reported confirming the limited deformability under cyclic strain. The targeted application of this polymer is the field of tissue engineering and drug delivery. The preliminary biocompatibility evaluations showed that this hydrogel does not support cell attachment, however, its pre-polymer chains are cytocompatible. Once inside the body, PXC degraded completely within two weeks and showed a comparable host response with PLGA. In general, this hydrogel is a promising candidate as a biomaterial for tissue engineering and drug delivery.

1.4.2.4 Biodegradable Aliphatic Photoluminescent Polymers (BPLP)

Biodegradable fluorescent polymers have attracted much attention in drug delivery and tissue engineering. However, in most of the published studies, biodegradable fluorescent polymers are made by either conjugating or encapsulating organic dyes or quantum dots (QDs) with the biodegradable polymers such as cyanine dye conjugated PLGA nanoparticles, rhodamine encapsulated PLA nanoparticles, porphyrin membrane-loaded polymer vesicles, or inorganic quantum dots encapsulated within polymers [97-101]. Unfortunately, the success and long-term biocompatibility of materials with toxic fluorescent imaging agents has not yet been fully understood.

Yang *et al.* has recently discovered a family of novel aliphatic biodegradable photoluminescent polymers, referred to as BPLPs [85]. Unlike traditional non-degradable aromatic fluorescent polymers used in the lighting industry, BPLPs are aliphatic degradable oligomers synthesized using biocompatible monomers including citric acid, aliphatic diols, and different amino acids via a very simple and cost-effective polycondensation reaction. BPLPs can be further polymerized into elastomeric crosslinked aliphatic biodegradable photoluminescent polymers (CBPLPs). These polymers offer advantages over the traditional fluorescent organic dyes, inorganic quantum dots, and non-degradable fluorescent polymers in terms of their

excellent cytocompatibility, controlled degradability, and tunable photoluminescent properties with fluorescence emissions up to 725 nm within the known BPLPs.

As seen in Figure 1.4, the synthesis of BPLPs is very simple and is based upon the previously published PDC. Briefly, one of the twenty (L-) amino acids is reacted with citric acid and aliphatic diols at 140 °C to prepare BPLPs such as BPLP-cysteine (BPLP-cys). The various forms of BPLPs (pre-polymer solution, crosslinked films, scaffold, and nanoparticles) have been shown to emit strong fluorescence.

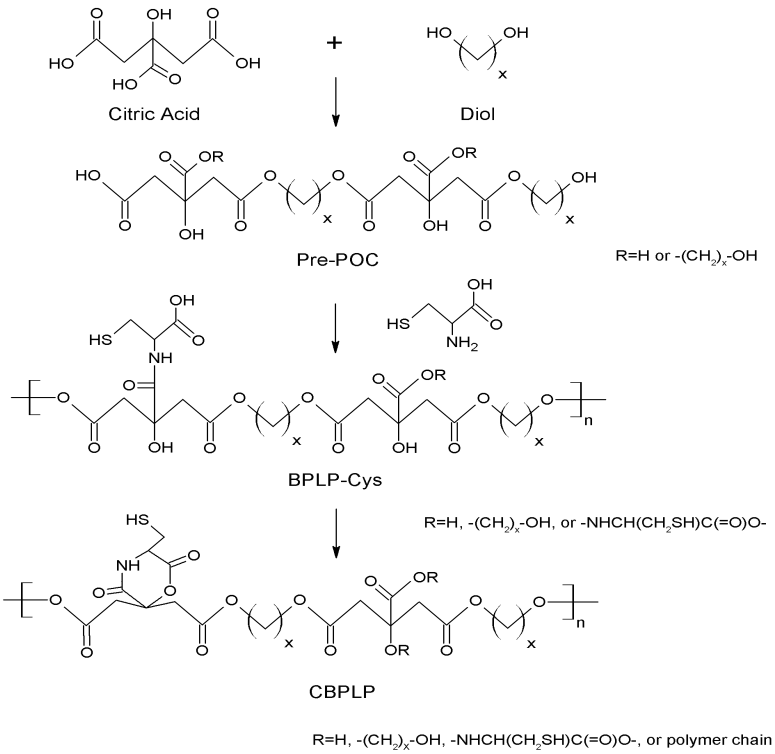

Figure 1.4 Biodegradable Aliphatic Photoluminescent Polymer Synthesis Schematic

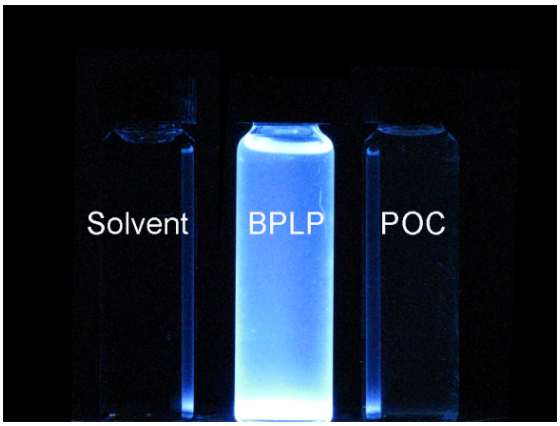

Figure 1.5 Biodegradable Aliphatic Photoluminescent Polymer Fluorescence

Figure 1.5 shows that only BPLP-cys emits strong fluorescence indirectly demonstrating that BPLP-cys differs from the POC polymer (the precursor of BPLP). The fluorescent emission wavelength can be tuned by adding different amino acids to POC for BPLP synthesis. All 20 amino acids have been used to synthesize a family of BPLPs, which emit tunable fluorescence color from blue to red with a quantum yield up to 62.3%. To test the potential of BPLP nanoparticles and CBPLP scaffolds for *in vivo* bioimaging purposes, BPLP-ser nanoparticles were injected subcutaneously into the back of nude mice. As shown in Figure 1.6, the images of BPLP-ser porous scaffolds emit a strong fluorescence *in vivo*. Strong fluorescence was also emitted from the BPLP nanoparticles implanted in the subcutaneous cavities. The findings from the *in vivo* bioimaging studies lend strong support that BPLP nanoparticles and CBPLP scaffolds can be fluorescence-imaged, and the signals can be quantitatively analyzed *in vitro* and *in vivo* potentially for cellular/tissue/scaffold bioimaging [85]. The development of BPLPs may address the urgent needs in nanomedicine for biodegradable theranostic biomaterials, which may deliver imaging agents and therapeutic probes in a single setting without using any inorganic imaging agents.

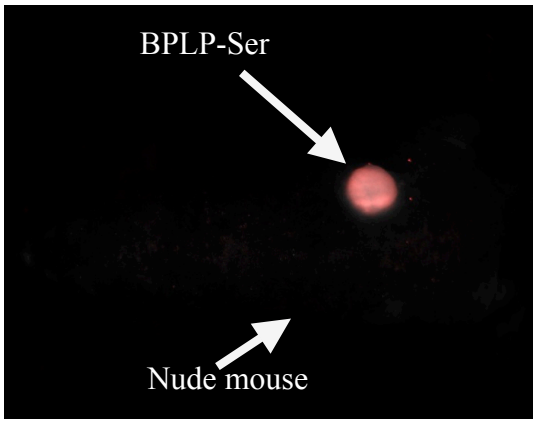

Figure 1.6 Biodegradable Aliphatic Photoluminescent Polymer Scaffold Implanted in Nude Mouse

In all CAB designs, there exists common innovations: 1) citric acid is a multifunctional monomer that can be reacted with various diols to form a crosslinked polymer network; 2) the incorporation of various diols provides flexibility to tune the overall material properties of the resulting polymer; 3) the incorporation of homogeneous biodegradable crosslinks confers elasticity to the resulting material while preserving free pendant functional groups, which can be used for later modification; and 4) polycondensation is a simple and cost effective synthesis strategies that can be used without toxic catalysts or harsh processing conditions, which can translate into higher manufacturing costs and hinder the commercial and clinical implementation of their use in tissue engineering.

1.5 Biomaterial Design and Requirements

In review of the recent literature, many important design criteria must be met when creating the starting materials for the intended target application. The following sections will discuss the design requirements and concerns that should be taken into consideration when creating an elastic material for soft tissue engineering applications.

1.5.1. Polymerization Mechanisms

The two main forms of polymerization for elastic polymers are polycondensation and polyaddition reactions. Polycondensation reactions have stepwise growth kinetics, and are

characterized by the formation of by-products during synthesis. For example, a diol can be reacted with a diacid to produce polyesters with water as a by-product. Polyaddition reactions display chain-growth kinetics, and require the use of an initiator. Chain initiation, propagation, and termination are steps that characterize a polyaddition reaction. Through this general mechanism, the average molecular weight of the polymer increases during the reaction. Thus, high molecular weight polymers can be produced in a polyaddition reaction.

1.5.2. Methods to Incorporate Elasticity

The two methods to incorporate the elasticity are physical crosslinking and chemical crosslinking. Certain segments of polymer chain will form a crystalline structure, which will serve as a means for physical crosslinking. In the case of polyurethanes, the clusters of hard segments act as “pseudo cross-links”, and allow the material to behave as an elastomer [46]. When the temperature is raised, the hard segment clusters disassociate, and the material can be made to flow. When subsequently cooled, the clusters reform and the material will again exhibit elastomeric properties. Some ABA triblock co-polymers will also show elastomeric properties [102]. For example, the thermal liable crosslinks in an ABA triblock co-polymer can aggregate to form physical crosslinking between polymer chains.

Chemical crosslinking joins the polymer chains together into a network linked by covalent or ionic bonds. Unlike physical crosslinks, the chemical crosslinks are generally irreversible, and display greater mechanical strength and elasticity. It is well known that natural extracellular matrix components such as collagen and elastin are crosslinked polymers. The crosslinking provides these natural materials with their elastic nature. Due to this phenomenon, researchers have utilized the concept of crosslinking in the creation of elastomers to meet the versatile needs in tissue engineering and other biomedical applications. In order to create a polymer with a 3D elastomeric network structure, at least one of the monomers chosen should be multifunctional. In addition to providing the needed functional groups for chain extension, a multifunctional monomer provides valuable functional groups, which can be used in later post-

processing to create a 3D crosslinked network. Thus, by creating crosslinked network structure, a material with elastic properties can be obtained.

1.5.3. Biocompatibility

Biocompatibility is a term used to describe the ability of a material to perform with an appropriate host response in a specific application. For the materials used in biomedical applications, the biocompatibility should always be put as the first concern. There are several factors that can affect the biocompatibility of a material. For example, the hydrophilicity or hydrophobicity of a material can greatly influence its biocompatibility. It has been demonstrated that the degree of hydrophilicity/hydrophobicity should be balanced to achieve optimal cell affinity [103, 104]. The acidity of a material can also influence its overall biocompatibility. Certain functional groups located on the polymer chain have the ability to greatly change the pH of the surrounding area. In addition to the chemistry of the bulk material causing pH changes, certain materials will degrade into acidic products to alter the pH of the immediate area. This deviation in pH from the body's normal values can create a cytotoxic effect, which can later lead to adverse reactions. The use of certain chemicals during the synthesis of elastomers can also cause biocompatibility issues. In the case of elastomers created through a polyaddition mechanism, one factor to influence the material's biocompatibility is the toxicity of initiator used during synthesis. In other situations, redox initiators and photoinitiators used to crosslink the polymer have been shown to be toxic to cells when used in large concentrations. Thus, the amount of initiator used for crosslinking should be strictly controlled, and any residual remaining initiator not used during the crosslinking mechanism should be removed.

1.5.4. Mechanical Properties

During the mechanical testing of a polymer, the stress–strain curve obtained is used to define many important parameters of a material's mechanical properties. The stress–strain curve is a graphical representation of the relationship between the amount of stress applied and the resulting strain of the sample. The tensile strength of a material is the maximum amount of

tensile stress that can be subjected to the material before failure. Normally for an elastomer, there is no yield point, and as a result, the peak stress of the stress–strain curve should appear at the break point. The compressive strength is usually obtained experimentally by means of a compression test, and is the value of uniaxial compressive stress reached when the material fails completely.

The elongation, also known as the stretch ratio, is a measure of the largest deformation of the material before failure during the tensile test. A higher elongation indicates the capability of a material to deform. The elastic modulus is also a very important parameter, and is used to determine the stiffness of a material. Depending on the type of mechanical test being performed, the three different types of modulus that can be obtained are the Young's modulus, shear modulus, and bulk modulus. The Young's modulus is the most commonly obtained for an elastomer in biomedical applications. It is defined as the ratio of stress over strain, and can be derived from the slope of the initial linear region of the stress–strain curve. The recovery from deformation is also a parameter used to characterize elastomers. Many of the tissues in the body are fully elastic within a certain deformation. The time to recover from deformation for elastomers should also be considered when characterizing elastomers.

1.5.5. Degradation Rate

In most cases, the degradability of an elastomer is due to the hydrolyzable bonds in the polymer network. Normally, the degradation rate displays a considerable difference *in vitro* when compared to *in vivo* settings. However, *in vitro* degradation studies are always used to predict the degradation rate and determine degradation structure-property relationships [105]. Enzymatic degradation and oxidative degradation are also two possible ways for the degradation of elastomer [105]. In some previous works, in vitro enzymatic degradation studies were carried out to evaluate the property of the polymer [3].

The process of hydrolysis is mainly dependent upon the amount of water penetration into the network structure. Normally, a more hydrophobic material will have a lower degradation

rate. Moreover, a lower glass transition temperature (T_g) will also affect the degradation rate due to the increased water diffusion rate into the material. In order to prevent any changes in the elasticity of a material, it is important to maintain the T_g below the normal body temperature. In the case of an elastomer, both the T_g and mechanical properties are affected by the degree of crosslinking. A higher crosslinked elastomer will normally have a slower degradation rate, stronger mechanical strength and smaller elongation rate.

1.5.6. Application Specific Requirements

In addition to these general requirements, specific applications place further restrictions and requirements on the material. For example, relatively strong and elastic materials may be required in situations where the device is subjected to large amounts of strain or load bearing. Materials capable of being crosslinked *in situ* for injection-based biomaterial cell/drug delivery using minimally invasive techniques are sometimes preferred over pre-fabricated constructs to reduce surgical trauma [106]. Attempts to meet this large number of demanding requirements have made necessary the development of new biomaterials with unique properties. However, many of the currently available degradable polymers do not fulfill all of these requirements, and significant chemical changes to their structure will be required if they are to be formulated for multiple applications. Thus, the introduction of a methodology for biomaterial development that is able to generate versatile biodegradable materials for a wide range of tissue engineering applications would represent a major advancement in the field of biomaterials.

CHAPTER 2

METHODOLOGY OF CITRATE-BASED BIOMATERIAL DEVELOPMENT

1.1 Introduction

Motivated by the unique advantages of citric acid and the recent success of previously reported citrate-based materials, the following sections will introduce a methodology of citrate-based biomaterial development to produce novel biodegradable materials with a variety of options to modify the resulting material's properties to fit a wide range of tissue engineering applications. Two new families of citrate-based biomaterials are discussed in detail to elucidate the structure-property relationship and cell/tissue compatibility of the developed materials. The understanding of these components allow for the creation of unique biodegradable materials to fit a particular application at will.

2.2 Citrate-Based In Situ Crosslinkable Elastomers

2.2.1 Introduction

Many tissue-engineering strategies using injectable, *in situ* forming systems have been reported for a variety of applications as unique treatment options for difficult to reach areas of the body using minimally invasive procedures [109, 110]. The ability to be injected and conform to any shape, irrespective of the defect geometry, gives *in situ* forming systems unique advantages over previous methods, and has prompted their use as injectable scaffolds to reinforce the mechanical properties of diseased/injured tissue and for the localized delivery of cells, drugs, or growth factors [111-113]. Previous citrate-based elastomers have shown great potential in soft tissue engineering, but the single thermal crosslinking strategy severely limits their mode of delivery to the site of interest and in applications involving temperature sensitive payloads. Therefore, the development of a new family of citrate-based elastomers, which can

be injected using minimally invasive procedures and crosslinked *in situ* to deliver cells and/or therapeutics would help expand the current repertoire of citrate-based polymers.

In this section, we describe the synthesis and characterization of a novel family of biodegradable polymers based upon citric acid and maleic anhydride, referred to as poly (alkylene maleate citrates) (PAMC). This new family of biomaterials features a dual crosslinking mechanism (DCM) (free radical polymerization in addition to the already present ester bond crosslinking strategy), which can be utilized to fine-tune the material properties, preserve valuable pendant chemistries, and deliver cells/therapeutics using *in situ* tissue engineering approaches. The rationale behind the biomaterial design are: 1) using the concept that collagen and elastin are crosslinked polymers that provide elasticity to the natural extracellular matrix (ECM), we chose crosslinking as a mechanism to confer elasticity to the biomaterial; 2) to increase the manufacturing potential, we chose to use inexpensive monomers and a cost-effective synthesis procedure performed under mild heating without the use of any catalysts. Citric acid (CA), maleic anhydride (MA), 1,8-octanediol (OD), and poly (ethylene glycol) (PEG) are inexpensive and have been used in many other biomaterials for tissue engineering [10, 84, 95, 107-111]; 3) the incorporation of ester bonds into the polymer backbone confers degradability to the crosslinked polymer network; 4) the introduction of a vinyl-containing moiety allows the polymer to be crosslinked *in situ* while preserving valuable citrate pendant carboxylic and hydroxyl chemistries; 5) the option to crosslink the material through the combination of two different crosslinking strategies (free radical polymerization and ester bond crosslinking) allows for a wide control over the mechanical properties, degradation, and functionality of the biomaterial; and 6) replacing hydrophobic diols with a more hydrophilic diol, such as PEG, can create water-soluble compositions to circumvent the use of toxic organic solvents unsuitable for *in situ* tissue engineering and cell/drug delivery applications.

The following sections will discuss the development of two new polymers within the PAMC family, poly (octamethylene maleate anhydride citrates) (POMaC) and poly (ethylene

glycol maleate citrates) (PEGMC), to better understand how the DCM and completely water-soluble formulations, respectively, affect the material properties of the resulting elastomers. The results from these studies show that PAMC are highly flexible materials, which can be modulated through a multitude of synthesis parameters to serve as a unique platform biomaterial for *in situ* tissue engineering applications.

2.2.2 Experimental

2.2.2.1 Synthesis of PAMC Pre-Polymers

All chemicals were purchased from Sigma-Aldrich (St. Louis, MO), unless stated otherwise, and used as received. To evaluate and characterize the effects of the DCM, POMaC pre-polymers were first synthesized by carrying out a controlled condensation reaction as described in Figure 2.1. Briefly, CA, MA, and OD were added to a 250 mL three-necked round bottom flask fitted with an inlet and outlet adapter. Next, a flow of nitrogen gas was introduced into the flask, and the contents were melted at 160 °C while stirring at 360 rpm. The temperature of the system was subsequently lowered to 140 °C and allowed to react for 3 h to form the unpurified pre-polymer. Next, the pre-polymer was dissolved in 1,4-dioxane and purified by drop wise precipitation in deionized water to remove any of the unreacted monomers. The undissolved pre-polymer was collected and lyophilized in a Freezone 6 Freeze Dryer (Labconco, Kansas City, MO) to obtain the purified pre-POMaC. Various pre-POMaC polymers were synthesized with different feeding ratios of CA to MA (2: 8, 4: 6, and 6: 4) to yield pre-POMaC 8, pre-POMaC 6, and pre-POMaC 4 (**Table 2.1**). The ratio of the acids to the diol was kept as 1: 1.

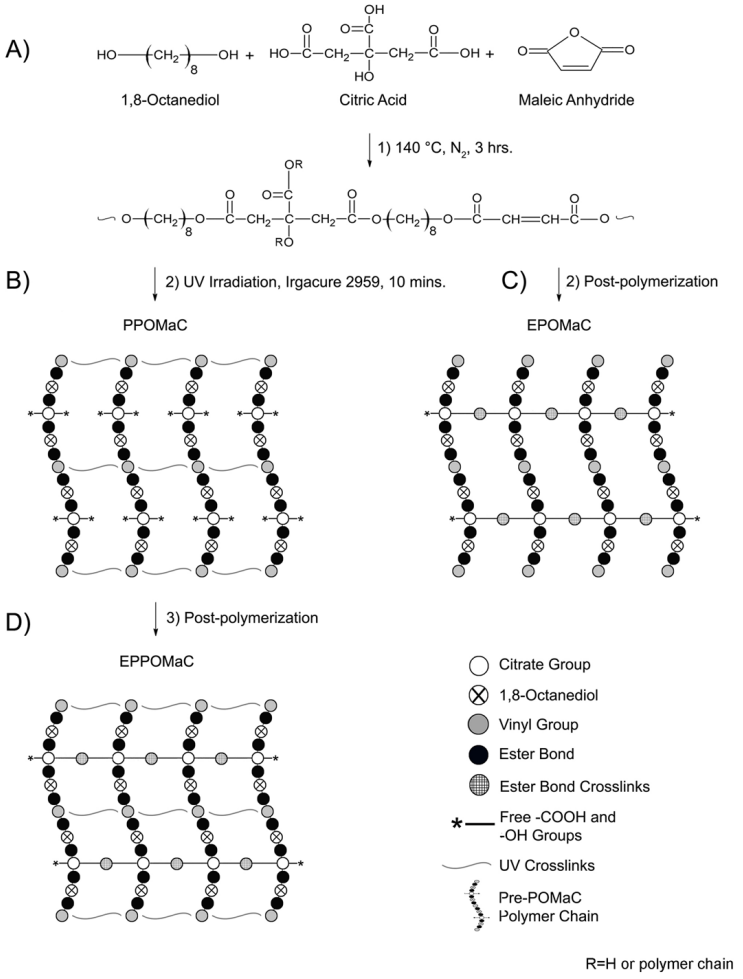

Figure 2.1 POMaC Networks A) Synthesis schematic, B) Free radical crosslinking, C) Ester bond crosslinking, and D) Dual crosslinking mechanism

Table 2.1 Feed Ratios, Actual Molar Composition, and Molecular Weight of POMaC Networks

	Feed Ratio (mol)			Composition (mol)			
Polymer Name	**Maleic Anhydride**	**Citric Acid**	**1,8-Octanediol**	**Maleic Anhydride**	**Citric Acid**	**1,8-Octanediol**	**Mw (Da)**
POMaC 4	2	3	5	1.94	3.26	4.90	624
POMaC 6	3	2	5	2.81	2.11	4.96	718
POMaC 8	4	1	5	3.77	1.12	4.92	945

To synthesize completely water-soluble pre-polymer compositions of PAMC, OD was replaced with PEG (MW 200) to create PEGMC (**Figure 2.2**). Briefly, CA, MA, and PEG were reacted together as previously described above. For purification, the prepared pre-polymer was

dissolved in deionized water and dialyzed with a 500 Da molecular weight cut off membrane for 1 day followed by lyophilization to achieve a purified pre-polymer (pre-PEGMC). Different ratios of acids MA to CA were synthesized in the initial composition of the pre-polymer as 8/2, 6/4, and 4/6, respectively, as shown in Table 2.2. The overall ratio of the acids over the diol was kept at 1:1.

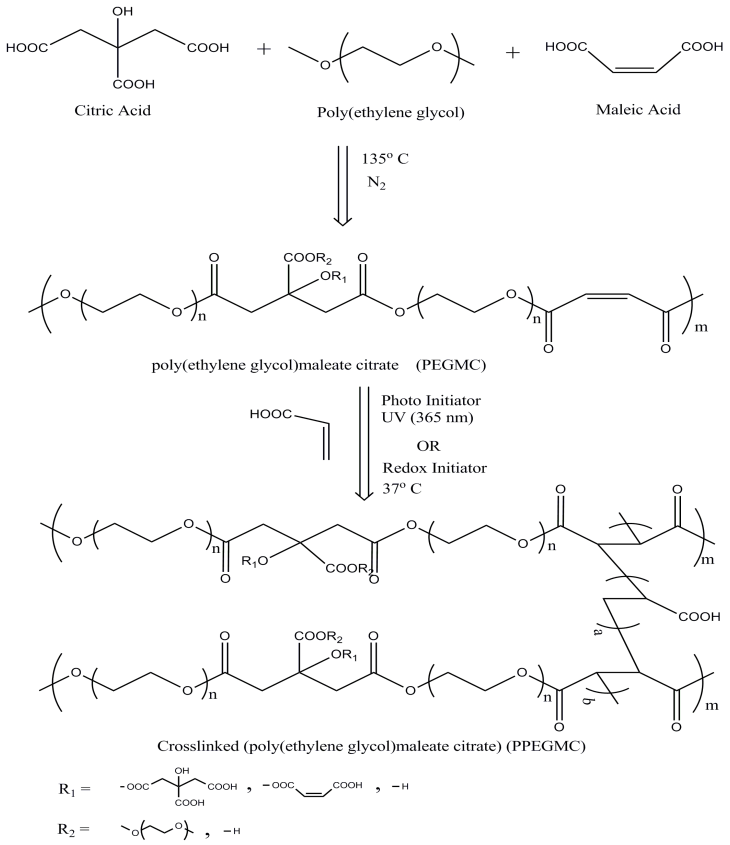

Figure 2.2 PEGMC Synthesis Schematic and Crosslinking Mechanisms

Table 2.2 Feed Ratios and Actual Molar Composition of PEGMC Networks

	Feed Ratio (mol)			Composition (mol)		
Polymer Name	**Maleic Anhydride**	**Citric Acid**	**PEG 200**	**Maleic Anhydride**	**Citric Acid**	**PEG 200**
PEGMC 8/2	4	1	5	3.70	1.20	4.90
PEGMC 6/4	3	2	5	2.80	2.01	5.20
PEGMC 4/6	2	3	5	1.70	3.10	4.80

2.2.2.2 PAMC Pre-Polymer Characterization

^{1}H NMR spectra for all pre-polymers were recorded on a JNM ECS 300 (JOEL, Tokyo, Japan) at 300 MHz. The pre-polymers were purified twice as mentioned above and dissolved in dimethyl sulfoxide-d6 (DMSO-d6) (3 mg mL^{-1}). The chemical shifts in parts per million (ppm) were referenced relative to tetramethylsilane (TMS, 0.00 ppm) as the internal reference. The average molecular weight was characterized by matrix assisted laser desorption/ionization mass spectroscopy (MALDI-MS) using an Autoflex MALDI-TOF Mass Spectrometer (Bruker Daltonics, Manning Park, MA). Fourier transform infrared (FT-IR) spectra were obtained using a Nicolet 6700 FT-IR spectrometer (Thermo Fisher Scientific, Waltham, MA) at room temperature. Pre-polymer samples were prepared by a solution casting technique. A dilute solution of the pre-polymers in 1,4-dioxane (3 wt. %) was cast onto a potassium bromide (KBr) crystals and allowed to dry for 12 h in a vacuum hood before being used to obtain the spectra.

2.2.2.3 Preparation and Characterization of PAMC Elastomers

In this study, three different POMaC networks were formed (**Figure 2.1**). Photocrosslinked POMaC networks were formed by crosslinking through free radical polymerization. Pre-POMaC was dissolved in dimethyl sulfoxide (DMSO) and mixed with photoinitiator (PI) 2-hydroxy-1-[4(hydroxyethoxy)phenyl]-2-methyl-1 propanone (Irgacure 2959) (1 wt. %) to generate the free radicals. The pre-polymer solution was cast into a poly (tetrafluoroethylene) (PTFE) circular dish, and the polymerization reaction was initiated upon exposure to a 365 nm long wave ultraviolet light (UVP, Upland, CA) (**Figure 2.1B**) at room temperature. The thermoset polymer achieved was then placed in an excess amount of DMSO to remove any unreacted polymer followed by immersion in deionized water to exchange the DMSO. The purified polymer was lyophilized to obtain photocrosslinked POMaC (PPOMaC).

PPOMaC has the option to be further crosslinked via post-polymerization at 80 °C for pre-determined times to create ester bond crosslinked, photocrosslinked POMaC (EPPOMaC) (**Figure 2.1D**). POMaC networks, absent of any photocrosslinking, were also formed using a

solution casting technique with 1,4-dioxane (30 wt. %) as the solvent to assist in the fabrication of uniform films. 1,4-dioxane was chosen here because it can be easily evaporated to facilitate POMaC film formation before it is post-polymerized. The pre-polymer solution was cast into a PTFE circular dish, and allowed to dry overnight in a vacuum hood. The pre-polymer was then placed into an oven maintained at 80 °C for pre-determined times to crosslink the network (**Figure 2.1C**). The thermoset polymer achieved was then placed in an excess amount of DMSO to remove any unreacted polymer followed by immersion in deionized water to exchange the DMSO. The purified polymer was lyophilized to obtain ester bond crosslinked POMaC (EPOMaC). The resulting crosslinked POMaC films were characterized by FT-IR to verify the crosslinking formation as compared to the pre-POMaC.

Water-soluble pre-PEGMC solutions were crosslinked into biodegradable gels using free radical polymerization mechanisms (photoinitiated or redox initiated) with acrylic acid as a crosslinker. First, purified pre-PEGMC was dissolved in deionized water to make a 30 wt. % concentration. The percentage of PI was fixed as 0.11 M, whereas the concentration of crosslinker was varied as 1.5 – 6 wt. % to study the effect of crosslinker on the overall material performance. Next, the solution was poured into a PTFE dish and placed under a UV irradiation for 60 s to obtain photocrosslinked PEGMC (PPEGMC). To crosslink pre-PEGMC using water-soluble redox initiated free radical polymerization, a 30 wt. % pre-polymer solution in water was mixed acrylic acid (3 wt. %) . The mixture was then added to an aqueous solution of 0.026 M ammonium persulfate (APS) and 0.11 m N,N,N',N'-tetramethylethylenediamine (TEMED). Next, the mixture was incubated at 37 °C for 60 s to obtain redox crosslinked PEGMC (RPEGMC). The resulting crosslinked PEGMC films were characterized by FT-IR to verify the crosslinking formation as compared to pre-PEGMC.

Tensile mechanical testing was conducted according to ASTM D412A on an MTS Insight 2 fitted with a 500 N load cell (MTS, Eden Prairie, MN). Briefly, the dog bone shaped samples (25mm x 6 mm x 1.5 mm, length x width x thickness) were pulled at a rate of 500 mm

min^{-1}, and elongated to failure. Values were converted to stress–strain and the initial modulus was calculated from the initial gradient of the curve (0 – 10% elongation). Compression tests were performed on freshly made cylindrical polymer samples (10 mm diameter; 10 mm height) in an unconfined state using MTS Insight II mechanical tester fitted with a 10 N load cell at a crosshead speed of 1 mm min^{-1} at various strain levels. The samples were cyclically preconditioned for 30% strain for the first cycle, and the hydrogels were subsequently subjected to additional loading and unloading cycles with increments of 10% strain level until the failure. The compressive modulus (0 – 10%) of the final cycle was obtained as the tangent slope of the stress–strain curve. The results are presented as means ± standard deviation (n = 6).

Polymer density was measured by the fluid displacement method using a density measurement kit (Mettler Toledo, Columbus, OH). The auxiliary liquid used was deionized water. The crosslink density (η) and molecular weight between crosslinks (M_c) was calculated by equation (1) according to the theory of rubber elasticity described elsewhere [80]:

$$\eta = \frac{E_0}{3RT} = \frac{\rho}{M_c} \qquad (1)$$

Where η represents the number of active network chain segments per unit volume; M_c represents the molecular weight between crosslinks; E_0 represents the initial modulus; R is the universal gas constant; T is the absolute temperature; and ρ is the polymer density as measured via the method above.

The sol content and swelling percentage was measured by the mass differential after incubation of the polymer network in DMSO. DMSO was chosen as the swelling agent due to its high boiling point. Briefly, polymer cylindrical discs (7 mm diameter; 2 mm thick) were cut from unpurified crosslinked films using a cork borer. The discs were weighed to find the initial mass (W_i), and suspended in DMSO for 72 h. The DMSO was changed every 24 h. The samples were removed from the DMSO, blotted with filter paper, and weighed (W_s). Next, the discs were suspended in deionized water for 24 h to exchange the DMSO, and lyophilized for 72 h. The

dried samples, absent of any unreacted polymer, were weighed to find the dry mass (W_d). The sol gel fraction was calculated using the formula from equation (2) [112]:

$$\text{sol } (\%) = \frac{W_i - W_d}{W_i} \times 100 \qquad (2)$$

The swelling percentage was calculated using the formula from equation (3) [113]:

$$\text{swelling } (\%) = \frac{W_s - W_d}{W_s} \times 100 \qquad (3)$$

The reported values are the means ± standard deviation (n = 6). In addition to DMSO, swelling in phosphate buffered saline (PBS pH 7.4), deionized water, and buffer solutions with different pH (2.4, 3.4, 4.4, 5.4, 6.4, 8.4, 9.4, 10.4) were evaluated.

2.2.2.4 In Vitro Degradation

Degradation studies were conducted in both PBS (pH 7.4) and NaOH solutions (0.05 M). NaOH degradation was used to screen the polymer degradation in a relatively short period of time. 6 Cylindrical disc specimens (7 mm in diameter; 2 mm thick) were cut from crosslinked, purified, and lyophilized films using a cork borer. The samples were weighed, placed in a tube containing PBS or NaOH (10 mL) for up to 10 weeks or 24 h respectively, and incubated at 37 °C. After incubation, samples were thoroughly washed with deionized water, lyophilized for 1 week, and weighed. The polymer morphology changes over the degradation period were evaluated with a Hitachi S-3000N scanning electron microscope (SEM) (Hitachi, Pleasanton, CA). The mass loss was calculated by comparing the initial mass (W_0) with the mass measured at the pre-determined time point (W_t), as shown in equation (4) [114]. The results are presented as the means ± standard deviation (n = 6).

$$\text{mass loss } (\%) = \frac{W_0 - W_t}{W_t} \times 100 \qquad (4)$$

2.2.2.5 In Vitro Drug Release

To evaluate release kinetics from PAMC, bovine serum albumin (BSA, MW = 67000 g mol^{-1}) was chosen as the model protein for the release studies. A BSA solution was first

prepared by dissolving 2.0 g of BSA in 40 mL of PBS solution (pH 7.4). Next, the BSA solution was mixed with the polymer solution to make a 1:20 protein to polymer ratio by weight. Polymer samples were then crosslinked, and the resulting BSA-loaded polymer samples were lyophilized for 48 h. The *in vitro* release was carried out in glass tubes at 37 °C in a PBS buffer solution (pH 7.4). At pre-determined times, a fixed amount of the BSA-released buffer solution was removed from the glass tube and replaced with fresh buffer solution. The resulting cumulative BSA release was quantified using a UV Spectrophotometer (Lambda Bio40 UV-vis Spectrometer, PerkineElmer) at 280 nm. To determine pH sensitivity, a sodium acetate-acetic acid buffer solution (pH 5.4) was also used as the incubation medium.

2.2.2.6 Microchannel Scaffold Fabrication

The microchannel pattern was transferred from polydimethylsiloxane (PDMS) molds to POMaC according to the procedures illustrated in Figure 2.3. Briefly, pre-POMaC was dissolved in 1,4-dioxane to make a 30 wt. % solution and mixed with PI (1 wt. %). The pre-polymer solution was cast onto the PDMS microchannel mold, and placed under vacuum to remove any air trapped in the channels. The microchannels filled with pre-POMaC were then exposed to a UV irradiation for 10 min (**Figure 2.3A**). Once the PPOMaC was formed in the microchannels, the particulate leaching method was used to fabricate porous POMaC scaffolds onto the microchannels. Pre-POMaC was dissolved in 1,4-dioxane to make a 30 wt. % solution, followed by the addition of sieved sodium chloride salt (99% purity) with an average size in the range of 106 – 150 mm in a (1: 9) polymer to salt ratio by weight. The polymer solution was mixed thoroughly with the salt and PI (1 wt. %) until a viscous paste was formed. The resulting slurry was cast onto the previously fabricated PPOMaC microchannels. The scaffold was exposed to a 365 nm long wave ultraviolet light for 30 min.

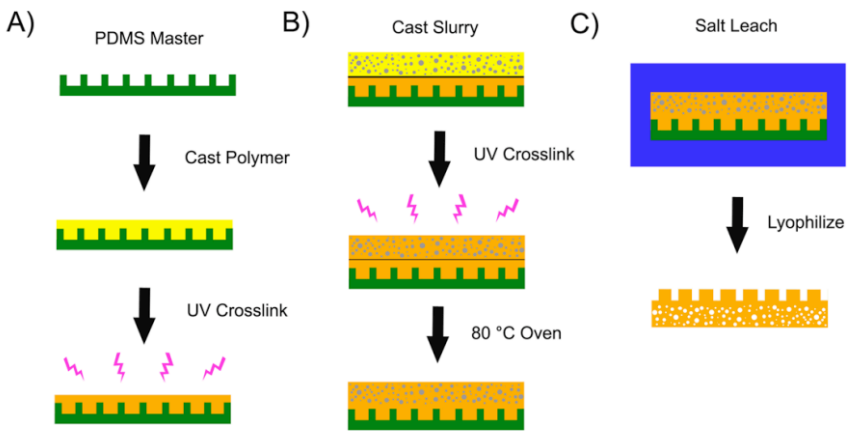

Figure 2.3 Microchannel Scaffold Fabrication Process A) Formation of microchannels, B) Formation of porous section, and C) Salt leaching followed by final lyophilization step

Following UV crosslinking, the entire construct was placed in an oven and cured at 80 °C to ensure that the scaffold bonded to the PPOMaC microchannels (**Figure 2.3B**). Next, the salt and any remaining solvent were leached out by immersion in deionized water for 72 h with water changes every 12 h. Finally, the scaffolds were lyophilized for 36 h to remove any traces of water (**Figure 2.3C**). To view the cross-sectional morphology, the scaffold sample was freeze-fractured using liquid nitrogen, sputter coated with silver, and examined under SEM. Image J analysis software was used to determine the channel widths and depths of the fabricated microchannels and scaffold pore sizes. To characterize the geometries, 3 random locations were selected and a total of 30 measurements performed. The dimensions reported are expressed as the means ± standard deviation.

2.2.2.7 In Vitro Cell Evaluation

Cell compatibility was evaluated *in vitro* using both qualitative and quantitative methods. Polymer films and scaffolds (pore size 106 – 150 mm; porosity ~90%) were cut into cylindrical discs (7 mm in diameter) and sterilized in 70% ethanol for 3 h. After incubation in ethanol, the samples were exposed to UV light for 30 min and washed with PBS. NIH 3T3 fibroblasts and human dermal fibroblasts (HDF) were used as model cells for this study. The cells were

cultured in Dulbecco's modified eagle's medium (DMEM), which had been supplemented with 10% fetal bovine serum (FBS) and 1% penicillin streptomycin. The culture flasks were kept in an incubator maintained at 37 °C, 5% CO2, and 95% relative humidity. The cells were allowed to grow to the fourth passage, trypsinized, centrifuged, and suspended into media to obtain a seeding density of 1 x 10^5 cells mL^{-1} for both the films and scaffolds. Immediately prior to the trypsin treatment, 3T3 fibroblasts were labeled with carboxyfluorescein diacetate, succinimidyl ester (CFDA-SE) green fluorescent cell tracer using the manufacturer's protocol.

After 3 days of culture for the films, the cells were fixed with the addition of a 2.5% (wt/v) gluteraldehyde PBS solution. The fixed films were then sequentially dehydrated by treatment with a graded series of ethanol, lyophilized, and sputter coated with silver. The samples were then observed under SEM to view the morphology of the attached cells. Separate samples were hematoxylin and eosin (H&E) stained, and viewed under a Zeiss Auxiovert inverted microscope (Carl Zeiss MicroImaging, Thornwood, NY). To evaluate cell encapsulation, sterilized pre-PEGMC solutions were mixed with a cell suspension to achieve a final concentration of 1 x 10^6 cells mL^{-1}, and crosslinked using redox initiated mechanisms as described above. After 48 h of incubation, the presence of live and dead cells in the RPEGMC gels were evaluated using a LIVE/DEAD Viability/Cytotoxicity Kit (Invitrogen, Carlsbad, CA), according to manufacture protocol. To observe the morphology of the encapsulated cells, cells were pre-stained with CFDA-SE.

The seeded polymer scaffolds were allowed to culture, and imaged every other day for two weeks with re-staining on the third day. The scaffolds were removed from culture at day 2, 7, and 14 for fluorescent imaging of tracer dye stained cells. After imaging, the cell containing scaffolds were fixed in cold methanol for 10 min and dried under vacuum. Scaffolds were then embedded in a liquid gelatin sucrose solution, placed under vacuum for 30 min, and frozen at -20 °C. Cross-sections of the scaffold were cut at 10 mm and H&E stained to visualize cell penetration and growth throughout the scaffold.

A quantitative assessment of the cell proliferation on polymer scaffolds was also performed using a methylthiazoletetrazolium (MTT) cell proliferation and viability assay kit. Polymer scaffolds were cut into cylindrical discs (7 mm in diameter), and sterilized as mentioned above. PLLA scaffolds were used as a relative control. 3T3 fibroblasts were seeded on the scaffolds in the same manner as mentioned previously. MTT assay analysis was performed at 1, 3, and 7 days of culture as specified by the manufacturer's protocol. Briefly, the old media was aspirated, and each sample was washed with PBS to remove any loosely attached or dead cells. Next, incomplete media (100 μL) (absent of any FBS) was added to the specimens. A 3-(4,5-dimethylthiazol-2yl)-diphenyltetrazolium bromide solution (10 μL) was then added to the samples, and allowed to incubate for 3 h. At the end of the incubation period, MTT solvent (100 μL) was added to the media. Dissolution of the formazan crystals was facilitated by constant agitation of the well plate on an orbital shaker for 20 min. The absorbance was measured on an Infinite200 microplate reader (Teacan Group Ltd., Switzerland) at 570 nm.

To evaluate pre-polymer *in vitro* cytoxicity, pre-PEGMC solutions were prepared in deionized water buffered with excess sodium bicarbonate until the pH was maintained at 7.4. The solutions were then lyophilized and diluted at various concentrations (1, 0.1, and 0.01 g/100 mL) using DMEM to create the cytotoxic media. All solutions were passed through a 0.22 μm syringe filter for sterilization. Next, approximately 10,000 3T3 mouse fibroblasts were seeded into each well of a 96-well plate and incubated with for 24 h. After 1 day of culture, the normal medium was replaced with 200 μL of the cytotoxic media, and the cells were allowed to incubate for an additional 24 h. A MTT cell proliferation and viability assay was used for a quantitative assessment of the viable cells according to the manufacturer's protocol. Poly (ethylene glycol) diacrylate (PEGDA) (3.5 KDa), diluted in the same manner as above, was used as a control. All absorbance values obtained were normalized to the viable cells cultured in DMEM absent of any cytotoxic media.

To evaluate the cytotoxicity of PEGMC degradation products, PPEGMC hydrogels of all three different monomer ratios were incubated in 0.2 M NaOH for accelerated degradation. Following complete polymer degradation, the pH of the solution was adjusted to pH 7.4 with 0.2 M HCl. The polymer degradation solutions were then diluted in DMEM into various concentrations to create the cytotoxic media. All solutions were passed through a 0.22 μm syringe filter for sterilization. Next, approximately 10,000 3T3 mouse fibroblasts were seeded into each well of a 96-well plate and incubated for 24 h. After 1 day of culture, the normal medium was replaced with 200 μL of the cytotoxic media, and the cells were allowed to incubate for an additional 24 h. A MTT cell proliferation and viability assay was used for a quantitative assessment of the viable cells according to the manufacturer's protocol. The degradation products of poly (L-lactide) (PLLA, 99 KDa) were used as a control. Viability of cells in the presence of polymer degradation products was normalized to the viable cells cultured absent of any cytotoxic media.

2.2.2.8 Foreign Body Response

PPOMaC, EPPOMaC, and PLLA (as relative control) were used to evaluate the *in vivo* foreign body response. The films were cut into discs (7 mm diameter; 1 mm thickness), and sterilized under UV light for 30 min and soaked in 70% ethanol. The films were then exchanged with PBS to remove the ethanol and dried under vacuum for 30 min. The sterilized films were then implanted subcutaneously in the back of healthy Balb/C mice (The Jackson Laboratories, Bar Harbor, ME). To demonstrate the *in situ* formation of PEGMC gels *in vivo* and understand the host response, 250 μL of sterilized pre-PEGMC was injected subcutaneously with a 27-gauge needle and crosslinked by redox initiated mechanisms. Animals were cared for in compliance with regulations of the animal care and use committee of University of Texas at Arlington. 12 mice were divided into three groups of four (2 male and 2 female) for the different time points of the study. The mice were anesthetized in a chamber through which an isofluorane-oxygen mixture was passed. The mice were monitored through recovery from

anesthesia and placed into single housing and monitored throughout the study. At the end of each time point, the mice were sacrificed by CO_2 inhalation, and the implant and surrounding tissue were frozen in OCT embedding media (Polysciences Inc., Warrington, PA) at -80 °C for histological analyses.

To assess the tissue responses to the implants, 10 mm tissue sections were H&E stained. Images of stained sections were taken at 10x magnifications using a Leica DMLP microscope (Leica Microsystems Inc., Bannockburn, IL) fitted with a Nikon E500 camera (Nikon Corp., Japan). Three images per section were collected from different parts of the section for analysis. A total of four sections per animal were examined in this manner. Response capsule thickness was measured in each of the images using Image J analysis software. At least 25 readings from different parts of the images were collected and averaged to determine the capsule thickness. Immunohistochemical stains were performed to determine inflammatory cell engraftment for biomaterial implants. Inflammatory cells were identified by CD11b positive expression [115]. All of the primary and second antibodies used in this work were purchased from Santa Cruz Biotech (Santa Cruz, CA). Stained sections were visualized using a Leica microscope and imaged with a CCD camera (Retiga EXi, Qimaging, Surrey BC, Canada). Slides were also immunostained with for CD68 positive expression (a glycoprotein expressed on monocytes/macrophages) using rabbit anti-rat CD68 primary antibody (1:200, Abcam, England, UK) followed by goat anti-mouse secondary antibody (Vector Burlingame, CA, USA) to identify macrophage recruitment. Samples were incubated with strepavidin horseradish peroxidase (1:100, Dako, Denmark) and developed with DAB substrate chromogen (Dako).

2.2.2.9 Statistical Methods

Data are expressed as means ± standard deviation. The statistical significance between two sets of data was calculated using a two-tail Student's t-test. Non-parametric one-way ANOVA tests were also performed where appropriate. Data were taken to be significant, when $p < 0.05$ was obtained.

2.2.3 Results

2.2.3.1 Synthesis of PAMC Pre-Polymers

All PAMC pre-polymers consisted of a transparent viscous liquid at room temperature after the initial polycondensation reaction. The stoichiometric ratios prepared for all polymers in this study are shown in Table 2.1 and 2.2. The average molecular weight (MW) of the pre-POMaC polymers was 624, 718, and 945 Da for pre-POMaC 4, pre-POMaC 6, and pre-POMaC 8, respectively, as determined by MALDI-MS. Pre-POMaC were found to be soluble in most organic solvents such as 1,4-dioxane, DMSO, dimethylformamide (DMF), tetrahydrofuran (THF), and acetone. Pre-PEGMC polymers were soluble in the above-mentioned organic solvents including deionized water.

2.2.3.2 Pre-Polymer Characterization

FT-IR analysis confirmed the presence of various functional groups in the polyester based pre-polymers. The peak located at 1647 cm^{-1} validated the successful incorporation of the vinyl group contributed by the MA (**Figures 2.4A and 2.5A**). Furthermore, the peaks located at 1720 and 3570 cm^{-1} confirmed the preservation of pendant carboxylic acid and hydroxyl groups, respectively, from CA. The broad peaks centered at 2932 cm^{-1} were assigned to methylene groups contributed by both OD and CA. The resonance of various hydrogens in the pre-polymer backbone was confirmed by analyzing the chemical shifts of the ^{1}H NMR peaks with respect to tetramethylsilane (TMS). Figures 2.4B and 2.5B show a typical ^{1}H NMR spectra of pre-POMaC and pre-PEGMC, respectively. The peaks located between 6 and 7 ppm (a) were assigned to the protons in –CH=CH– incorporated into the polymer chain. The peaks (b) located at 2.79 ppm were assigned to –CH2– from CA. The peaks (c,d) located at 1.53 ppm were assigned to in –O–CH2CH2– from OD and PEG [84, 116]. The chemical compositions of the pre-polymers were determined by calculating the ratios of the signal intensities of the characteristic proton peaks from each monomer: MA, CA, and diol. As shown in Table 2.1 and

2.2, the actual polymer composition can be well controlled by varying the feeding ratio of the monomers in the initial polycondensation reaction.

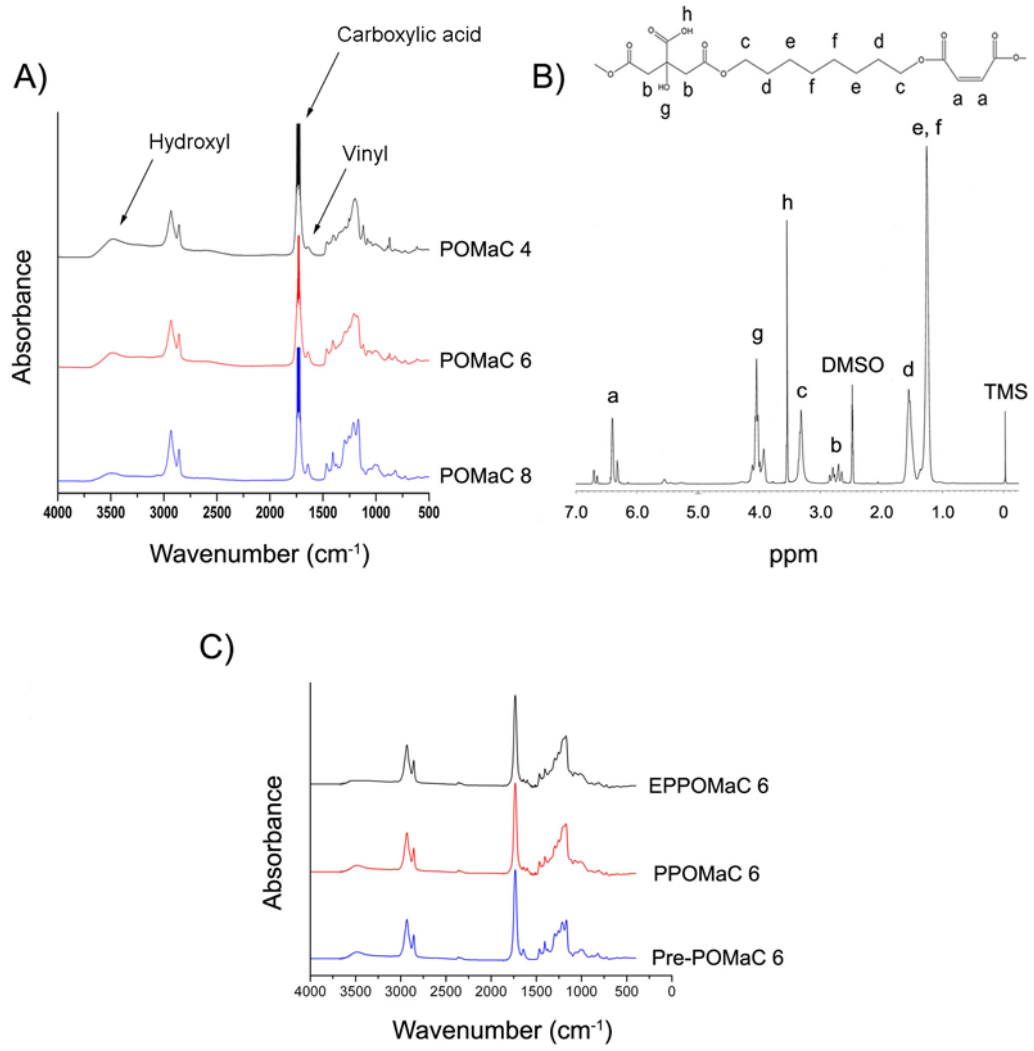

Figure 2.4 Structural Characterizations of POMaC Networks A) FT-IR spectra of pre-POMaC, B) ^{1}H NMR spectra of pre-POMaC 8, and C) FT-IR spectra of crosslinked POMaC films

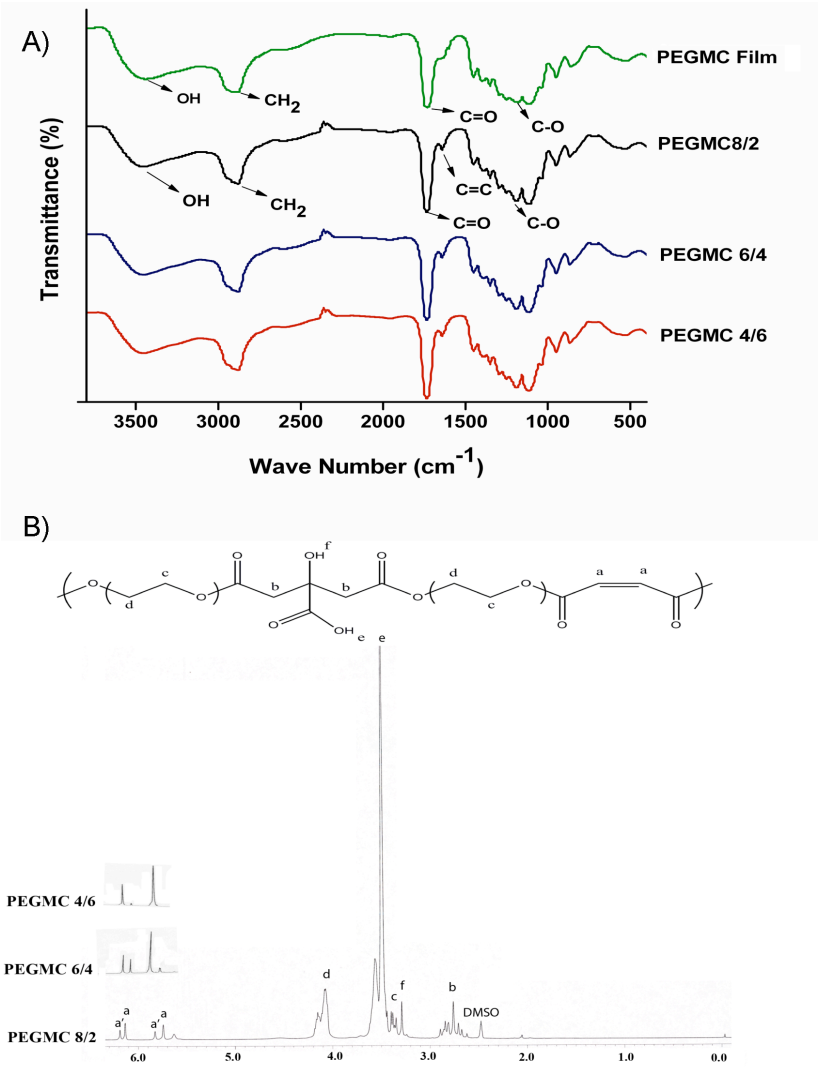

Figure 2.5 Structural Characterization of PEGMC Networks A) FT-IR and B) ^{1}H NMR spectra

2.2.3.3 Preparation and Characterization of PAMC Elastomers

Three different networks using two different modes of crosslinking were utilized to polymerize pre-POMaC into a thermoset polyester elastomer as summarized in Figure 2.1: free radical polymerization, ester bond crosslinking, and a combination of both free radical polymerization followed by ester bond polymerization. The former crosslinking mechanism utilized the vinyl groups present in the pre-polymer, which can be directly polymerized into a hydrogel like material within 10 min (**Figure 2.1B**). FT-IR analysis on UV crosslinked films

shows a significant reduction of the peak located at 1647 cm^{-1}, which was designated to the vinyl group from MA. Whereas ester bond crosslinks were formed through post-polycondensation of the CA pendant carboxylic and hydroxyl groups in the presence of heat (**Figure 2.1C**). Furthermore, both crosslinking mechanisms can be combined in order to produce a higher crosslinked network as needed for a particular application (**Figure 2.1D**). When the pre-polymer was crosslinked via ester bond formation, a significant reduction in the hydroxyl peak (3570 cm^{-1}) was evident (**Figure 2.4C**). PEGMC hydrogels can be formed using photoinitiated or redox initiated mechanisms. Crosslinking of the PEGMC network was achieved by the consumption of the vinyl moiety contributed via MA whereas pendant carboxylic and hydroxyl functionalities were still preserved as indicated by FT-IR in Figure 2.5A. The crosslinking of PEGMC was aided with the use of a terminal alkene crosslinker (acrylic acid).

The mechanical properties of POMaC networks are summarized in Table 2.3. A significant reduction in the initial modulus (0.29 to 0.04 MPa) and peak stress (611 to 245 KPa) was exhibited as the molar concentration of the MA was reduced from 8 to 4, respectively. However, the elongation at break increased (194 to 441%) when the MA ratio was reduced in the same manner. The crosslinking density of photopolymerized PPOMaC films also decreased (39.78 ± 4.76 to 5.48 ± 1.38 mol m^{-3}) as the molar ratio of the MA was reduced from 8 to 4, respectively. The relative molecular mass between crosslinks of the PPOMaC films was shown to be inversely proportional to the density of the crosslinks within the polymer network.

Table 2.3 Density Measurements, Mechanical Properties, and Crosslinking Characterization of Photocrosslinked POMaC Networks

Sample	Density (g/cm^3)	Peak Stress (KPa)	Initial Modulus (MPa)	Elongation (%)	η (mol/m^3)	M_c (g/mol)
PPOMaC 4	1.08 ± 0.01	245 ± 41.29	0.04 ± 0.01	441 ± 93	5.48 ± 1.38	206098 ± 45482
PPOMaC 6	1.09 ± 0.01	319 ± 74.58	0.08 ± 0.01	360 ± 20	10.56 ± 0.66	104208 ± 6799
PPOMaC 8	1.11 ± 0.02	611 ± 24.48	0.29 ± 0.04	194 ± 10	39.78 ± 4.76	28560 ± 4098

The mechanical properties of POMaC were also tuned through the DCM. Table 2.4 shows the mechanical properties of POMaC crosslinked using photopolymerization and/or ester bond crosslinking. When photopolymerization was avoided, in the case of EPOMaC, a peak stress of 326.32 ± 85.46 KPa, initial modulus of 0.12 ± 0.02 MPa, and elongation at break of 327 ± 56% was observed when crosslinked at 80 °C without vacuum for a 1 day time period. There was a significant increase in the peak stress (781.16 ± 60.04 KPa) and initial modulus (1.36 ± 0.16 MPa), but a decrease in elongation at break (90 ± 6%) when the post-polymerization time was lengthened to 2 days ($p < 0.05$). A similar trend in mechanical properties was reported for the previously published elastomer poly (diol citrates) [95].

Table 2.4 Density Measurements, Mechanical Properties, and Crosslinking Characterization of Photocrosslinked and Ester Bond Crosslinked POMaC Networks

Sample	Density (g/cm^3)	Peak Stress (KPa)	Initial Modulus (MPa)	Elongation (%)	η (mol/m^3)	M_c (g/mol)
EPOMaC 6 (1 Day)	1.13 ± 0.01	326.32 ± 85.46	0.12 ± 0.02	327 ± 56	15.79 ± 2.58	73287 ± 12109
EPOMaC 6 (2 Days)	1.16 ± 0.01	781.16 ± 60.04	1.36 ± 0.16	90 ± 6	185.63 ± 22.15	6351 ± 748
EPPOMaC 6 (1 Day)	1.17 ± 0.01	503.64 ± 50.30	0.25 ± 0.01	269 ± 22	34.71 ± 1.77	33776 ± 1699
EPPOMaC 6 (2 Days)	1.17 ± 0.01	994.14 ± 38.00	1.52 ± 0.02	51 ± 3	206.92 ± 3.28	5655 ± 89

When photocrosslinking and ester bond crosslinking was combined as the mode of polymerization in EPPOMaC, there was a significant increase in the peak stress, initial modulus, and reduction in elongation at break for both EPPOMaC 6 (1 day) and EPPOMaC 6 (2 days), (503.64 ± 50.30 KPa, 0.25 ± 0.01 MPa, 269 ± 22%) and (994.14 ± 38 KPa, 1.52 ± 0.02 MPa, 51 ± 3%), respectively. The mass densities of POMaC networks ranged from 1.08 to 1.17 g cm^{-3} and were dependent upon the composition and crosslinking method used. The crosslinking densities of both EPOMaC and EPPOMaC showed an increase when the post-polymerization time was increased from 1 to 2 days (15.79 ± 2.58 to 185.63 ± 22.15 and 34.71 ± 1.77 to 206.92 ± 3.28 mol m^{-3}), respectively.

PPEGMC with a higher molar ratio of MA exhibited higher tensile and compressive modulus. The initial tensile modulus of PPEGMC 8/2 (777.2 ± 109.4 KPa) was significantly higher than that of both PPEGMC 6/4 (450.0 ± 25.6 KPa) and PPEGMC 4/6 (388.7 ± 54.8 KPa) (**Figure 2.6A**). Redox-initiated crosslinked RPEGMC hydrogels were compressed to 70% strain under cyclic compression, and it was found that the materials did not undergo any permanent deformation. Under cyclic compression, very minimal hysteresis was observed for all three types of hydrogels as compared to other reported hydrogels, demonstrating their excellent elastic properties (**Figure 2.6B**) [1]. The compressive modulus of PPEGMC 8/2 (18.0 ± 1.5 KPa) was significantly higher than both PPEGMC 6/4 (11.0 ± 1.2 KPa) and PPEGMC 4/6 (8.0 ± 1.5 KPa) (**Figure 2.6C**).

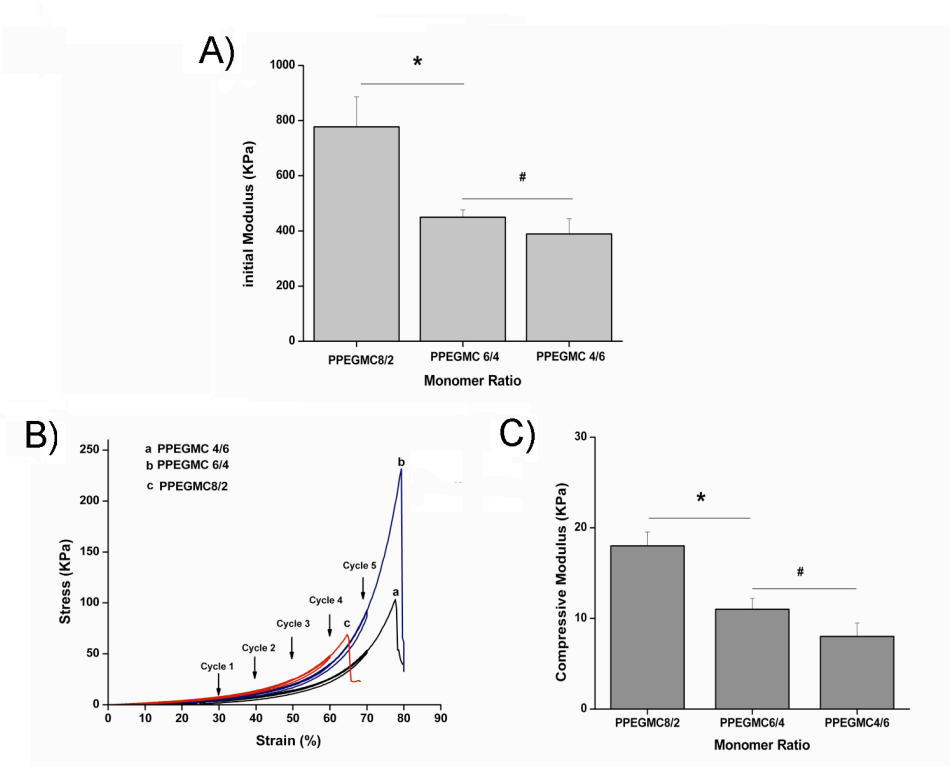

Figure 2.6 Mechanical Properties of PEGMC Hydrogels A) Tensile initial modulus, B) Compressive hysteresis, and C) Compressive initial modulus

The sol content of PPOMaC networks varied between 52 and 18% by mass, and was reduced by increasing the MA ratio, polymer concentration while crosslinking, and photoinitiator

concentration (data not shown). POMaC networks exhibited a solvent uptake, which varied from 146 to 2265% by mass across composition and crosslinking conditions. The percentage of swelling was inversely related to the amount of MA in the polymer network. As seen in Figure 2.7A, the swelling percentage decreased from 2143.12 ± 121.90% to 1344.19 ± 84.66% as the ratio of the MA increased from 4 to 8. A similar trend was observed when PBS was used as the swelling agent (1011.23 ± 137.23 to 276.55 ± 11.32%).

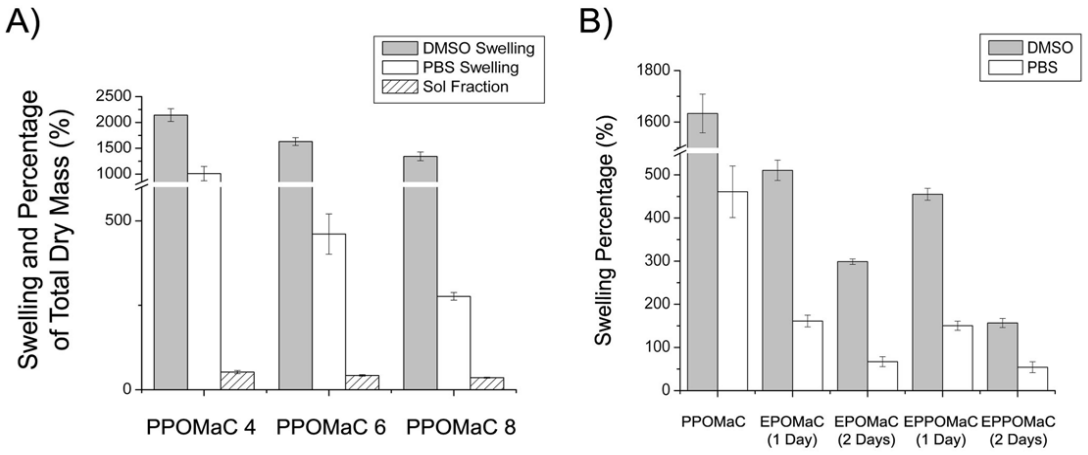

Figure 2.7 Swelling Ratio and Sol Content of POMaC Networks in Response to A) Maleic anhydride ratio and B) The dual crosslinking mechanism

The swelling characteristics of the polymer networks were also evaluated on POMaC using different modes of crosslinking. As shown in Figure 2.7B, there was a significant reduction in swelling properties with all three swelling agents when the ester bond crosslinking time was increased from 1 to 2 days ($p < 0.05$). For example, EPOMaC 6 (1 day) exhibited a solvent uptake of 510.57 ± 23.54%, whereas EPOMaC 6 (2 days) swelled only 298.80 ± 62.39%. The same decrease in swelling was observed for EPPOMaC, and when PBS was used as the swelling agent for the DCM. Interestingly, a significant difference in the solvent uptake between EPOMaC and EPPOMaC was seen ($p < 0.05$), but no significant difference was observed when PBS was used as the swelling agent ($p > 0.05$).

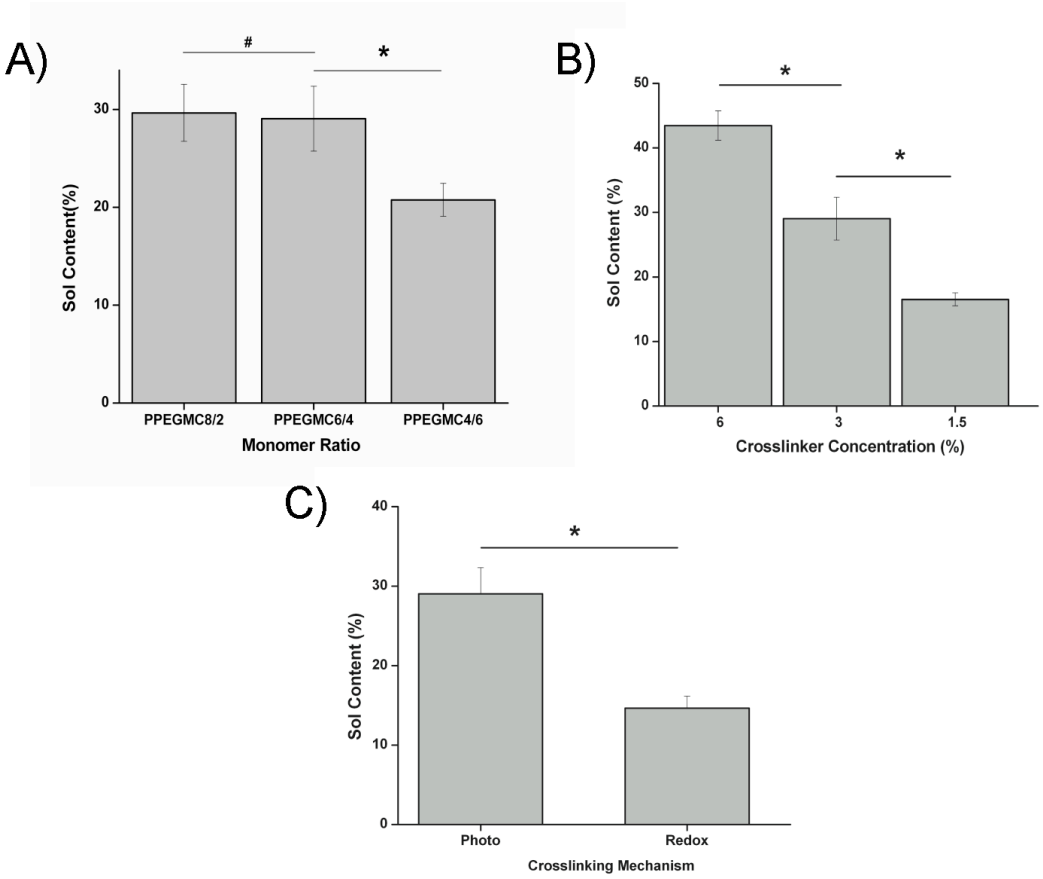

Figure 2.8 Sol Content of PEGMC Networks in Response to A) Monomer ratios, B) Amount of crosslinker, and C) Crosslinking mechanism

Figure 2.8 shows the effect of monomer molar ratios, crosslinker concentration, and mode of crosslinking on the sol content of PEGMC. The results indicated that there was no significant difference in sol content when the concentration of MA was higher than CA as in case of PPEGMC 8/2 (29.6 ± 2.9%) and PPEGMC 6/4 (29.0 ± 3.3%), but was significantly reduced when the concentration of CA exceed MA as in the case of PPEGMC 4/6 (20.7 ± 1.7%) (**Figure 2.8A**). The sol content could be significantly reduced with increased amounts of crosslinker. For example, sol content decreased significantly from 45.0 ± 1.0% to 15.0 ± 14.9% as crosslinker concentration increased from 1.5% to 6.0% (v/v) ($p < 0.01$) (**Figure 2.8B**). It was also observed that the crosslinking mechanism had a significant effect on the sol content of

PEGMC. A 2-fold decrease in sol content was observed for redox crosslinked RPEGMC (14.6 ± 1.5%) when compared to photocrosslinked PPEGMC (29.0 ± 3.3%) (**Figure 2.8C**). This could be explained with the fact that a homogeneous crosslinking might not be achieved in photocrosslinking due to the uneven light distribution throughout the polymer solution.

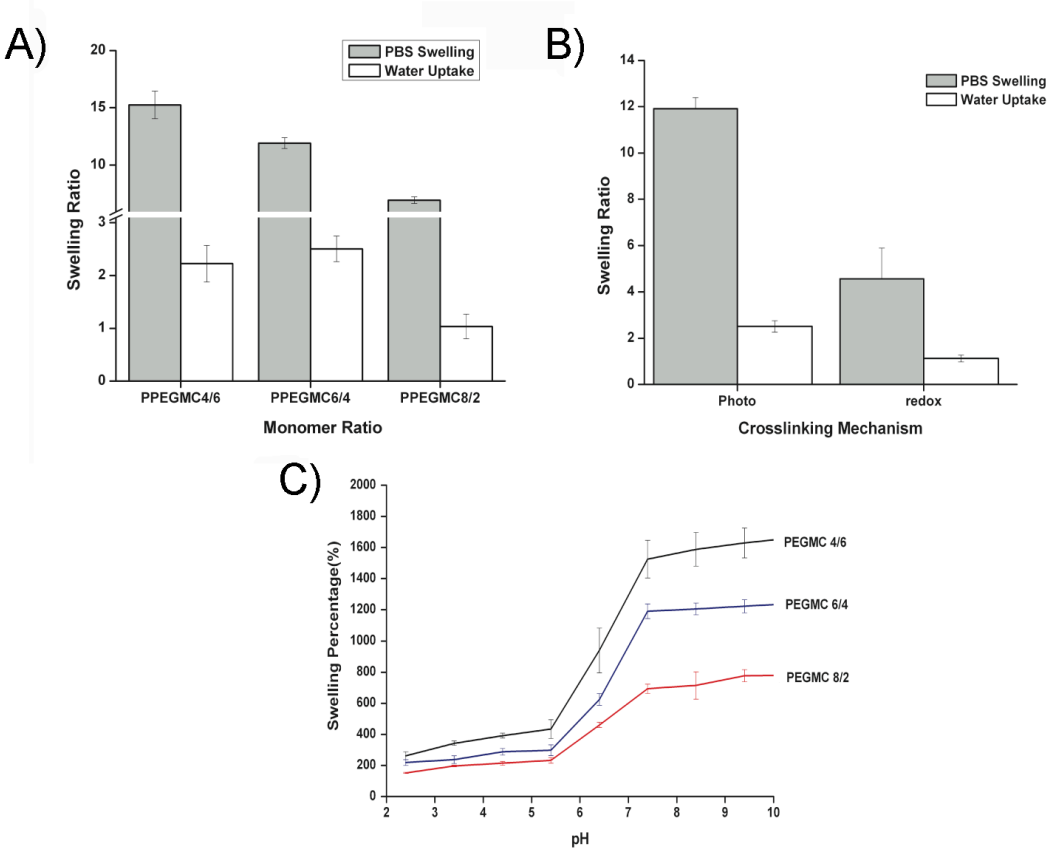

Figure 2.9 Swelling Ratio of PEGMC Networks in Response to A) Monomer ratios, B) Crosslinking mechanism, and C) pH of medium

The swelling of the PPEGMC hydrogels were investigated by incubating the polymers in PBS, water, and buffers with different pH at 37 °C for 48 h. Figure 2.9 shows the effect of monomer molar ratio (MA/CA), crosslinking modes, and medium pH on the swelling degree of PEGMC hydrogels. The results showed that the swelling increased in both PBS (6.9 ± 0.3 to 15.2 ± 1.2%) and H_2O (1.0 ± 0.2 to 2.5 ± 0.2%) when monomer ratio of MA to CA decreased (**Figure 2.9A**). However, the swelling ratios were higher in all the cases for PBS than those in

water. This clearly demonstrates that PEGMC were saturated with ionizable functionalities (i.e., COOH groups). In addition to this, the swelling ratio of PEGMC was significantly reduced in the hydrogel RPEGMC 6/4 in both PBS and water as compared to that of PPEGMC 6/4 (**Figure 2.9B**). For a more in depth understanding of the ionizable functionalities presented in these hydrogels, we performed another swelling study on buffers with various pH levels. Figure 2.9C indicates that all the hydrogels restricted their swelling ability when pH was lower than 5.4. There was a significant increase in the swelling ability of all hydrogels in the pH levels between 5.4 and 7.4. Furthermore, this gradient in the swelling was more significant on hydrogels with a higher CA content.

2.2.3.4 In Vitro Degradation

In addition to degradation in PBS, accelerated degradation studies were performed to ensure that the material's hydrolytically liable bonds were accessible and that the degradation products are completely soluble. Complete degradation of all POMaC polymers were confirmed by degradation in the presence of 0.05 M NaOH. The data for the degradation characterization of POMaC networks are presented in Figure 2.10. The degradation rate of the polymer could be adjusted by varying the molar ratio of the MA, and through the DCM. PPOMaC polymers with higher MA ratios resulted in slower degradation rates. The additional crosslinking through ester bond formation also resulted in longer degradation rates. PPOMaC 4 was shown to have degraded 77.50 ± 1.93%, whereas EPPOMaC 8 (2 days) degraded only 18.45 ± 4.44% by week 10 in PBS.

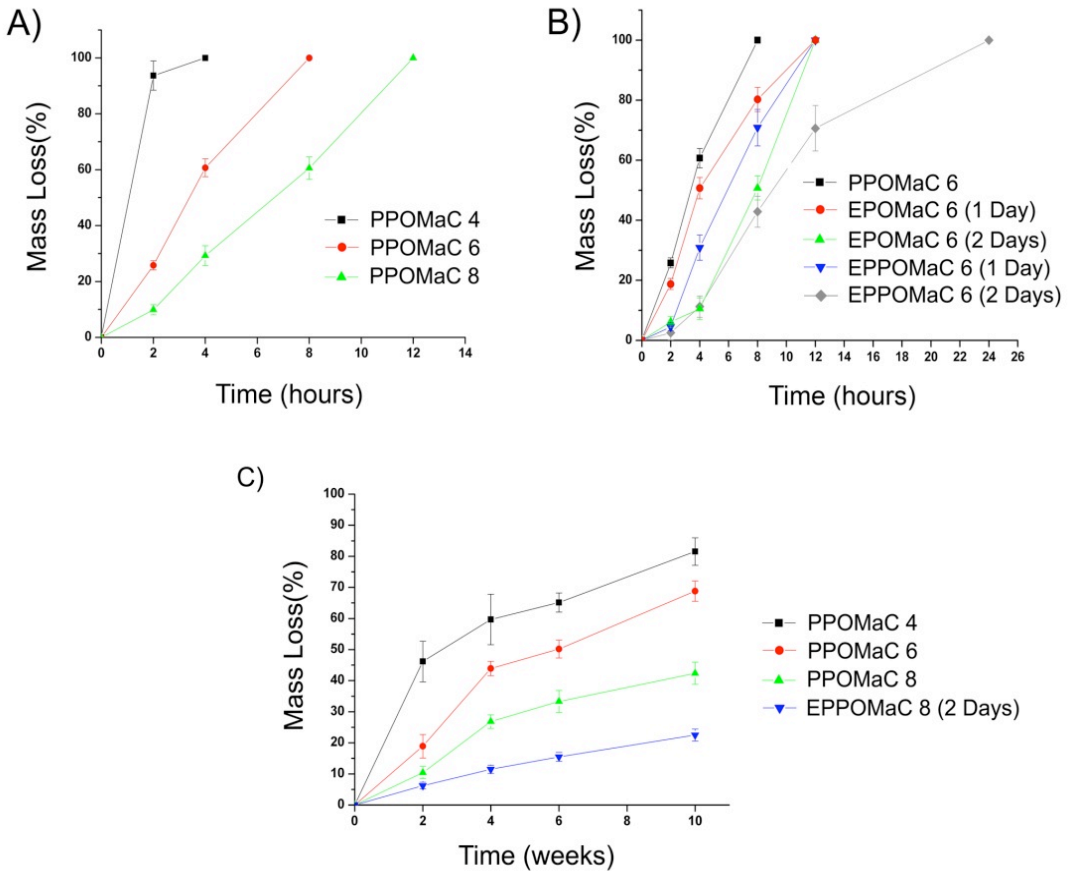

Figure 2.10 Degradation Profiles of POMaC Networks in Response to A) Maleic anhydride ratio in 0.05 M NaOH, B) Dual crosslinking mechanism in 0.05 M NaOH, C) Incubation in PBS (pH 7.4; 37 °C)

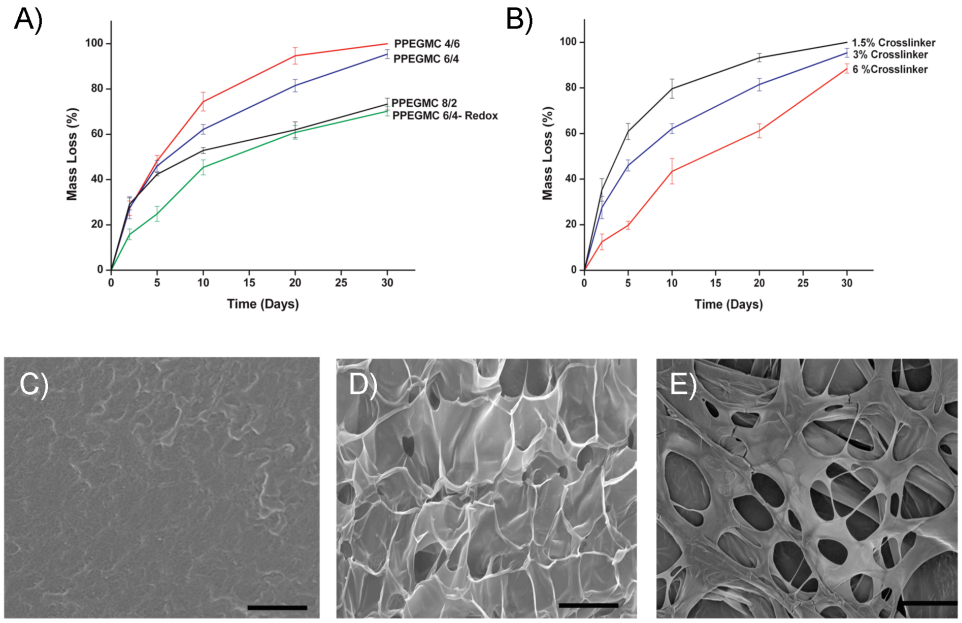

Figure 2.11 Degradation Profiles of PEGMC in Response to A) Crosslinking mechanism B) Crosslinker concentration, and C-E) Changes in surface morphology over degradation period (Scale bar 200 μm)

Figure 2.11 shows the degradation kinetics of PPEGMC hydrogels and surface morphology changes throughout the degradation period. Photocrosslinked PPEGMC 4/6 was completely degraded within 30 d time period whereas PPEGMC 8/2 lost 73.3 ± 2.6% of its initial mass. When compared to redox initiator crosslinked RPEGMC 6/4, which lost 70.1 ± 2.03% of its mass, photocrosslinked PPEGMC 6/4 already lost 95.4 ± 1.9% of its initial mass within 30 d (**Figure 2.11A**). It was also observed that the amount of crosslinker used for crosslinking also influenced the degradability of the hydrogels (**Figure 2.11B**). PPEGMC hydrogels prepared with 6% of crosslinker degraded 78.5 ± 2.0% of its mass compared to hydrogels prepared with 1.5% of crosslinker which degraded completely within 30 d. It was observed that as the degradation proceeded, the hydrogels became more porous (**Figures 2.11C-E**). This might be an important property of PEGMC as scaffolding materials for tissue engineering, where cell infiltration to the matrix is very critical as the matrix degrades.

2.2.3.5 In Vitro Drug Release

The *in vitro* release of BSA from PPEGMC hydrogels was observed over a 5-day period in PBS buffer (pH 7.4) and sodium acetate-acetic acid buffer (pH 5.4). After an initial burst release, the BSA release rate was in the sequence of PPEGMC 4/6 (92.7 ± 2.0%) > PPEGMC 6/4 (85.2 ± 3.8%) > PPEGMC 8/2 (73.1 ± 1.8%) over 5 d period at pH 7.4 (**Figure 2.12A**). However, the release rate was in the sequence of PPEGMC 8/2 (61.8 ± 2.9%) > PPEGMC 6/4 (32.1 ± 3.5%) > PPEGMC 4/6 (28.2 ± 1.4%) when incubated at pH 5.4 (**Figure 2.12B**).

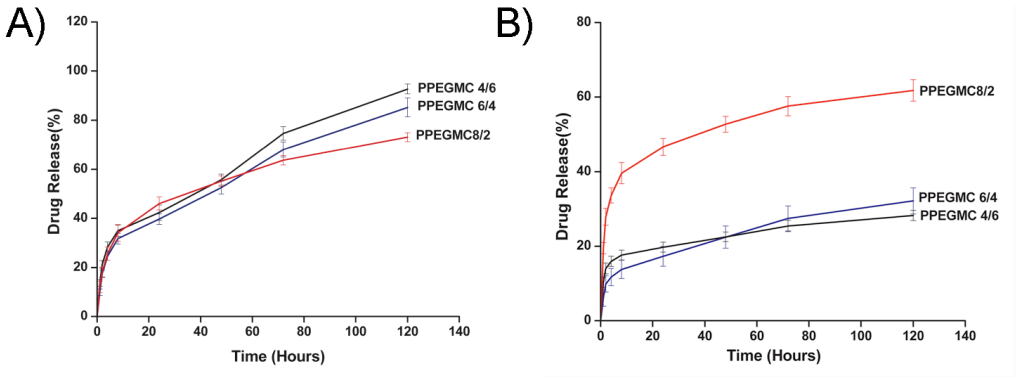

Figure 2.12 PEGMC BSA Release in A) PBS (pH 7.4) and B) Sodium acetate-acetic acid buffer solution (pH 5.4)

2.2.3.6 Microchannel Scaffold Fabrication

The microchannels and microchannel scaffold (**Figure 2.13**) demonstrate the processability of PAMC. The surface topology of the micropatterned PPOMaC created by a replica molding technique was verified using SEM. Figures 2.13A and B show that the fabricated microchannels resulted in column and channel widths of 210.77 ± 0.82 and 78.24 ± 0.84 mm, respectively. The SEM images of PPOMaC microchannel cross-sections show that the depth of each channel was 131.53 ± 1.66 mm as seen in Figure 2.13C. The microchannel scaffold construct produced pore sizes ranging from 106 – 150 mm in size with interconnectivity as seen in Figure 2.13D. All POMaC scaffolds were soft and could recover from bending deformations.

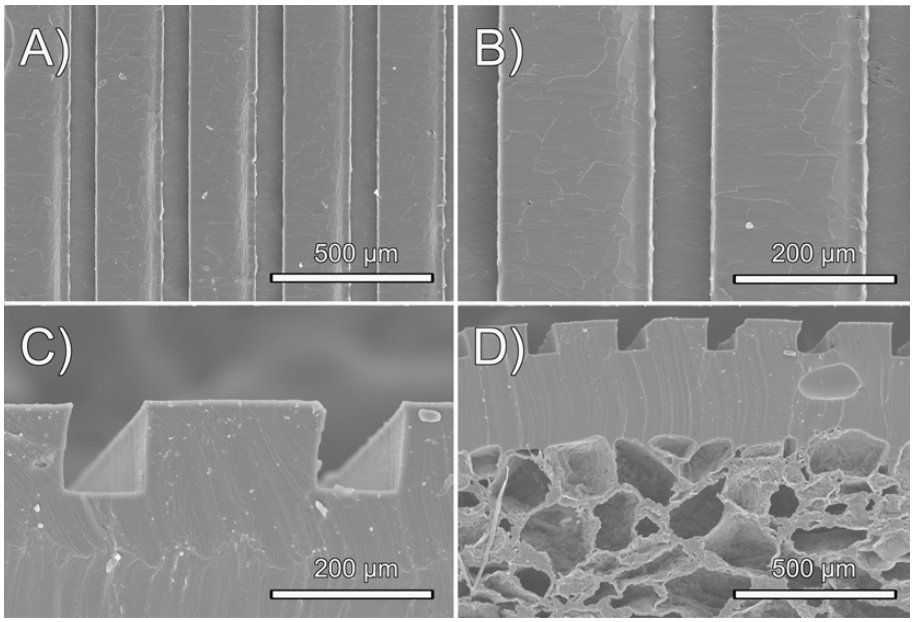

Figure 2.13 POMaC Microchannel Scaffold SEM Images A-B) Microchannel surface topography and C-D) Scaffold cross-sections

2.2.3.7 In Vitro Cell Evaluation

Cell adhesion of POMaC was observed 72 h after cell seeding. As shown in Figure 2.14A and B, 3T3 fibroblasts cultured on EPPOMaC films attached and displayed a normal morphology. Cell adhesion and proliferation were quantitatively evaluated on EPPOMaC and PLLA porous scaffolds using a MTT assay (**Figure 2.14C**). The results indicated that the cell adhesion and proliferation were initially higher on the PLLA scaffolds (day 1 and 3). However, EPPOMaC scaffolds showed a higher rate of cell proliferation and were almost comparable to the PLLA cell numbers by day 7 ($p > 0.05$).

Figure 2.15 shows the behavior of CFDA-SE labeled 3T3 fibroblasts seeded onto EPPOMaC scaffolds monitored over 2 weeks. Initially, a light density of cells accumulated along the scaffold surface (day 2). By day 7, the cell proliferation and density increased along the scaffold surface as seen by the dense cell clusters. After 14 days, the cells continued to proliferate along the exterior and started to migrate into the interior of the scaffold. H&E

photomicrographs of 3T3 fibroblasts cultured up to two weeks show that cells were able to colonize on POMaC scaffolds.

EPPOMaC scaffold cross-sections at 1 and 2 weeks of cell culture are shown in Figure 2.16. At 1 week, cells are found scattered in dense groups on the scaffold surface. By week 2, thick bands of 3T3 fibroblasts were observed growing along the outside of the scaffold along with increased infiltration of cells through the porous scaffold network.

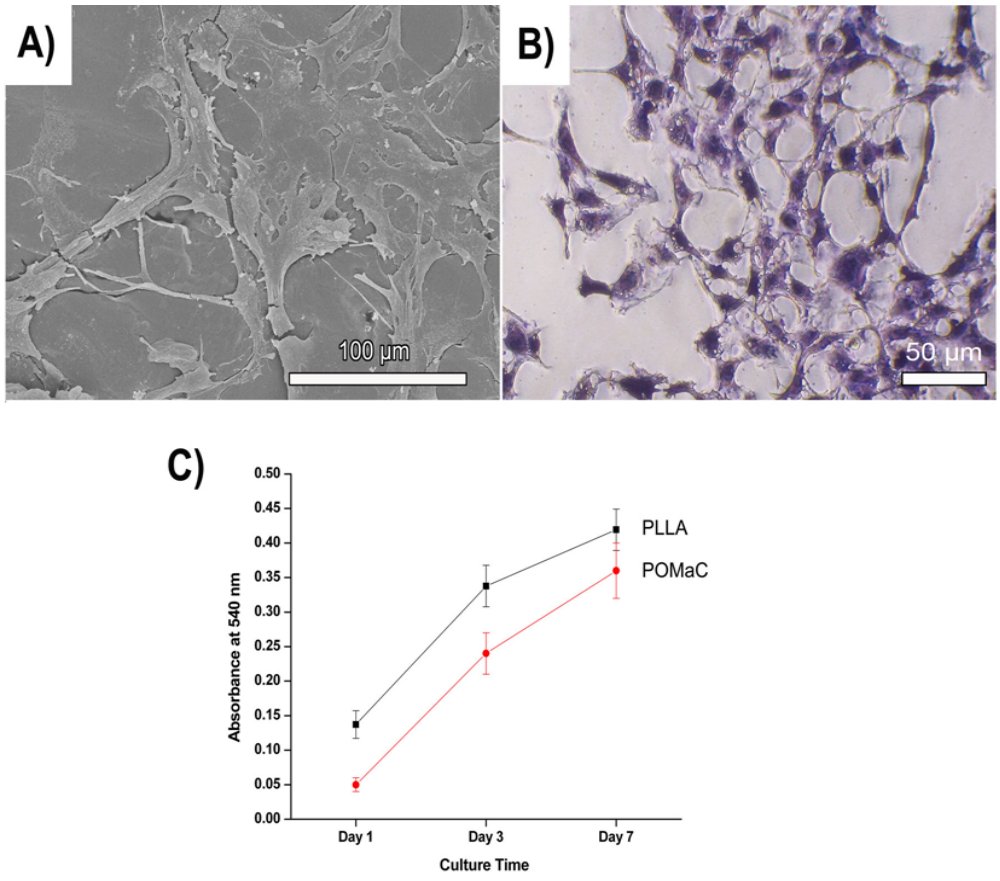

Figure 2.14 In Vitro POMaC Cytocompatibility A) SEM image of NIH 3T3 fibroblast cell monolayer, B) H&E stained NIH 3T3 fibroblast cell monolayer, C) MTT cell proliferation assay of NIH 3T3 fibroblast on PLLA (relative control) and POMaC scaffolds

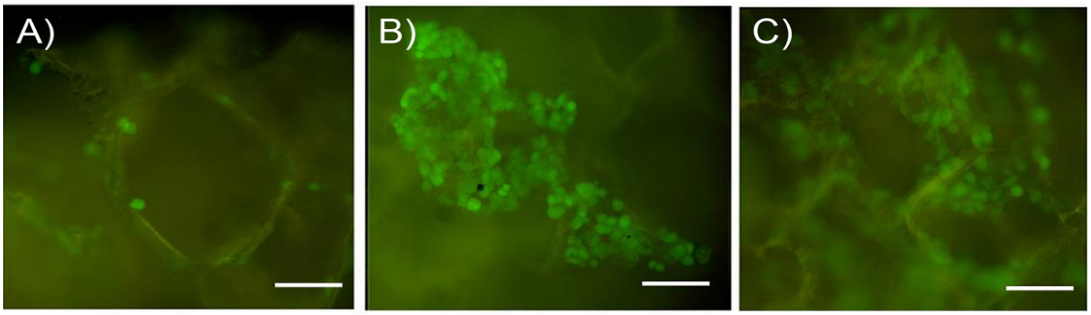

Figure 2.15 Behaviour of CFDA-SE Labelled NIH 3T3 Fibroblasts Seeded onto EPPOMaC Scaffolds A) After 2 days of culture, B) After 7 days of culture, and C) After 14 days of culture (Scale bar 50 μm)

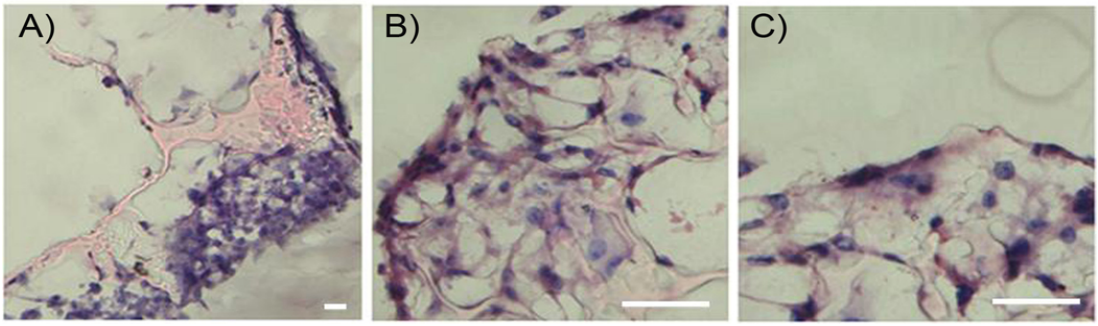

Figure 2.16 Photomicrographs of POMaC Scaffold Cross-Sections A) Scaffold periphery after 1 week of culture, B) Scaffold periphery after 2 weeks of culture, and C) Scaffold interior after 2 weeks of culture (Scale bar 50 μm)

Figure 2.17 shows that the PPEGMC hydrogel provided a good substrate for cells seeded on the surface or embedded within the *in situ* forming hydrogel. Both cell types, NIH-3T3 fibroblasts (**Figure 2.17A**) and human dermal fibroblasts (**Figure 2.17B**), adhered and spread upon the hydrogel surfaces within 48 h. When encapsulated in the network of the PPEGMC hydrogels, more than 80% of NIH 3T3 fibroblasts were stained alive (**Figure 2.17C**). These cells began to spread within the networks of PPEGMC 48 h after encapsulation and gel formation (**Figure 2.17D**).

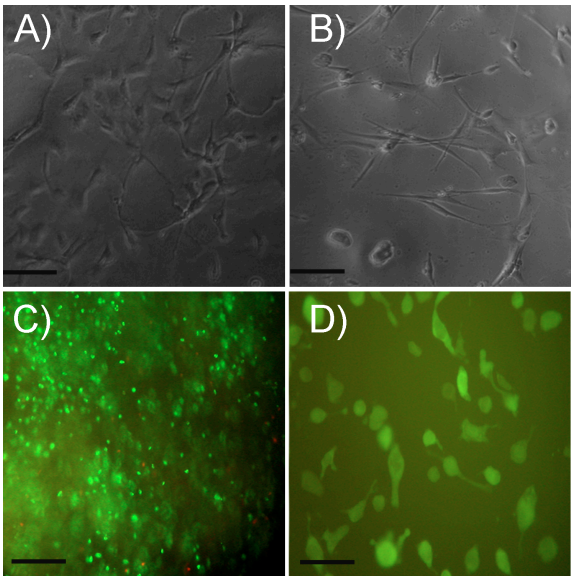

Figure 2.17 In Vitro PEGMC Cytocompatibility A) SEM image of NIH 3T3 fibroblast cell monolayer B) SEM image of human dermal fibroblast cell monolayer, C) Live/dead stain of encapsulated NIH 3T3 fibroblasts, D) CFDA-SE labeled encapsulated NIH 3T3 fibroblasts (Scale bar 200 μm)

The cytotoxicity of PEGMC pre-polymers and the degradation products of crosslinked PPEGMC were also evaluated. We evaluated the viability of NIH 3T3 fibroblasts in the presence of pre-PEGMC compared to the pre-polymer of PEGDA (**Figure 2.18A**) and degradation products of PPEGMC compared to degradation products of PLLA (**Figure 2.18B**) at various concentrations. After 12 h of incubation, there was no difference in cell viability for both PEGMC and PEGDA pre-polymers. However, there was a slight increase in the level of cell viability as the concentration of PEGMC decreased. Similarly, cells cultured with the degradation products of PPEGMC hydrogels also showed similar viability to the cells cultured with the degradation products of PLLA under similar concentrations.

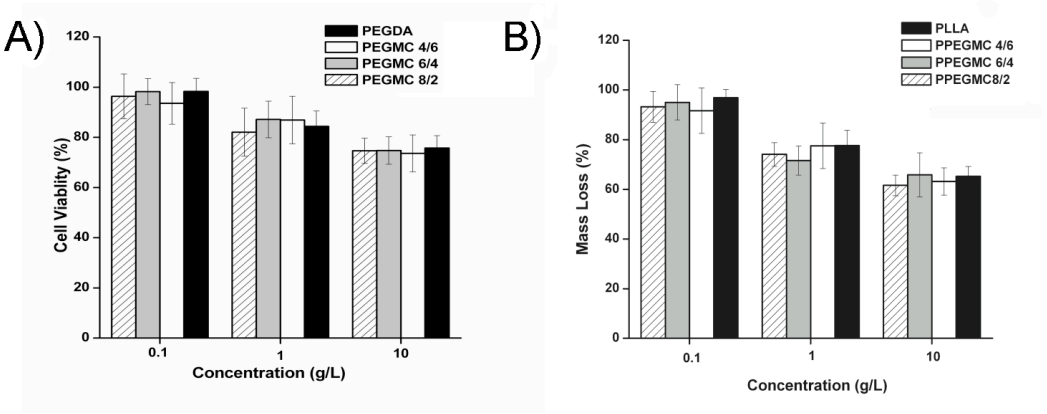

Figure 2.18 Cytotoxicity of A) PEGMC pre-polymer degradation products and B) Photocrosslinked PEGMC degradation products

2.2.3.8 Foreign Body Response

The foreign body response of PPOMaC and EPPOMaC was evaluated via subcutaneous implantation in mice. Figure 2.19 shows photomicrographs of H&E stained cross-sections of PPOMaC and EPPOMaC implants and the surrounding tissues. Given that biomaterial implants elicit varying degrees of tissue responses, the thickness of inflammatory cell infiltrate was quantified. This thickness was correlated to estimate the degree of inflammatory cell response (**Figure 2.20**). PLLA films were implanted and characterized as a model biomaterial implant. Consistent with many prior observations, PLLA films initiated inflammatory cell accumulation at week 1 (~100 mm), which gradually decreased into week 2 (~50 mm) and week 4 (~75 mm) consistent with a decrease in cells of leukocyte morphology and an increase in cells of fibroblast morphology.

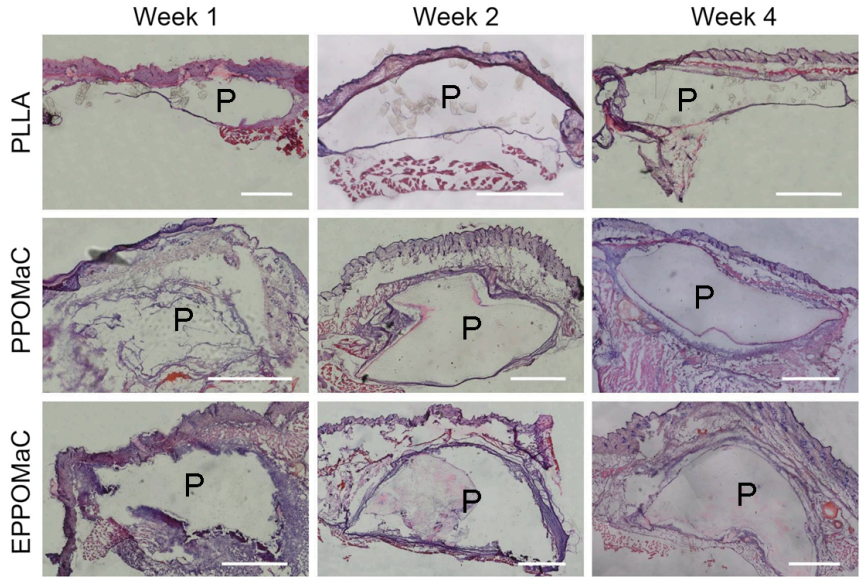

Figure 2.19. Photographs of H&E Stained Tissue Explants Demonstrating the Foreign Body Response of PLLA (control) and POMaC Films Implanted Subcutaneously in Balb/C Mice ("P" represents polymer section)

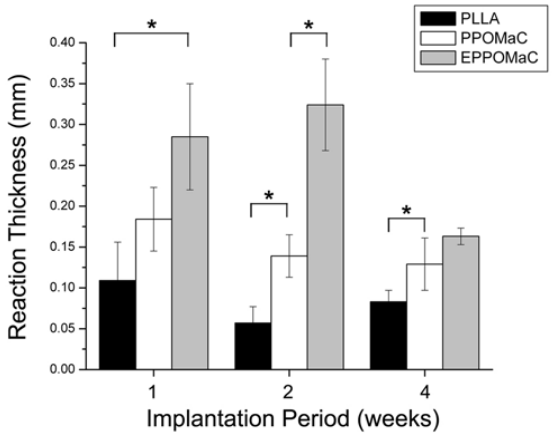

Figure 2.20 Characterization of the Foreign Body Response to PLLA and POMaC Implants

Interestingly, PPOMaC and EPPOMaC displayed different degrees of inflammatory cell responses. EPPOMaC generated a more pronounced response than PPOMaC at each time point investigated. Similar to the PLLA response, PPOMaC had an accumulation of cells around the implant at week 1 (175 mm), which showed a decreasing trend at weeks 2 and 4 (both ~125 mm). However, the EPPOMaC film generated an increased number of encapsulating cells at

both week 1 (1.5 x PPOMaC) and week 2 (3 x PPOMaC), significantly higher than both PLLA and PPOMaC ($p>0.05$). After 4 weeks of implantation, the response thickness for both PPOMaC and EPPOMaC significantly decreased by 30% (184 ± 39 to 129 ± 32 mm) and 43% (285 ± 65 to 163 ± 10 mm), respectively.

To further characterize the foreign body response, the CD11b expression in the cell-encapsulating layer at week 2 was examined as a measure of the neutrophil and monocyte/macrophage responses. This time point was chosen based on tissue responses to the polymer films, which exhibited the greatest difference in cell accumulation at week 2. In all implant groups, a mutli-cell layer staining positive for CD11b was seen. PLLA (**Figure 2.21A**) had a layer of $CD11b^+$ of only a few cells in thickness, while both PPOMaC (**Figure 2.21B**) and EPPOMaC (**Figure 2.21C**) had a more pronounced, multi-cell thick response.

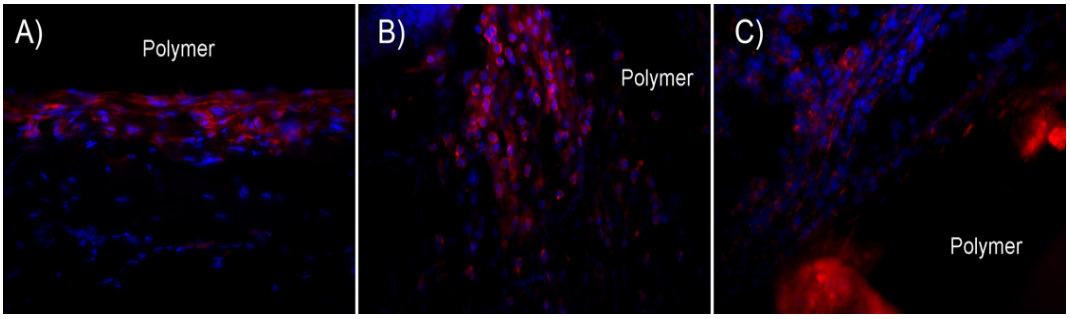

Figure 2.21 $CD11b^+$ Stained Sections Demonstrating the Foreign Body Response of A) PLLA (control), B) PPOMaC, and C) EPPOMaC implants after 2 weeks

Interestingly, the density of these cells inside the infiltrate layers is similar among all groups (**Figure 2.22A**). However, when the thickness of the $CD11b^+$ cell layer between groups was quantified (**Figure 2.22B**), a significant difference in the degree of the response was observed. Similar to measurements of thickness for the total cell layer, we find the $CD11b^+$ cell response decreases from EPPOMaC > PPOMaC > PLLA.

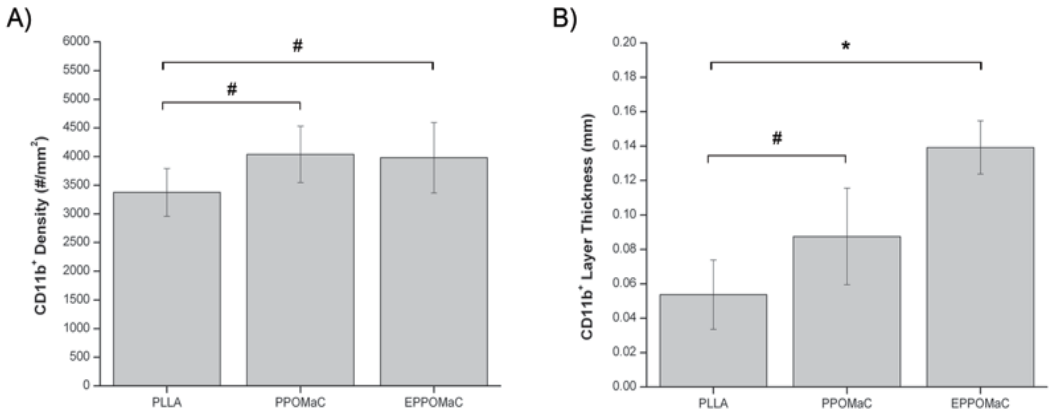

Figure 2.22 Characterization of the $CD11b^+$ Foreign Body Response to PLLA and POMaC Implants after 2 Weeks A) $CD11b^+$ density and B) $CD11b^+$ thickness

To demonstrate the injectability and *in situ* crosslinking of PEGMC, pre-PEGMC aqueous solutions were injected into a rat animal model using a 27-gauge needle (**Figures 2.23A and B**) and crosslinked using redox mechanisms. Pre-PEGMC quickly formed gel *in situ* within a few minutes after injection (**Figure 2.23C**). It was later (after 30 d) confirmed that the crosslinked hydrogels were completely absorbed by the host without any noticeable changes to the surrounding tissues (**Figure 2.23D**).

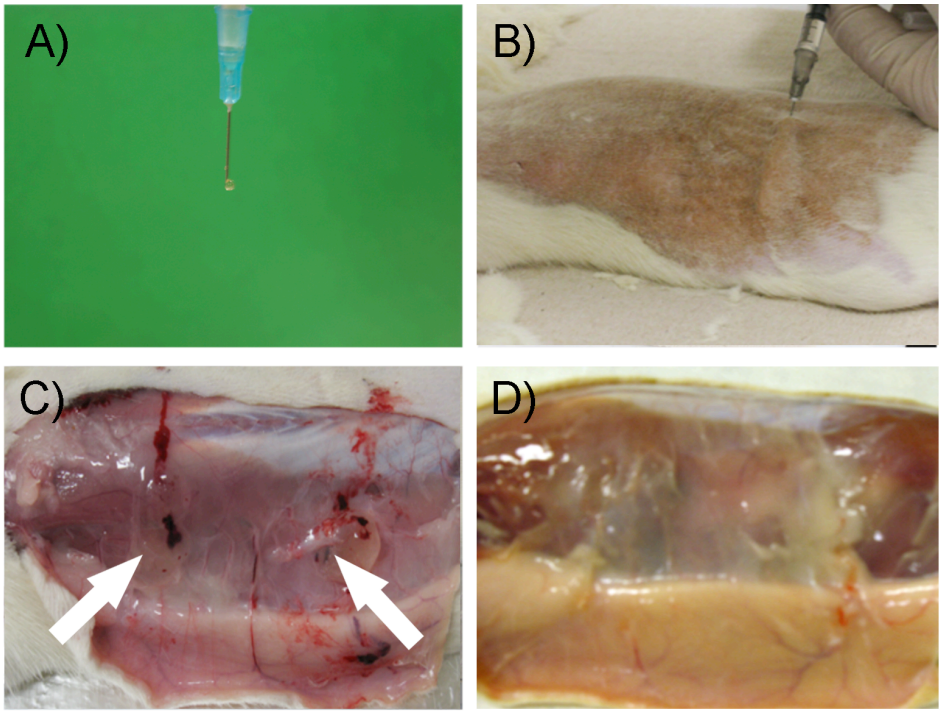

Figure 2.23 Demonstration of PEGMC Injectability and In Situ Crosslinking A) PEGMC pre-polymer injected through 27-gauge needle, B) Crosslinking of PEGMC solution, C) Hydrogel formation following subcutaneous injection, and D) Injection site after 30 days of implantation

Over the course of experiment, test animals did not show any abnormalities in their physical and behavioral patterns such as weight loss, lethargy, anorexia, dehydration, or distress. Histological analysis showed a presence of inflammatory cells at both 5 d and 15 d implantation (**Figure 2.24**). However, the number of cells around implants was significantly decreased after 30 days (**Figure 2.25**). The CD68 positive cells (monocytes/macrophages) around the implants (**Figure 2.25**) were counted and normalized to the total stained tissue area to determine the extent of inflammation. The number of CD68 positive cells did not significantly increase with increasing implant duration from day 5 to day 15. However, the number of macrophages was significantly decreased as the material was completely absorbed by the host at 30 d.

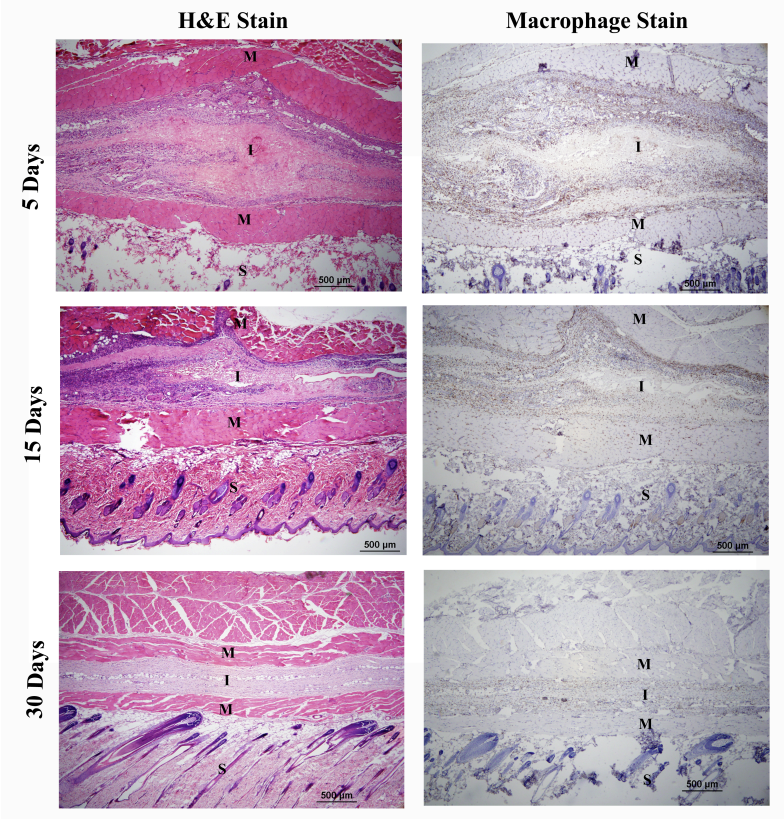

Figure 2.24 CD68^{+} Stained Sections Demonstrating the Foreign Body Response of PEGMC Implants after Subcutaneous Injection (S, M, and I represent skin, muscle, and injected site, respectively)

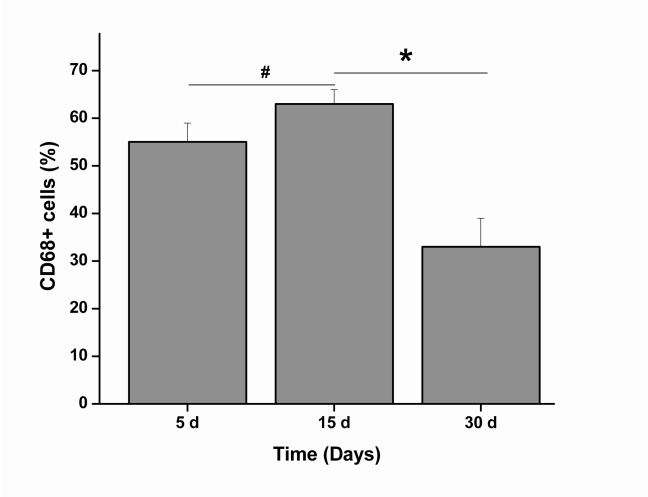

Figure 2.25 Characterization of CD68^{+} Foreign Body Response to PEGMC Implants after 2 weeks (* $p < 0.01$; # $p > 0.05$)

2.2.4 Discussion

The purpose of this study was to synthesize and evaluate a new family of biodegradable citrate-based biomaterials, PAMC. The basic components of PAMC were based upon the previously reported biodegradable elastomer, poly (diol citrates) (PDC), which has shown excellent biocompatibility both *in vitro* and *in vivo* [84]. By combining the advantages of free radical polymerization and ester bond crosslinking in the DCM, a new class of polyester elastomers has been created with the ability to be crosslinked into a three-dimensional network using a combination of two different mechanisms. Thus, the rapid *in situ* crosslinking of the network into a hydrogel is possible, and additional degradable ester crosslinks can be introduced throughout the polymer network to tune or enhance the mechanical properties without compromising the degradation capability for pre-fabricated scaffolding strategies. The materials synthesized in this study cover a wide range of swelling ratios, mechanical properties, degradation profiles, and functionalities, which are important in controlling the biological response to an implanted material [117]. The free functional groups available after free radical polymerization are useful moieties for the potential modification of the material with proteins or peptides to activate a desired cellular response [93]. Unlike other materials, PAMC offers an additional advantage in that extra treatment to create these chemical moieties is not needed [49, 118].

The synthesis of pre-POMaC, which is conducted through a controlled polycondensation reaction between MA, Ca, and OD, is simple and cost-effective. The melting polymerization provides an easy way to scale up the biomaterial preparation [119]. POMaC are inexpensive to produce, easy to synthesize, and are adaptable to most polymer processing capabilities [120]. The reaction was driven forward by the removal of water through the addition of heat to produce a random copolymer with degradable ester bonds throughout the polymer backbone. MA was chosen as a means to incorporate a vinyl group into the pre-POMaC backbone in order to crosslink the polymer network through free radical polymerization. CA was

chosen as a multifunctional monomer, which contributed pendant carboxylic acid and hydroxyl groups in the pre-polymer backbone for the future incorporation of specific factors, and the option for further post-polymerization. When PEG was substituted for OD in the reaction of pre-PEGMC, the polycondensation reaction yielded a low molecular weight, low viscosity pre-polymer, which could be easily be dissolved in water and avoids the need for toxic organic solvent system for in situ tissue engineering applications.

Most of the existing materials lack free functional group(s) that are important for potential biofunctionalization [121]. Pre-polymer FT-IR analysis shows the successful incorporation of the vinyl group and preservation of the carboxylic and hydroxyl functionalities in all pre-PAMC polymers. As the molar ratio of the MA is decreased, the ratio of the vinyl group peak to the hydroxyl group peak was reduced, which is also supported in the ^{1}H NMR evaluation. The reduction of the double bond peak located at 1647 cm^{-1} in the photocrosslinked films verified the consumption of the vinyl group during the free radical polymerization, and the preservation of the broad peak located at 3750 cm^{-1} confirmed the presence of the unreacted pendant functional groups, which were partially consumed in the oven crosslinked films.

The chemical compositions determined from ^{1}H NMR were consistent with the feed ratios to show that the molar ratios can be precisely controlled during synthesis (**Table 2.1 and 2.2**). The two pairs of vinyl hydrogen peaks located between 6 and 7 ppm were contributed by MA vinyl groups located in the middle and at the end of the polymer chain [116]. Decreasing the MA ratio during the pre-polymer synthesis resulted in networks with increased functionalities, which was confirmed by an increase in the area of the hydroxyl proton peaks. Thus, the functionalities in the pre-polymer can be easily modulated towards a specific application, which is an important parameter in the outcome of the material properties for PAMC.

In the case of photocrosslinked films, the swelling capability of the polymer was directly correlated to the amount of MA in the polymer. As shown in Figure 2.7A, the total uptake ability of the polymer was significantly lowered for all swelling agents as the amount of MA was

increased. This is due to the fact that the vinyl functionality contributed by the MA was solely responsible for the crosslinking of the network in the free radical polymerization. This was supported by the calculated values of the crosslinking density where the increased amount of MA in the polymer resulted in a higher number of crosslinks in the network. In addition, a decrease in the MA corresponded to an increase in the CA, which contained carbonyl and hydroxyl chemistries to increase the hydrophilicity of the polymer. Thus, swelling for the polymer with a higher molar ratio of MA was restricted.

As seen in the swelling study (**Figure 2.9**), there was a sudden increase in the swelling ability of PEGMC hydrogels in the buffer of pH 5.4 to 7.4. The difference in the swelling of hydrogels at pH 5.4 to 7.4 revealed that PEGMC chains contained ionizable groups with their pKa values somewhere between 6 and 7. It was believed that these groups are the second carboxylic group of MA (pK2 = 6.27) and the third carboxylic group of CA (pK3 = 6.4). Carboxylic and hydroxyl groups have been recognized as the highly favored pendant chemistries for the functionalization of biomaterials with drugs or biomolecules. The availability of such groups on the PEGMC polymer chains provides sites for potential biofunctionalization.

These findings from the swelling studies were confirmed by the degradation characteristics of the polymer. The degradation rate for POMaC polymers was controlled through the hydrophilicity and crosslinking density of the resulting network. Thus, increasing the CA content and lowering the crosslinking degree created a polymer with a faster degradation rate. Degradation studies also revealed that PEGMC networks were able to degrade through hydrolysis, which was expected, as the polymer chains between crosslinks are polyesters. Interestingly, SEM images of the partially degraded PEGMC samples showed the development of a highly porous matrix over the course of the degradation period (**Figure 2.11**), which is potentially beneficial for the infiltration of migrating cells and exchange of nutrients and metabolic waste. Results also revealed that as the vinyl moiety in the hydrogel precursor was increased (either increased in MA concentration or crosslinker concentration), the rate of

degradation reduced. Redox crosslinked gels showed a further decrease in degradation rates compared to that of photocrosslinked hydrogels. These data conclude that higher crosslinking due to increased concentration of double bonds and homogeneous crosslinking during redox crosslinking resulted in a reduction of degradation rate. It was also observed that redox crosslinked hydrogels were only degraded 70% of their mass in PBS.

Engineering soft and elastic tissues such as lung tissue (5 – 30 kPa), skeletal muscle (100 kPa), and cardiac muscle (20 – 150 kPa) have sparked the development of soft biodegradable elastomers [122]. It has been recognized that the mechanical properties of tissue engineered scaffolds potentially have an influence on the inflammatory response, angiogenesis, and wound healing process [123]. In addition, previous research has shown that soft and elastic scaffolds are more conducive to angiogenesis when compared to stiffer scaffolds [88]. Therefore, it is important to closely match the mechanical properties of scaffolds with the targeting tissues for tissue engineering. The reported mechanical properties of PAMC cover most of the above soft tissues. POMaC are unique in that the mechanical properties of polymer networks can be fine tuned by adjusting monomer ratios and balancing the carbon-carbon crosslinking with ester bond crosslinking. Unlike other reported biodegradable elastomers, in which increasing the crosslinking degree to obtain higher mechanical strength results in the loss of valuable pendant functional groups, the multiple crosslinking mechanisms will allow for a more flexible design [84, 95].

For example, decreasing the MA amount in the polymer backbone resulted in a very soft and elastic polymer when crosslinked only through the free radical polymerization. Adjusting the free radical crosslinking degree may adjust material properties without sacrificing pendant functional groups. An additional control over the ester bond crosslinking may increase the stiffness and strength of the polymers if needed. Thus, there is a fine balance between the amount of MA and Ca along with the multiple crosslinking mechanisms in order to achieve the proper material properties for the target application. Tensile properties of PPEGMC showed that

an increase in molar concentration of MA (relatively less CA) resulted in an increase in initial modulus (**Figure 2.6A**). These data clearly suggested that crosslinking density had a significant effect on the mechanical properties of the resulting polymers. Cyclic compression conditioning tests conducted on RPEGMC demonstrated that these hydrogels were highly elastic and showed 100% recovery with negligible hysteresis (**Figure 2.6B**). All PEGMC hydrogels were soft as confirmed by the low initial modulus (100 – 500 KPa) (**Figure 2.6C**) at dry state in tensile test and 8 – 28 KPa at wet state in compression tests.

The *in vitro* BSA release studies showed a 40% initial burst release followed by a more sustained release over a 5-day period from PPEGMC hydrogels in buffer solutions at both pH 7.4 and 5.4. The *in vitro* drug release studies also confirmed the pH sensitivity of PEGMC networks. BSA release was more restricted from PPEGMC hydrogels at pH 5.4, and was attributed to the increased hydrogen bonding with the pendant carboxyl groups from citrate units. As seen in Figure 2.12, as the citrate content was increased, a slower release of BSA was seen from PEGMC networks. The BSA release studies support that the water soluble PEGMC can potentially be a viable material for controlled in situ protein/drug delivery applications.

The combination of elastomers with micro-electro-mechanical systems (MEMS) technologies has sparked a new area of research with increasing practical applications [124]. The capability to specifically control the size and shape of biologically relevant materials has provided new opportunities in addressing some of the challenges in tissue engineering such as vascularization, tissue architecture, tissue organization, and cell seeding [125]. POMaC has demonstrated versatile processability and the ability to be fabricated into complex geometries as shown by the microchannel scaffold (**Figure 2.13D**). By using a soft lithographic approach, replica-molded POMaC constructs were created for future research in developing vasculature and organized tissues in contact guidance applications.

The preliminary *in vitro* and *in vivo* biocompatibility evaluations of PAMC confirm their potential as a suitable biomaterial. *In vitro* results of cell adhesion and proliferation demonstrate

good cell-material interaction. 3T3 fibroblasts seeded onto POMaC films were viable and displayed a normal morphology. However, quantitative analysis from MTT assay showed that cells did not initially proliferate as well as PLLA, but did display a similar growth pattern. Unlike many other hydrogels which require pre-treatment with adhesion peptides or proteins for cell culture, the in vitro cell attachment and proliferation on POMaC were performed without any pre-treatment [112, 126]. Furthermore, POMaC offer room for improvement through the available pendant groups available for the conjugation of proteins or other cell specific factors if needed.

To demonstrate the utility of PEGMC hydrogels as a cell delivery system, cells were seeded on the surface of and encapsulated within the *in situ* forming networks of PEGMC. Both NIH 3T3 fibroblasts and human dermal fibroblasts adhered and spread on the surface of PEGMC (**Figure 2.17**). Upon encapsulation, more than 80% of cells were viable within the networks of RPEGMC and began to spread after 48 h of encapsulation to show the potential of RPEGMC as an injectable cell delivery vehicle. A clear advantage of PEGMC over previous citrate-based materials is its ability to be used as an *in situ* forming cell delivery vehicle due to the water-soluble properties of the pre-polymer and free radical crosslinking ability. Pre-polymeric PEGMC demonstrated similar cytotoxicity to the commercially available injectable polymer (PEGDA) (**Figure 2.18A**). The degradation products of the crosslinked PEGMC (PPEGMC) also elicited a similar cytotoxicity when compared to PLLA (**Figure 2.18B**), a biodegradable polymer widely used in FDA approved medical devices.

Several recent papers have used the thickness of the cellular infiltrate around the biomaterial to assess the degree of tissue response [69, 127, 128]. This buildup of inflammatory cells and fibroblasts initiates the formation of granulation tissue and fibrotic capsule surrounding biomaterial implants. PLLA films were chosen as a model comparison to PPOMaC implants due to their ubiquitous use in biomedical applications. The degree of *in vivo* cell encapsulation to PPOMaC implants is similar to previously published reports using biodegradable elastomers

assessed over the first 4 weeks of implantation [95, 127]. In addition, the nature of this response appears related to the crosslinking methods used to create the material, as the PPOMaC films had a substantially decreased response at weeks 1 and 2 compared to EPPOMaC films. Beyond the cell accumulation around the implants, the nature of the neutrophil and macrophage responses was investigated, as the degree of activation of these adherent cell types to the biomaterial can dictate fibroblast interactions and fuel fibrotic encapsulation [127, 129].

Using the responses to PLLA films as comparison, PPOMaC accumulated only slightly more $CD11b^+$ cells around film implants, suggesting a similar degree of response and activation to PLLA. A similar crosslinking effect was observed for EPPOMaC, as these films appear to accumulate substantially more $CD11b^+$ cells than PPOMaC films. This can perhaps be explained by the difference in material physical properties, with the higher modulus EPPOMaC films potentially causing more mechanical agitation in the subcutaneous implantation model over the course of the 2-week implantation period. In addition, PPOMaC networks exhibit more hydrogel like properties, which have been shown to be very biocompatible due to their mechanical compliance and mass transfer properties [130].

To further demonstrate the injectability of PEGMC for *in vivo* applications, we have demonstrated that PEGMC could be injected into rats subcutaneously using a 27G needle and crosslinked *in situ* within a few minutes (**Figure 2.23**). Histological analysis demonstrated that RPEGMC elicited slight inflammation in the early stages post-injection (**Figures 2.24 and 2.25**). Upon complete degradation of the hydrogel (30 d), the inflammatory active zone was significantly reduced with minimal cell infiltration in the implantation sites. The relatively faster degradation in vivo might result from enzyme degradation that would normally occur to many other types of polyesters when implanted in the body. The above animal studies indicate the *in situ* formation of PEGMC hydrogels and the excellent *in vivo* tissue compatibility and degradability. However, more thorough analysis of the inflammatory cell response and long-

term fibrotic response is needed to validate whether the tissue response to these materials is indeed comparable.

2.2.5 Conclusion

We have developed a new class of novel elastomeric biomaterials that are synthesized using inexpensive monomers and a cost effective synthesis procedure. The application of PAMC is not limited to any single application in that the DCM allows for the option of crosslinking the material through UV irradiation and/ or polycondensation. PAMC exhibit a wide range of material properties that can be controlled using the DCM. The softness of the material can be fine tuned to meet the requirements for soft tissue engineering applications. Water-soluble formulations demonstrated excellent injectability, *in situ* crosslinking, adequate functionalities, elastic mechanical properties, and controlled degradability. Collectively, the development of this new platform biomaterial further expands upon the current repertoire of citrate-based biodegradable polymers and presents unique opportunities to address the current needs many biomedical applications.

2.3 Citrate-Based Urethane-Doped Polyesters

2.3.1. Introduction

Previous citrate-based elastomers are soft and elastic (100% recovery from deformation) with excellent cell/tissue compatibility, but their success for *in vivo* tissue engineering is still not proven. These materials are inherently weak and hence, unsuitable for engineering tissues like ligaments, which are characterized by high tensile strength. In addition, an ideal tissue-engineering scaffold should possess sufficient mechanical strength to support surgical handling soon after initial cell seeding. Unfortunately, the tensile strength of poly (diol citrate) (PDC) films is significantly reduced upon pore introduction, and can only be improved by increasing the crosslinking degree, which sacrifices material elasticity and renders the resulting material brittle. Therefore, it is important to design biomaterials that are able to compensate for the loss of material strength upon scaffold fabrication.

Biodegradable polyurethanes are a class of elastic biomaterials that have been developed for an assortment of tissue engineering applications with varied success [37, 40, 41, 49, 131]. Although biodegradable polyurethanes have shown good mechanical strength (up to 29 MPa tensile strength) and elasticity (up to 895% elongation), these materials are susceptible to permanent creep under cyclic mechanical loading, which limits their long-term success as scaffold materials for tissues located in dynamic environments like blood vessels and ligaments. Therefore, the development of a strong, soft, and totally elastic biodegradable material, which can maintain the required mechanical strength upon scaffold fabrication and function immediately after implantation, would be a great advancement in the field of biomaterial science.

To address the limitations of the previous mechanically weak citrate-based materials, we have recently reported on the synthesis and characterization of crosslinked urethane-doped polyesters (CUPE), which combines the advantages of completely elastic and cytocompatible crosslinked polyester networks with the strength of polyurethanes [10]. A simple doping of a diisocyanate (hexamethylene diisocyanate) (HDI) into the previously developed poly (octanediol citrate) (POC) network significantly increased the material tensile strength while maintaining a soft and elastic nature. By varying the POC: HDI ratios and the post-polymerization crosslinking conditions, a new form of polyesters was developed with a 30-fold increase in tensile strength over previous materials while maintaining a soft, elastic, biocompatible, and hemocompatible nature. Tensile strengths of up to 45.2 ± 7.4 MPa with a corresponding elongation at break of 222.7 ± 27.6% were obtained from CUPE networks, and all samples demonstrated 100% recovery up to the breaking point. CUPE was also shown to support smooth muscle cell (SMC) adhesion and proliferation *in vitro,* and the *in vivo* host response demonstrated that CUPE has superior short and long-term tissue compatibility when compared to PLA.

While the synthesis and characterization of CUPE has already been reported, the effects of the diol component were still unknown. Our previous work focused on the use of a

single length aliphatic diol (1,8-octanediol) in the soft segment synthesis, and used the HDI concentrations and post-polymerization conditions to control the material properties of the resulting elastomer [10]. Previous studies on PDC have shown that the choice of various aliphatic diols (C6-C12) and macrodiols such as poly (ethylene glycol) (PEG) can be used to generate versatile elastomers able to cover a wide range of mechanical properties, degradation profiles, and surface energy characteristics, which are all important to control the biological response to the implanted material [95]. The purpose of this study is to elucidate the influence of the diol component on the material properties of CUPE. The incorporation of diols with various methylene lengths, hydrophilic macrodiols, and charged monomers are all investigated to determine the structure-property relationship of the resulting materials in the development of a new generation of CUPE elastomers.

The rationale behind the biomaterial design are: 1) using the concept that collagen and elastin are crosslinked polymers that provide elasticity to the natural extracellular matrix (ECM), we chose crosslinking as a mechanism to confer elasticity to the biomaterial; 2) to increase the manufacturing potential, we chose to use inexpensive monomers and a cost-effective synthesis procedure performed under mild heating without the use of any catalysts; 3) the incorporation of ester bonds into the polymer backbone confers degradability to the crosslinked polymer network; 4) the choice of aliphatic diol (C4-C12) and post-polymerization condition can be used to fine-tune the material properties of the polymer; 5) partially substituting hydrophobic aliphatic diol with hydrophilic macrodiols (PEG) can be used to balance the material surface energy characteristics and degradation profiles; and 6) the introduction of urethane bonds into the polyester chains between ester crosslinks can enhance the hydrogen bonding and strengthen the CUPE network while maintaining elasticity.

The following sections will discuss the development of two new polymers within the urethane-doped polyester elastomers, CUPE Family and CUPE PEG, to better understand how the aliphatic diol length and incorporation of hydrophilic segments, respectively, affect the

material properties of the resulting elastomers. The results from these studies show that CUPE are highly flexible materials, which can be modulated through a multitude of synthesis parameters to serve as a unique platform biomaterial for soft tissue engineering applications.

2.3.2. Experimental

2.3.2.1 CUPE Synthesis

All chemicals, cell culture medium and supplements were purchased from Sigma–Aldrich (St. Louis, MO), except where mentioned otherwise and used as received. To evaluate the effects of diol length, different CUPE Family polymers were synthesized by a three-step procedure as shown in Figure 2.26. Step 1 involves the polycondensation reaction of citric acid with different C4-C12 aliphatic diols: 1,4-butanediol (≥99%) (BD), 1,6-hexanediol (99%) (HD), 1,8-octanediol (98%) (OD), 1,10-decanediol (98%) (DD), or 1,12-dodecanediol (99%) (DOD). Step 2 involves the introduction of urethane linkages to form the final CUPE Family pre-polymer, and step 3 involves a post-polymerization step for final thermal crosslinking.

Briefly, citric acid and diols of various lengths were bulk polymerized in a three-neck flask equipped with an inlet and outlet adapter using a monomer ratio of 1: 1.1 (acid to diol) for the all synthesis procedures. The monomer mixture was first melted at 160-165 °C, and then allowed to continue for 1 hour at 140 °C to obtain the soft segment pre-polymer. The resulting pre-polymer was purified by drop-wise precipitation in de-ionized (DI) water under constant stirring, collected from the aqueous phase, and lyophilized for 48 hours to remove traces of water. In step 2, the purified pre-polymer was dissolved in 1,4-dioxane to form a 3 wt. % solution, and reacted with 1,6-hexamethylene diisocyanate (HDI) under constant stirring. The reaction was carried out at 55 °C, and reaction completion was indicated by the absence of a diisocyanate peak in the FT-IR spectrum of the reaction mixture at 2267 cm^{-1}. In step 3, the pre-CUPE synthesized in step 2 was cast in Teflon molds, air dried to remove all solvent, and then crosslinked in an oven maintained at 80 °C for time periods ranging from 1-4 days, to obtain the final crosslinked urethane doped polyester. The different crosslinked urethane-doped polyesters

obtained were designated as CUPE X, where X denotes the number of carbon atoms in the diol used as the monomer for the reaction with citric acid. For example, CUPE 10 indicates that 1,10-decanediol was the monomer used in the reaction. For all the different polymers obtained, the soft segment pre-polymer to diisocyanate ratio of 1: 1.2 was maintained. Table 2.5 depicts the complete monomeric composition for each CUPE Family synthesized in this study.

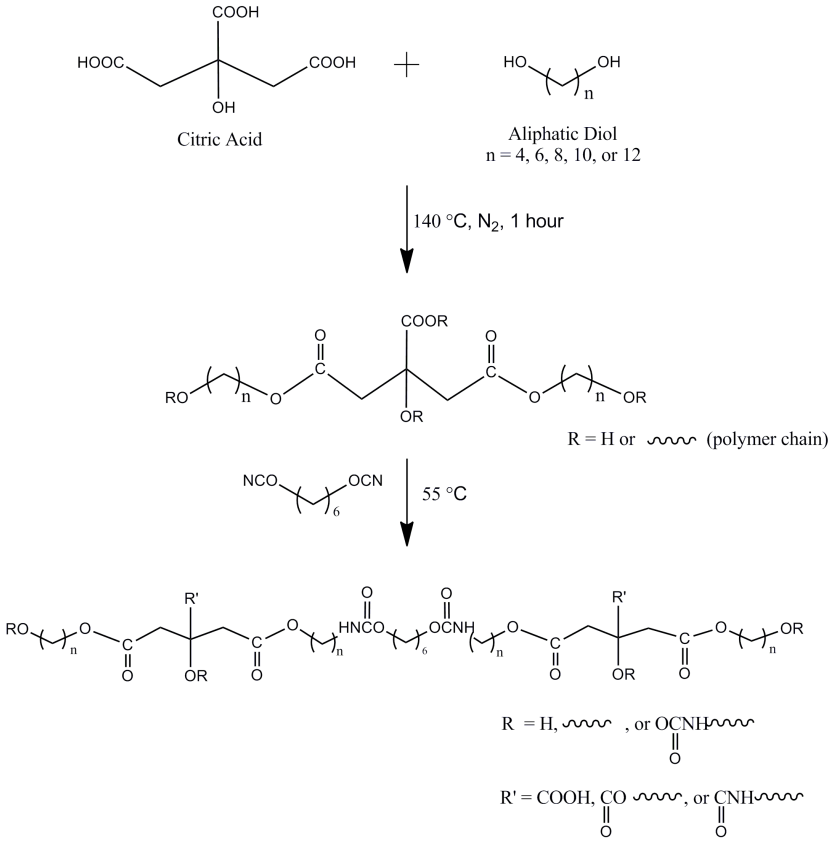

Figure 2.26 CUPE Family Synthesis Schematic

Table 2.5 CUPE Family Monomer Compositions

	Feed Ratios (mol)						
Polymer Name	**Citric Acid**	**Butane-diol**	**Hexane-diol**	**Octane-diol**	**Decane-diol**	**Dodecane-diol**	**HDI Ratio**
CUPE 4	1.0	1.1	–	–	–	–	1.2
CUPE 6	1.0	–	1.1	–	–	–	1.2
CUPE 8	1.0	–	–	1.1	–	–	1.2
CUPE 10	1.0	–	–	–	1.1		1.2
CUPE 12	1.0	–	–	–	–	1.1	1.2

To investigate the effects of incorporating hydrophilic segments into the polymer network, CUPE PEG polymers were synthesized according to the three-step schematic shown in Figure 2.27. Step 1 involves the polycondensation reaction of citric acid with 1,8-octanediol to produce a poly (octanediol citrate) (POC) pre-polymer soft segment (hydrophobic segment). In a completely separate reaction, citric acid was reacted with poly (ethylene glycol) (PEG) (MW 200) to produce a poly (ethylene glycol citrate) (PEC) pre-polymer soft segment (hydrophilic segment). Step 2 involves the introduction of urethane linkages into various ratios of the soft segments to obtain the final CUPE PEG pre-polymer, and step 3 involves a post-polymerization step for final thermal crosslinking.

Briefly, citric acid and 1,8-octanediol were bulk polymerized in a three-neck flask equipped with an inlet and outlet adapter using a monomer ratio of 1: 1.1 (acid to diol). The monomer mixture was first melted at 160-165 °C, and then allowed to continue for 1 hour at 140 °C to obtain the hydrophobic soft segment pre-polymer. The resulting pre-polymer was purified by drop-wise precipitation in de-ionized (DI) water under constant stirring, collected from the aqueous phase, and lyophilized for 48 hours to remove traces of water to form pre-POC. In a completely separate reaction, citric acid and PEG were bulk polymerized in a three-neck flask equipped with an inlet and outlet adapter using a monomer ratio of 1: 1.1 (acid to diol). The monomer mixture was first melted at 160-165 °C, and then allowed to continue for 3 hours at 140 °C to obtain the hydrophilic soft segment pre-polymer. The resulting pre-polymer was purified by dialysis using a 500 MW cut off dialysis membrane, and lyophilized for 48 hours to remove traces of water to form pre-PEC.

In step 2, various ratios of purified pre-POC and pre-PEC were dissolved in 1,4-dioxane to form a 3.0 wt. % solution, and reacted with HDI under constant stirring. The reaction was carried out at 55 °C, and reaction completion was indicated by the absence of a diisocyanate peak in the FT-IR spectrum of the reaction mixture at 2267 cm^{-1}. In step 3, the pre-CUPE PEG synthesized in step 2 was cast in Teflon molds, air dried to remove all solvent, and then cured in

an oven maintained at 80 °C for time periods ranging from 1-4 days, to obtain the final CUPE PEG. The different crosslinked urethane-doped polyesters obtained were designated as CUPE PEG X, where X denotes the percentage of the hydrophilic segment used in the total soft segment composition. For example, CUPE PEG 25 indicates that of the total soft segment composition, 25% was made up of pre-PEC and 75% pre-POC. For all the different polymers obtained, the soft segment pre-polymer to diisocyanate ratio of 1: 1.2 was maintained. Table 2.6 depicts the complete monomeric composition for each CUPE PEG X synthesized in this study.

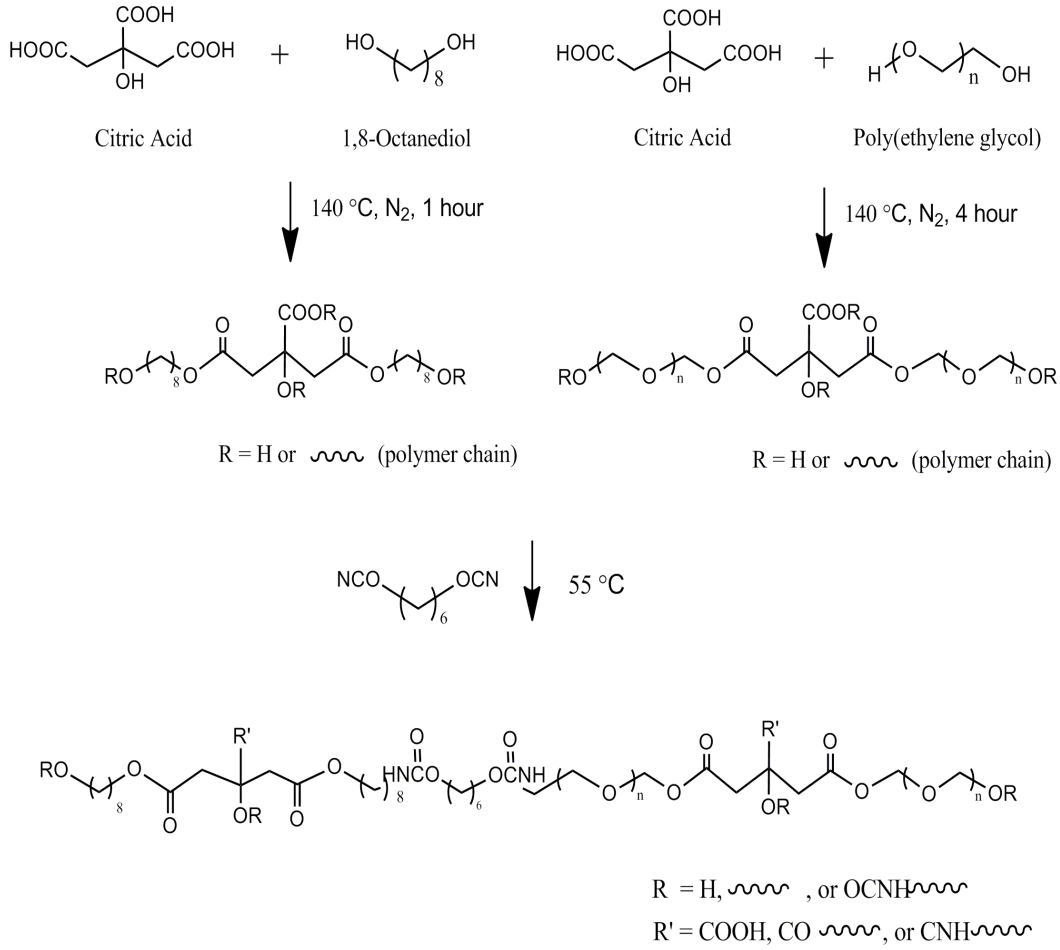

Figure 2.27 CUPE PEG Synthesis Schematic

Table 2.6 CUPE PEG Hydrophobic and Hydrophilic Segment Compositions

	Feed Ratios					
Polymer Name	**CA (mol)**	**OD (mol)**	**PEG (mol)**	**HDI Ratio**	**POC (%)**	**PEC (%)**
POC	1.0	1.1	–	–	100	–
PEC	1.0	–	1.1	–	–	100
CUPE PEG 0	–	–	–	1.2	100	0
CUPE PEG 25	–	–	–	1.2	75	25
CUPE PEG 50	–	–	–	1.2	50	50
CUPE PEG 75	–	–	–	1.2	25	75
CUPE PEG 100	–	–	–	1.2	0	100

2.3.2.2 Polymer Characterization

A Nicolet 6700 FT-IR spectrometer (Thermo Fisher Scientific) was used to obtain Fourier transform infrared (FT-IR) spectra of the different polymers synthesized. Briefly, a dilute solution (3.0 wt. %) of the CUPE pre-polymer dissolved in 1,4-dioxane was cast onto a clean potassium bromide (KBr) crystal, and allowed to dry in vacuum for 6 hours prior to spectrum acquisition.

The glass transition temperature (T_g) of the different CUPE polymers synthesized was determined by differential scanning calorimetry (DSC) on a DSC2010 Differential Scanning Calorimeter (TA Instruments, New Castle, DE). The different polymer samples were subjected to two heating cycles. In the first cycle, the polymers were scanned to 150 °C, under nitrogen atmosphere with a step size of 10 °C min^{-1} and then cooled rapidly to -60 °C at a cooling rate of -40 °C min^{-1}. The second cycle comprised of heating the sample to 230 °C with a step size of 10 °C min^{-1}. All readings were collected during the second heating scan. The T_g value was determined from the middle of any step changes in the heat capacity from the second scan.

All mechanical testing was conducted on a MTS Insight 2 mechanical tester equipped with a 500 N load cell (Eden Prairie, MN). All films were cut into dog bone shape as per ASTM D412a standard (25 x 6 x 1.5mm, length x width x thickness). The samples were stretched at a deflection rate of 500 mm min^{-1} until break. The initial modulus was derived from the gradient of the curve at 10% elongation in the stress strain curve. A minimum sample size of n = 6 was

maintained for all the films tested. A density measurement kit (Mettler Toledo, Columbus, OH) was used to determine the density of the different CUPE polymers synthesized. The auxiliary fluid used in the density measurement experiments was DI water.

In order to determine the molecular weight between crosslinks and the crosslink density, the theory of rubber elasticity was used (**Equation 1**) [80, 84, 132, 133]:

$$\eta = \frac{E_0}{3RT} = \frac{\rho}{M_c} \quad (1)$$

Where η is the number of moles of active network chains per unit volume, E_0 is the initial modulus of the polymer, R is the universal gas constant, T is the absolute temperature, ρ is the density of the polymer and M_c is the relative molar mass between crosslinks.

Contact angle measurements were made on the different CUPE thin films using the sessile drop method. A KSV101 Optical Contact Angle and Surface Tension meter (KSV Instruments Inc, Helsinki, Finland) was used for obtaining the contact angle values. Thin films of the different CUPE pre-polymers were made by smearing 1 ml of a dilute polymer solution in 1,4-dioxane (3.0 wt. %) on a clean glass slide. All readings were collected within 10 s after drop elution. Deionized water and di-iodomethane were used for measurements. A minimum of 10 readings was collected from different regions of the different thin films from each sample. The surface energy was calculated according to the harmonic mean equations by Matlab software and expressed as follows:

$$(1 + \cos\theta_1)\,\gamma_1 = 4\left(\left(\gamma_1^d\gamma_s^d\right) / \left(\gamma_1^d + \gamma_s^d\right) + \left(\gamma_1^p\gamma_s^p\right) / \left(\gamma_1^p + \gamma_s^p\right)\right) \quad (2)$$

$$(1 + \cos\theta_2)\,\gamma_2 = 4\left(\left(\gamma_2^d\gamma_s^d\right) / \left(\gamma_2^d + \gamma_s^d\right) + \left(\gamma_2^p\gamma_s^p\right) / \left(\gamma_2^p + \gamma_s^p\right)\right) \quad (3)$$

Where the γ^d and γ^p are the dispersive component, and polar component, respectively; θ_1 and θ_2 are the contact angles to water and to di-iodomethane, respectively. For water, γ_1 = 72.8 mJ m^{-2}, γ_1^d = 22.2 mJ m^{-2} and γ_1^p = 50.7 mJ m^{-2}. For di-iodomethane, γ_2 = 50.8 mJ m^{-2}, γ_2^d = 44.1 mJ m^{-2} and γ_2^p = 6.7 mJ m^{-2}.

2.3.2.3 In Vitro Degradation

Polymer films were cut into 7 mm discs using a cork borer and the initial weights of these discs was recorded. The discs were transferred to clean test tubes containing 10 mL of phosphate buffered saline (pH 7.4) or 0.05 M NaOH to rapidly obtain relative degradation rates among samples and incubated at 37 °C. A minimum of 6 specimens per time point was present for each polymer being tested. At each time interval, first the incubation medium was aspirated out of the test tube and the polymer samples were washed thoroughly with DI water twice. The polymer samples were then lyophilized for 72 hours to remove traces of water and weighed to obtain the final degraded weight corresponding to that time interval. The initial weight of the specimen and the degraded weight at a particular time interval were used to determine the rate of degradation of the polymer corresponding to that time interval using Equation (4):

$$\text{mass loss}\ (\%) \ = \ \frac{W_0 - W_t}{W_t} \times 100 \qquad (4)$$

Where W_0 = initial weight of polymer disc and W_t = final weight of the degrading polymer disc. A long-term degradation study was also conducted as per the aforementioned method using PBS as the degrading agent and CUPE 8 as the representative polymer. The degradation of the polymer discs was monitored over a total period of 8 months.

2.3.2.4 In Vitro Cell Culture

The cytocompatibility of CUPE polymers was evaluated with two different cell lines. Human aortic smooth muscle cells (HASMCs) and the NIH 3T3 fibroblasts were selected as the model cells lines and assessed based upon overall cell morphology and proliferation on CUPE films. Briefly, the polymer samples were cut into 10 mm diameter discs using a cork borer. These discs were sterilized by a two-step process comprising of ultraviolet (UV) light treatment for 1 hour followed by immersion in 70% ethanol for 30 minutes. The sterilized discs were washed thoroughly with sterile PBS to remove any traces of alcohol and then allowed to dry completely prior to cell seeding. Cells were cultured in 75 cm^2 culture flasks with Dulbecco's

modified Eagle's medium (DMEM) supplemented with 10% fetal bovine serum. For seeding, the cells were trypsinized, centrifuged and re-suspended in fresh complete culture medium. The volume of culture medium used to re-suspend the cell pellet was adjusted to obtain a seeding density of 3 x 10^5 cells ml^{-1}. 200 µL of the cell suspension was evenly spread over the surface of each of the CUPE films being tested. After 1 hour of incubation at 37 °C, 5 mL of complete culture medium was added to each of the petri dishes containing the cell seeded films. The cells were cultured on the films for 3 days during which the media was changed daily.

At the end of the culture period, the cells on the polymer discs were fixed by addition of 5 mL of 2.5% (wt/vol) gluteraldehyde-PBS solution. All samples were kept in the fixating medium for at least 2 hours. After fixation, the cells were sequentially dehydrated in a graded series of ethanol (50, 75, 90 and 100%) and lyophilized to remove any minute traces of water. The dehydrated cell seeded polymer discs were mounted on stubs, sputter coated with silver for 2 minutes, and observed under a Hitachi S300N (Hitachi Corp, Tokyo, Japan) scanning electron microscope (SEM). Different images of cellular morphology were captured at different magnifications to gauge the pattern of cellular growth and proliferation on the polymer surfaces.

A quantitative assessment of the 3T3 cell proliferation on polymer films was also performed using a methylthiazoletetrazolium (MTT) cell proliferation and viability assay kit. Polymer films were cut into cylindrical discs (7 mm in diameter), and sterilized as mentioned above. 3T3 fibroblasts were seeded on the films in the same manner as mentioned previously. MTT assay analysis was performed at 1, 3, and 7 days of culture as specified by the manufacturer's protocol. Briefly, the old media was aspirated, and each sample was washed with PBS to remove any loosely attached or dead cells. Next, incomplete media (100 µL) (absent of any FBS) was added to the specimens. A 3-(4,5-dimethylthiazol-2yl)-diphenyltetrazolium bromide solution (10 µL) was then added to the samples, and allowed to incubate for 3 h. At the end of the incubation period, MTT solvent (100 µL) was added to the media. Dissolution of the formazan crystals was facilitated by constant agitation of the well plate

on an orbital shaker for 20 min. The absorbance was measured on an Infinite200 microplate reader (Teacan Group Ltd., Switzerland) at 570 nm.

2.3.2.5 Foreign Body Response

CUPE 8 was used as the representative polymer to study the extent of foreign body response incited by the presence of the polymer for a medium term implantation period of 8 weeks and a long-term implantation period of 6 months. CUPE 8 scaffolds and PLLA control scaffolds were prepared by salt leaching with a salt size of 150 – 250 μm. The scaffolds were cut into discs (10mm X 1mm, diameter X thickness) using a cork borer and implanted subcutaneously in the back of healthy, female Sprague Dawley (SD) rats (Harlan Sprague Dawley, Inc., Indianapolis, IN). Animals were cared for in compliance with regulations of the animal care and use committee of the University of Texas at Arlington. Prior to implantation, the discs were sterilized by treatment with 75% ethanol for 1 hour followed by 1 hour of UV light treatment. A total of 8 rats were used for this study; 4 rats each for each time point of 8 weeks and 6 months. The rats were anesthetized using an isofluorane-oxygen mixture and the test samples were implanted in the upper back by blunt dissection.

At the end of each time period the rats tagged for that time period were sacrificed by CO_2 asphyxiation. The implant and the surrounding tissue was collected and frozen in OCT embedding media (Polysciences Inc., Warrington, PA), at -80 °C for further histological analysis. The tissue blocks were sectioned into 10 μm sections using a cryostat and stained with hematoxylin and eosin (H&E) to examine the tissue responses. Stained section images were acquired at 10x magnifications using a Leica DMLP microscope fitted with a Nikon E500 camera (Nikon Corp., Japan). A minimum of three images was obtained from each section for analysis, and three sections were examined per animal sacrificed. Image J software was used to determine the fibrous capsule thickness in each of the analyses performed. In order to determine an average fibrous response, at least 25 readings of capsule thickness were obtained from different parts of the section images obtained and averaged.

2.3.2.6 Statistical Analysis

All data obtained are presented as the mean ± standard deviation. The statistical significance between independent data sets was calculated using Student's two-tail t-test. A $p < 0.05$ value was used as a measure of significant difference.

2.3.3 Results and Discussion

Although elastomeric biomaterial development has been largely driven by the prerequisites of most soft tissues, elastic tissues vary greatly and cover a wide range of mechanical properties. For example, the mechanical properties of bladder tissue [132] vary greatly when compared to that of aortic tissue [133] or skin [134]. It has been well established that for successful tissue engineering one of the main requirements that need to be fulfilled is a similarity between the properties of the extracellular matrix of the target tissue and the replacement scaffold [23, 135-138]. Being able to control the properties of a polymer through multiple modalities is especially important to improve the utility of a bio-polymer for diverse soft tissue engineering applications [20].

In our previous work [10], we successfully synthesized and characterized the physical and biological properties of crosslinked urethane doped polyesters. From the results obtained, we were able to establish CUPE as a biodegradable, biocompatible, and strong yet soft elastomer. Although only the effects of different molar ratios of isocyanate to pre-polymer were characterized, previously developed PDC demonstrated that the polymer materials properties could be manipulated by varying the diol component as well. The ability to control the material performance through various diols motivated us to explore the development of novel CUPE polymers, which provides a multitude of options to fine-tune the resulting material through various synthesis parameters. Thus, the purpose of this study was to develop a new generation of strong and elastic CUPE polymers through the use of diols of varying methylene lengths and by partially replacing hydrophobic diol segments with more hydrophilic macrodiols segments.

FT-IR spectra obtained for CUPE Family and CUPE PEG polymers are depicted in Figures 2.28 and 2.29, respectively. The absence of an isocyanate peak at 2267 cm^{-1} was characteristic of all the CUPE spectra obtained, which indicated that the synthesis of the different CUPE polymers consumed all the diisocyanate in the reaction process. The peaks centered at 1733 cm^{-1} were assigned to carbonyl groups of the free carboxylic acid functional groups on the citric acid backbone and carbonyl groups of the ester bonds in the polymer backbone. Peaks between 2931 cm^{-1} and 2919 cm^{-1} were assigned to the methylene units in the polymer backbone [84, 139]. FT-IR also confirmed the incorporation of the isocyanate in the polymer backbone by urethane bond formation. All the CUPE polymers had sharp peaks at 1670 cm^{-1} and 1560 cm^{-1} that was attributed to amide I and II vibrations, respectively. A narrow shoulder peak at 3350 cm^{-1} also suggests the presence of urethane linkages in the polymer chains [40].

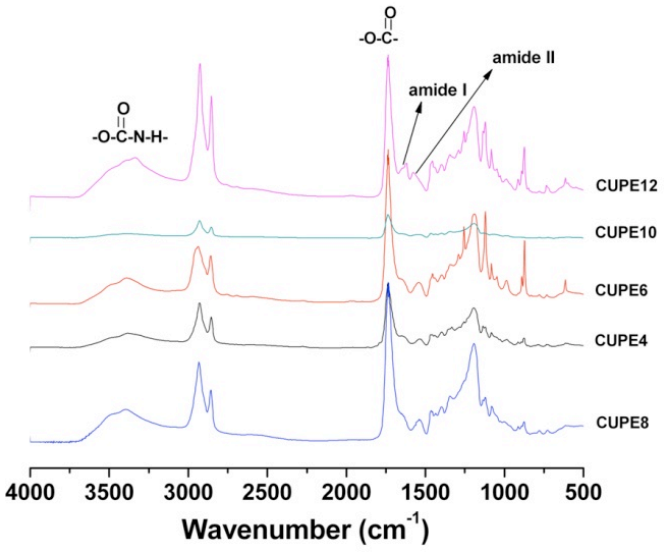

Figure 2.28 FT-IR Spectra of Pre-CUPE Family Polymers

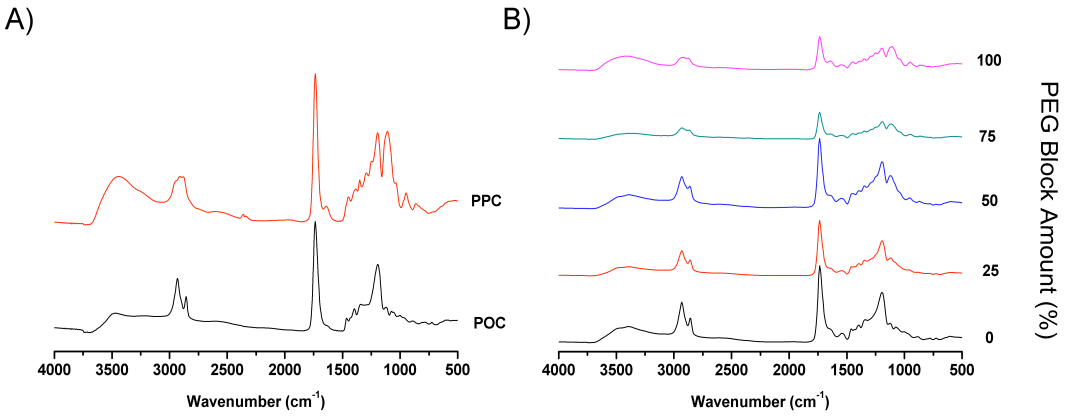

Figure 2.29 FT-IR Spectra of A) CUPE PEG pre-polymer soft segments and B) Pre-CUPE PEG polymers

FT-IR spectra comparing the hydrophobic POC segment with the hydrophilic PEC segment are shown in Figure 2.29A. In both the POC and PEC segments, an intense C=O stretch located at 1737 cm^{-1} confirms the presence of degradable ester bonds, and the broad stretch at 3460 cm^{-1} indicates that the hydroxyl groups are hydrogen bonded, which can contribute to polymer network hydrophilicity and mechanical properties. In addition, both segments also displayed bands at 1172 cm^{-1}, which were attributed to ester C-O stretching. However, as seen in the PEC spectra, the introduction of the PEG macrodiol resulted in the formation of a new peak located at 1100 cm^{-1} indicative of ether C-O stretching. All pre-CUPE PEG spectra (**Figure 2.29B**) show the characteristic peaks in CUPE as listed above for CUPE Family spectra. However, as more of the total soft segment composition was replaced with PEC, the appearance of the ether C-O bands was seen.

Figure 2.30 depicts the glass transition temperature of the different CUPE polymers, as determined by DSC. No obvious hard segment transitions were observed in the DSC thermograms indicating a low degree of microphase separation in all the CUPE Family polymers examined [140-142]. Furthermore, all thermograms lacked any crystallization and melting peaks, indicating the absence of hard segment crystallization [143]. The glass transition temperature of the polymers varied as an inverse function of the length of the diol component.

CUPE 12, which had the longest diol chain, had the lowest glass transition temperature (T_g = -3.22 °C), whereas CUPE 4, which had the smallest diol component, demonstrated a higher value of T_g (27.47 °C). CUPE8 which had a T_g value of 3.06 °C also supports this trend [10]. This increase in glass transition temperature with decreasing diol length may be explained by the segmented architecture of urethanes wherein strong hydrogen bonding between the polymer chains may function as physical crosslinks [38]. Increasing the length of the diol may serve to reduce the crosslink density by increasing the separation between the urethane groups in the polymer backbone, thus increasing the polymer chain mobility and subsequently lowering T_g. A decrease in the molecular weight of the soft segment would also promote an increase in the hard segment effect on the chain mobility as a result of phase mixing, thus increasing the glass transition temperature of the CUPE synthesized with smaller diols [144].

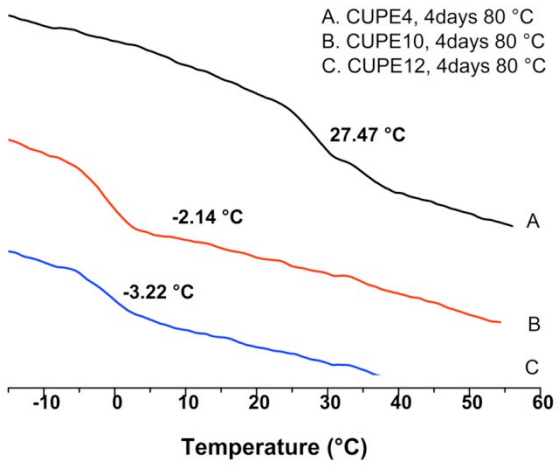

Figure 2.30 DSC Thermograms of CUPE Family Networks

Assuming the different polymers recovered completely after deformation, the effect of diol length on the crosslink density of the crosslinked polyester network was further examined using the theory of rubber elasticity, which has been used in previous studies to evaluate other biodegradable polyester elastomers [80, 84, 145, 146]. Data represented in Table 2.6 indicate that formulations with increasing diol length did indeed reduce the ester bond crosslink density allowed for by the citric acid component of the CUPE polymer. Under similar post-

polymerization conditions (2 days at 80 °C) CUPE 6 had the highest crosslink density of all the polymers evaluated (η = 1142.12 ± 120.79 mol m^{-3}) while CUPE 10 had the lowest crosslink density (η = 783.07 ± 167.52 mol m^{-3}). Increasing the post-polymerization duration to 4 days, also led to an increase in crosslink density due to the formation of more inter-chain ester bond crosslinking (CUPE10_4D η = 978.31 ± 157.26 mol m^{-3}). As a result of the growing length of methylene units in the polymer backbone with the incorporation of longer diols and subsequent increase in the molecular weight between crosslinks, the specific density of the different CUPE polymers decreased with increasing diol size (**Table 2.7**) [84].

Table 2.7 Density, Mechanical Properties, and Crosslink Characteristics of CUPE Family Polymers

Sample	Density (g/cm^3)	Young's Modulus (MPa)	Tensile Strength (MPa)	*n* (mol/m^3)	Mc (g/mol)
CUPE6_2D	1.30 ± 0.05	8.00 ± 1.22	9.56 ± 2.00	1144.12 ± 120.79	1148.21 ± 140.97
CUPE8_2D	1.24 ± 0.01	7.02 ± 0.85	17.38 ± 2.34	951.40 ± 123.59	1320.47 ± 187.36
CUPE10_2D	1.15 ± 0.02	6.02 ± 1.07	24.19 ± 2.04	783.07 ± 167.52	1522.97 ± 351.14
CUPE10_4D	1.17 ± 0.02	7.22 ± 0.90	38.36 ± 1.69	978.31 ± 157.26	1130.972 ± 145.74

All the CUPE polymers displayed break elongations exceeding 100% and elastomeric properties: full recovery of the sample dimensions after removal of applied stress. Increasing the length of the diol resulted in stronger polymers (**Figure 2.31A**). Under similar polymerization conditions of 2 days in an oven maintained at 80 °C, CUPE 10 had the highest peak stress (38.36 ± 1.69 MPa) and CUPE 6 was the weakest polymer (9.56 ± 2.00 MPa). This may be attributed to an increase in the molecular weight of the polymer due to the incorporation of higher molecular weight diols. The initial Young's modulus of the different polymers varied from 6.02 ± 1.07 MPa to 8.00 ± 1.22 MPa, with CUPE 6 being the most stiff (**Figure 2.31B**), which could be attributed to the higher crosslink density in CUPE 6 thereby necessitating higher initial stress to cause deformation [145, 146]. The higher crosslink density of polymers with lower number of methylene units in the diol also results in the polymers being more brittle, as can be seen from the increase in the final strain with increasing diol size (**Figure 2.31C**). In addition to

diol concentration, increasing polymerization conditions resulted in stronger, stiffer and more brittle polymers, which corresponds to our earlier results [10]. In order to assess the material's elastomeric properties in detail, hysteresis cycle was performed at room temperature. As a typical example, hysteresis cycle of CUPE 8 films after the 10^{th} elongation is shown in Figure 29D: 50% elongation and back at room temperature. CUPE 8 samples showed excellent recovery with no loss of energy, which could be attributed to the strong intermolecular cohesive energy between the crosslinked polyester network components.

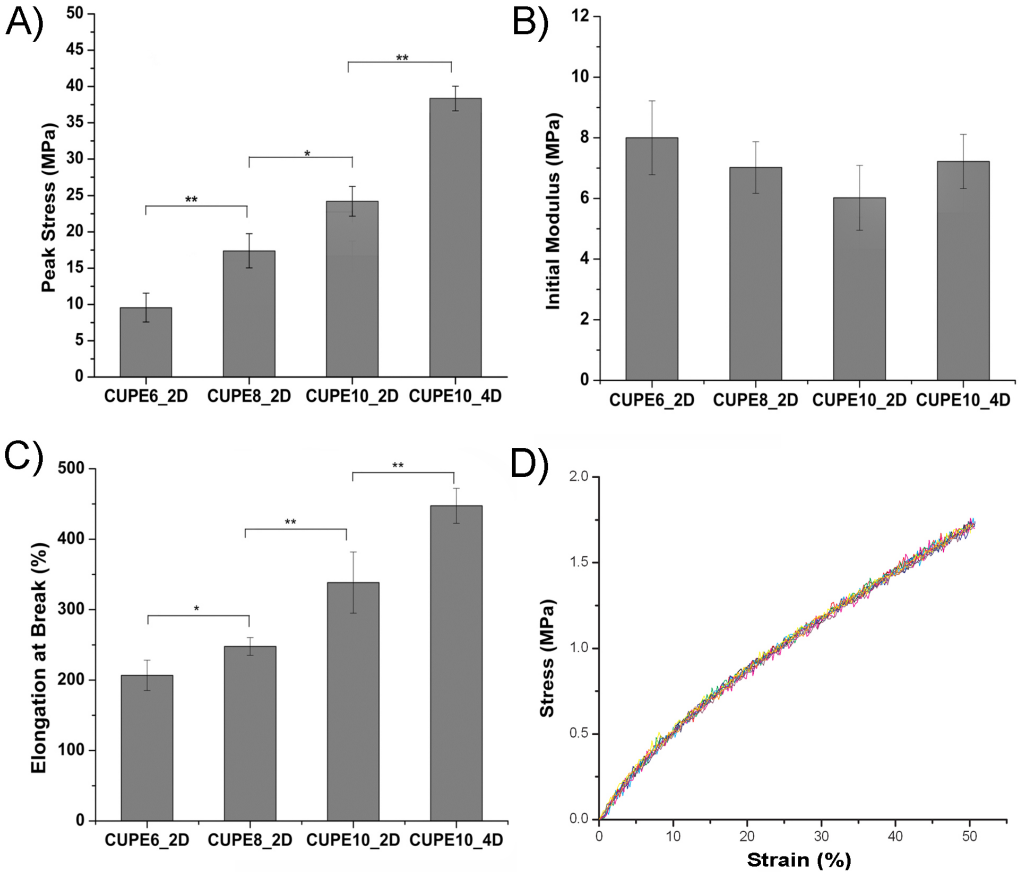

Figure 2.31 Mechanical Properties of the CUPE Family Polymers A) Peak stress, B) Initial modulus, C) Break strain, and D) Hysteresis (** $p < 0.01$; * $p < 0.05$)

The introduction of PEC into the CUPE network resulted in the development of weaker polymers. As seen in Figure 2.32, when no PEC segments were incorporated into the CUPE

synthesis (CUPE PEG 0) a peak stress of 28.03 ± 2.83 MPa was obtained. As the percentage of PEC was increased, the tensile peak stress was reduced to 3.15 ± 0.33 MPa in the case of CUPE PEG 100, which was only composed of PEC segments. Although a significant reduction in strength was observed, the tensile strength of CUPE PEG 100 was comparable to the previously developed POC elastomers.

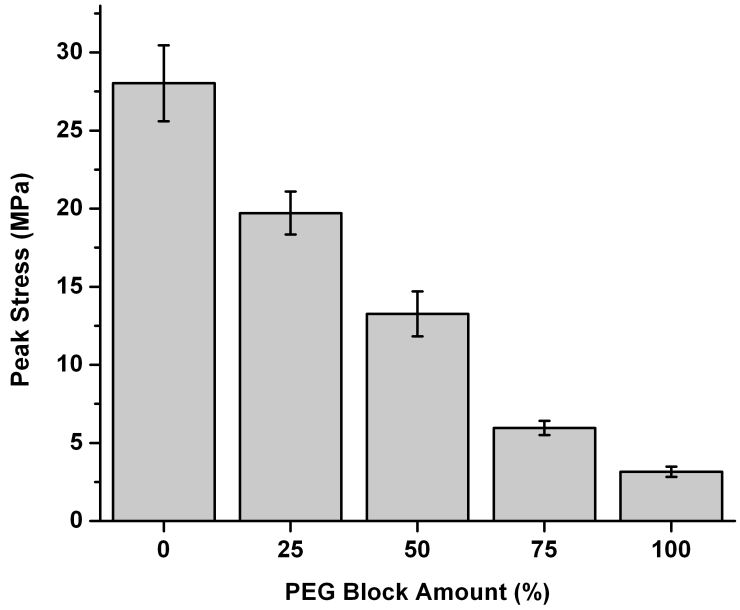

Figure 2.32 Tensile Peak Stress of CUPE PEG Polymers

The influence of the monomers on the surface properties of the CUPE Family polymers is summarized in Figure 2.33. As expected, using a more hydrophobic diol in the synthesis of CUPE Family resulted in more hydrophobic polymers. CUPE 4 had the most hydrophilic nature with an initial water in air contact angle value of 77.00 ± 1.28°, while CUPE 12 was most hydrophobic, with a contact angle value of 98.91 ± 1.34°.

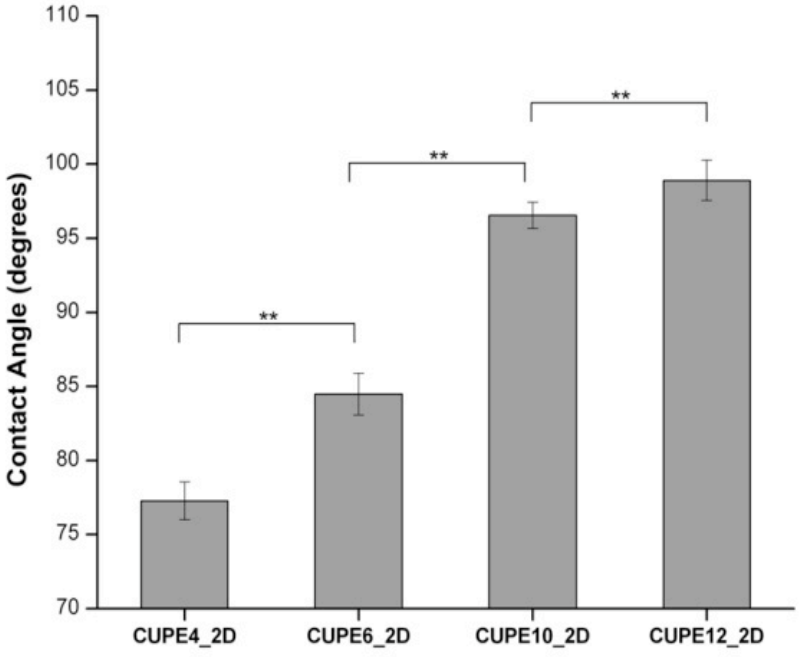

Figure 2.33 Initial Water Contact Angles of the CUPE Family Polymers (** $p < 0.01$)

The introduction of hydrophilic segments had a large influence on the surface energies of CUPE PEG networks. As seen in Table 2.8, a series of CUPE PEG materials have been developed with different hydrophilicities. As the developed CUPE Family materials are considered hydrophobic with water contact angles between 77 and 100°, an increase in the percentage of PEC used during synthesis improved surface wettability with a decrease in water contact angle from 79.62 down to 52.76 for CUPE PEG 0 and 100, respectively. An increase in surface energy (y_s) and fractions of polar components (X^p) was seen in more hydrophilic films, which indicates a greater contribution of polar components [147]. Thus, overall surface energy and hydrophilicity could be improved by replacing 1,8-octanediol soft segments with PEG segments.

Table 2.8 Material Surface Energies of CUPE PEG Networks

Sample	θ to H_2O (°)	θ to CH_2I_2 (°)	γ_s ($mJ \cdot m^{-2}$)	γ_s^d ($mJ \cdot m^{-2}$)	γ_s^p ($mJ \cdot m^{-2}$)	X^p ($mJ \cdot m^{-2}$)
CUPE PEG 0	79.62	36.56	42.95	33.13	9.81	0.23
CUPE PEG 25	68.58	37.38	46.40	30.68	15.72	0.34
CUPE PEG 50	65.27	37.16	47.87	30.34	17.53	0.37
CUPE PEG 75	59.89	38.22	50.03	29.33	20.69	0.41
CUPE PEG 100	52.76	42.94	51.02	27.04	23.98	0.47

Swelling studies indicated that the choice of monomer diol also affected the bulk properties of the CUPE Family polymers. CUPE 4 and CUPE 12 had the highest (168.50 ± 24.38%) and lowest (10.26 ± 2.83%) degrees of swelling in PBS, respectively, as depicted in Figure 2.31. The bulk swelling of the polymers decreased with increasing number of carbon atoms in the diol monomer used in the synthesis due to the hydrophobic nature of the larger methylene diol. Thus, one would expect that with a higher degree of crosslinking the CUPE polymers with lower number of methylene units would exhibit the lowest degree of swelling. However, the results demonstrate that the hydrophobicity of the diol plays a more predominant role than the crosslink density in determining water uptake and hence swelling, which is in agreement with published literature [145].

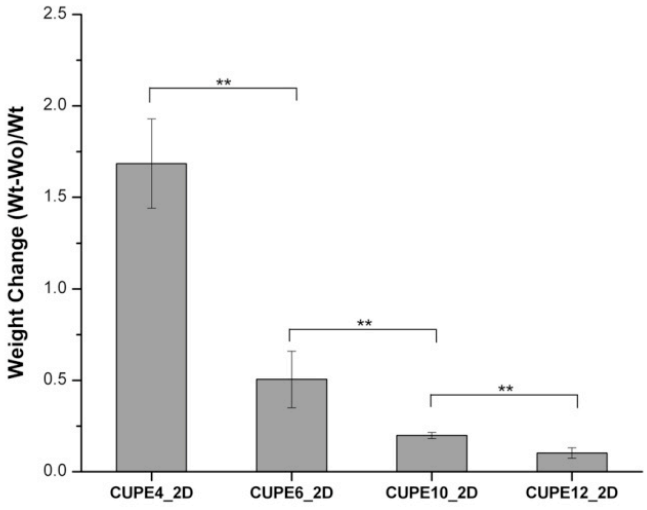

Figure 2.34 Bulk Water Uptake of CUPE Family Polymers (** $p < 0.01$)

This phenomenon was also evident in the accelerated degradation studies conducted on the different CUPE polymers in 0.05 M sodium hydroxide solutions. As seen from Figure 2.35, it can be noted that the intrinsic nature of the polymers composed of more hydrophobic diols degraded slower than those containing more hydrophilic monomers. CUPE 4 underwent complete degradation within 9 hours, whereas other polymers were still present at the final time point of 12 hours. In contrast, CUPE 12 demonstrated the slowest degradation profile, with 96.68 ± 0.97% of the polymer still remaining at the 12-hour time point. The increased water uptake of the hydrophilic CUPE polymers would provide greater access to the hydrolytically labile ester bonds in the polymer backbone resulting in faster degradation through hydrolysis to yield to yield the original monomers, which can be metabolized and eliminated from the body. In addition to NaOH degradation, a long-term degradation study was also conducted on CUPE 8 in PBS (**Figure 2.35**). The results indicate that CUPE 8 degraded steadily for 8 months, with only 37.99 ± 7.39% of the polymer remaining at the end of the last time point in the study.

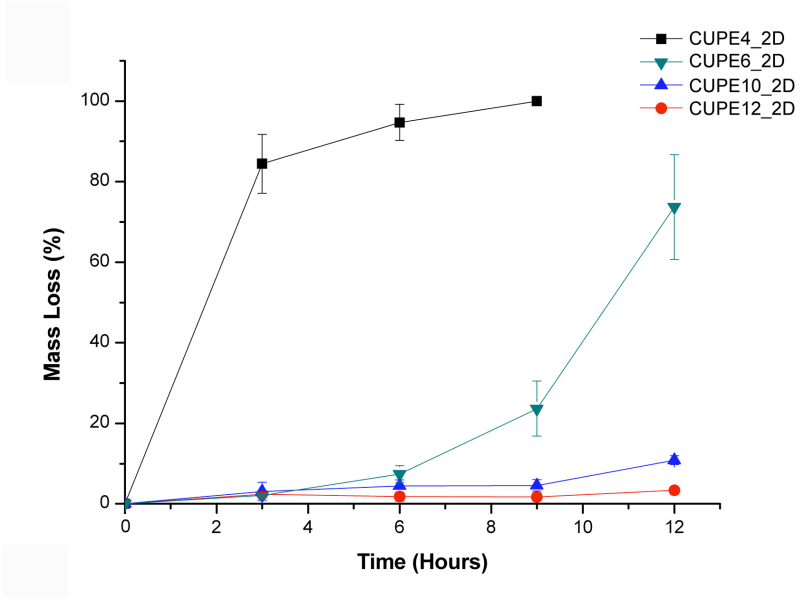

Figure 2.35 CUPE Family Accelerated Degradation in 0.05 M NaOH

A long-term degradation study of CUPE PEG polymers was conducted in PBS (pH 7.4) over a 24 week time period. As illustrated in Figure 2.36, the degradation rate of CUPE could be

controlled through the incorporation of the hydrophilic segment. As expected, CUPE PEG 0 containing only hydrophobic segments displayed the slowest degradation rates with 68.76 ± 10.91 % of the polymer remaining at 24 weeks. As increasing amounts of the hydrophobic segment were replaced with PEC, the resulting polymer degradation rates significantly increased. For example, CUPE PEG 100 and 75 showed complete degradation at 1 week and 3 weeks, respectively. As hydrolysis is the primary mechanism of degradation, the more hydrophilic polymer networks allowed for enhanced water penetration and diffusion to access the hydrolytic liable ester bonds. Thus, balancing the hydrophobicity/hydrophilicity of CUPE using various POC/PEC segments can be used to tailor the degradation kinetics of the material to fit a specific application.

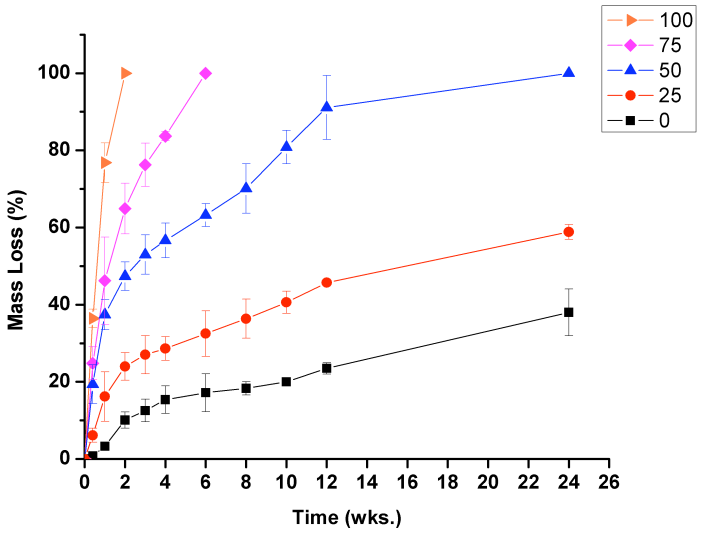

Figure 2.36 CUPE PEG Degradation in Phosphate Buffered Saline (pH 7.4; 37 °C)

CUPE Family polymers were seeded with NIH 3T3 fibroblasts and human aortic smooth muscle cells (HASMC) to determine the initial cytocompatibility of the material through cell morphology. Photomicrographs of the seeded films (**Figures 2.37 and 2.38)** indicate that both the cell types used were able to adhere to the CUPE polymers and express a normal phenotype with higher cell densities on CUPE polymers synthesized from longer length diols [10, 84].

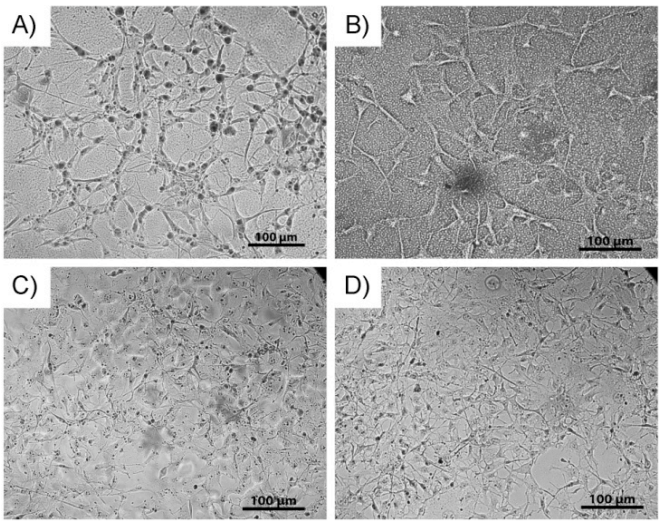

Figure 2.37 SEM Images of NIH 3T3 Fibroblasts on CUPE Family Films A) CUPE 4, B) CUPE 6, C) CUPE 10, and D) CUPE 12

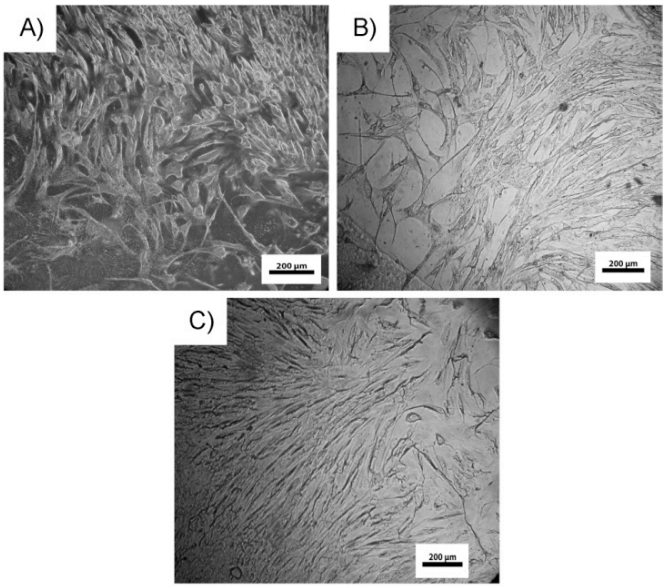

Figure 2.38 SEM Images of HASMC on CUPE Family Films A) CUPE 6, B) CUPE 10, and C) CUPE 12

3T3 fibroblast cell adhesion and proliferation were quantitatively evaluated on CUPE PEG films using a MTT cell viability assay (**Figure 2.39**). CUPE PEG 100 films were not reported due to the rapid degradation rates; however, cells were able to proliferate in the presence of media containing the completely degraded polymer (data not shown). Interestingly,

cell proliferation was enhanced as the percentage of the hydrophilic segment was increased. Absorbance values were in the order of CUPE PEG 0 < 25 < 50 < 75 for all time points, which can be explained due to the more favorable contact angles of the resulting materials. These results are in agreement with previous studies, which have shown that 3T3 adhesion and proliferation is enhanced on surfaces expressing water contact angle of 50-60° [148]. Thus, modulation of the surface energy characteristics by balancing the hydrophobicity of CUPE with hydrophilic segments can be a viable route to improve cell cytocompatibility.

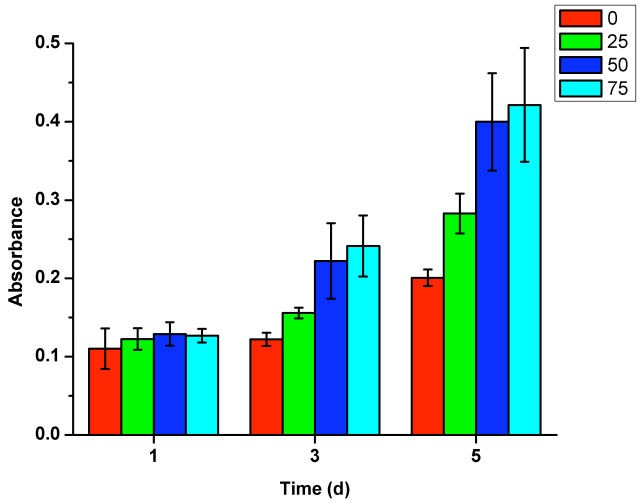

Figure 2.39 Comparison of 3T3 Fibroblast Growth on CUPE PEG Films

In our previous report [10], we presented the foreign body response over a relatively short period of 1 week and 4 weeks with CUPE 8 scaffolds as the representative polymer. Figure 2.40 represents the foreign body response to CUPE 8 scaffolds over a longer time period of 8 weeks and 24 weeks with PLLA as the control. Although significant degradation could be observed in both at the later time period, CUPE and PLLA scaffolds were still present at 24 weeks. The absence of necrosis in and around the implants indicated a healthy healing response to both the materials. From Figure 2.40, it can be seen that even at 8 weeks 100% cellular infiltration was achieved in the CUPE and PLLA scaffolds. Both the scaffolds indicated the presence of a thin, non-uniform fibrous capsule. At 24 weeks, no tissue necrosis was

observed in all test animals. The capsule could not be distinguished from the infiltrating cells. The scaffolds also lost their shape and showed reduced size compared to 8 weeks samples for both materials tested (**Figure 2.40**). These results indicate that, in addition to demonstrating better acute inflammatory responses than PLLA, CUPE also undergoes bio-degradation in vivo and does not incite a significant long-term chronic inflammatory response. Although the gross inflammatory response was presented in this work, future studies will be focused on characterizing the specific cell types as part of the inflammatory response surrounding the implant.

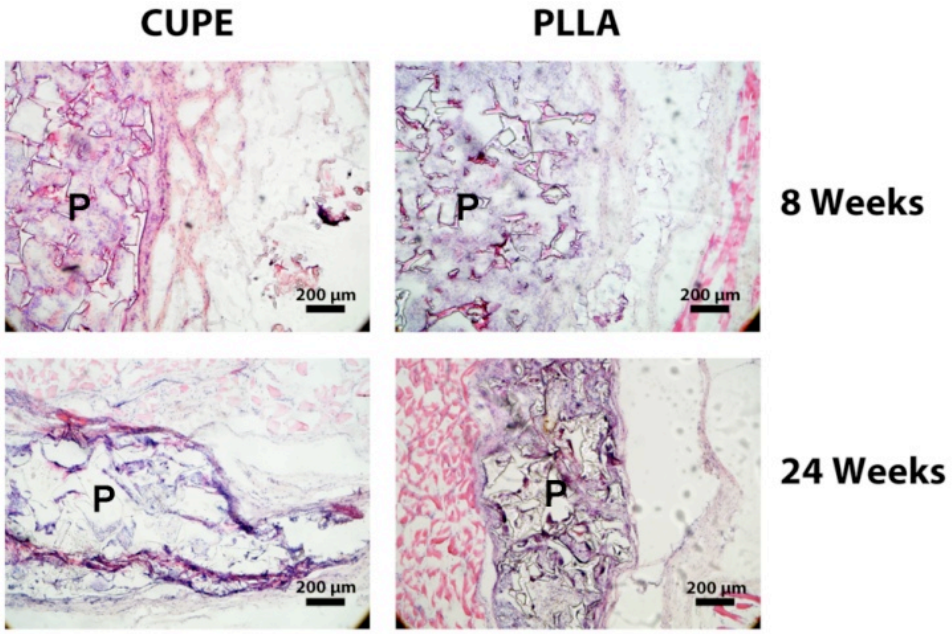

Figure 2.40 Host Response to CUPE and PLLA (control) Films Implanted Subcutaneously in Sprague-Dawley Rats ("P" indicates the polymer regions)

2.3.4 Conclusion

A new generation of CUPE polymers with different diol components was synthesized and characterized. Varying the diol component was found to affect the different physical properties of the CUPE to establish the diol component as an important parameter in controlling the structure-property relationship of the polymer in addition to diisocyanate concentration and post-polymerization conditions. This demonstrates the versatility with which the properties of

CUPE can be varied, thereby rendering this polymer family attractive for a wide variety of tissue engineering applications.

2.4 Conclusions

A methodology of citrate-based biomaterial development has been presented with special focus on *in situ* crosslinkable (POMaC and PEGMC) and urethane-doped polyesters (CUPE Family and CUPE PEG). The newly developed materials were characterized to elucidate the structure-function relationship of each type of polymer, and the preliminary biocompatibility was assessed through *in vitro* cell culture and *in vivo* subcutaneous implantation. The results show that citric acid can be used as a universal multifunctional monomer and reacted with various diols to produce the next generation of soft biodegradable elastic polymers with great flexibility in tuning the material properties of the resulting material to meet a wide range of biomedical applications. The newly developed citrate-based materials reported here can be used as platform biomaterials for the design of novel tissue engineering scaffolding, which will be the focus of the following sections. These enabling new biomaterials should address many of the existing challenges in tissue engineering and advance the field as a whole.

CHAPTER 3

APPLICATION OF CITRATE-BASED MATERIALS

3.1 Introduction

In the previous chapter, a methodology of citrate-based biomaterial development was presented with the ability to design a library of biodegradable elastomers, which can accommodate a wide range of biomedical applications. Motivated by these results, the current chapter aims to demonstrate the potential application of the newly developed citrate-based polymers as platform biomaterials in the design of novel tissue engineering scaffolding, which applies microengineering approaches to generate complex cell-cell and cell-microenvironment interactions to mimic tissue complexity and architecture. The following sections discuss the fabrication and characterization of a new pore generation technique, scaffold sheet design strategy, multiphasic small diameter vascular grafts, multichanneled nerve guides, and an injectable drug eluting system to assist in endoscopic surgical procedures.

3.2 New Generation of Sodium Chloride Porogen

3.2.1 Introduction

Tissue engineering is a multidisciplinary field, which aims to provide therapeutic treatments to maintain, restore, or replace damaged or diseased tissues, and may one day provide better alternatives for whole organ transplantation [23, 149]. Within the past decade, monumental strides have been made in the regeneration various tissues such as skin [150], bone [151], cartilage [152], tendons [153], ligaments [154], liver [155], cardiac tissues [156], blood vessels [157], esophagus [158], adipose [159], renal [160], lung [161], and neural tissues [162]. One of the main principle methods behind tissue engineering involves growing relevant cells into a three dimensional (3D) tissue or organ. However, cells alone lack the ability to grow

into 3D orientations similar to the native tissues. Therefore, the preferred multidimensional cellular growth is achieved by seeding the desired cells onto porous matrices, known as scaffolds, which serve as a temporary extracellular matrix (ECM) during new tissue formation [163]. This temporary ECM is not only responsible for defining the 3D architecture of the construct, but also plays a large role in regulating cellular phenotype and functional properties through the dynamic interplay between the cells and ECM structure [164]. Thus, by mimicking the native ECM and serving as a temporary suitable microenvironment for initial cell attachment and 3D tissue formation, the scaffold has become a very important component of the tissue engineering paradigm with its ability to influence cellular behavior and ultimately determine the success of the tissue engineered construct [165].

The requirements for tissue engineering scaffolds are multifaceted and tissue specific. In general, tissue engineering scaffolds should be biocompatible in that cell attachment, differentiation, and proliferation should all be promoted while minimizing the host foreign body response to the implanted construct [166]. Scaffolds should also degrade to match the rate of new tissue formation, and precisely match the mechanical properties of the surrounding tissues to avoid compliance mismatch, which has been shown to be a major cause of implant failure [167]. In addition to biological and biomechanical performance, the scaffold must also possess key morphological characteristics. Scaffold morphologies should resemble the micro/nanoscale architectures of the native ECM [168], and consist of a highly interconnected porous network, which can encourage cellular infiltration and allow for the proper exchange of nutrients and metabolic waste throughout the scaffold [169, 170]. Since the resulting scaffold morphology characteristics are primarily determined by the fabrication method used to create them, intense research focus has now shifted towards developing new fabrication methodologies to control the scaffold pore size [171], shape [172], porosity [173], and interconnectivity [174] for various tissue engineering applications.

For example, thermally induced phase separation (TIPS) methods have been extensively studied and rely on the principle that a solvent's effectiveness will decrease when introduced into a non-solvent or when the temperature of the system is lowered [175, 176]. Although the creation of pore sizes in the range of nanometers [177] to a few micrometers [178] can be obtained, the phase separation technique cannot produce pore sizes in the upper micrometer size range, which limits its use in applications involving skin or bone where the required pore sizes are 20-400 μm [179]. Thus, phase separation techniques must be combined with other methods such as porogen leaching in order to be realized in a wider variety of applications [180]. Another frequently used method in the fabrication of porous scaffolds for tissue engineering is a foaming process technique [181], which utilizes foaming agents such as water [182], carbon dioxide [183], nitrogen [184], or fluoroforms [185] as expanding substances to generate pores. Although the foaming method is relatively inexpensive and a wide range of pore sizes (30-700 μm) [186] can be obtained, this process is generally plagued by the creation of "dead" or closed pores structures leading to very low levels of interconnectivity [187]. The foaming technique, similar to phase separation methods, must be combined with porogen leaching techniques to increase porosity and interconnectivity [188].

Other methods developed to precisely control the resulting scaffold pore size and shape all rely on a computer-aided design (CAD) data sets [189]. For example, rapid prototyping (RP) [190], solid free-form fabrication (SSF) [163], 3D printing [191], shape deposition manufacturing [192], fused deposition modeling [193], selective laser sintering [194], and stereolithographic principles all use a step-by-step, layer-by-layer construction mechanism to fabricate scaffolds with highly reproducible and precisely controlled porosities, interconnectivity, pore sizes, and pore shapes. However, these methods are restricted in terms of the resolution of the engineered machine tools used (200-500 μm) [195], lengthy fabrication times [196], costly/complex fabrication methods, small final scaffold sizes (0.4-3.5 cm3) [197], and the demand for specific scaffold material properties [198]. Another established process for the

fabrication of tissue engineering scaffolds is an electrospinning process, which produces fibers in the micrometer or nanometer scale by electrically charging a suspended droplet of polymer solution. Nonwoven two-dimensional (2D) fiber meshes can be constructed into 3D fibrous meshes with a wide range of pore size distributions and porosities with a high surface area to volume ratio [199]. However, similar to phase separation methods and techniques utilizing CAD designs, the electrospinning process places a demand for specific scaffold material properties, which limits the scope of these fabrication methods to select biomaterials [198]. For example, low molecular weight biodegradable polyester elastomers such as poly (diol citrates) (PDC) [95], poly (octamethylene alkylene maleate citrates) (PAMC) [93, 167, 200], and poly (glycerol sebacate) (PGS) [80] cannot be used in these methods to fabricate porous scaffolds.

Unlike the previous methods mentioned above, porogen leaching, also known as solution casting/particulate leaching, is a widely used, facile, convenient, and cost-effective method that can be applied with a wide range of polymers to introduce porosity into tissue engineering scaffolds [201]. This method involves the casting of a polymer/porogen solution followed by solvent evaporation and removal of the incorporated porogen through aqueous washing methods. Various porogens including NaCl [202], paraffin spheres [203], sugar crystals [204], gelatin [205], and polymers [90] have been successfully used to fabricate porous structures. NaCl is perhaps the most widely used porogen, but the wide variations of pore sizes, lack of interconnectivity, irregular pore geometry, and the inability to produce submicron and nanoscale pore sizes have limited the use of this porogen in current tissue engineering applications. Therefore, a convenient, cost-effective pore creation technology to fabricate scaffolds with controlled architectures and that can be applied to a wide range of biomaterials would be a valuable tool for the field of tissue engineering.

Crystallization is a process that occurs naturally in the formation of minerals and snowflakes, and has been utilized in industrial settings for the past 30 years to produce salts, powders, and silicon crystal wafers [206]. Recent research involving nucleation and

crystallization science has been directed towards a variety of biological applications including protein research [207] and the fabrication of microstructures and nanoparticles [208]. The process of crystallization (**Figure 3.1A**) is based upon a change in phase of a material from a solvated state to a crystal lattice structure due to a reduction in free energy of the solution. As the transition from high to low free energy occurs, the solute molecules cluster into nuclei in the nanometer scale in a process termed nucleation (**Figure 3.1C**). Once the nuclei reach a critical size, the molecules of the solute rearrange into a crystal structure, and crystal growth is initiated (**Figure 3.1D**) [209]. We hypothesize that controlling specific parameters of the crystallization process such as the nature of the solute, supersaturation level, solution temperature, stirring/mixing, and crystal growth time can potentially produce crystals with high level of control over the shapes and sizes for tissue engineering scaffold fabrication [206, 209].

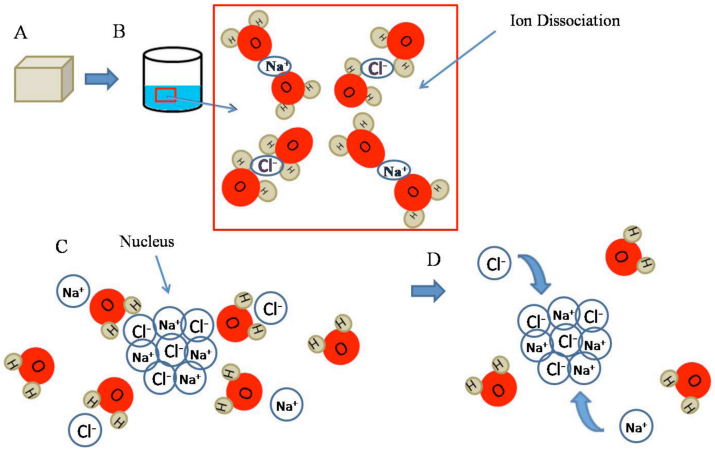

Figure 3.1 Schematic Representation of the Nucleation and Crystallization Process A-B) Solute ion dissociation, C) Nucleus formation, and D) Crystal formation

The rationale behind this approach is that 1) crystallization technology can be used to generate NaCl porogens of a controlled size with a narrow size distribution to fabricate tissue engineering scaffolds with better control over porosity and pore size; 2) crystallization technology can be used to generate pores of a distinct shape to create scaffolds with regular pore geometry; 3) crystallization can allow for the generation of NaCl porogens in the submicron and nanoscale range to fabricate scaffolds with topographies that better mimic the native ECM;

4) incorporation of the submicron NaCl with other fabrication methods will increase the interconnectivity of the resulting scaffold for enhanced cellular communication and mass transport; 5) the salt generated in this technique can be applied with microelectromechanical system (MEMS) based technologies to control cellular organization while providing a means for cell communication; 6) unlike some of the previous techniques, this scaffold fabrication process used in this technique can be applied to a wide variety of materials; and 7) this pore technology is easy, convenient, cost-effective, and does not require the use of complex machinery, which facilitates widespread use in academic labs and industry.

The aim of the present study is to explore the feasibility of using the principles behind crystallization to create NaCl porogens, which can be used to address the limitations of previous ground and sieved porogens for various biomedical applications. We focus on characterizing the effects of various crystallization parameters such as solution concentration, solution temperature, and crystallization time on the resulting NaCl crystal size. To show the feasibility and future potential of this new pore generation technique, the resulting NaCl porogens produced were used to increase the interconnectivity of traditional salt leached scaffolds, and the fabrication of microchanneled elastomeric scaffolds and multiphasic vascular grafts.

3.2.2 Experimental

All materials were purchased from Fisher Scientific (Pittsburg, PA, USA), and all chemicals were purchased from Sigma-Aldrich (St. Louis, MO, USA) unless specified otherwise and used as received.

3.2.2.1 Sodium Chloride Porogen Fabrication

NaCl porogens were fabricated according to the schematic representation shown in Figure 3.2. Briefly, NaCl salt (99.0% purity) was dissolved in deionized water produced from a Direct-Q Water Purification System (Millipore, Billerica, MA, USA) at various concentrations above the supersaturation level at 25 °C. The supersaturated NaCl solution was placed in a round bottom glass flask fitted with a magnetic pear shaped stir bar. The flask containing the

supersaturated solution was then lowered into an oil bath maintained at 115 °C. The contents were stirred at 400 rpm, and allowed to boil under reflux. After 30 minutes, the temperature of the system was reduced to predetermined crystallization temperatures, and allowed to stir for predetermined crystallization times to initiate nuclei formation and crystal growth. Following the end of the crystallization time period, the contents of the flask were filtered in an oven maintained at the respective crystallization temperature to collect the salt crystals. Various NaCl solution concentrations, crystallization times, and crystallization temperatures were studied to determine the effects on the resulting NaCl crystal size and shape.

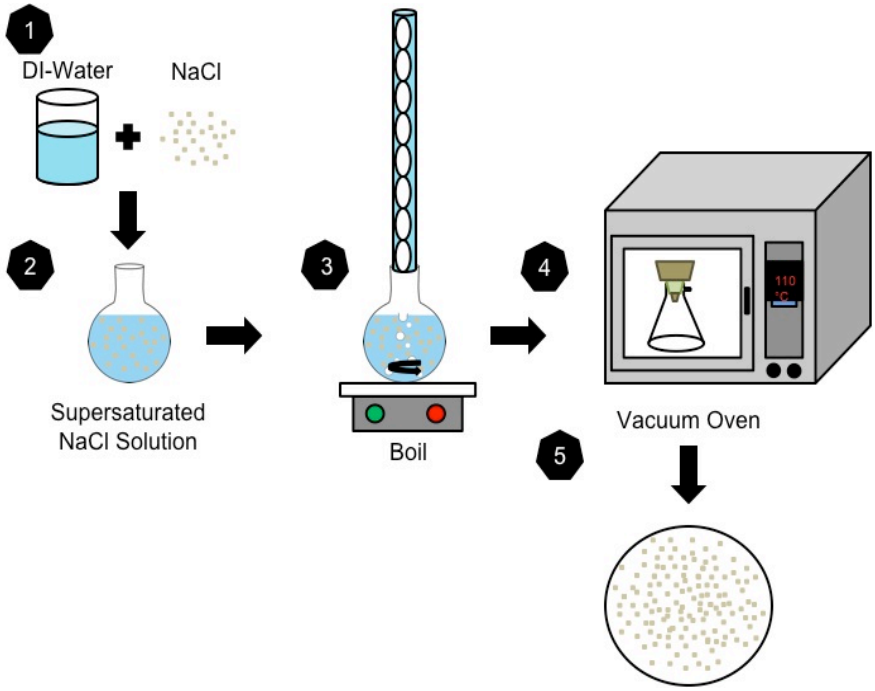

Figure 3.2 Schematic Representation of the Nucleation and Crystallization Experimental Set Up 1) NaCl is combined with deionized water to make a supersaturated solution (2), 3) Contents are heated under reflux and cooled to desired crystallization temperature, 4) Solution is filtered in a vacuum oven maintained at supersaturation temperature to collect crystallized NaCl (5)

3.2.2.3 Porogen Characterization

The collected NaCl porogens were dried under vacuum, sputter coated with silver, and examined under a Hitachi S-3000N scanning electron microscope (SEM) (Hitachi, Pleasanton, CA, USA). Image J analysis software was used to determine the salt porogen sizes. To

characterize the salt porogen geometries, 10 random locations were selected and a total of 30 measurements (latitudinal and longitudinal widths) were recorded at each location.

3.2.2.4 Crosslinked-Urethane Doped Polyester (CUPE) Synthesis

CUPE pre-polymers were synthesized in two distinct steps similar to previously published methods [10]. The first step involves the synthesis of a pre-POC oligomer, which is chain extended by 1,6-hexamethyl diisocyanate (HDI) in the second urethane-doping step. Briefly, a POC pre-polymer was first synthesized by reacting a 1.0:1.1 monomer ratio of citric acid and 1,8-octanediol, respectively, in a three-necked round bottom flask fitted with an inlet and outlet adapter at 160 °C under a constant flow of nitrogen [95]. Once all the monomers had melted, the temperature of the system was lowered to 140 °C, and the reaction mixture was allowed to continue for 60 minutes to create the POC pre-polymer. The POC pre-polymer was then purified by drop wise precipitation in deionized water. The undissolved pre-polymer was collected and lyophilized for 48 hours to obtain the pre-POC oligomer (MW 820). In the second step, pre-CUPE was synthesized through the chain extension of the pre-POC. Pre-POC was dissolved in 1,4-dioxane (3.0 wt. %), and the resulting solution was allowed to react with HDI in a clean reaction flask under constant stirring at 55 °C using stannous octoate as a catalyst (0.1 wt. %).

3.2.2.5 Traditional Scaffold Fabrication

To fabricate traditional NaCl salt leached scaffolds, pre-CUPE was mixed with sodium chloride salt with an average crystal size in the range of 150-250 μm in a 1:10 polymer to salt ratio by weight using traditional grinding and sieving methods. The pre-polymer solution was mixed until a viscous paste was formed. The resulting slurry was placed in a Teflon mold, placed in a laminar flow hood overnight for solvent evaporation, and then transferred to an oven maintained at 80 °C to crosslink the polymer through the condensation of pendant citric acid –COOH and –OH on the polymer backbone or branches. Next, the salt was leached out by

immersion in deionized water for 72 hours with water changes every 12 hours. Finally, the resulting scaffolds were lyophilized for 36 hours to remove any traces of water.

3.3.2.6 Interconnected Scaffold Fabrication

To fabricate traditional scaffolds with improved interconnectivity, pre-CUPE was mixed with equal amounts of sodium chloride salt (average crystal size in the range of 150-250 μm from traditional grinding and sieving methods) in combination with sodium chloride salt (average crystal size in the range of 1-10 μm from nucleation and crystallization) in a 1:10 polymer to combined salt ratio by weight. The pre-polymer solution was mixed until a viscous paste was formed. The resulting slurry was placed in a Teflon mold, placed in a laminar flow hood overnight for solvent evaporation, and then transferred to an oven maintained at 80 °C to crosslink the polymer. Next, the salt was leached out by immersion in deionized water for 72 hours with water changes every 12 hours. Finally, the resulting scaffolds were lyophilized for 36 hours to remove any traces of water.

3.2.2.7 Porous Microchanneled Scaffold Fabrication

Microchanneled scaffolds were fabricated similar to previously published methods [167]. The microchannel pattern was transferred from polydimethylsiloxane (PDMS) molds to CUPE. Briefly, pre-CUPE was mixed with sodium chloride salt with an average crystal size in the range of 1-10 μm in a 1:5 polymer to salt ratio by weight using nucleation and crystallization methods. The pre-polymer solution and salt were cast onto the PDMS microchannel mold, and placed under vacuum to remove any air trapped in the channels. The microchannels filled with polymer and salt were then transferred to an oven maintained at 80 °C to crosslink the polymer. Next, the salt was leached out by immersion in deionized water for 72 hours with water changes every 12 hours. Finally, the microchanneled scaffolds were lyophilized for 36 hours to remove any traces of water.

3.2.2.8 Multiphasic Small Diameter Graft Fabrication

Briefly, 3 mm outside diameter steel rods (McMaster-Carr, Atlanta, GA, USA) were dipped once into a dilute solution of pre-CUPE in 1,4-dioxane (1.0 wt.-%). Before the solution could dry, the rods were coated with the salt porogen created from nucleation and crystallization methods with an average pore size in the range of 1-10 μm. After the salt application, the rods were coated one additional time with pre-CUPE. Following the fabrication of the elastic membrane, a pre-CUPE solution was mixed with sodium chloride salt with an average crystal size in the range of 150-250 μm in a 1:10 polymer to salt ratio by weight using traditional grinding and sieving methods. The polymer solution was mixed thoroughly with the salt until a viscous paste was formed. The resulting slurry was cast onto the steel rods, and then placed in a laminar flow hood overnight for solvent evaporation. Once the solvent was removed, the scaffolds were post-polymerized in an oven maintained at 80 °C to crosslink the polymer. Next, the salt in the tubular scaffold was leached out by immersion in deionized water for 72 hours with water changes every 12 hours. The scaffolds were removed from the steel rods by immersion in 50% ethanol. Finally, the scaffolds were lyophilized for 36 hours to remove any residual water.

3.2.2.9 Scaffold Geometry Characterization

To view the cross sectional morphology, scaffold samples were freeze fractured using liquid nitrogen, sputter coated with silver, and examined under SEM. Image J analysis software was used to determine the scaffold geometries. To characterize the scaffold geometries, 3 random locations were selected and a total of 30 measurements were recorded at each location.

The individual sections of the scaffold porosity were measured using the Archimedes' Principle similar to previously published methods [147]. Briefly, a density bottle was used to measure the density and porosity of the scaffold using ethanol (density ρe) as the displacement liquid at 30 °C. The density bottle filled with ethanol was weighed (W1). A scaffold sample of

weight WS was immersed into the density bottle, and the air trapped in the scaffold was evacuated under vacuum. Next, the density bottle was supplemented with ethanol, filled, and weighed (W2). The ethanol-saturated scaffold was removed from the density bottle, and the density bottle was weighed (W3). The following parameters of the scaffold were calculated: the volume of the scaffold pore (VP), the volume of the scaffold skeleton (VS), the density (ρS), and the porosity (ε). The following formulas for the volume mass index (VP/VS) were used [147]:

VP = (W2 - W3 - WS) / ρe

VS = (W1 - W2 + WS) / ρe

ρS = WS / VS = WSρe / (W1 - W2 + WS)

ε = VP / (VP + VS) = (W2 - W3 - WS) / (W1 - W3)

Scaffold interconnectivity was determined with Image J software. Briefly, the total area of a pore (At) and the area of each micropore above 20 μm in diameter (A1, A2, A3, etc.) were calculated. The interconnectivity index was defined as described by previous methods [210]:

$$Interconnectivity\ \ Index\ (\%)\ =\ \frac{Total\ \ Area\ \ of\ \ Micropores\ (A_1 + A_2 + A_3 + \cdots)}{Total\ \ Area\ (A_t)} \times 100$$

The interconnectivity index for all the different pores in the image was calculated and an average of this value was taken as the final value. More than 10 SEM pictures for each sample were analyzed.

3.2.2.10 Statistical Methods

Data was expressed as the means ± standard deviation. The statistical significance between two sets of data was calculated using a two-tail Student's t-test. Non-parametric one-way ANOVA tests were also performed where appropriate. Data was taken to be significant when a $p < 0.05$ was obtained.

3.2.3 Results and Discussion

A new generation of NaCl porogen was created to address the limitations of previous porogen leaching designs. The principles behind nucleation and crystallization science were

used as a means to produce NaCl crystals with control over the resulting porogen shape and size within a narrow size distribution, which is not possible using the current grinding and sieving methods. By controlling the free energy of the NaCl solution through the supersaturation concentration and nucleation temperature, various NaCl shapes and size distributions were created, which can be used in a wide variety of tissue engineering scaffold applications where the pore size, porosity, and interconnectivity need to be precisely controlled to meet the tissue specific requirements for proper regeneration.

SEM images for NaCl porogens nucleated at various concentrations at a fixed crystallization temperature (95 °C) are shown in Figures 3.3A-C. The results show that the resulting NaCl porogen shape could be controlled through the solubility of the NaCl. At a lower concentration (0.36 g mL^{-1}), the NaCl porogens were spherical in morphology (**Figure 3.3A**). As the concentration of the NaCl increased (0.37 g mL^{-1} and 0.38 g mL^{-1}), the resulting NaCl crystals were rhomboidal and cuboidal in geometry, respectively. The resulting NaCl porogen geometry was ultimately dictated by the solubility, or concentration of the supersaturated solution, which ultimately affected the crystal growth. As the NaCl nuclei are initiated through the reduction of free energy (temperature reduction), the porogen shapes begin spherical in shape. Using the same conditions, a further reduction in free energy, through the increased supersaturated concentrations, initiated the crystal growth phase resulting in the rhomboidal and final cuboidal geometries.

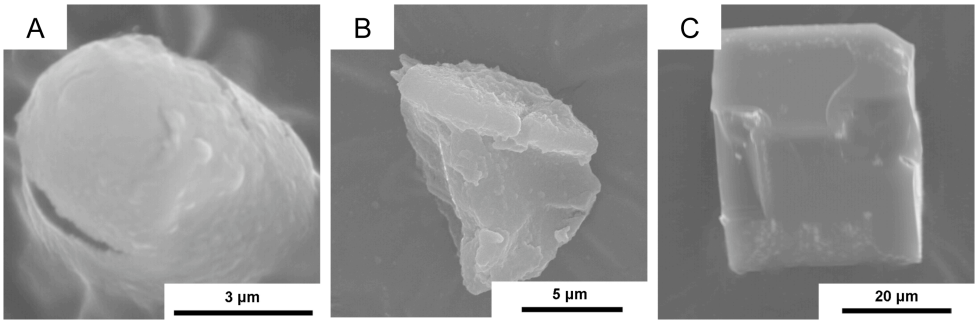

Figure 3.3 SEM Images of NaCl Salt Crystallized at Different Concentrations A) 0.36, B) 0.37 g, and C) 0.38 g mL^{-1}

The resulting NaCl porogen size could also be controlled through the nucleation temperature. Figures 3.4A-f show the SEM images of NaCl porogens nucleated at 90, 85, 80, 70, 60, and 50 °C at a fixed concentration of 0.38 g mL^{-1}. The results show that as the nucleation temperature was reduced, the resulting NaCl crystal increased in size due to the reduction in free energy of the solution. The salt sizes produced ranged from 2.59 ± 0.90 μm at 95°C up to 95.39 ± 11.46 μm at 50 °C (**Figure 3.5A**). As the results show, the resulting NaCl porogen size can be precisely controlled within a narrow range to meet the needs for specific tissue engineering applications where the pore sizes must be consistent. Although the results show a maximum size of 76 μm, increased sizes can be obtained by lowering the nucleation temperature. Salt sizes as small as 461.56 ± 98.86 nm can be produced when nucleated at 99 °C at 0.38 g mL^{-1}, showing the ability to produce porogens in the nanoscale range.

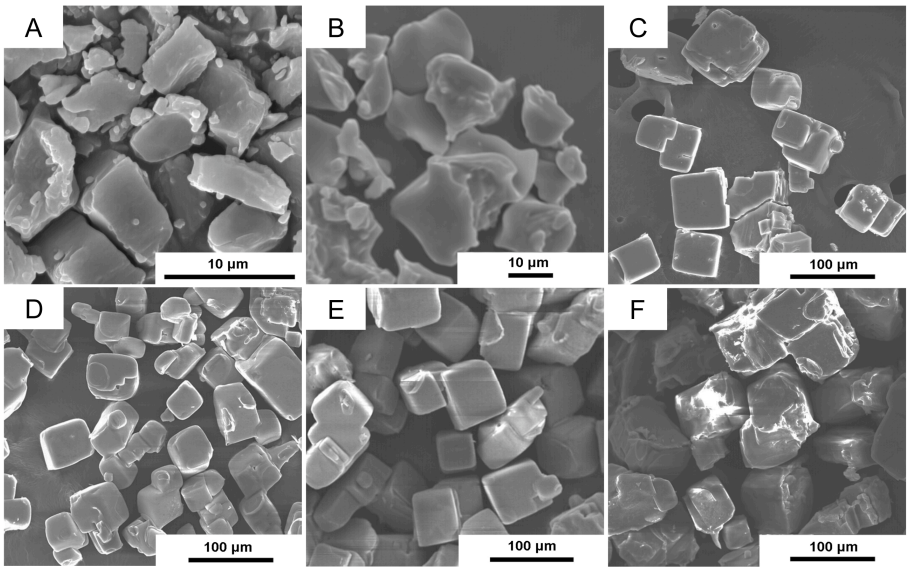

Figure 3.4 SEM Images of NaCl Salt Crystallized at Different Temperatures A) 90, B) 85, C) 80, D) 70, E) 60, and F) 50 °C

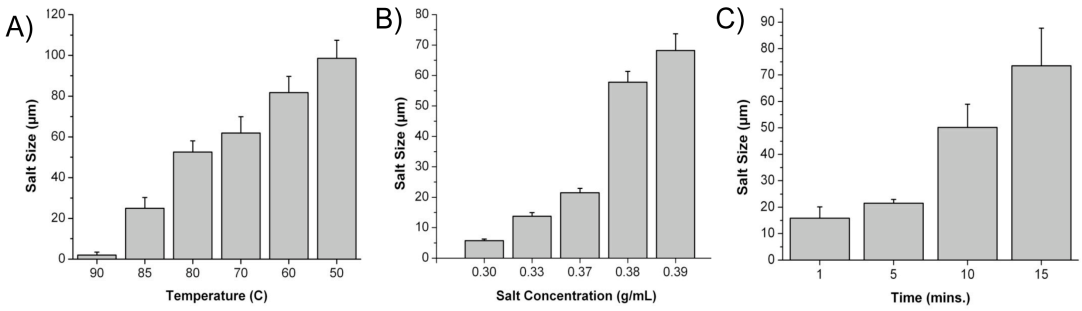

Figure 3.5 Resulting NaCl Crystal Sizes Obtained by Crystallizing at Various A) Nucleation temperatures, B) NaCl concentrations, and C) Nucleation times

Adjusting the supersaturation concentration can also control the NaCl porogen size. Figure 3.5B shows the results from the NaCl porogen study in which the supersaturation concentration was increased from 0.30 g mL^{-1} up to 0.39 g mL^{-1} with a fixed nucleation temperature of 80 °C. As the supersaturation concentration was increased from 0.30 g mL^{-1} to 0.39 g mL^{-1}, the resulting porogen size increased from 5.74 ± 0.57 to 68.23 ± 5.49 μm, respectively. In addition, the nucleation time was also controlled to evaluate the effects on NaCl crystal size. Figure 3.5C shows a correlation between the increased nucleation time and resulting crystal size. Thus, similar to using the temperature to control the porogen size, the concentration of the supersaturated solution and crystallization time can be used as an additional method to fine-tune the NaCl size within a narrow range.

When compared to traditional grinding and sieving methods to produce NaCl porogens, the nucleation and crystallization technique provides superior control over the resulting size distribution. Figure 3.6A shows the SEM images of NaCl produced after being sieved through a 50 μm sieve, and ground using a coffee grinder to produce even smaller porogen sizes. We believe method will produce the smallest porogen sizes possible in normal laboratory settings without the use of expensive equipment. Figure 3.6B shows the SEM images of NaCl nucleated at a concentration of 0.33 g mL^{-1} and 80 °C. The results show that the grinding and sieving method produces NaCl porogens 13.89 ± 12.49 μm, whereas the nucleation and crystallization

method produced NaCl porogens 13.78 ± 1.18 μm (**Figure 3.6C**). No significant difference in the mean size was seen between the two methods due to the large size distribution of the grinding method ($p > 0.05$). However, the nucleation and crystallization method allows for the generation of porogen sizes with a narrow size distribution, which will be beneficial in creating tissue engineering scaffolds with uniform pore sizes throughout the construct.

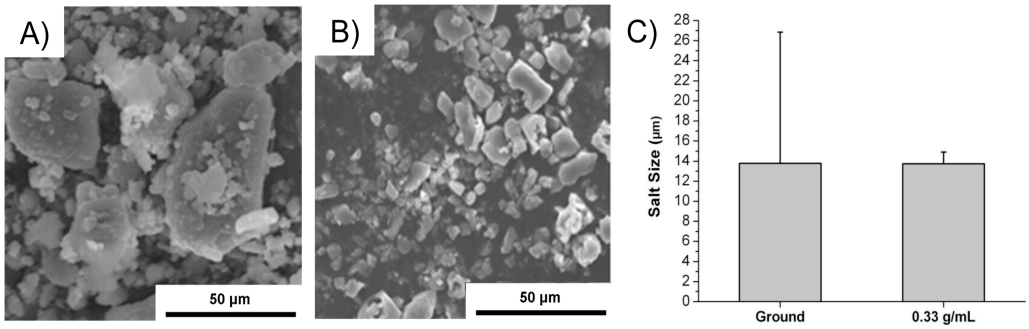

Figure 3.6 SEM Images of A) Traditional sieved and ground NaCl, B) Crystallized NaCl at a concentration of 0.33 g mL^{-1} at 80 °C, and C) Graphical representation of the sieved and ground salt versus salt obtained from the nucleation and crystallization method

Tissue engineering scaffolds produced by traditional salt leaching methods typically are plagued by the presence of “dead” pores, which hinder cell-cell communication, mass transport, and cell infiltration. Figure 3.7A shows an SEM image of a CUPE 1.2 scaffold prepared using traditional salt leaching methods. Figure 3.7B shows the pore structure, which reveals the closed walls and dead pores. The interconnectivity index of the scaffold was measured as 2.98 ± 0.67%. When NaCl porogens produced from the nucleation and crystallization method were incorporated with the traditional salt leaching methods, the interconnectivity was greatly improved. Figures 3.7C and D show the SEM images from CUPE 1.2 scaffolds created using both traditional and nucleation techniques to prepare scaffolds with improved interconnectivity with the potential for enhanced cell-cell communication and mass transport, which play a large role in the overall success in a tissue engineering scaffold. For example, studies have shown that the reciprocal interactions from the cell-cell communication between endothelial cells and mesenchymal stem cells have shown promise in generating vascularized bone-tissue

engineering constructs [211]. Scaffolds created from this method showed an interconnectivity index of 19.17 ± 2.91%, which shows a great improvement over the previous traditional scaffold fabrication technique ($p < 0.01$). The pore morphology of the interconnected scaffolds also show micro and nanoscale topographies, which can be beneficial in reproducing surfaces that better mimic the native extracellular matrix for enhanced cell adhesion and differentiation. As the pore interconnectivity is an important aspect and plays a large role in the success of tissue engineering scaffolds, future research will focus on the use of alternative approaches such as mercury intrusion porosimetry [212], 3D microtomography [213], or 2D image analyses [214] to provide an improved quantification evaluation of the pore interconnection.

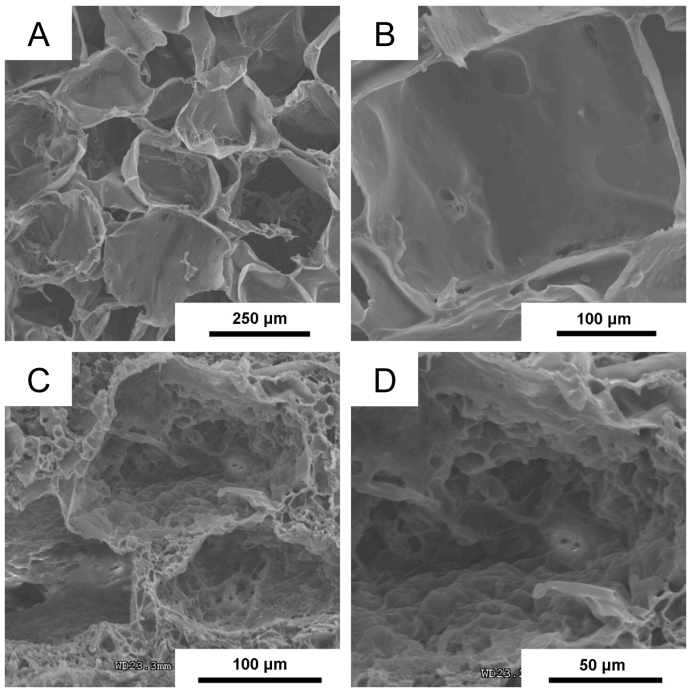

Figure 3.7 SEM Images of Crosslinked Urethane-doped Polyester Scaffolds Prepared Using Only Sieved 150-250 μm Salt A) 100X and B) 250X. SEM Images of CUPE Scaffolds Prepared Using 150-250 μm Salt in Combination with Crystallized Submicron NaCl Porogens to Increase Scaffold Interconnectivity C) 200X and D) 600X

The nucleation and crystallization porogen method allowed for the fabrication of uniform porogen sizes smaller than traditional methods, which can be used in MEMS based tissue engineering applications. MEMS technologies has recently been used with hydrogels and

biodegradable elastomers to fabricate 3D structures with the ability to control cell adhesion, cell morphology, and create microvasculature using the physical cues of the construct to influence cell behavior [7, 124, 215]. Porous microchanneled MEMS scaffolds offer unique advantages in that cells can be evenly seeded onto the channels, the seeded scaffolds can be stacked together to form complex heterogeneous tissue constructs, the submicron porosity of the scaffold can allow for cell communication without cell migration into different layers, and the microchannel space can allow for nutrient supply through culture medium perfusion, and influence cell organization by aligning the cells using contact guidance [216]. However, the introduction of submicron pores into MEMS based scaffolds for cell communication while preventing cell migration has been primarily accomplished using TIPS techniques [217]. Figure 3.8A shows the SEM image of porous microchanneled CUPE 1.2 scaffolds using MEMS based techniques in combination with nucleation and crystallization pore generation methods. Through this new pore generation technique, submicron porosity can now be introduced into MEMS based techniques. Although only CUPE was used as the material to fabricate porous scaffolds in this study, the nucleation and crystallization pore generation technique can potentially be applied to a wider selection of available materials to accommodate for the strict requirements of engineering various tissues.

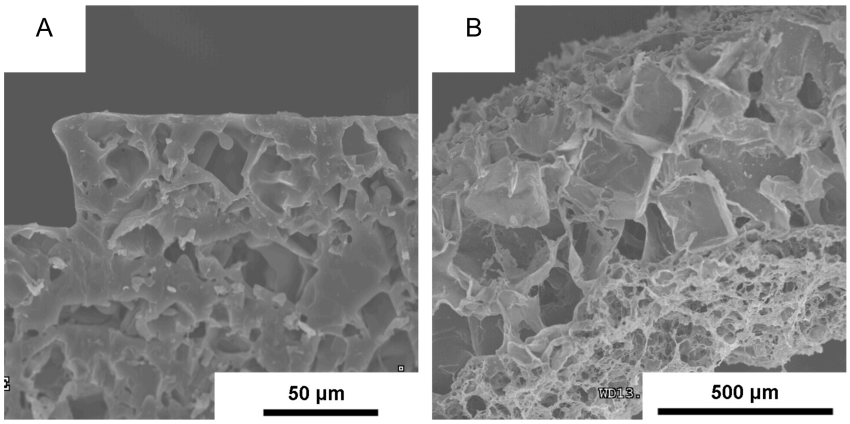

Figure 3.8 Cross-sectional SEM Images of Crosslinked-Urethane Doped Polyester A) Porous microchanneled scaffolds and B) Multiphasic small diameter vascular grafts using submicron salt obtained from the nucleation and crystallization method

We have also shown the fabrication of novel small diameter grafts using the nucleation and crystallization pore generation technology for vascular tissue engineering. In order to recreate the stratified cellular architecture of native vessels, we have proposed the fabrication of anatomically correct multiphasic small diameter grafts. As shown in Figure 3.8B, we have constructed vascular grafts with two distinct layers 1) a microporous luminal permeable elastic membrane to promote graft endothelialization while allowing for cell communication; and 2) a porous tunica medial layer for smooth muscle and fibroblast cell proliferation. We believe that a small diameter vascular graft created with this type of distinct layered architecture will better mimic the native vessel anatomy to potentially improve graft function. In native blood vessels, endothelial cells and smooth muscle cells influence each other via the signaling molecules secreted by both cell types [218-222] through the internal elastic lamina. The failure of previously developed vascular grafts has been correlated with the lack of a functional endothelial luminal layer due to inappropriate luminal topographies, which result in graft thrombosis and neointimal hyperplasia [223]. The microporous luminal layer created using the nucleation and crystallization methods will provide the topography necessary for endothelial cell adhesion and proliferation while allowing for endothelial and smooth muscle cell communication. This scaffold fabrication method in combination with nucleation and crystallization pore generation technology provides a new avenue to fabricate complex heterogeneous porous scaffolds with different porosities, pore sizes, pore shapes, and interconnectivity among each layer to accommodate for specific cell types in the regeneration of multicellular tissues such as skin, blood vessels, liver, pancreas, and cartilage where the compartmentalization of different cell types is necessary [88, 196, 224].

3.2.4 Conclusion

A new generation of NaCl porogen has been developed for tissue engineering scaffold fabrication using the principles behind nucleation and crystallization science. This new porogen technology provides a facile, convenient, more precise, and cost-effective method over

traditional sieving and grinding techniques to generate NaCl porogens within a narrow size range, which can be applied to a wide variety of biomaterials. The submicron NaCl porogens created using this new technique were used to fabricate porous and elastic multiphasic small diameter vascular grafts and microchanneled scaffolds for potential use in soft tissue engineering applications. This new pore generation technique may serve as a powerful tool and add to the current repertoire of tissue engineering scaffold design methods.

3.3 Scaffold Sheet Design Strategy

3.3.1 Introduction

Tissue engineering is a multi-disciplinary field that combines the principles of polymer chemistry, engineering, and biological sciences in efforts to develop biological substitutes to improve or replace the functions of failing tissues and organs [125]. One of the main principle methods behind tissue engineering involves growing relevant cells into a three-dimensional (3D) tissue or organ. Although cells alone lack the ability to grow into 3D orientations similar to the native tissues, the preferred multidimensional cellular growth is achieved by seeding the desired cells onto porous matrices, known as scaffolds [163]. By serving as a temporary suitable microenvironment for extracellular matrix (ECM) and 3D tissue formation, the scaffold has become a very important component of tissue engineering [165].

Scaffold requirements for tissue engineering are multifaceted and particular to the structure and function of the tissue of interest [225]. Many scaffold processing and fabrication techniques such as fiber meshes [226], phase separation [227], solvent casting and particulate leaching [228], membrane lamination [229], and melt molding [230] have been utilized in a wide variety of applications including bone [231], cartilage [152], blood vessels [232], and heart valves [233]. Although these scaffolds have demonstrated promise, uneven cell distribution and nutrient delivery in the deep portion of the synthetic scaffolds (> 200 μm) due to the random mobility of cell suspension often compromise their successful uses in tissue engineering [234, 235]. The seeded cells and matrix produced by cells at the scaffold periphery also act as a

barrier to the diffusion of oxygen and nutrients into the interior of the scaffold. Unfortunately, these constraints limit the majority of successful tissue engineering applications to the maximum diffusion distance of 200 μm [216, 236].

A pioneering 2D cell-sheet tissue engineering strategy was proposed to regenerate several types of tissues such as blood vessel [237], skin [238], corneal epithelium [239], urothelium [240], and periodontal ligament [241]. By using a layer-by-layer technique, stratified tissues were created from the stacking of single cell sheets to create more complex structures such as liver lobules and kidney glomeruli [242]. Although problem of uneven cell distribution is not a concern in this case, cell sheets are too fragile to handle and the cell-sheet constructs require long in vitro culture time to mature prior to implantation, which is a considerable limitation of this technology [243]. Also, cells grown in a 2D culture dishes could bring some concerns such as losing important cell characteristics during the long-term culture, and only a limited number of cell types are able to form cell sheets thereby restricting the potential to engineer various types of tissues [237].

In this study, we show the proof of concept for the scaffold sheet tissue engineering strategy using thin and elastic crosslinked urethane-doped polyester (CUPE) scaffolds. CUPE are a new class of biodegradable elastomers that we have been developing to engineer soft, but strong scaffolds for soft tissue engineering applications. CUPE are easy to synthesize, potentially cost effective, and have demonstrated a wide range of mechanical properties with tunable degradation profiles [10]. In this work, we introduce a new scaffold sheet design with the following advantages: 1) single CUPE scaffold sheets can be fabricated and post-polymerized together to form complex constructs composed of layers with different pore structures; 2) single CUPE scaffold sheets can be seeded with cells and stacked together similar to the 2D cell-sheet tissue engineering strategy to form stratified tissues; 3) The use of thin (~200 μm thick) scaffold sheets should address the issues of uneven cell distribution, which is a common concern in the use of synthetic scaffolds for tissue engineering applications; 4) The CUPE

scaffolds can provide a 3D microenvironment for cell proliferation without the potential loss of cell characteristics; 5) the scaffold sheet design strategy in combination with a layer-by-layer approach has the potential to enable the compartmentalization of multiple cell types in the engineering of complex tissues; 6) the scaffold sheets are strong and compliant so that they may be implanted *in vivo* soon after cell seeding, which should eliminate the long *in vitro* culture times needed for construct maturation. The CUPE scaffold sheets were evaluated via mechanical tests and cell culture experiments to assess its potential use in soft tissue engineering.

3.3.2 Experimental

All chemicals, cell culture medium, and supplements were purchased from Sigma-Aldrich (St. Louis, MO, USA), unless mentioned otherwise, and used as received.

3.3.2.1 Crosslinked Urethane-doped Polyester (CUPE) Pre-Polymer Synthesis

CUPE pre-polymers were synthesized in two distinct steps similar to previously published methods [10]. The first step involves the synthesis of a POC soft segment, which is chain extended by 1,6-hexamethyl diisocyanate (HDI) in the second polyurethane synthesis step. Briefly, a POC pre-polymer was first synthesized by reacting a 1:1.1 monomer ratio of citric acid and 1,8-octanediol, respectively, in a three-necked round bottom flask fitted with an inlet and outlet adapter at 160 °C under a constant flow of nitrogen [95]. Once all the monomers had melted, the temperature of the system was lowered to 140 °C, and the reaction mixture was allowed to continue for 60 minutes to create the POC pre-polymer. The POC pre-polymer was then purified by drop-wise precipitation in deionized water. The undissolved pre-polymer was collected and lyophilized for 48 hours to obtain the pre-POC soft segment.

In the second step, chain extension was achieved by dissolving pre-POC in 1,4-dioxane (3 wt. %), and the resulting solution was allowed to react with HDI in a clean reaction flask under constant stirring at 55 °C using stannous octoate as a catalyst (0.1 wt. %). Various CUPE pre-polymers were synthesized using three different molar feeding ratios of the pre-POC: HDI

(1:1.2, 1:1.5, and 1:1.8 which are referred to as pre-CUPE 1.2, pre-CUPE 1.5, and pre-CUPE 1.8, respectively). The reaction was terminated upon the disappearance of the isocyanate peak located at 2267 cm-1, which was determined by FT-IR analysis.

3.3.2.2 CUPE Scaffold Sheet Fabrication

CUPE scaffold sheets were fabricated using a particulate leaching technique and according to the procedures illustrated in Figure 3.9. Briefly, a pre-CUPE solution was mixed with sieved sodium chloride salt (99% purity) with an average pore size in the range of 50–106 μm in a (1:9) polymer to salt ratio by weight (**Figure 3.9A**). The polymer solution was mixed thoroughly with the salt until a viscous paste was formed. The resulting slurry was cast onto an aluminum mold machined to have a cavity approximately 200 μm deep (**Figure 3.9B**), and then placed in a laminar flow hood overnight for solvent evaporation. Once the solvent was removed, the scaffold sheets were post-polymerized in an oven maintained at 80°C (**Figure 3.9C**) for predetermined times to crosslink the pre-CUPE into CUPE. Next, the salt in the scaffold was leached out by immersion in deionized water for 72 hours with water changes every 12 hours (**Figure 3.9D**). Finally, the scaffolds were lyophilized for 36 hours to remove any residual water.

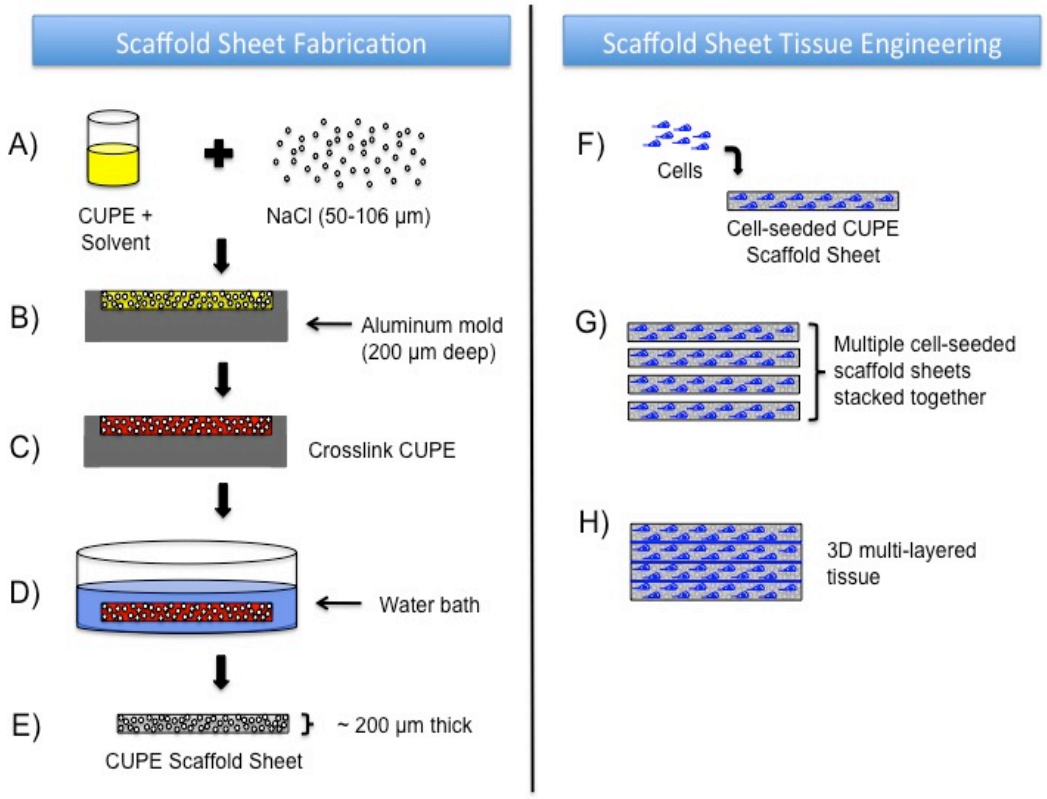

Figure 3.9 Schematic of the Scaffold Sheet Fabrication Process and Scaffold Sheet Tissue Engineering Design Strategy A) pre-CUPE is combined with NaCl, B) The CUPE/salt mixture is placed into an aluminum mold, C) The mixture is crosslinked at 80°C, D) The salt in the obtained scaffold sheet is removed by water, E) Final scaffold sheet (~200 µm thick), F) Cells are seeded onto individual scaffold sheets, G) Multiple scaffold sheets are stacked together, and H) 3D multi-layered tissue construct is obtained

POC and PLLA scaffold sheets were also fabricated as described above to serve as a control. To study the effects of the post-polymerization conditions, single scaffold sheets were placed in an oven maintained at 80 °C for 2 days (80 °C-2), 80 °C for 4 days (80 °C-4), and 80 °C for 4 days followed by additional post-polymerization at 120°C under vacuum for 1 day (120 °C-1). To study the effects of the number of scaffold layers, multiple pre-CUPE scaffold sheets were stacked together and post-polymerized at 120 °C-1. To study the effects of the HDI ratio on the resulting constructs, pre-CUPE 1.2, pre-CUPE 1.5, and pre-CUPE 1.8 were used to fabricate scaffold sheets and post-polymerized at 120 °C-1.

3.3.2.3 CUPE Scaffold Sheet Characterization

To view the cross-sectional morphology, CUPE scaffold sheet samples were freeze-fractured using liquid nitrogen, sputter coated with silver, and examined under a Hitachi S-3000N scanning electron microscope (SEM) (Hitachi, Pleasanton, CA, USA). Image J analysis software was used to determine the scaffold sheet thickness. To characterize the scaffold geometries, 3 random locations were selected and a total of 30 measurements were recorded. The dimensions reported are expressed as the means ± standard deviation.

The scaffold porosity was measured using the Archimedes' Principle similar to previously published methods [244]. Briefly, a density bottle was used to measure the density and porosity of the scaffold using ethanol (density ρe) as the displacement liquid at 30°C. The density bottle filled with ethanol was weighed (W1). A scaffold sample of weight WS was immersed into the density bottle, and the air trapped in the scaffold was evacuated under vacuum. Next, the density bottle was supplemented with ethanol, filled, and weighed (W2). The ethanol-saturated scaffold was removed from the density bottle, and the density bottle was weighed (W3). The following parameters of the scaffold were calculated: the volume of the scaffold pore (VP), the volume of the scaffold skeleton (VS), the density (ρS), and the porosity (ε). The following formulas for the volume-mass index (VP/VS) were used [244]:

$VP = (W2 - W3 - WS) / \rho e$

$VS = (W1 - W2 + WS) / \rho e$

$\rho S = WS / VS = WS\rho e / (W1 - W2 + WS)$

$\varepsilon = VP / (VP + VS) = (W2 - W3 - WS) / (W1 - W3)$

The porosity of single scaffold sheets was recorded, and the results are reported as the means ± standard deviation (n = 6).

Tensile mechanical testing was conducted according to ASTM D412A standard on a MTS Insight 2 fitted with a 10 N load cell (MTS, Eden Prairie, MN, USA). Briefly, scaffold sheet strips (10 mm length × 2 mm width) were pulled at a rate of 500 mm min^{-1} and elongated to

failure. Values were converted to stress-strain and the initial modulus was calculated from the initial gradient of the resulting curve (0–10% elongation). The results are presented as the means ± standard deviation (n = 6). The suture retention strength was obtained similar to previously reported methods [245]. Briefly, one end of a CUPE scaffold sheet sample (10 mm length × 5 mm width) was fixed with the stage clamp of the tester, and the other end was connected to the opposite clamp through the suture material (5–0 Prolene, Ethicon, Piscataway, NJ, USA). The suture was placed 2 mm from the end of the sample. The measurement was performed using a 10 N load cell, and pulled at a rate of 8 mm/min until failure. The load at rupture was recorded (N), and the results are reported as the means ± standard deviation (n = 6).

3.3.2.4 In Vitro Cell Culture Attachment and Proliferation

Cell compatibility of the CUPE scaffold sheets was evaluated in vitro using both quantitative and qualitative methods using NIH 3T3 fibroblasts (ATCC) as model cells. A quantitative assessment of the cell proliferation was performed using a Methylthiazoletetrazolium (MTT) cell proliferation and viability assay kit. CUPE 1.2, PLLA, and POC scaffold sheet samples were cut into cylindrical discs (7 mm in diameter) and sterilized in 70% ethanol for 3 hours. After incubation in ethanol, the samples were exposed to UV light for 30 minutes, and washed with phosphate buffered saline (PBS). The cells were cultured in Dulbecco's modified eagle's medium (DMEM), which had been supplemented with 10% fetal bovine serum (FBS) and 1% penicillin streptomycin. The culture flasks were kept in an incubator maintained at 37 °C, 5% CO2, and 95% relative humidity. The cells were allowed to grow to the fourth passage, trypsinized, centrifuged, and suspended into media to obtain a seeding density of 1×10^5 cells mL^{-1}.

MTT Assay analysis was performed at 1, 3, and 5 days of culture. At the pre-determined time point, the assay was conducted as per the manufacturer's protocol. Briefly, the old media was aspirated, and each sample was washed with PBS to remove any loosely

attached or dead cells. Next, 100 μL of 3-(4,5-dimethylthiazol-2yl)-diphenyltetrazolium bromide solution was then added to the samples, and allowed to incubate for 3 hours. At the end of the incubation period, the mixture of the MTT solution and incomplete media was aspirated and replaced with 100 μL of MTT solvent. Dissolution of the formazan crystals was facilitated by constant agitation of the well plate on an orbital shaker for 20 minutes. The absorbance was measured with an Infinite 200 microplate reader (Teacan Group Ltd., Switzerland) at 570 nm, with a reference wavelength of 690 nm, within 30 minutes of MTT solvent addition.

The feasibility of the scaffold sheet tissue engineering design strategy was evaluated according to the procedure described in Figure 3.9. CUPE 1.2 scaffold sheet strips were prepared for cell culture as described above. Cells were seeded on both sides of the scaffold sheets at a density of 1×10^6 cells mL^{-1} (**Figure 3.9F**). After 1 day of culture, the scaffold sheets are stacked together (**Figure 3.9G**), and allowed to culture for a two-week time period with media change every third day. After 2 weeks, the cells were fixed with the addition of cold methanol for 10 minutes and dried under vacuum. Scaffolds were then embedded in a liquid gelatin-sucrose solution, placed under vacuum for 30 minutes, and frozen at -20 °C. Cross-sections of the scaffold were cut at 10 μm and hematoxylin and eosin (H&E) stained to visualize cell penetration, growth throughout the scaffold, and scaffold sheet bonding (**Figure 3.9H**).

3.3.2 Results and Discussion

Many scaffold fabrication techniques previously reported have resulted in an uneven distribution of cells within the construct [233-235]. In the case of most *in vivo* tissue, a network of vascularization offers a maximum nutrient diffusion distance of about 200 μm, which is most likely the reason why most successful tissue engineered applications have resulted in the growth of tissues with cross sections less than 500 μm from the external surface of the scaffold [216, 246]. In this study, we report on the feasibility of using a new scaffolding design strategy named scaffold sheet tissue engineering. The concept behind this new approach involves the use of thin (~200 μm) strong and compliant scaffold sheets in combination with a layer-by-layer

approach to form stratified 3D constructs without the issues of uneven cell distribution or the potential loss of cell characteristics seen in 2D cell-sheet tissue engineering.

The morphology of the CUPE scaffold sheets were fabricated according to Figure 3.9A-E, and were verified using SEM and NIH ImageJ analysis software. Figure 3.10 presents SEM images of a single porous CUPE scaffold sheet and multiple scaffold sheets stacked and crosslinked (or post-polymerized) together. The scaffold sheets produced from this technique displayed an overall scaffold thickness of 179.16 ± 8.16 μm, porosity of 86.60 ± 3.05%, and interconnected pore size 78.04 ± 13.59 μm (**Figure 3.10A**). The pore sizes created from this technique were limited to less than 150 μm due to restrictions in the depth of the machined aluminum mold. The above parameters, however, can easily be adjusted by changing the mold dimensions, polymer: salt ratio, and porogen size to fit the needs of a specific application. The images shown in Figure 3.10B and C represent the cross sections of two and four scaffold sheets crosslinked together, respectively, showing the ability to stack multiple layers together to form one continuous construct. This layer-by-layer technique opens a way to fabricate complex heterogeneous porous scaffolds with different porosities, pore sizes, pore shape, and interconnectivity amongst each layer while maintaining a porous interface to accommodate for specific cell types in the regeneration of multi-cellular tissues such as skin, blood vessels, liver, pancreas, and cartilage where the compartmentalization of different cell types is necessary [88, 196, 224].

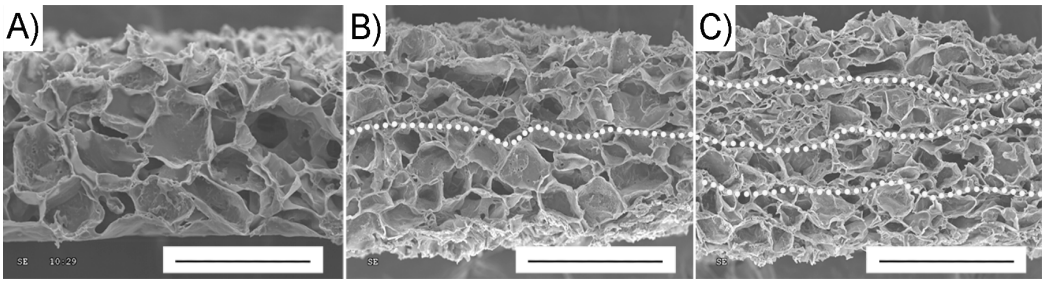

Figure 3.10 Representative SEM Image Cross Sections A) Single CUPE 1.2 scaffold sheet (Scale bar 150 μm), B) Two CUPE 1.2 scaffold sheets crosslinked together (Scale bar 300 μm), and C) 4 CUPE 1.2 scaffold sheets crosslinked together (Scale bar 600 μm)

Early efforts in tissue engineering have mainly focused on the use of biodegradable synthetic polymers, such as polylactic acid (PLA), polyglycolic acid (PGA), poly (caprolactone) (PCL), and their copolymers, to support ECM production. Unfortunately, these previous materials have been limited in their success due to their lack of strength and elasticity causing a mismatch in compliance [22, 247-251]. Biodegradable elastomers, such as poly (diol citrates) (PDC), poly (glycerol sebacate) (PGS), and more recently crosslinked biodegradable photoluminescent polymer (CBPLP) have received much attention recently as materials for vascular tissue engineering due to their elastic nature and excellent cell/tissue compatibility [57, 62, 71, 80, 84, 85, 95, 127, 252, 253]. However, these materials lack the sufficient strength when fabricated into porous scaffolds. In an effort to add strength while maintaining elasticity, we have recently reported on the synthesis and characterization of a novel biomaterial, CUPE, which combines the elasticity of polyesters with the strength of polyurethanes. A simple doping of a urethane group into the POC network resulted in films with a 10-fold increase in tensile strength, while maintaining a soft and elastic nature [10].

A comparison between the mechanical properties of POC and CUPE scaffold sheets are shown in Figure 3.11. A significant increase in the peak tensile stress (160.67 ± 24.48 KPa to 377.12 ± 36.87 KPa) and elongation at break (149.09 ± 12.78% to 195.29 ± 11.80%) was observed when CUPE was used as the material for scaffold sheet fabrication. The enhanced mechanical properties from the addition of HDI into the POC pre-polymer can be explained due to the increased hydrogen bonding between the urethane groups, which are not present in the POC scaffolds, to produce higher peak tensile strength while preserving the elasticity of the material.

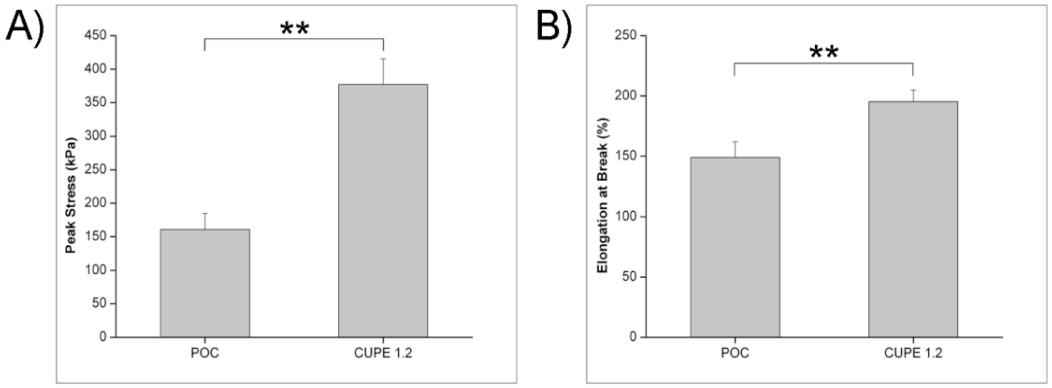

Figure 3.11 Mechanical Comparison Between POC and CUPE 1.2 Scaffold Sheets A) Tensile peak stress and B) Elongation at break (** $p < 0.01$; $n = 6$)

Figure 3.12A presents a photomicrograph of a single CUPE 1.2 scaffold sheet, and a scaffold sheet rolled around a Teflon rod. All CUPE scaffold sheets fabricated in this study were soft, elastic, and showed 100% recovery after deformations with the ability to be folded and rolled into any desired shape without kinking. Based on the stress-strains of the scaffold sheets, the tensile strength, initial modulus, and elongation at break were calculated. As shown in Figure 3.12B, the stress-strains curves were characteristic of elastomers with no yield point in any of the scaffold mechanical tests. Multiple scaffold sheet stress-strain curves produced single breaks indicating that the individual sheets were bonded together through the post-polymerization process (**Figure 3.12C**).

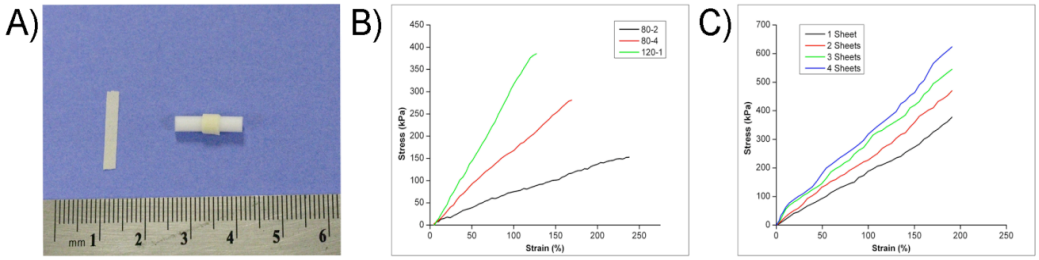

Figure 3.12 A) Photograph CUPE scaffold sheets, B) Stress-strain curves of single CUPE 1.2 scaffold sheets, and C) Stress-strain curves of multiple CUPE 1.2 scaffold sheets

The compliance mismatch between the scaffold and host tissue is a biomechanical problem that has been cited to inhibit the successful integration of the construct with native tissue, and ultimately results in implant failure [88]. Thus, the ability to engineer the appropriate scaffold mechanical properties to suit a particular application plays an important role in the success of the implant. One advantage in the CUPE scaffold sheet design is that the mechanical properties can be controlled through a variety of options such as the post-polymerization condition, pre-polymer chemistry, and the number of scaffold layers. The mechanical properties of single CUPE 1.2 scaffold sheets post-polymerized under different reaction conditions are summarized in Table 3.1. As the post-polymerization time and temperature were increased, a significant increase in the peak stress, initial modulus, and suture retention strength was observed with a corresponding drop in elasticity. A significant increase in the peak stress was observed from 2 days at 80 °C to 4 days at 80 °C (150.25 ± 17.38 to 294.54 ± 38.30 KPa, respectively). The same trend was also displayed as the post-polymerization temperature was increased from 80 °C to 120 °C.

Table 3.1 Mechanical Properties of Single CUPE 1.2 Scaffold Sheets [a]

Post-Polymerization Condition	Peak Stress (KPa)	Initial Modulus (MPa)	Elongation at Break (%)	Suture Retention (N)
80°C-2	150.25 ± 17.38	0.07 ± 0.01	230.63 ± 9.25	0.07 ± 0.01
80°C-4	294.54 ± 38.30	0.15 ± 0.02	212.08 ± 9.68	0.10 ± 0.01
120°C-1	377.12 ± 36.87	0.21 ± 0.02	195.29 ± 11.80	0.12 ± 0.01

[a] Values are given as the means ± standard deviation (n = 6)

Although the elongation at break was sacrificed with the harsher post-polymerization conditions, single CUPE 120 °C-1 scaffold sheets showed a maximum peak stress of 377.12 ± 36.87 KPa with an elongation at break of 195.29 ± 11.80 %, which is close to the elasticity and elongation of native vessels [254]. In the case of in vivo tissue engineering, the elastomeric nature of the CUPE scaffolds can permit the transmission of dynamic mechanical stimuli exerted by the cardiovascular system. The increase in mechanical properties from the harsher post-polymerization conditions was contributed to an increase in the crosslinking density of the

resulting material to create a stronger and stiffer scaffold. By varying the post-polymerization conditions, the mechanical properties of the scaffold sheets can be tuned for the intended application.

The effects of the pre-polymer isocyanate concentration on the resulting construct mechanical strength were also evaluated (**Figure 3.13**). A significant increase in the scaffold peak stress and initial modulus with a corresponding decrease in elasticity was observed as the pre-polymer HDI concentration was increased. However, no difference was observed in peak stress for CUPE 1.5 and CUPE 1.8 scaffold sheets ($p > 0.05$). In addition to the pre-polymer compositions, the effects of the number of stacked scaffold sheet layers on the mechanical properties were determined. As the number of stacked scaffold sheet layers was increased, an increasing trend in the peak stress was observed. However, the results also showed that the number of stacked scaffold sheets had no effect on the construct initial modulus or elongation at break (**Figures 3.13B and C**). By increasing the number of scaffold layers, the CUPE scaffold sheet design strategy can potentially meet the mechanical surgical requirements of implantation.

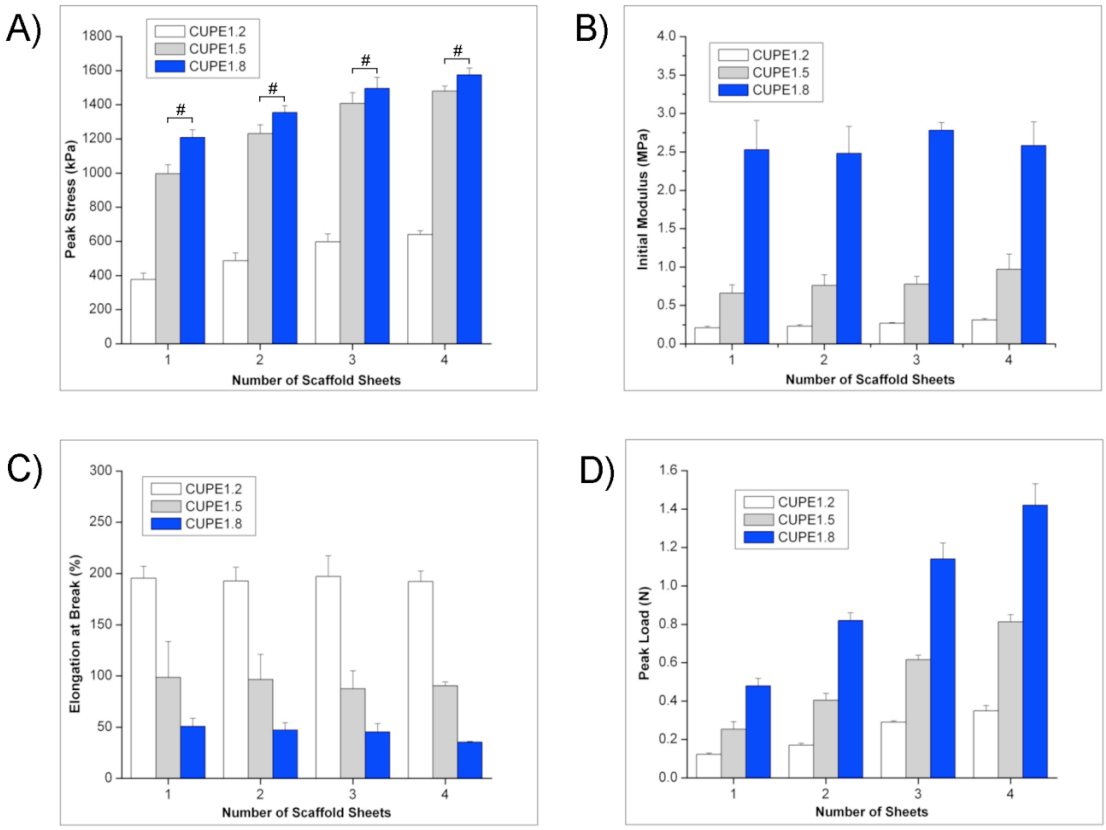

Figure 3.13 Mechanical Properties of Multiple CUPE Scaffold Sheets A) Tensile peak stress, B) Initial modulus, C) Elongation at break, and D) Suture retention strength

The suture retention strength is a crucial factor in the fabrication of tissue engineering scaffolds as it directly relates to the success of the construct during the implantation process. In these experiments, both an increase in the pre-polymer HDI concentration and number of scaffold sheets resulted in higher suture retention strengths (**Figure 3.13D**). Although, the suture retention strength for single CUPE 1.2 scaffold sheets were relatively low (0.12 ± 0.01 N), CUPE 1.8 scaffold sheets, when stacked into 4 layers, were close to the accepted adequate suture retention strength of 1.8 N [255].

3T3 cell adhesion and proliferation were quantitatively assessed using the MTT assay. Results indicated that a larger number of cells attached and proliferated to the CUPE scaffolds when compared to that of POC scaffolds at all time points. However, no significant difference in

cell growth was observed when comparing the CUPE scaffolds to that of PLLA control scaffolds (**Figure 3.14**). Future studies will involve the in vitro cell compatibility using other cell lines such as human aortic endothelial and smooth muscle cells to evaluate the cell compatibility of the CUPE scaffold sheets for multi-cellular applications.

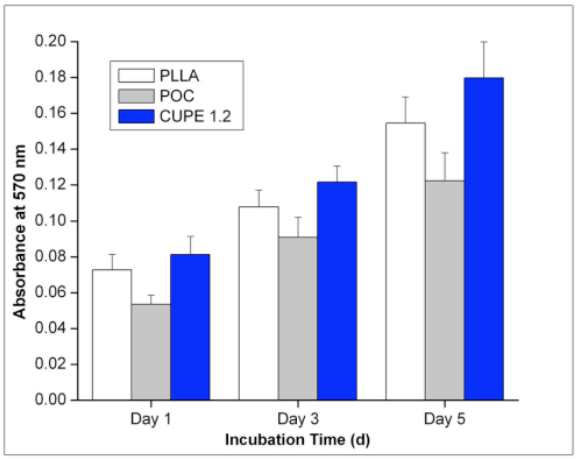

Figure 3.14 Comparison of 3T3 Fibroblast Growth and Proliferation on Single PLLA, POC, and CUPE 1.2 Scaffold Sheets

Although we understand that chemically bonded scaffold sheet constructs may not relate to cell culture bonded constructs, a quick screen to fabricate tissue interlocked constructs was performed to assess the feasibility of the approach. The layer-by-layer fabrication process depicted in Figure 3.9 was evaluated using 3T3 fibroblast cell culture to bond individual scaffold sheets. H&E stained cross-sections of cell seeded scaffolds show that cells attached and proliferated along the exterior with an even distribution throughout the interior of the scaffold (**Figure 3.15**). The photomicrographs shown in Figure 3.15B present the H&E stained cross-sections of two scaffold sheets stacked together and allowed to culture over a two-week time period. The scaffold layers were shown to have bonded between the interfaces of each scaffold layer through ECM production by the seeded cells. These results provide evidence that the scaffold sheet design can potentially be used to combine multiple seeded scaffold sheets to produce a stratified construct.

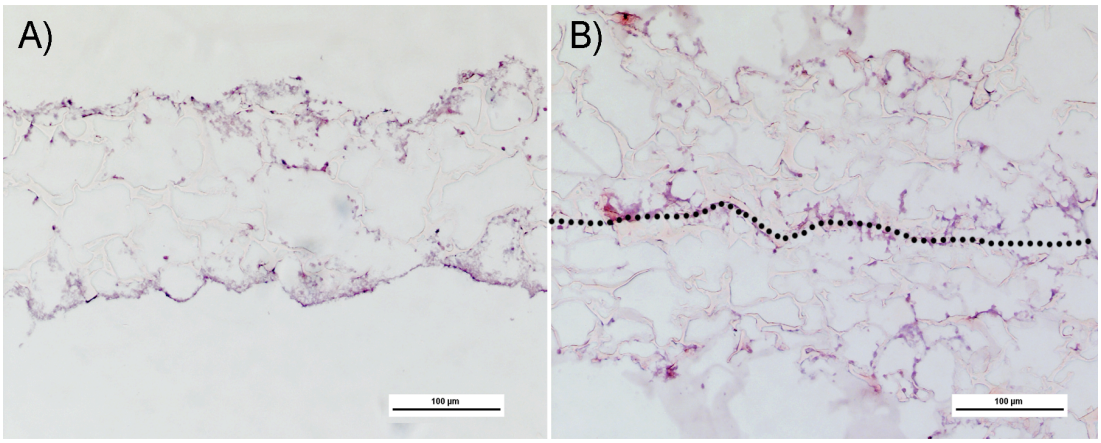

Figure 3.15. Photomicrographs of H&E Stained CUPE 1.2 Cross Sections after 2 weeks of Cell Culture A) Single scaffold sheet and B) 2 scaffold sheets (Scale bar 100 μm)

3.3.4 Conclusions

A novel scaffold sheet design strategy has been presented for use in the tissue engineering of complex multi-cellular tissues, which consist of a stratified cellular architecture. The development of this new scaffolding strategy should add the current repertoire of tissue engineering strategies.

3.4 Multiphasic Small Diameter Vascular Grafts

3.4.1 Introduction

Cardiovascular disease remains the leading cause of mortality in western nations accounting for approximately 30% of all deaths each year. According to the American Heart Association, it is estimated that nearly half of all cardiovascular disease related deaths result from coronary artery or peripheral artery disease, which creates an enormous economic burden totaling over $448.5 billion in health care costs annually for the United States [256, 257]. Despite the considerable enhancements in our understanding of vascular diseases, coronary artery bypass using autologous vessels, including saphenous veins, mammary, and radial arteries, remain the “gold standard” for high-risk patients with over 1 million arterial bypass procedures performed each year in the United States alone [258]. Unfortunately, the success of the aforementioned procedure relies on the availability of suitable, healthy autologous vessels

of sufficient length for grafting, which are not present in 33% of patients due to pre-existing vascular disease and vein harvesting from prior surgical procedures [259]. Taken together with other limitations such as the surgical morbidity from autologous vessel harvesting, high surgical costs, and the need for vascular grafts in other medical procedures such as vascular trauma, aneurysms, plastic reconstruction, and organ transplantation, an enormous clinical need remains for a readily available, off-the-shelf, and functional graft substitute [260].

Early attempts to develop an ideal replacement vessel have mainly focused on the use of synthetic grafts fabricated from expanded polytetrafluorethylene (ePTFE) or polyethylene terepthalate (PET, Dacron), which have shown to maintain patency for more than 10 years in large inner diameter (> 6 mm) applications due to the ample volumetric blood flow and large cross-sectional area [261]. However, their success is severely diminished when replacing vessels located in the smaller regions of the vascular system, such as the coronary or peripheral arteries where the inner diameter is smaller than 5 mm [262]. In areas of low blood flow, the non-hemocompatible nature of these materials and mismatch in mechanical compliance causes a massive activation of cellular defense mechanisms and initiation of different cascades of the hemostatic system resulting in early thrombosis formation, high occlusion rates, and graft failure [263, 264].

To address these issues, researchers are now looking towards the field of regenerative medicine to engineer small inner diameter blood vessels (SDBV) as an ideal replacement graft. Since Weinberg and Bell's first report on the *in vitro* construction of blood vessels, there has been considerable advancements in the area of vascular tissue engineering [265]. To date, several attempts have been made to develop an ideal SDBV including, the use of decellularized matrices [266, 267], hydrogel suspensions [268], cell sheets [269], and cell-seeded synthetic scaffolds based upon biodegradable polymers such as polyglycolic acid (PGA) [24], polylactic acid (PLA) [270], co-polymers of PLGA [250], polycaprolactone (PCL) [271], polyhydroxyalkanoates (PHA) [272], and biodegradable polyurethanes [11], While no clear

consensus on which approach might produce an ideal SDBV with long-term patency, it is agreed upon that the majority of the previous designs have been plagued with mechanical compliance issues, incomplete graft luminal endothelialization, and long *in vitro* graft maturation times, which is not a suitable option during times of emergency [256, 273].

To address the limitations of previous tissue-engineered SDBV, recent research has indicated a paradigm shift towards the development a new generation of mechanically compliant and biomimetic grafts, which are mechanically similar to native vasculature, strong enough for immediate implantation, and resemble the stratified layered vessel architecture to accommodate for the appropriate compartmentalized cell types needed for complete graft maturation. Yang *et al.* [88] and Dey *et al.* [274] have recently reported on the development of elastic biphasic SDBV fabricated from poly (diol citrates) (PDC) and crosslinked urethane-doped polyesters (CUPE), respectively. The reported biphasic designs consisted of a continuous non-porous luminal phase for endothelial cell proliferation and graft strength, surrounded by a porous phase to facilitate smooth muscle cell expansion and maturation. While these graft designs were able to provide adequate mechanical and burst pressures strengths, the smooth non-porous luminal wall may not be the optimal topographical environment for rapid endothelialization. Recent studies have shown that submicron topographies on stent and graft surfaces promote enhanced endothelial cell densities, adhesion, and spreading [275, 276].

Soletti *et al.* have developed a novel elastic poly (ester-urethane) urea (PEUU) biphasic SDBV, which incorporates a highly porous inner layer fabricated using a thermally induced phase separation techniques (TIPS), and an external, fibrous reinforcing layer deposited by electrospinning (ES) [11]. The developed grafts displayed mechanical properties similar to that of native vessels, adequate burst pressure, required suture retention strengths, and high endothelial cell seeding efficiencies using a rotational vacuum seeding method. While the TIPS method produces a highly porous graft luminal wall with an average pore size of ~ 53 μm for improved cell adhesion and expansion, the TIPS and ES scaffold fabrication techniques cannot

be applied to all materials, and are limited to select materials of high molecular weight. Therefore, the development of a biomimetic and mechanically compliant SDBV using fabrication techniques that can be applied to a wide range of materials would be beneficial in efforts to produce an ideal tissue-engineered SDBV.

In review of the previous SDBV, we set out to develop novel graft scaffolding with the following criteria in order to move research closer to clinical application: 1) Biocompatibility and biodegradability. The implanted graft should be non-toxic, illicit a minimal host inflammatory response, and slowly resorbed by the body during neo-tissue formation; 2) Mechanically compliant. The SDBV should mimic the softness and elasticity of native vasculature under dynamic pulsatile conditions; 3) Biomimetic design. An appropriate scaffold architecture should allow for the compartmentalized simultaneous seeding of endothelial and smooth muscle cells; 4) Luminal submicron topography. The graft lumen should present the necessary submicron topographies to enhance and speed complete graft endothelialization; 5) Strong mechanical strength. A graft with adequate mechanical strength should allow for immediate implantation to reduce long *in vitro* graft maturation times; and 6) Facile and easily transferable fabrication methods. The fabrication methods used to construct the SDBV should be cost-effective, simple, and easily applied to a wide variety of materials.

To test the above hypotheses, the purpose of this study is to fabricate and characterize novel CUPE multiphasic grafts, which can be constructed in a variety of architectural configurations to fit the requirements for various vascular tissue engineering applications. CUPE is a highly strong, soft, and biodegradable elastomer developed in our lab, which has shown excellent biocompatibility and hemocompatibility [10]. It is expected that a SDBV fabricated using CUPE will have adequate strength and elasticity to withstand arterial pressures, retain sutures, and be suited for immediate implantation. To impart porosity into the grafts, we chose to use particulate leaching technique, which is a simple, cost-effective scaffold fabrication method that can be applied to a wide range of biomaterials. As shown in Figure 3.16,

multiphasic grafts will be composed of the following layers to better mimic the native stratified vessel architecture: 1) A subendothelial layer will be fabricated with submicron porosity and topography to enhance graft endothelialization; 2) A submicron porous internal elastic lamina layer will be employed to provide graft strength, and prevent smooth muscle cell migration towards the graft lumen while still allowing for endothelial-smooth muscle cell communication; 3) A tunica media layer will be composed of larger pore sizes to provide a suitable extracellular matrix for smooth muscle cell expansion; and 4) A non-porous external lamina should greatly enhance graft tensile strength, suture retention, and maximum burst pressures.

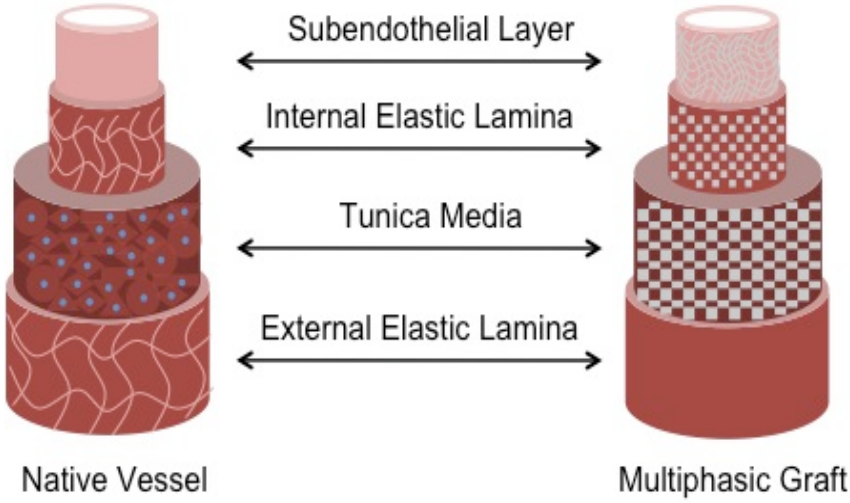

Figure 3.16 Schematic Representation of the Native Blood Vessel Anatomy and Corresponding Multiphasic Graft Components

The focus of this study is to fabricate CUPE multiphasic SDBV using different combinations of the above layers to determine the how various graft architectures affects the resulting mechanical properties, suture retention strength, and maximum burst pressures of the engineered SDBV.

3.4.2 Experimental

All chemicals, cell culture medium, and supplements were purchased from Sigma-Aldrich (St. Louis, MO, USA), unless mentioned otherwise, and used as received.

3.4.2.1 Crosslinked Urethane-doped Polyester (CUPE) Pre-Polymer Synthesis

CUPE pre-polymers were synthesized in two distinct steps similar to previously published methods [10]. The first step involves the synthesis of a poly (octanediol citrate) (POC) soft segment, which is chain extended by 1,6-hexamethyl diisocyanate (HDI) in the second polyurethane synthesis step. Briefly, a POC pre-polymer was first synthesized by reacting a 1:1.1 monomer ratio of citric acid and 1,8-octanediol, respectively, in a three-necked round bottom flask fitted with an inlet and outlet adapter at 160 °C under a constant flow of nitrogen. Once all the monomers had melted, the temperature of the system was lowered to 140 °C, and the reaction mixture was allowed to continue for 60 minutes to create the POC pre-polymer. The POC pre-polymer was then purified by drop-wise precipitation in deionized water. The undissolved pre-polymer was collected and lyophilized for 48 hours to obtain the pre-POC soft segment. In the second step, chain extension was achieved by dissolving pre-POC in 1,4-dioxane (3 wt. %), and the resulting solution was allowed to react with HDI using a molar feeding ratio of 1:1.8 POC to HDI in a clean reaction flask under constant stirring at 55 °C using stannous octoate as a catalyst (0.1 wt. %). The reaction was terminated upon the disappearance of the isocyanate peak located at 2267 cm^{-1}, which was determined by FT-IR analysis.

3.4.2.2 Biphasic SDBV Fabrication

Biphasic SDBV scaffolds were fabricated according to the method illustrated in Figure 3.17A. Briefly, 3 mm outside diameter steel rods (McMaster-Carr, Atlanta, GA, USA) were dipped once into a solution of pre-CUPE (3 wt. % in 1,4-dioxane). Before the solution could dry, the rods were coated with sodium chloride salt (average size 1-10 μm). After the salt application, the rods were coated one additional time with pre-CUPE. Following the fabrication of the inner layer, a pre-CUPE solution was mixed with sieved sodium chloride salt (99% purity) with an average pore size in the range of 150-250 μm in a (1:10) polymer to salt ratio by weight. The polymer solution was mixed thoroughly with the salt until a viscous paste was formed. The

resulting slurry was cast onto the steel rods, and then placed in a laminar flow hood overnight for solvent evaporation. Once the solvent was removed, the scaffolds were post-polymerized in an oven maintained at 80 °C for 4 days to crosslink the pre-CUPE into CUPE. Next, the salt in the tubular scaffold was leached out by immersion in deionized water for 72 hours with water changes every 12 hours. The scaffolds were removed from the steel rods by immersion in 50% ethanol. Finally, the scaffolds were lyophilized for 36 hours to remove any residual water.

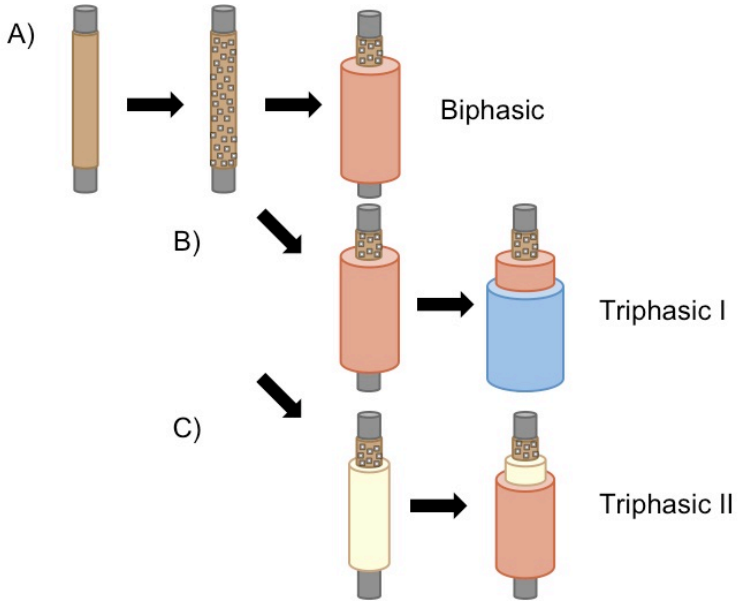

Figure 3.17 Schematic Representation of A) Biphasic, B) Triphasic I, and C) Triphasic II Graft Fabrication Process

3.4.2.3 Triphasic I SDBV Fabrication

Triphasic I SDBV scaffolds were fabricated according to the method illustrated in Figure 3.17B. Briefly, biphasic SDBV were first prepared as described above. However, a solid non-porous sheath was fabricated around the biphasic SDBV by dip-coating the scaffolds with a pre-CUPE solution (3 wt. % in 1,4-dioxane). After skin formation, the scaffolds were post-polymerized in an oven maintained at 80 °C for 4 days to crosslink the pre-CUPE into CUPE. Next, the salt in the tubular scaffold was leached out by immersion in deionized water for 72

hours with water changes every 12 hours. The scaffolds were removed from the steel rods by immersion in 50% ethanol. Finally, the scaffolds were lyophilized for 36 hours to remove any residual water.

3.4.2.4 Triphasic II SDBV Fabrication

Different variations of the triphasic scaffold design were fabricated in this study. Instead of creating a solid (non-porous) film on the outer layer of the graft, separate triphasic scaffolds were created with 3 distinct layers: 1) a microporous luminal layer (pore size < 10 μm); 2) a porous internal elastic lamina (pore size < 10 μm); and 3) a porous medial layer (pore size 150-250 μm). The triphasic II scaffolds were fabricated according to Figure 3.17C. Briefly, 3 mm outside diameter steel rods were dipped once into a solution of pre-CUPE (3 wt. % in 1,4-dioxane). Before the solution could dry, the rods were coated with sodium chloride salt (average size 1-10 μm). After the salt application, the rods were coated one additional time with pre-CUPE to form the luminal layer. Next, a pre-CUPE solution was mixed with sieved sodium chloride salt (99% purity) with an average pore size in the range of 1-10 μm in various polymer to salt ratios by weight to control the resulting porosity. The polymer solution was mixed thoroughly with the salt until a viscous paste was formed. The resulting slurry was cast onto the steel rods, and then placed in a laminar flow hood overnight for solvent evaporation to form the internal elastic lamina layer. Next, a pre-CUPE solution was mixed with sieved sodium chloride salt (99% purity) with an average pore size in the range of 150-250 μm in a 1:10 polymer to salt ratio by weight. The polymer solution was mixed thoroughly with the salt until a viscous paste was formed. The resulting slurry was cast onto the steel rods to form the porous medial layer. Finally, the scaffolds were post-polymerized in an oven maintained at 80 °C for 4 days to crosslink the pre-CUPE into CUPE. Next, the salt in the tubular scaffold was leached out by immersion in deionized water for 72 hours with water changes every 12 hours. The scaffolds were removed from the steel rods by immersion in 50% ethanol. Finally, the scaffolds were lyophilized for 36 hours to remove any residual water.

3.4.2.5 CUPE SDBV Geometry Characterization

To view the cross-sectional morphology, scaffold samples were freeze-fractured using liquid nitrogen, sputter coated with silver, and examined under a Hitachi S-3000N scanning electron microscope (SEM) (Hitachi, Pleasanton, CA, USA). Image J analysis software was used to determine the scaffold geometries. To characterize the scaffold geometries, 3 random locations were selected and a total of 30 measurements were recorded. The dimensions reported are expressed as the means ± standard deviation.

The individual sections of the scaffold porosity were measured using the Archimedes' Principle similar to previously published methods [244]. Briefly, a density bottle was used to measure the density and porosity of the scaffold using ethanol (density ρ_e) as the displacement liquid at 30 °C. The density bottle filled with ethanol was weighed (W_1). A scaffold sample of weight W_S was immersed into the density bottle, and the air trapped in the scaffold was evacuated under vacuum. Next, the density bottle was supplemented with ethanol, filled, and weighed (W_2). The ethanol-saturated scaffold was removed from the density bottle, and the density bottle was weighed (W_3). The following parameters of the scaffold were calculated: the volume of the scaffold pore (V_P), the volume of the scaffold skeleton (V_S), the density (ρ_S), and the porosity (ε). The following formulas for the volume-mass index (V_P/V_S) were used [244]:

$$V_P = (W_2 - W_3 - W_S) / \rho_e$$

$$V_S = (W_1 - W_2 + W_S) / \rho_e$$

$$\rho_S = W_S / V_S = W_S\rho_e / (W_1 - W_2 + W_S)$$

$$\varepsilon = V_P / (V_P + V_S) = (W_2 - W_3 - W_S) / (W_1 - W_3)$$

The porosity of individual scaffold layers was recorded, and the results are reported as the means ± standard deviation (n = 6).

3.4.2.6 CUPE SDBV Two-Dimensional Uniaxial Tensile Tests

Tensile mechanical testing was conducted according to ASTM D412A standard on a MTS Insight 2 fitted with a 10 N load cell (MTS, Eden Prairie, MN, USA). Briefly, scaffold strips

(10 mm length × 2 mm width) were pulled at a rate of 500 mm/minute and elongated to failure. Values were converted to stress-strain and the initial modulus was calculated from the initial gradient of the resulting curve (0-10% elongation). The results are presented as the means ± standard deviation (n = 6).

3.4.2.7 CUPE SDBV Suture Retention Tests

The suture retention strength was obtained similar to previously reported methods [245]. Briefly, one end of a scaffold sample (10 mm length × 5 mm width) was fixed with the stage clamp of the tester, and the other end was connected to the opposite clamp through the suture material (5-0 Prolene, Ethicon, Piscataway, NJ, USA). The suture was placed 2 mm from the end of the sample. The measurement was performed using a 10 N load cell, and pulled at a rate of 8 mm min^{-1} until failure. The load at rupture was recorded (N), and the results are reported as the means ± standard deviation (n = 6).

3.4.2.8 CUPE SDBV Maximum Burst Pressure Tests

Burst pressure testing was carried out on tubular scaffolds using previously described techniques [88]. Briefly, one end of the scaffold was connected to a digital pressure gauge (VWR International) and the other end was connected to a 60 mL syringe. The syringe was filled with milk of magnesia and mounted on an Infusion/Withdrawal pump (Harvard Apparatus Co, Inc. Millis, MA), which had been pre-programmed with an output rate of 0.67 mL min^{-1}. The burst pressure was recorded as the maximum pressure (mmHg) measured by the gauge before the scaffold burst, and the results are reported as the means ± standard deviation (n = 6).

3.4.2.9 Statistical Methods

Data was expressed as the means ± standard deviation. The statistical significance between two sets of data was calculated using a two-tail Student's t-test. Non-parametric one-way ANOVA tests were also performed where appropriate. Data was taken to be significant when a $p < 0.05$ was obtained.

3.4.3 Results and Discussion

The mechanical and microarchitectural characteristics of a tissue-engineered SDBV have been shown to be important factors in controlling the phenotype of seeded cells, neotissue formation, and overall tissue organization. In the present study, we have fabricated novel elastic and biomimetic multiphasic SDBV using a simple and cost-effective sodium chloride particulate leaching technique, and evaluated the affects of the scaffold architecture on the resulting mechanical properties for blood vessel tissue engineering. CUPE was chosen as a platform biomaterial for graft fabrication due to the material's previously reported high strength, elasticity, and softness while maintaining a biocompatible and hemocompatible nature [10]. The use of CUPE should maintain graft strength upon pore introduction and reduce compliance mismatch between the graft and host vessel, which is a biomechanical problem that has been well documented as a factor of graft failure [88].

In response to the biomimetic microarchitectural requirements for vascular tissue engineering, it is hypothesized that recreating the native tissue architecture at the macro-, micro-, and nano- scales can facilitate cell and extracellular matrix compartmentalization to engineer a more native-like and functional vessel for *in vivo* tissue engineering [277]. For vascular graft design, it is important that the engineered graft contain microporous luminal topographies to promote rapid endothelialization while simultaneously functioning as a barrier for smooth muscle cell migration into the graft lumen. In order to better recreate the heterogeneous layered architecture of native vessels, we have proposed the fabrication of novel biphasic and triphasic small diameter grafts using a layer-by-layer approach. Biphasic SDBV grafts with two distinct layers 1) a microporous subendothelial layer to promote graft endothelialization (<10 μm pore size) and 2) a porous medial layer (150-250 μm pore size) for smooth muscle and fibroblast cell proliferation. Figure 3.18A shows the SEM images of CUPE biphasic scaffolds to reveal the overall cross-section of the biphasic graft to reveal the inner luminal microporosity of the subendothelial layer required for endothelialization, and the outer

layer composed of larger pores for smooth muscle and fibroblast cell expansion. Pore characterization studies show that the average pore size and porosity of the subendothelial layer were measured as 8.80 ± 2.88 μm and 57.55 ± 3.92%, respectively. The overall pore size and porosity for the outer phase were measured as 210.45 ± 27.45 μm and 88.01 ± 1.36%, respectively (**Table 3.2**).

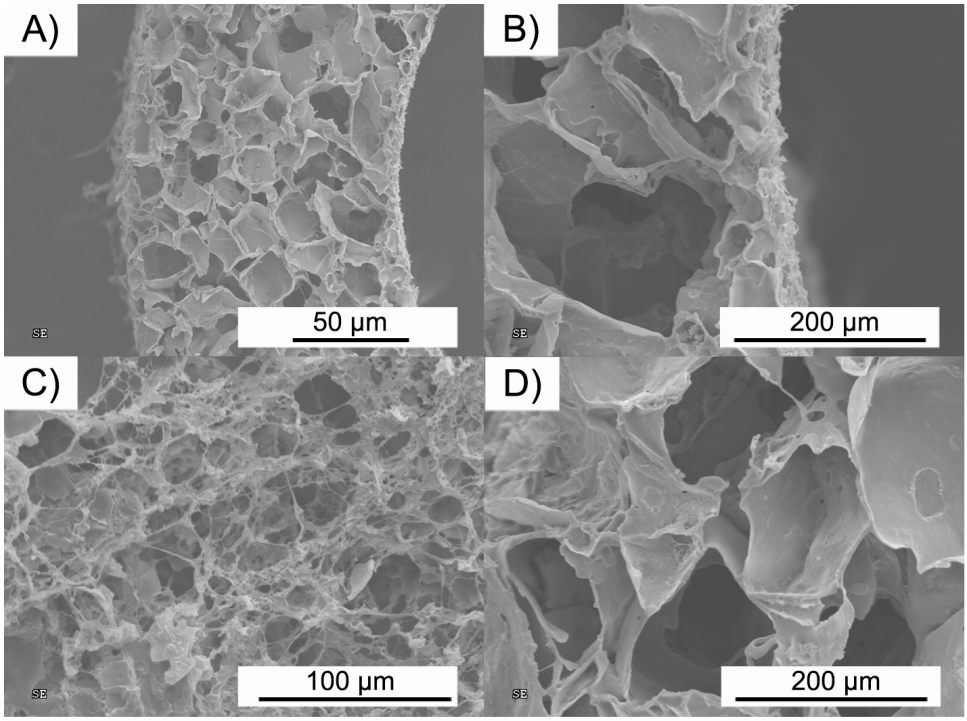

Figure 3.18 SEM Images of Biphasic Graft A) Overall cross section, B) Subendothelial layer interface, C) Luminal microporous topography, and D) Tunica media layer

Table 3.2 Average Pore Size and Porosity Measurements of Individual Graft Layers

Layer Name	**Average Pore Size (μm)**	**Average Porosity (%)**
Subendothelial	8.80 ± 2.88	57.55 ± 3.92
Tunica Media	210.45 ± 27.45	88.01 ± 1.36
Internal Elastic Lamina – 90	5.48 ± 2.02	86.46 ± 3.04
Internal Elastic Lamina – 75	7.16 ± 1.76	73.84 ± 1.06
Internal Elastic Lamina – 50	9.47 ± 3.32	56.43 ± 2.31

Figure 3.18B shows the seamless boundary interface of the two phases connected through the post-polymerization fabrication step, which can potentially allow for the necessary

endothelial-smooth muscle cell communication. Figure 3.18C shows the inside lumen of the biphasic grafts, which reveal the microporous topography of the biphasic scaffold. The failure of previously developed vascular grafts has been correlated with the lack of a functional endothelial luminal layer resulting in graft thrombosis and neointimal hyperplasia [223]. The microporous topography of the luminal layer created using the this type of fabrication methods will provide the contact guidance surface cues necessary for endothelial cell density, adhesion, and proliferation while preventing smooth muscle cell infiltration from the medial layer. Previous attempts to create this type of topography have primarily relied on the use of TIPS or electrospinning technologies [11, 278], which are limited in regards to specific biomaterials. We believe that a small diameter vascular graft created with this type of architecture will better mimic the native vessel architecture for improved function.

Table 3.3 Uniaxial Tensile Mechanical Properties of Multiphasic Grafts

Graft Name	Peak Stress (MPa)	Initial Modulus (MPa)	Elongation at Break (%)
Biphasic	0.81 ± 0.12	0.51 ± 0.13	155.64 ± 14.13
Triphasic I	2.73 ± 0.38	2.94 ± 0.51	338.41 ± 15.69
Triphasic II	1.36 ± 0.12	0.81 ± 0.13	264.54 ± 41.39

The results from the uniaxial tensile mechanical tests of the CUPE biphasic grafts are shown in Table 3.3. The recorded peak stress, modulus, and elongation at break for CUPE biphasic grafts was 0.81 ± 0.12 MPa, 0.51 ± 0.13 MPa, and 155.64 ± 14.13%, respectively. The burst pressure and suture retention strength is a crucial factor in the fabrication of tissue engineering scaffolds as it directly relates to the success of the construct during the implantation process. As shown in Figure 3.19A and B, a maximum burst pressure of 160.75 ± 42.45 mmHg and suture retention of 0.30 ± 0.09 N was obtained for CUPE biphasic grafts. Although these values of ultimate tensile strength, burst pressure, and suture retention do not meet the requirements for small diameter vascular graft tissue engineering, the thickness of the distinctive phases of the grafts using this technique can be controlled to modify the mechanical properties. For example, increasing the thickness of the luminal layer can potentially be a

means to increase the mechanical properties of the resulting graft. These grafts also show great potential in that the separate phases can be individually seeded and cultured *in vitro*. As cells proliferate throughout the construct, the deposited ECM can provide additional mechanical support.

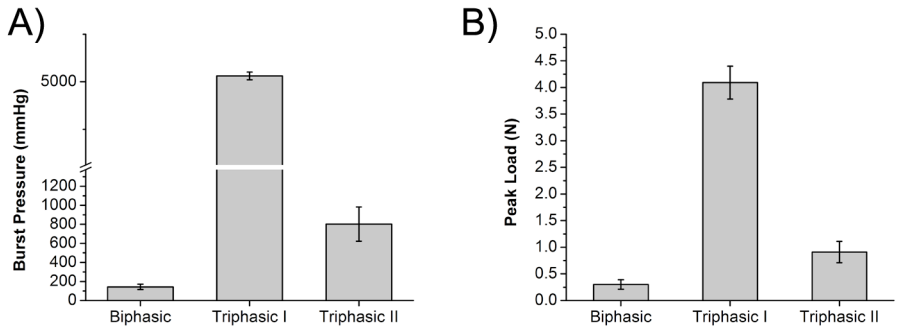

Figure 3.19 Mechanical Properties of Multiphasic Grafts A) Maximum burst pressure and B) Suture retention strength

To improve the mechanical properties of the biphasic design and better meet the requirements for an off-the-shelf graft replacement, novel triphasic scaffolds were fabricated based upon the biphasic design. In addition to the inner luminal microporosity and larger medial porosity, a third non-porous skin has been introduced to confer mechanical strength to the small diameter vascular graft for the strict requirements for *in vivo* tissue engineering. As shown in Figure 3.20, we have constructed triphasic small diameter vascular grafts with three distinct layers 1) a microporous subendothelial luminal layer (<10 μm pore size) for endothelialization, 2) a porous medial layer (150-250 μm pore size) for smooth muscle and fibroblast cell proliferation, and 3) an adventitial solid nonporous film layer for enhanced mechanical strength. Figure 3.20 shows the overall cross-section of the triphasic graft to reveal the inner luminal microporosity required for endothelialization, the medial layer composed of larger pores for smooth muscle and fibroblast cells, and the outer non-porous film for mechanical strength.

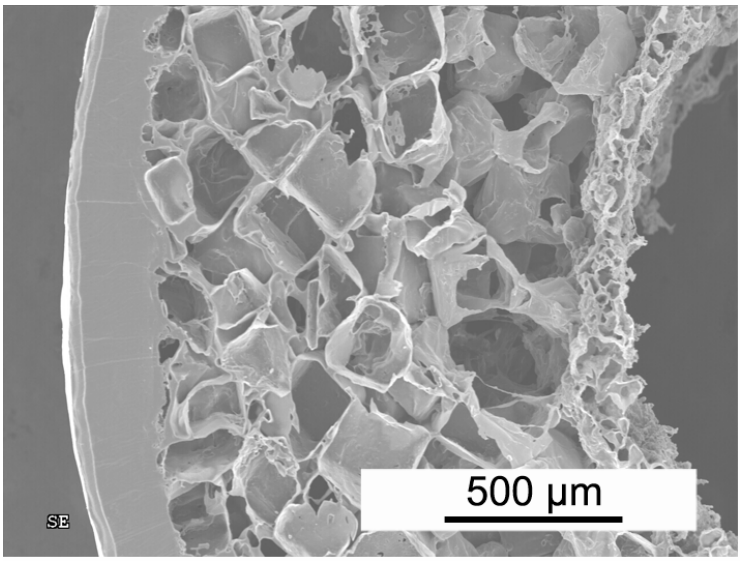

Figure 3.20 SEM Image of Triphasic I Graft Cross-Section

The SEM image shows that the layer-by-layer approach followed by polymer post-polymerization results in a graft containing seamless boundaries between each distinct phase. The results from the uniaxial mechanical tests for CUPE triphasic grafts show a significant increase in the peak stress and initial modulus (**Table 3.3**) when compared to the biphasic design. A maximum peak stress of 2.73 ± 0.38 with a corresponding elongation at break of 338.41 ± 15.69% was recorded for CUPE triphasic I grafts, which meets the elasticity and elongation of native vessels [193]. A similar trend in the burst pressure and suture retention was seen when comparing the triphasic design to the biphasic design. The addition of the non-porous film layer greatly contributes to the mechanical properties of the triphasic graft. As shown in Figures 3.19A and 3.19B, the maximum burst pressure and suture retention strength were as high as 1142.25 ± 218.33 mmHg and 1.59 ± 0.11 N, which is close to the surgical requirements for vascular tissue engineering [194]. The triphasic design provides a fabrication method to produce unique small diameter grafts, whose mechanical properties can meet the requirements of *in vivo* tissue engineering. In the case of *in vivo* tissue engineering, the elastomeric nature of the CUPE scaffolds can permit the transmission of dynamic mechanical

stimuli exerted by the cardiovascular system. Thus, the triphasic design can be immediately implanted as a vascular graft without the long *in vitro* culture times necessary for previous designs.

We have also fabricated different versions of the triphasic graft design for *in vivo* tissue engineering. Although the solid non-porous outer film of the above triphasic I design can significantly increase mechanical strength, suture retention strength, and burst pressure values, cell migration and infiltration of microvasculature to the graft may be hindered by the presence of a solid film. To address this issue, we have designed alternative triphasic II grafts without a solid non-porous outer film. To compensate for added strength which this solid non-porous phase provides, we have extended the luminal microporous layer thickness to ~200 μm in thickness based on the biphasic graft design (**Figure 3.21**), and have tuned the strength of the resulting grafts through the porosity of this new internal elastic lamina layer. We believe this scaffold design will provide the added strength necessary for *in vivo* tissue engineering, while allowing for cell infiltration through chemotaxis approaches.

Figure 3.21 shows the SEM images of CUPE triphasic scaffolds created using the porogen leaching layer-by-layer approach. The overall cross-section of the triphasic II graft reveals the inner luminal microporosity required for graft endothelialization, the internal elastic lamina layer for added graft strength, and the medial layer composed of larger pores for smooth muscle and fibroblast cells. The additional internal elastic lamina layer can provide the additional strength necessary for *in vivo* tissue engineering, while still allowing for cell communication between endothelial cells in the luminal layer and the smooth muscle/fibroblast cells in the medial layer. We have chosen to keep the pore size under 10 μm in this phase to prevent smooth muscle cell infiltration to the inside of the graft. Additionally, we have chosen a maximum internal elastic lamina thickness of ~200 μm as this is the maximum diffusion rate of oxygen [216, 246]. As shown in Figure 3.21B, C, and D, we have controlled the porosity of the

internal elastic lamina at 90, 75, and 50% porosity, respectively, to tune the SDBV mechanical properties.

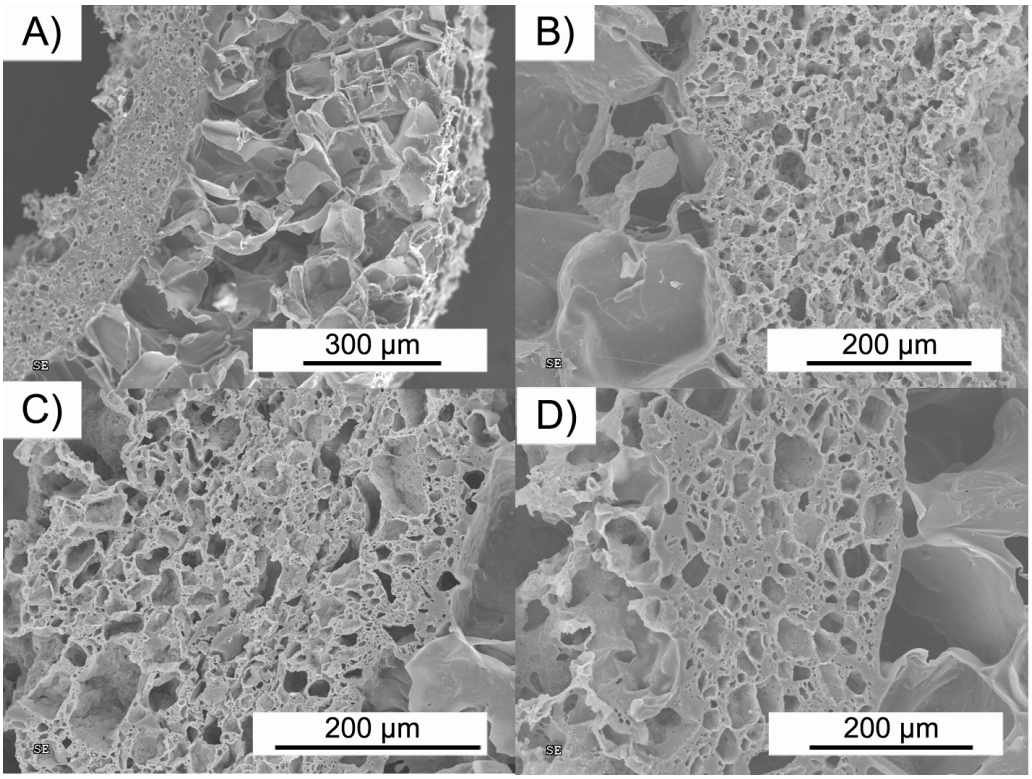

Figure 3.21 SEM Images of Triphasic II Grafts A) Overall cross-section, B) 90% porous, C) 75% porous, and D) 50% porous internal elastic lamina

As shown in Table 3.3, the addition of an internal elastic lamina layer can greatly increase graft mechanical strength over the previous biphasic design while maintaining a porous outer architecture for cell recruitment. By controlling the overall porosity of the internal elastic lamina through the polymer: salt ratios, an increase in burst pressure and suture retention strength was observed as the porosity of the internal elastic lamina was decreased (**Figure 3.22**). While triphasic II SDBV with internal elastic lamina of 90% porosity did not meet the surgical requirements for *in vivo* tissue engineering, grafts constructed with 75 and 50% porosities met and exceeded the reported benchmarks for burst pressure and suture retention strengths.

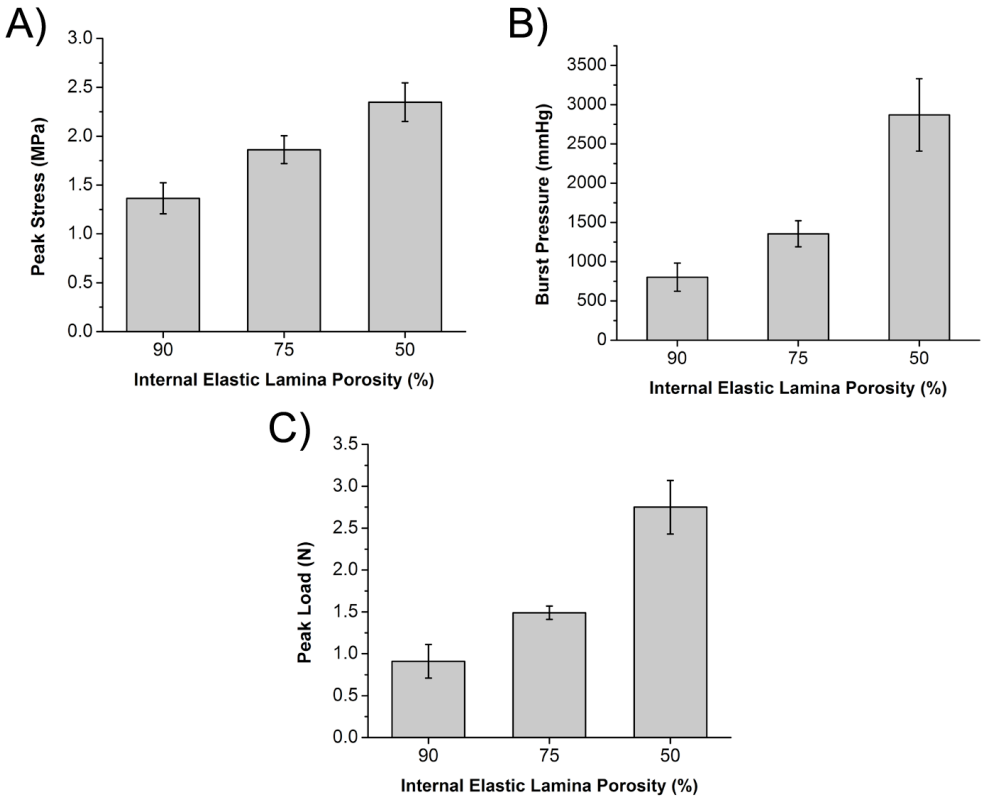

Figure 3.22 Triphasic II Graft Mechanical Properties A) Tensile peak stress, B) Maximum burst pressure, and C) Suture retention strength

This scaffold fabrication method opens a way to fabricate complex heterogeneous porous scaffolds with different porosities and pore sizes amongst each layer while maintaining a porous interface to accommodate for specific cell types in the regeneration of multi-cellular tissues such as skin, blood vessels, liver, pancreas, and cartilage where the compartmentalization of different cell types is necessary [174-176]. Another advantage in the CUPE multiphasic design is that the mechanical properties can be controlled through a variety of options such as the post-polymerization condition, pre-polymer chemistry, and the thickness of the individual phases.

3.4.4 Conclusion

In conclusion, a novel library of multiphasic SDBV scaffolds consisting of microporous luminal topography were fabricated using particulate leaching techniques and evaluated

mechanically for potential use in vascular tissue engineering. The scaffolds were made from CUPE, a new type of strong, soft, and hemocompatible biodegradable polyester elastomer. These studies represent the first step toward the investigation of the role of scaffold architecture on the resulting tensile, suture retention, and burst pressure strengths. The multiphasic scaffolds could potentially be used to implement co-culture of smooth muscle cells and endothelial cells *in vitro*, thereby shortening culture time and reducing the risk of contamination. If the scaffold design is implemented for *in vivo* tissue engineering, it could potentially reduce the negative side effects associated with compliance mismatch between a graft and the host vessel, thereby improving long-term patency.

3.5 Multichanneled Nerve Guides

3.5.1 Introduction

Peripheral nerve injury remains a difficult and challenging problem in reconstructive surgery [279]. When the nerve defect or "gap" size is smaller than a few millimeters, the damaged proximal axonal stump is able to regenerate axonal sprouts towards the distal segment to re-establish motor and sensory function [280]. However, this form of neural regeneration does not always result in full functional recovery due to misdirection of the regenerating axons or inappropriate target reinnervation [281]. Surgical interventions such as end-to-end suture repair is the preferred option for small gap sizes, but cannot be performed in areas which may cause high tension [282]. To complicate matters, without the presence of specific guidance, nerve ends separated by a gap size greater than 1 cm in length generally result in the backwards growth of axons into the proximal nerve stump forming neuromas [283]. Therefore, for large gap sizes or in cases where tension-free suture repair is not possible, a nerve bridge is required to reconnect the two nerve stumps. To increase the prospects of axonal regeneration and functional recovery, the current clinical "gold standard" for large gap repair involves the use of nerve autografts, which rely on the premise that viable Schwann cells (SC) located in the basal lamina tubes release a synergistic combination of growth factors and cell

adhesion molecules to support and direct oriented axonal regeneration [284, 285]. Unfortunately, autologous grafting is frequently associated with limitations including the need for multiple surgeries, donor site morbidity, distal donor site denervation, neuroma formation, and the limited availability of suitable grafts for harvesting [286]. To address the aforementioned limitations, several laboratories are actively pursuing the development of synthetic alternatives to replace nerve autografts in bridging the gap between transected nerve ends.

Tissue engineering is a multidisciplinary field, which holds great potential for creating viable tissue constructs to replace defective or diseased tissues and organs. Tissue engineered nerve guides (TENG) are a promising option for large gap nerve repair in that they can provide a biodegradable conduit for the delivery of therapeutic cell types, mechanical support, and chemical stimulation for axonal growth and nerve regeneration [287, 288]. A variety of materials such as collagen [289], poly (L-lactide) [290], polyamide [291], poly (phosphoesters) [292], and poly (ethylene) [293] have been used with numerous processing strategies including thermally induced phase separation and injection molding [294] techniques to fabricate synthetic alternatives to bridge neural defects. Due to the ease of manufacturing, many of the previous TENG designs have been predominantly based upon the entubulation model, where the proximal and distal stumps of the damaged nerve are inserted into either end of a porous foam rod or hollow tube to induce fibrin matrix production in an oriented direction [295, 296]. Unfortunately, the use of a single hollow conduit is not optimal for nerve regeneration due to the limited available surface area for cell seeding/proliferation, lack of internal support to resist conduit collapse from the constriction caused by scar tissue formation, and the inability to recreate the proper native spatial arrangement of cells and extracellular matrix within the conduit [297].

As many of the tissues are highly oriented in architecture and require the appropriate cellular alignment along one or more axes for optimal function, the ideal TENG should provide a suitable environment to promote direction oriented neuronal growth to create the necessary cell

alignment crucial for nerve regeneration and signal transmission [298]. Recent years have witnessed the development of TENG with increasingly sophisticated and intricate internal structures based upon mechanisms of contact guidance and basement membrane microtube theory for nerve regeneration, which hypothesize that axon elongation requires guidance by contact with the appropriate substrate through topographical control [299, 300]. By creating longitudinally oriented channels to fill the interior of the conduit, novel TENG have been produced to support the systems' natural pattern of growth [286]. The multichanneled designs are advantageous in that they provide better nerve target reinnervation, a greater surface area for cell growth, the topography necessary to direct the growth of regenerating nerve fibers (Bands of Büngner), and internal support to prevent against conduit collapse [281, 286-288, 301, 302].

In review of the previous TENG, we set out to develop a novel nerve guide scaffold with the following criteria in order to move research closer to clinical application: 1) Biocompatibility and biodegradability. The implanted guide should be non-toxic, illicit a minimal host inflammatory response, and slowly resorbed by the body during neo-tissue formation; 2) Mechanically compliant. The TENG should mimic the softness and elasticity of native tissue under dynamic conditions; 3) Biomimetic design. An appropriate scaffold architecture should allow for increased surface area for adequate cell densities while promoting cellular alignment along the length of the guide; 4) Nutrient exchange. The engineered nerve guide should facilitate the exchange of metabolites and nutrients through a porous and interconnected structure; and 5) Facile and easily transferable fabrication methods. The fabrication methods used to construct the TENG should be cost-effective, simple, and easily applied to a wide variety of materials.

To test the above hypotheses, the purpose of this study is to fabricate and characterize novel crosslinked urethane-doped polyester (CUPE) multichanneled TENG to meet the limitations of the previous designs. CUPE is a highly strong, soft, and biodegradable elastomer

developed in our lab, which has shown excellent biocompatibility and hemocompatibility [10]. It is expected that a TENG fabricated using CUPE will have adequate strength and elasticity to withstand tension, retain sutures, and be suited for immediate implantation. In order to better recreate the native parallel channels of nerve basal lamina tubes, we have proposed the fabrication of novel porous multichanneled nerve guides (**Figure 3.23**) with the following advantages over previous designs: 1) To impart porosity into the grafts, we chose to use particulate leaching technique, which is a simple, cost-effective scaffold fabrication method that can be applied to a wide range of biomaterials; 2) The parallel multichannel design can better mimic the native architecture of nerve basal lamina tubes and promote nerve cell alignment through contact guidance; 3) The introduction of microporosity (<10 μm) between the channels can minimize fibrous tissue infiltration, increase permeability for cell-to-cell communication, and limit cell dispersion to enhance nerve target reinnervation; and 4) The outer sheath of the nerve guide conduit can provide the necessary mechanical strength for surgical implantation. The fabricated scaffolds were thoroughly characterized for their resulting geometries, mechanical strength, and in vivo performance.

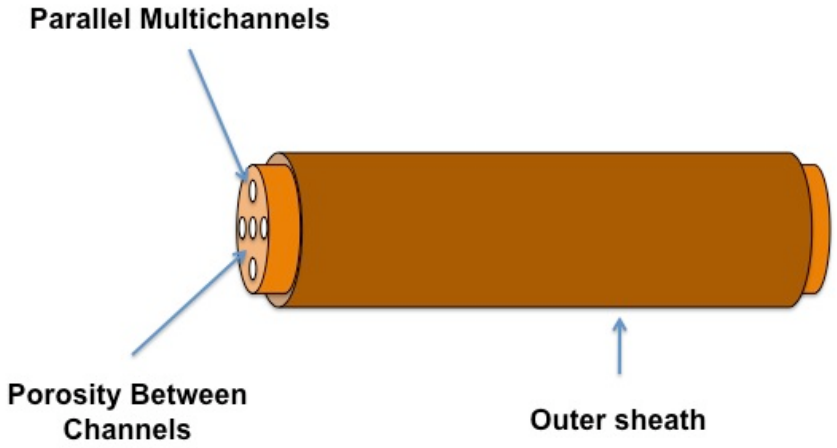

Figure 3.23 Schematic Representation of Multichanneled Nerve Guides

3.5.2 Experimental

All chemicals, cell culture medium, and supplements were purchased from Sigma-Aldrich (St. Louis, MO, USA), unless mentioned otherwise, and used as received.

3.5.2.1 Crosslinked Urethane-doped Polyester (CUPE) Pre-Polymer Synthesis

CUPE pre-polymers were synthesized in two distinct steps similar to previously published methods [10]. The first step involves the synthesis of a poly (octanediol citrate) (POC) soft segment, which is chain extended by 1,6-hexamethyl diisocyanate (HDI) in the second polyurethane synthesis step. Briefly, a POC pre-polymer was first synthesized by reacting a 1:1.1 monomer ratio of citric acid and 1,8-octanediol, respectively, in a three-necked round bottom flask fitted with an inlet and outlet adapter at 160 °C under a constant flow of nitrogen. Once all the monomers had melted, the temperature of the system was lowered to 140 °C, and the reaction mixture was allowed to continue for 60 minutes to create the POC pre-polymer. The POC pre-polymer was then purified by drop-wise precipitation in deionized water. The undissolved pre-polymer was collected and lyophilized for 48 hours to obtain the pre-POC soft segment. In the second step, chain extension was achieved by dissolving pre-POC in 1,4-dioxane (3 wt. %), and the resulting solution was allowed to react with HDI using a molar feeding ratio of 1:1.8 POC to HDI in a clean reaction flask under constant stirring at 55°C using stannous octoate as a catalyst (0.1 wt. %). The reaction was terminated upon the disappearance of the isocyanate peak located at 2267 cm^{-1}, which was determined by FT-IR analysis.

3.5.2.2 Multichanneled Nerve Guide Fabrication

Multichanneled nerve guide scaffolds were fabricated according to the method illustrated in Figure 3.23. Briefly, nerve guide molds (**Figure 3.24A**) were made with 127-µm thick titanium shims by a programmable 355-nm 5-W *Oxford* laser micro-machining system. The design was sketched by *Alphacam* software and translated into a *G-code* program. A layer of

photoresist was coated on the titanium piece before machining to protect the samples. After cutting was done, the molds were cleaned by acetone to remove the photoresist and debris.

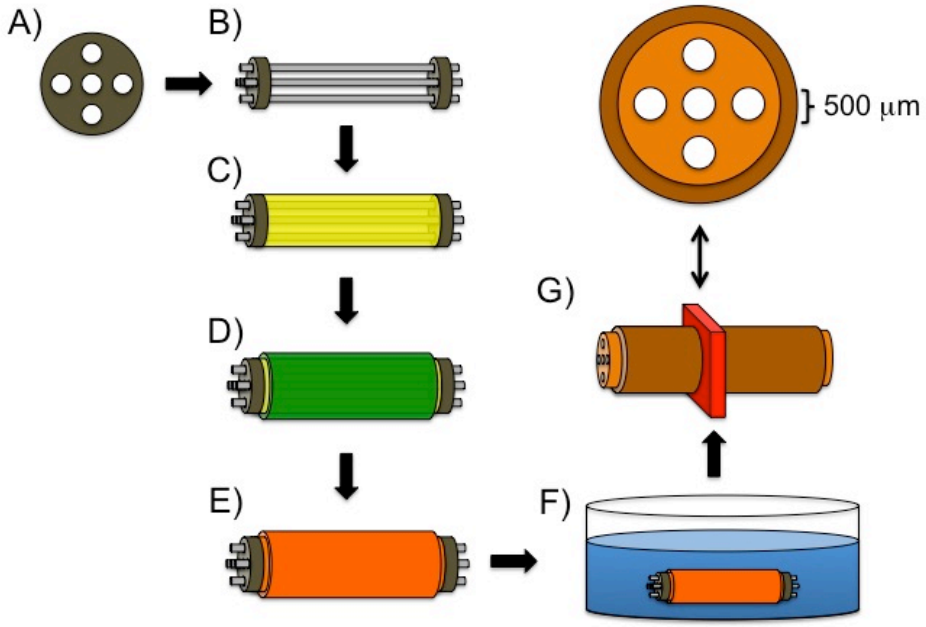

Figure 3.24 Schematic Representation of Multichanneled Nerve Guide Fabrication Process A) Microengineered titanium shim, B) Insertion of acupuncture needles, C) Application of pre-CUPE/NaCl mixture, D) Formation of outer skin, E) Guide crosslinking, F) Removal of NaCl in deionized water, and G) Representative cross-section

Next, combinations of five 500 μm steel acupuncture needles (Lhasa Oms Inc., Weymouth, MA) were inserted through two-titanium nerve guide molds (**Figure 3.24B**). Following the insertion of the acupuncture needles, a pre-CUPE solution was mixed with nucleated sodium chloride salt (99% purity) with an average pore size in the range of 1-10 μm in a (1:5) polymer to salt ratio by weight. The polymer solution was mixed thoroughly with the salt until a viscous paste was formed. The resulting slurry was cast onto the acupuncture needles (**Figure 3.24C**), and then placed in a laminar flow hood overnight for solvent evaporation. Following solvent evaporation, the scaffolds were dip-coated again with pre-CUPE to form an outer non-porous polymer skin (**Figure 3.24D**). Finally, the scaffolds were post-polymerized in an oven maintained at 80°C for predetermined times to crosslink the pre-CUPE into CUPE (**Figure 3.24E**). Next, the salt in the

tubular scaffold was leached out by immersion in deionized water for 72 hours with water changes every 12 hours (**Figure 3.24F**). The scaffolds were removed from the acupuncture needles by immersion in 50% ethanol. Finally, the scaffolds were lyophilized for 36 hours to remove any residual water.

3.5.2.3 Multichanneled Nerve Guide Geometry Characterization

To view the cross-sectional morphology, scaffold samples were freeze-fractured using liquid nitrogen, sputter coated with silver, and examined under a Hitachi S-3000N scanning electron microscope (SEM) (Hitachi, Pleasanton, CA, USA). Image J analysis software was used to determine the scaffold geometries. To characterize the scaffold geometries, 3 random locations were selected and a total of 30 measurements were recorded. The dimensions reported are expressed as the means ± standard deviation.

The individual sections of the scaffold porosity were measured using the Archimedes' Principle similar to previously published methods [244]. Briefly, a density bottle was used to measure the density and porosity of the scaffold using ethanol (density ρ_e) as the displacement liquid at 30 °C. The density bottle filled with ethanol was weighed (W_1). A scaffold sample of weight W_S was immersed into the density bottle, and the air trapped in the scaffold was evacuated under vacuum. Next, the density bottle was supplemented with ethanol, filled, and weighed (W_2). The ethanol-saturated scaffold was removed from the density bottle, and the density bottle was weighed (W_3). The following parameters of the scaffold were calculated: the volume of the scaffold pore (V_P), the volume of the scaffold skeleton (V_S), the density (ρ_S), and the porosity (ε). The following formulas for the volume-mass index (V_P/V_S) were used [244]:

$$V_P = (W_2 - W_3 - W_S) / \rho_e$$

$$V_S = (W_1 - W_2 + W_S) / \rho_e$$

$$\rho_S = W_S / V_S = W_S\rho_e / (W_1 - W_2 + W_S)$$

$$\varepsilon = V_P / (V_P + V_S) = (W_2 - W_3 - W_S) / (W_1 - W_3)$$

The porosity of individual scaffold layers was recorded, and the results are reported as the means ± standard deviation (n = 6).

3.5.2.4 Multichanneled Nerve Guide Two-Dimensional Uniaxial Tensile Tests

Tensile mechanical testing was conducted according to ASTM D412A standard on a MTS Insight 2 fitted with a 10 N load cell (MTS, Eden Prairie, MN, USA). Briefly, complete multichanneled nerve guides (10 mm length) were pulled at a rate of 500 mm min^{-1} and elongated to failure. Values were converted to stress-strain and the initial modulus was calculated from the initial gradient of the resulting curve (0-10% elongation). The results are presented as the means ± standard deviation (n = 6).

3.4.2.7 Multichanneled Nerve Guide Suture Retention Tests

The suture retention strength was obtained similar to previously reported methods [245]. Briefly, one end of a scaffold sample (10 mm length × 5 mm width) was fixed with the stage clamp of the tester, and the other end was connected to the opposite clamp through the suture material (5-0 Prolene, Ethicon, Piscataway, NJ, USA). The suture was placed 2 mm from the end of the sample. The measurement was performed using a 10 N load cell, and pulled at a rate of 8 mm min^{-1} until failure. The load at rupture was recorded (N), and the results are reported as the means ± standard deviation (n = 6).

3.5.2.5 Multichanneled Nerve Guide In Vivo Evaluation

To evaluate the CUPE multichanneled TENG *in vivo*, Lewis rats (3 months old; 300-350 g in weight) were used as the animal model. The rates were housed in the Laboratory Animal Unit (LAU) (The University of Hong Kong) with 12-hour light/dark cycle, and freely accessible food and water. The University Ethics Committee, The University of Hong Kong, and the Licensing Office, The Department of Health of Hong Kong reviewed and approved all the protocols in this study. All rats were randomized for four studies. Animals were anesthetized 30 minutes before the operation by a mixture of Ketamine (20 mg kg^{-1}) and Xylazine (2 mg kg^{-1}) in a 2:1 ratio through intra-muscular injection. Temgesic (0.05 mg kg^{-1}) and Terramycin (60 mg kg^{-}

^{1}) were also injected subcutaneously to relief any pain caused. The operation sites were located on the right side of hind legs, which were shaved and disinfected with 0.5% chlorhexidine. An incision was made from the rat's midline to the tibiofemoral articulation. The sciatic nerve from the right hind leg was dissected free from the surrounding tissues. After the right sciatic nerve was exposed, a one centimeter long nerve was transacted and followed by an immediate replacement of the following grafts: 1) CUPE multichanneled TENG (CUPE – S), 2) PCL hollow tube (PCL Tube) as a control, and 4) Nerve autograft, which was reversed 180°C and implanted. Following the surgical procedure, the wound was sutured and dressed by marcaine block. After the operation, a three-day course of Ketoprofen (5 mg kg^{-1}) and Temgesic (0.05 mg kg^{-1}) were injected subcutaneously for pain relief. The rats also received 1 mg kg^{-1} terramycin (anti-biotics) for four days post-operation.

3.4.2.9 Histological Analysis

After eight weeks post-operation, the rats were euthanized by an overdose sodium pentobarbital solution. The sciatic nerves from the operated side were harvested and were separated into five sections as 1) proximal nerve, 2) proximal conduit, 3) central conduit, 4) distal conduit and 5) distal nerve. The nerves were fixed in 4% parafomaldehyde overnight followed by a series of tissue process for histology, and embedded in paraffin. Semi-thin sections (7 μm) of nerve explants were sectioned and then stained with 0.05% Toluidine blue and H&E separately. Finally, the morphology of samples was investigated under light microscopy. For each sample, six random areas from five cross-sections were evaluated. The population, density and diameter of myelinated fibers were analyzed at 100x magnification.

3.4.2.10 Statistical Methods

Data was expressed as the means ± standard deviation. The statistical significance between two sets of data was calculated using a two-tail Student's t-test. Non-parametric one-way ANOVA tests were also performed where appropriate. Data was taken to be significant when a $p < 0.05$ was obtained.

3.5.3 Results and Discussion

Despite significant advancements in the development of sophisticated tissue engineering scaffolding, the current clinical gold standard for peripheral nerve repair has not changed for over 30 years [280]. To date, no other repair strategy has been able to offer the numerous advantages autologous nerve grafts provide. Although a variety materials and scaffold fabrication methods have been investigated as potential autologous nerve graft replacements, the use of a single hollow tube as a TENG has shown limited success. Recent research has indicated that the mechanical and microarchitectural characteristics of a TENG have been shown to be important factors in controlling the orientation seeded cells, neotissue formation, and overall tissue organization/architecture. In response to the biomimetic microarchitectural requirements for nerve regeneration, it is hypothesized that recreating the native tissue architecture at the macro-, micro-, and nano- scales can facilitate cell and extracellular matrix compartmentalization to engineer a more native-like and functional nerve. For TENG design, it is important that the engineered conduit contain an array of longitudinally oriented parallel microchannels to replicate the native basal lamina. Through the use of parallel multichanneled TENG, an improvement in nerve target reinnervation, surface area for cell growth, the topography necessary to direct the growth of regenerating nerve fibers was seen while providing the necessary internal support to prevent against conduit collapse.

In the present study, we have fabricated novel elastic and biomimetic multichanneled TENG using a simple and cost-effective sodium chloride particulate leaching technique in combination with micro-engineering approaches, and evaluated the resulting scaffold architecture, mechanical properties, and in vivo performance for neural tissue engineering. CUPE was chosen as a platform biomaterial for guide fabrication due to the material's previously reported high strength, elasticity, and softness while maintaining a biocompatible and hemocompatible nature [10]. The use of CUPE should maintain guide strength upon pore introduction and reduce compliance mismatch between the graft and host vessel, which is a

biomechanical problem that has been well documented as a factor of implant failure [88]. In order to better recreate the micro-tubular architecture of autologous nerves, we have proposed the fabrication of novel TENG using a micro-engineering approach. Using computer-aided design, titanium shims 2.55 ± 0.05 mm in diameter with 5 micro-machined holes of 539.38 ± 8.57 μm were created (**Figure 3.25A and B**), and used as a mold for the location and dimensions of the longitudinally oriented channels. Figures 3.25C and D show representative SEM images to reveal the uniformity of the overall size, location, and diameter of each individual hole.

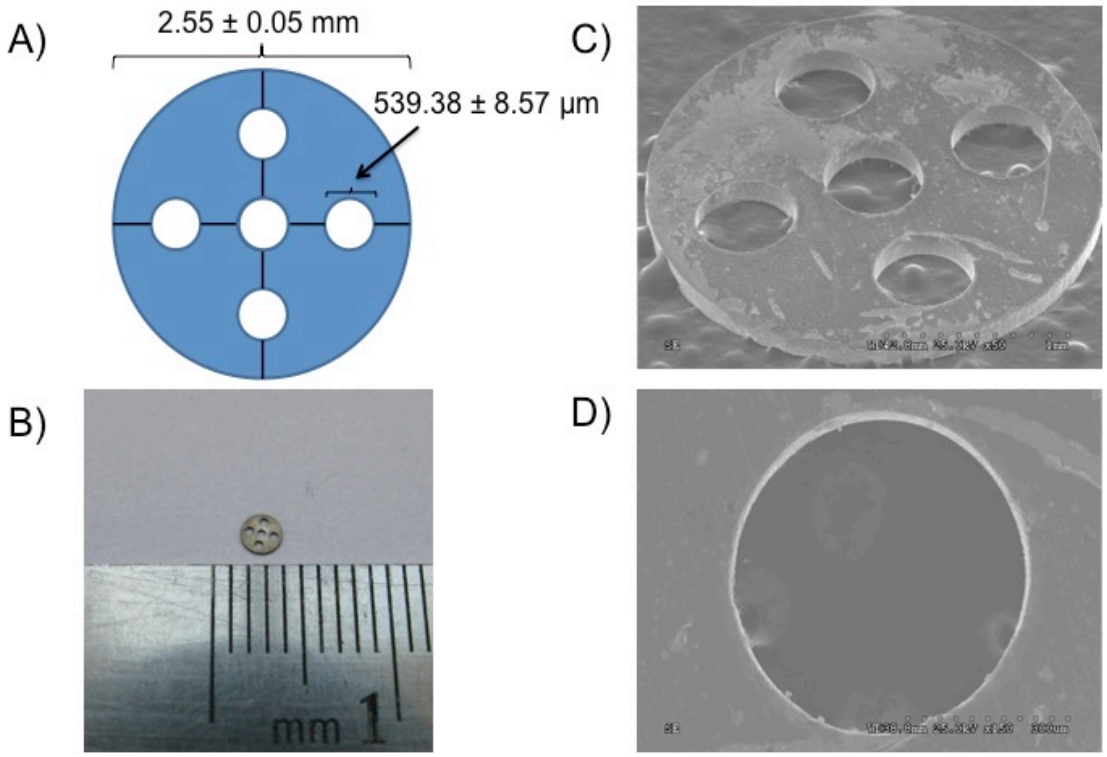

Figure 3.25 Titanium Mold Characterization A) Design, B) Photograph, C) Overall SEM image, and D) SEM image of single hole

After mold fabrication, steel acupuncture needles were then inserted through the machined holes, and secured by 2 titanium molds. Acupuncture needles were chosen to form the channels due wide availability of various diameters, high corrosion resistance, and cleanliness [280]. The acupuncture needles, which served as a mandrel to define the longitudinally aligned

microchannels, are commercially available, and can be purchased with diameters ranging from 140 to 500 μm. One major advantage of this approach is that the number, diameter, and distribution of the channels can be finely controlled through computer-aided design to produce novel TENG in accordance with the parameters of a particular application.

Macroscopic image in Figure 3.26A reveal, that the acupuncture needle length determined the resulting guide length, with a majority of the commercially available needles a minimum of 4 cm in length. The cross-sectional geometry of the TENG scaffolds was circular with slight irregularities in the porous phase of the guide (**Figure 3.26B**). Figures 3.26C and D, show the elastic nature of the CUPE TENG, as bending over 180° and applied force with multiple angles did not result in guide kinks, which could be detrimental in implantation sites with large amounts of movement.

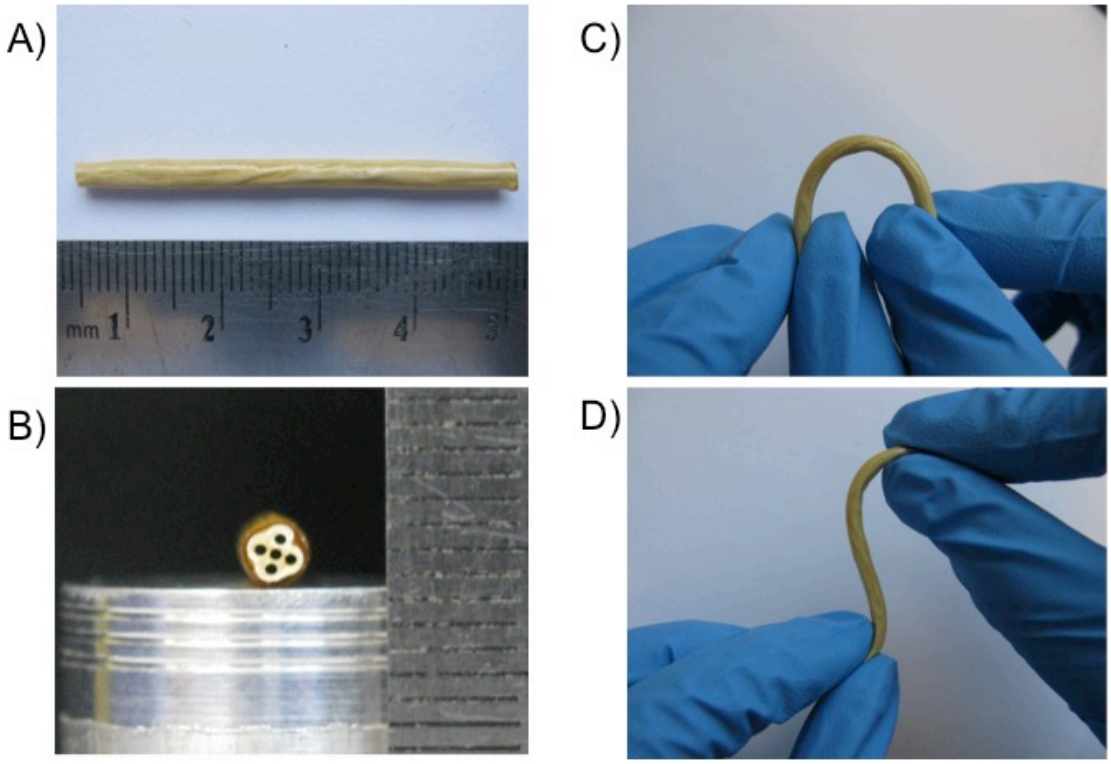

Figure 3.26 CUPE Multichanneled Nerve Guide Photographs A) Entire guide, B) 180° bend, C) Cross-section, and D) Multidirectional bend

Sequential slices throughout the length of the CUPE TENG showed the ability of the acupuncture needles to retain a well-defined parallel orientation of each channel throughout the length of the guide. Cross-sections throughout the length of the guide had almost the same transverse morphology to indicate a continuous microchanneled design.

Representative SEM images of the overall architecture of the CUPE TENG are shown in Figure 3.27. The overall diameter of the CUPE TENG was determined using ImageJ Analysis Software and measured to be 2.99 ± 0.23 mm. Individual channel diameters measurements were 515.24 ± 19.03 μm, which was similar in diameter to the acupuncture needles used during fabrication. The 180X magnification shows the circular uniformity of each individual channel, which was designed to replicate the basal lamina of native nerves. Upon further inspection of the channels, 450X magnifications revealed a submicron topography for the inside lumen of each channel, which can potentially aid in cell communication and nutrient/waste exchange.

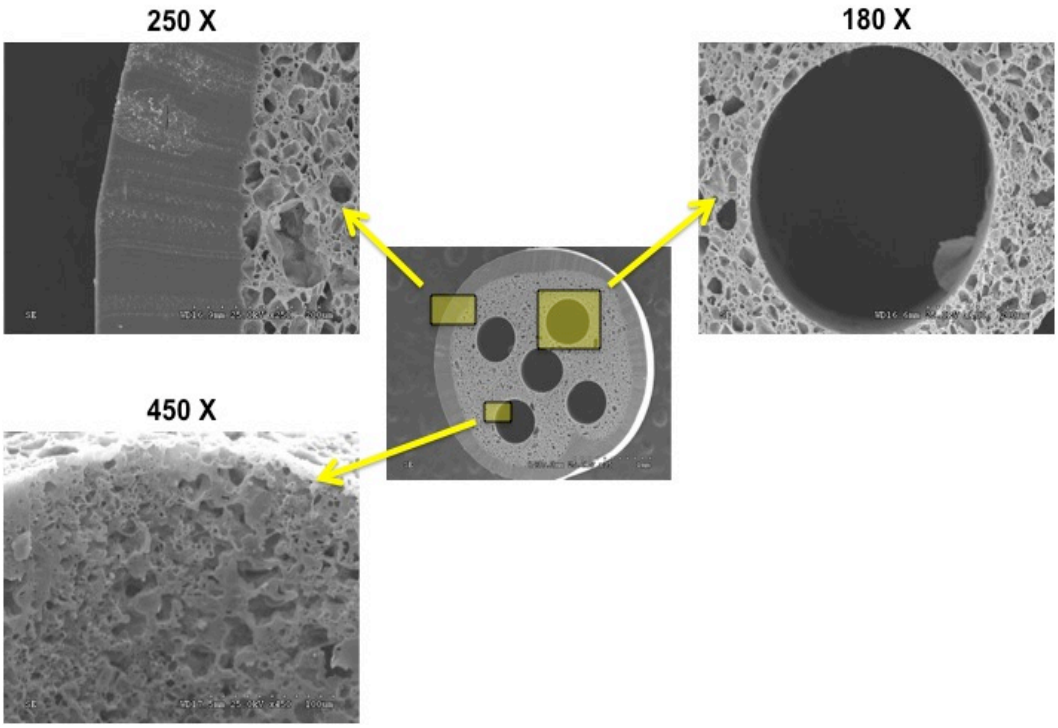

Figure 3.27 CUPE Multichanneled Nerve Guide SEM Images

Outer film thickness was measured to be 232.55 ± 48.10 μm, and was incorporated into the CUPE TENG design to provide mechanical support for increased suture retention strengths. In addition to providing mechanical support, the presence of the outer film can potentially aid in the prevention of fibrous tissue infiltration into the guide. Future studies will be focused on creating a semi-porous outer film to balance the mechanical strength while also allowing for nutrient exchange and guide vascularization.

Figure 3.28 shows representative SEM images of the porous internal structure between each channel. The NaCl particulate leaching technique was able to produce a highly porous internal structure with pores sizes of 12.14 ± 6.94 μm and a corresponding porosity of 67.52 ± 6.27 %. Although the presence of dead pores was visible, the majority of pores were interconnected as shown in the 2,000X magnification.

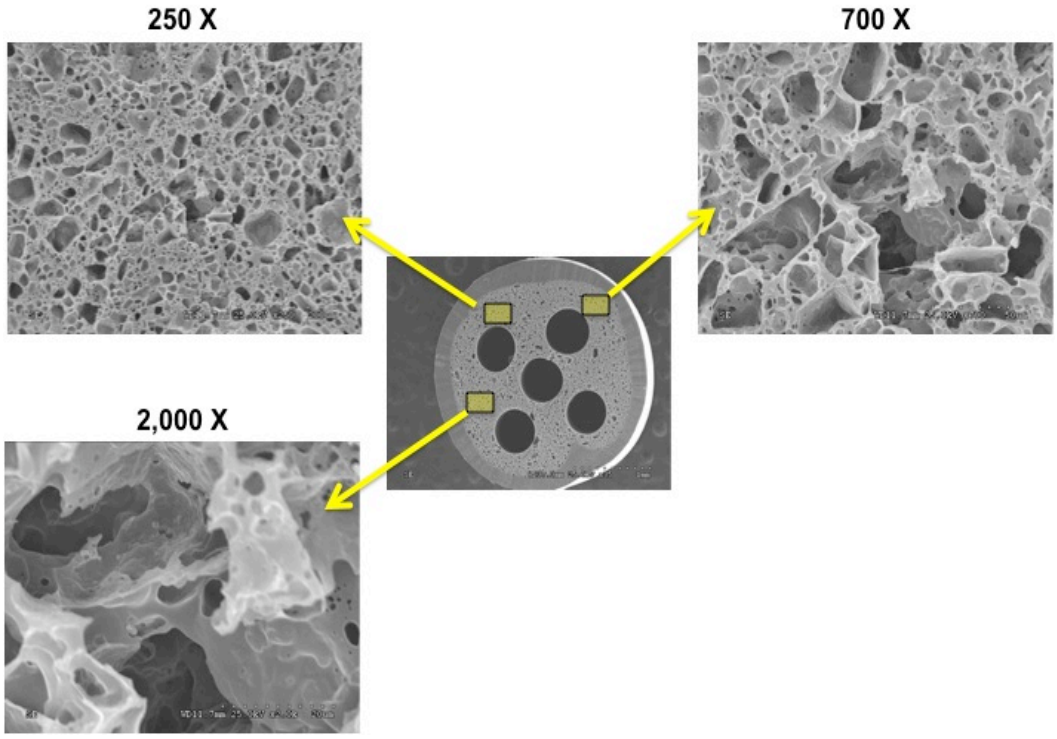

Figure 3.28 CUPE Multichanneled Nerve Guide SEM of Porous Sections

The internal structure of the CUPE TENG can be potentially beneficial over previous hollow tube designs in that the porous structure can provide internal support to prevent conduit collapse from scar tissue constriction. As nerve regeneration requires an orchestrated combinational response of matrix topography and secreted cellular signals, the porous matrix fabricated in this study can potentially enhance peripheral nerve regeneration relative to impermeable conduits [281]. The size of the pores were chosen to be approximately ~ 10 μm in order to maintain a permeable matrix for metabolite transport, while minimizing the possibility for cell migration in between individual channels to promote proper target reinnervation.

Figure 3.29 shows representative SEM images of various CUPE TENG fabricated using a single machined mold design. CUPE TENG with channels ranging from 1-5 in number can be fabricated using the molds from computer-aided design to fit the needs of a particular application. However, changing the design of the machined mold in combination with different acupuncture needle sizes can allow for great flexibility in designing TENG with various channel numbers, diameters, and spatial position.

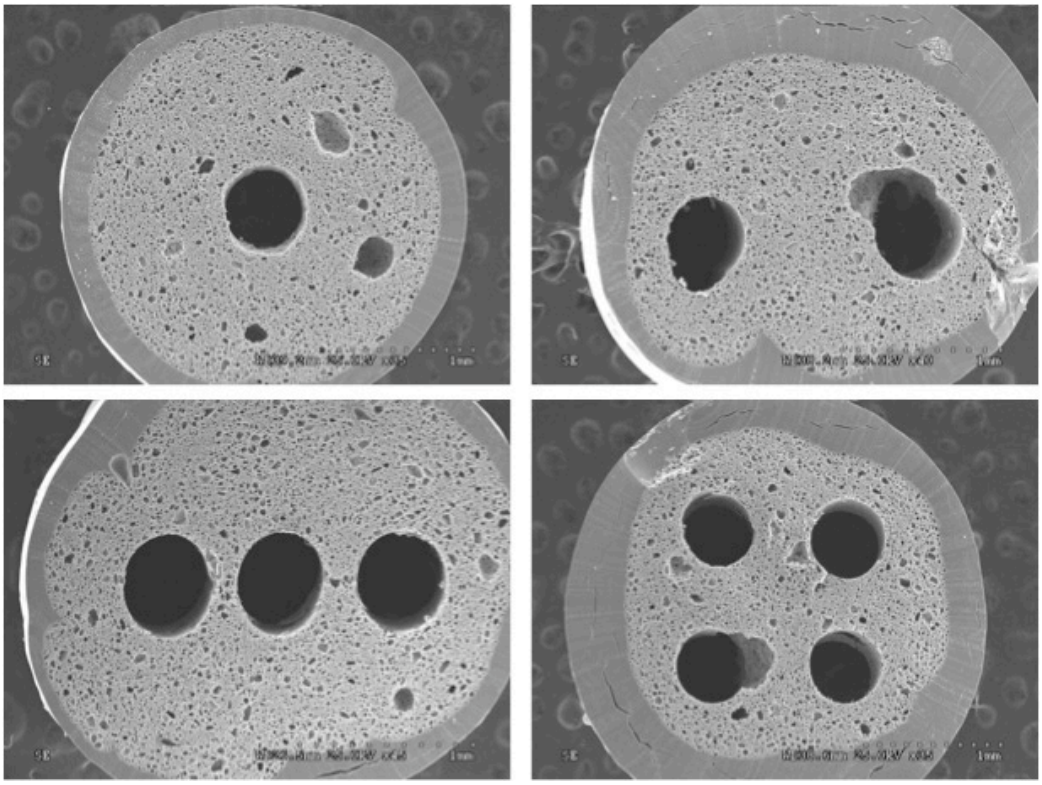

Figure 3.29 Various CUPE Multichanneled Nerve Guide Configurations

Native nerves are strong and elastic in nature with tensile strengths of 9.8 – 21.6 and elongations at break between 8 – 21%. Previous TENG designs have been primarily focused on the use of biodegradable materials, which are stiff and inelastic in nature. The mismatch in compliance often leads to increased scar tissue formation at the implant/tissue interface, and causes implant failure in mechanically dynamic environments were constant movement, tension, and elasticity are vital. The CUPE TENG fabricated in this study were strong and highly elastic as shown in Figure 3.30. The chronological pictorial depiction of uniaxial two-dimensional tensile testing showed the ability of CUPE TENG to be elongated up to 300% their original length without failure. Upon release of tensile force, the CUPE TENG were completely elastic and showed complete recovery to their original size.

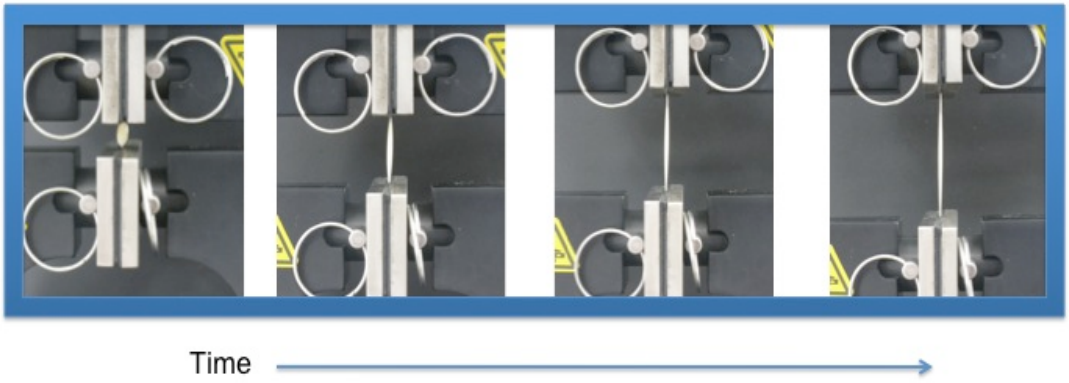

Figure 3.30 CUPE Multichanneled Nerve Guide Uniaxial Tensile Mechanical Test Photographs

The fabricated CUPE TENG were evaluated for their tensile peak stress, modulus, elongation at break, and suture retention strength. As shown in Figure 3.31A, an increase in peak stress and initial modulus were seen as the CUPE crosslinking time and temperature was increased. The increased crosslinking degree provided by elevated temperatures resulted in TENG with a tensile peak stress of 1.38 ± 0.22 MPa with a corresponding elongation at break of 122.76 ± 42.12%, which all coincide with that of native nerves. As the crosslinking condition time and temperature was increased, a reduction in elongation at break was observed. Similar to peak stress, an increasing trend in suture retention strength was observed with longer crosslinking conditions. A suture retention strength of up to 2.4 ± 0.12 N was obtained for the tested CUPE TENG, which exceed the surgical requirement of 1.6 N.

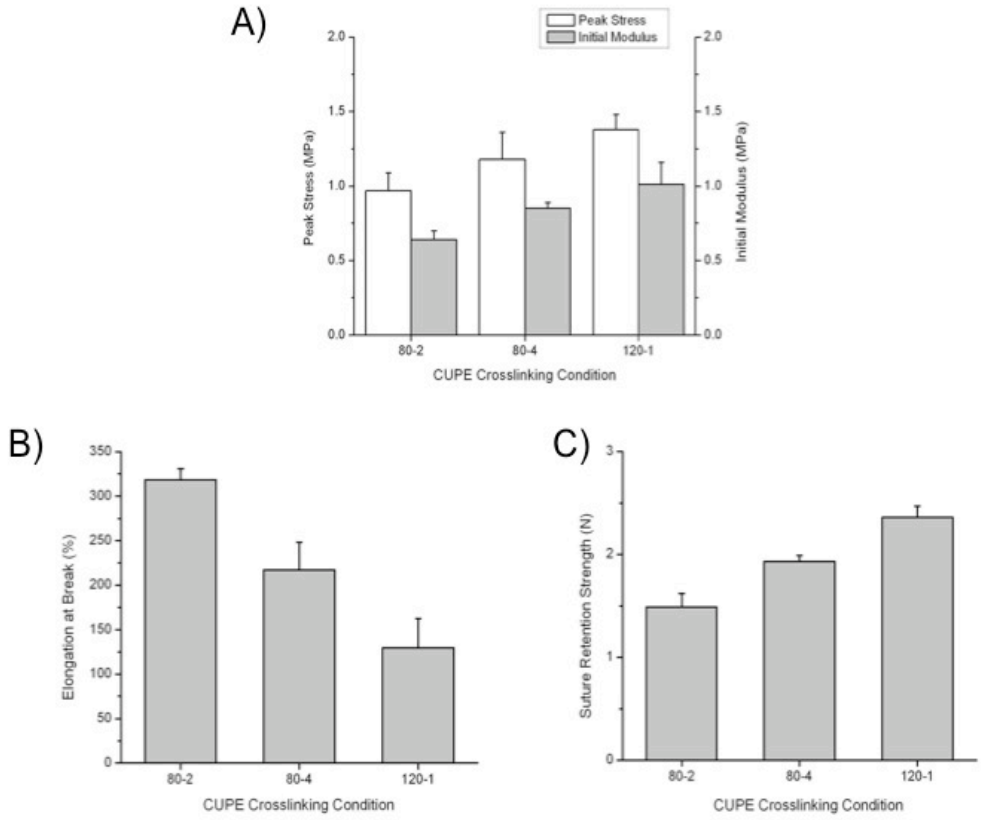

Figure 3.31 CUPE Multichanneled Nerve Guide Mechanical Properties A) Peak stress and initial modulus, B) Elongation at break, and C) Suture retention strength

To determine the affect of the total channel number on the resulting TENG mechanical strength, various CUPE TENG with total channel numbers ranging from 1-5 were evaluated for tensile peak stress. Interestingly, it was observed that no significant difference in peak stress was observed as the total number of channels was increased. This observation indicates that the mechanical strength of the CUPE TENG was primarily due to the presence of the outer film.

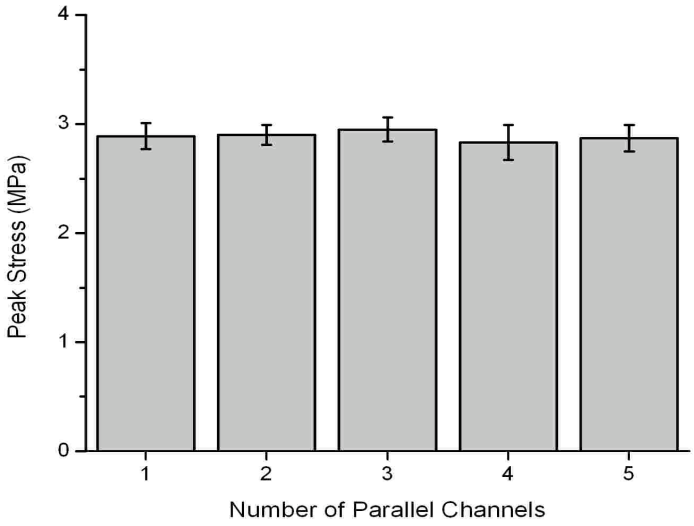

Figure 3.32 Effect of Channel Number on Scaffold Tensile Peak Stress

In addition to mechanical testing, the fabricated CUPE TENG were evaluated *in vivo* using a rat model to determine their ability to regenerate nerve. Photograph images in Figure 3.30 show that the peripheral nerve system injury was successfully re-innervated by the use of CUPE multichanneled TENG (CUPE-S) (**Figure 3.30A**), nerve autograft (**Figure 3.30B**), and PCL hollow tubes (**Figure 3.30C**). Upon implantation of the implants, it was observed that suturing of the CUPE TENG was easily accomplished with no dislocation of the samples to the native nerve stumps.

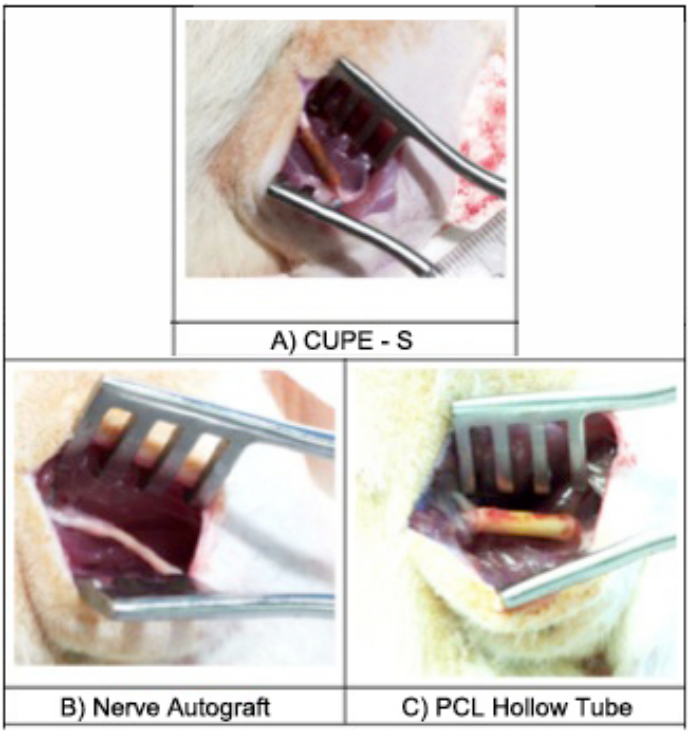

Figure 3.33 Photographs of Various Implanted Nerve Guides A) CUPE multichanneled nerve guide (CUPE – S), B) Nerve autograft, and C) PCL hollow tube

Figures 3.34 – 3.36 show microscopic images of five sections taken throughout the implanted guides, which were stained with H&E (**Figures 3.34-3.36**) and Toluidine blue (**Figures 3.37-3.39**). From the figures, the proximal nerves are said to be normal in appearance consisting of myelinated axons with thick myelin rings, Schwann cells, and blood vessels. Large amounts of axon bundles were observed in all the samples, and the presence of fascicles were also observed in the proximal nerve. Along the graft, a decrease in axonal recoveries was observed in all groups especially in the group of PCL tube. In the central conduits, the nerves were still intact in all groups but the density of tissue occupied was the lowest. In particular, the density of tissue observed in the PCL was the smallest. Other than the PCL tube, the myelinated axons were evenly distributed at the central conduit. In the distal nerve, the axonal recovery in the nerve autograft and PCL tube appeared to be better than the CUPE-S, which

may be due to the smaller cross-sectional area for reinnervation when compared to the other groups.

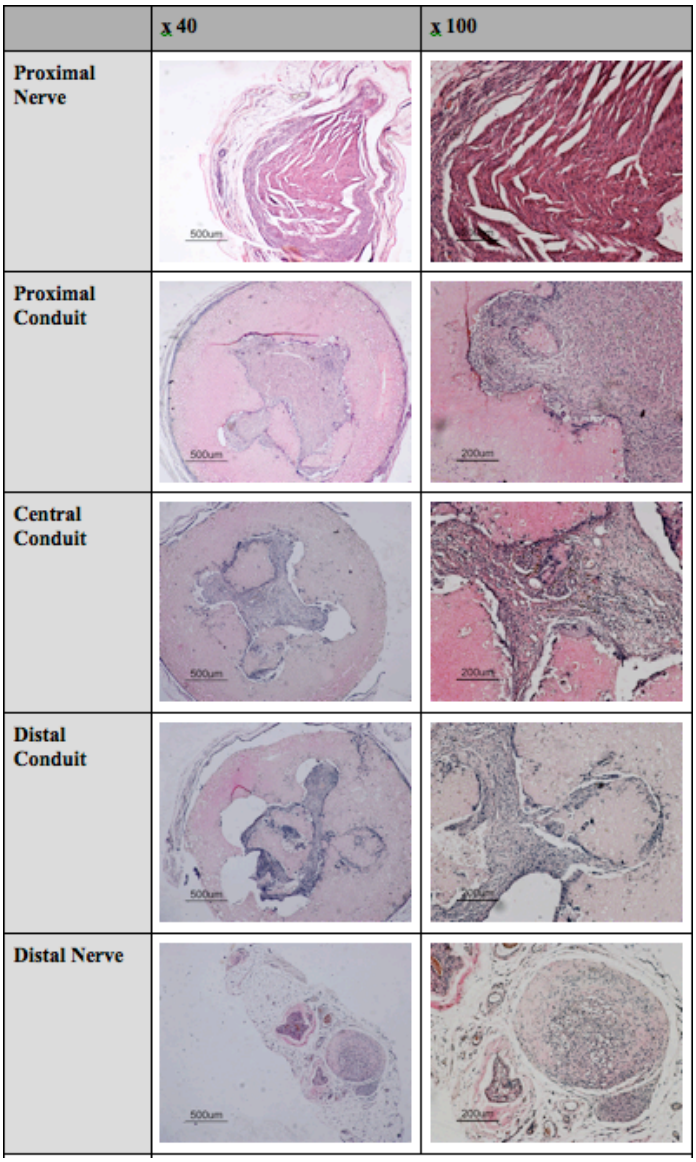

Figure 3.34 Microscope Images of H&E Stained Sections from CUPE Multichanneled Nerve Guides

	x 40	x 100
Proximal Nerve	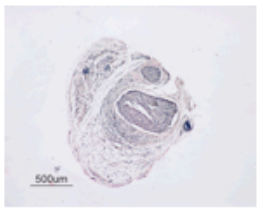	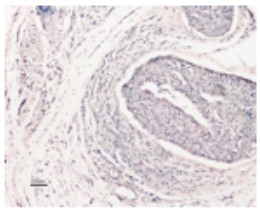
Proximal Conduit	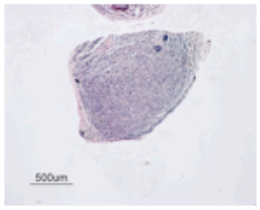	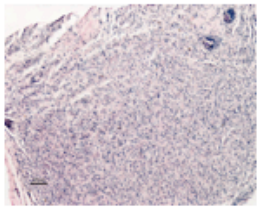
Central Conduit	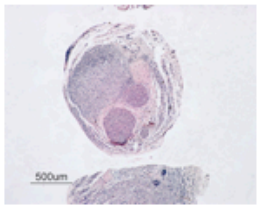	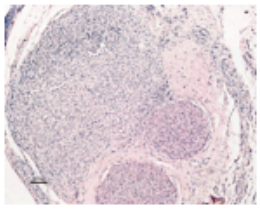
Distal Conduit	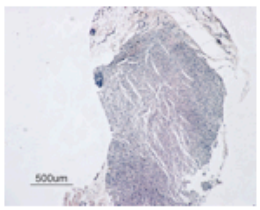	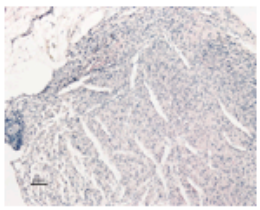
Distal Nerve	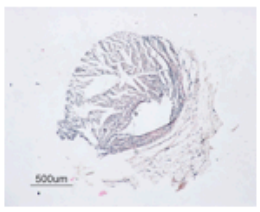	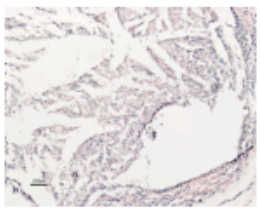

Figure 3.35 Microscope Images of H&E Stained Sections from Nerve Autografts

	x 40	x 100
Proximal Nerve	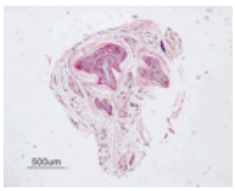	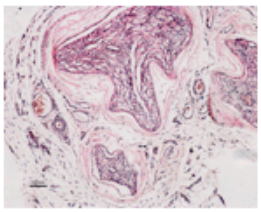
Proximal Conduit	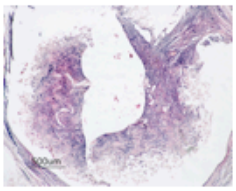	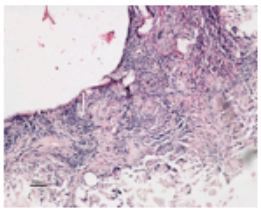
Central Conduit	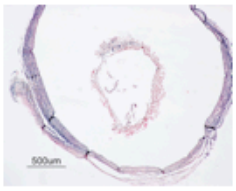	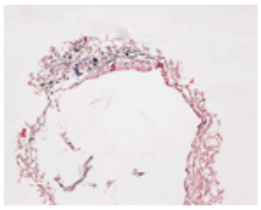
Distal Conduit	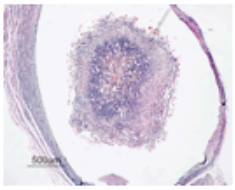	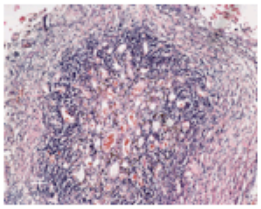
Distal Nerve	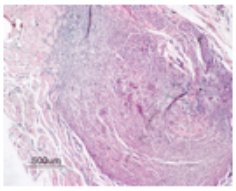	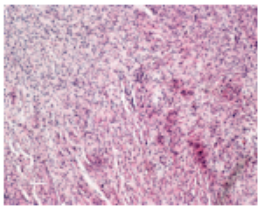

Figure 3.36 Microscope Images of H&E Stained Sections from PCL Hollow Tubes

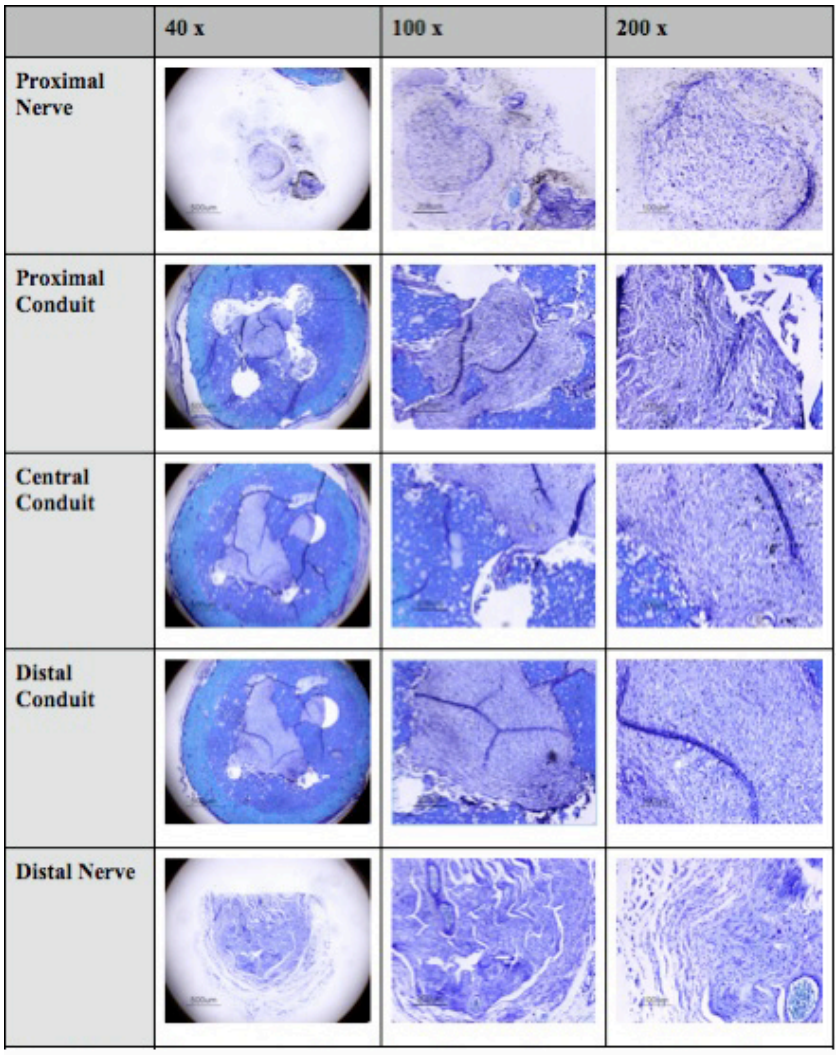

Figure 3.37 Microscope Images of Toluidine Blue Stained Sections from CUPE Multichanneled Nerve Guides

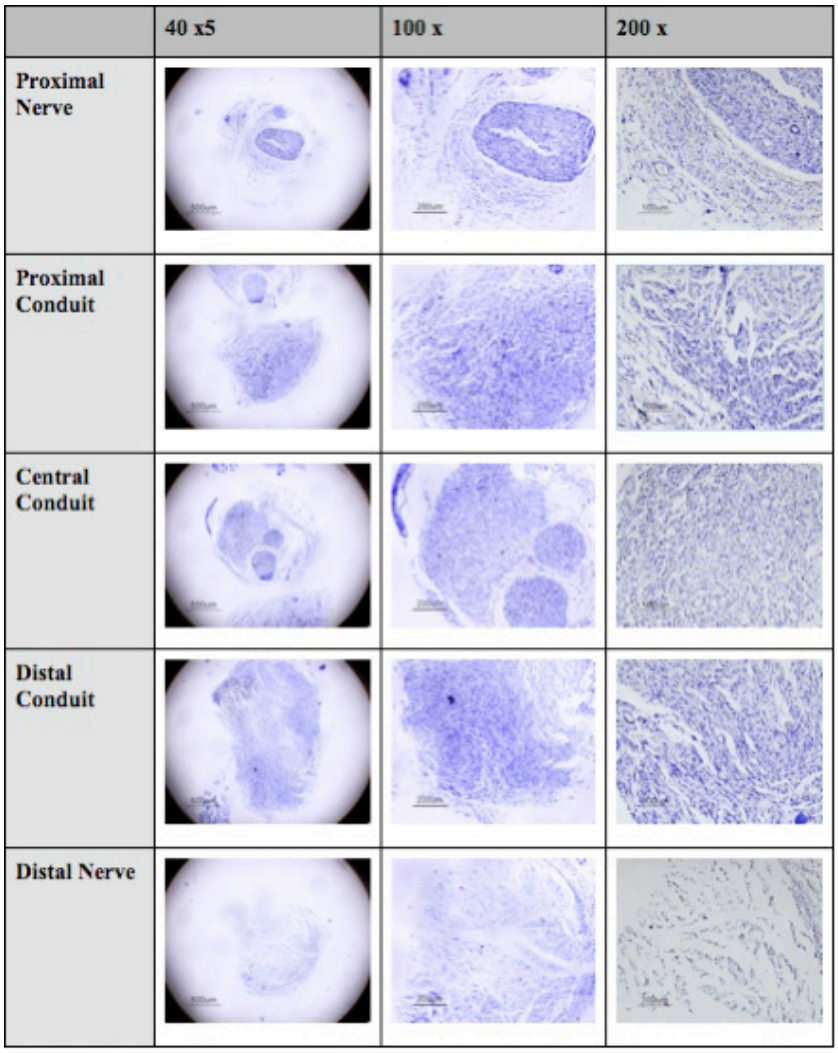

Figure 3.38 Microscopic Images of Toluidine Blue Stained Sections from Nerve Autografts

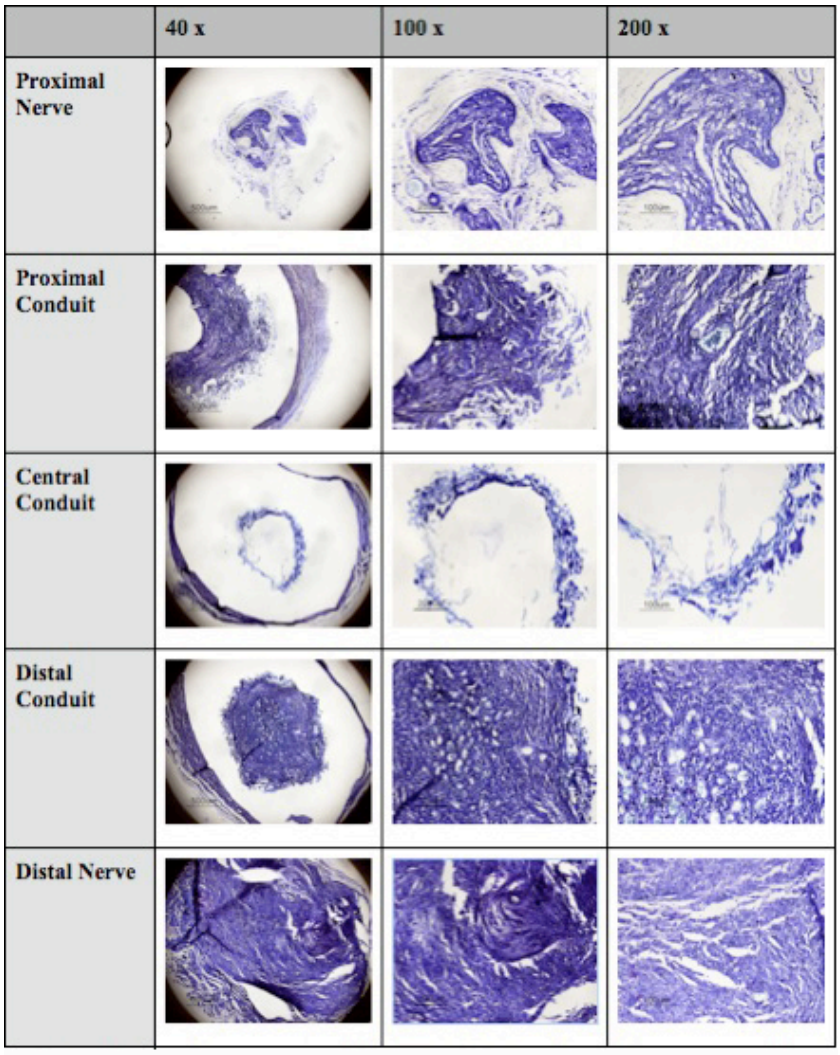

Figure 3.39 Microscopic Images of Toluidine Blue Stained Sections from PCL Hollow Tubes

The inner structure of CUPE-S collapsed (**Figure 3.34**) after eight weeks implantation. The micro-architecture of CUPE-S was not preserved in the animal hind limb possibly due to the vigorous movement of rats. This provides information on the future improvement on the toughness of microchannels in the TENG. It was possible that the area between the channels was insufficient in providing the needed strength to withstand the vigorous movement of the animals. This could be modified by enhancing the strength of the material, which can be done by increasing the density of crosslinking in CUPE or by reducing the size channels to enhance

the sustainability in future studies. Considering the sections of the central conduit, healthy neural tissue was seen in the CUPE-S and the nerve autograft. However, a nearly disconnected neural fiber was observed in the PCL tube. Also, when comparing the neural fiber pattern, CUPE-S showed a similar structure as that in the nerve autograft in terms of the myelinated fiber density and population. This proves that the development of micro-architecture could facilitate the axonal regeneration.

Table 3.4 summarizes the average fiber population from 0.01 mm^2 and the average diameter in the central conduits of CUPE-S, nerve autograft and PCL tube. Among these groups, the CUPE-S has the most dense fiber population. It showed a similar fiber population and density to the nerve autograft, but was significantly different from those in the PCL tube. However, the fiber diameter in CUPE-S was relatively smaller than that measured in the nerve autograft. The fluctuation of diameter along the nerve autograft is the smallest among all the samples while that along PCL tube is the largest. There is an increasing trend in the diameter of CUPE-S from the proximal nerve to the distal nerve. The ultimate fiber diameter at the distal nerve of CUPE-S reaches the closest value to the nerve autograft.

Table 3.4 Average Nerve Fiber Populations, Density, and Diameter in Implanted Nerve Guides

Group	Fiber Population	Fiber density (mm^2)	Fiber diameter (μm)
CUPE Multichanneled TENG	143 ± 27	12,914 ± 2454	0.7774 ± 0.17
Nerve Autograft	120 ± 26	10,872 ± 2318	0.8723 ± 0.16
PCL Hollow Tube	52 ± 10	4,655 ± 915	0.8471 ± 0.15

3.5.4 Conclusion

In conclusion, a novel CUPE TENG consisting of longitudinally oriented parallel microchannels were fabricated using particulate leaching techniques and evaluated mechanically and in vivo for potential use in peripheral nerve tissue engineering. The scaffolds were made from CUPE, a new type of strong, soft, and hemocompatible biodegradable polyester elastomer. These studies represent the first step toward the investigation of the role of scaffold architecture on the resulting tensile, suture retention, and in vivo performance. Using

this design, TENG can be produced with tunable strength and architecture to fit the needs of a particular application. CUPE TENG performed as well as nerve autografts in the *in vivo* evaluation studies.

3.6 Injectable Drug Eluting Elastic Polymer for Endoscopic Mucosal Resection

3.6.1 Introduction

Gastrointestinal (GI) cancers occur frequently in industrialized countries with new cases of esophagus, gastric, and colorectal cancers affecting 3.6%, 11.4% and 30.1%, respectively, of the developed world's population in 2008 [303]. The early stages of GI cancers exhibit non-specific symptoms, and are difficult to diagnose. This usually results in the majority of cases diagnosed at advanced stages when bleeding, pain, or obstructions have already occurred [304, 305]. As a result of late presentation, the 5-year survival rate of gastrointestinal cancers is below 30% despite surgical, radio, and chemotherapeutic interventions. Lesions of the gastrointestinal tract typically exhibit dysplasia, which is identified by neoplastic growth within the mucosal layer [305]. Due to the lack of gross features that would normally facilitate early characterization, identification of high-grade dysplasia often occurs only after cancer develops into later stages for patients [306]. Early gastric cancers progress into either intestinal or diffuse type carcinomas, 95% of which are adenocarcinoma [305], with approximately 16% of all cancers remaining of mixed or unclassifiable type [307].

Endoscopic mucosal resection (EMR) is a surgical method used to separate the mucosal and muscle layers by physically grasping the upper mucosal layer and resecting the mucosal layer in a manner that minimizes bleeding and perforation. EMR is employed to remove lesions 2 cm or smaller in size [308], and is best suited for the removal of early cancer lesions of the gastrointestinal tract [309]. Originally, resection was accomplished by mechanical separation and resection of the lesion. However, perforation, bleeding, and damage to the lower muscle layer were common occurrences. In order to improve efficacy and safety, EMR techniques require the injection of a solution underneath the mucosa into the submucosal space

to provide a “safety-cushion” for the underlying muscle layer [310]. Although numerous injection solutions have been proposed and tested, saline or diluted epinephrine is the most commonly used in clinic due to its low cost and ease of use, but is hampered by rapid dispersion within the submucosal plane resulting in the need for repeated injections [311]. In order to improve submucosal lift durations, sodium hyaluronate (SH) is currently being studied owing to its high viscosity, ease of injection, and ability to provide long lasting submucosal lift durations [312-315]. However, high costs and concerns for tumor stimulation limit its large-scale use [310, 316].

Recent research has indicated a paradigm shift towards the development of EMR injection solutions, which rely on gel formation to provide extended submucosal lift durations [317]. Photocrosslinkable chitosan and thermoresponsive poloxamers have been recently reported for EMR with great enthusiasm, but are limited by administration difficulties [318, 319]. For example, the liquid to gel transformation using photoinitiated free radical polymerization requires the use of an ultraviolet light, which may be difficult in hard-to-reach areas, and thermoresponsive polymers have been shown to clog inside long delivery tools at normal body temperature [17, 319].

We have recently reported on the development of biodegradable elastomeric hydrogel, poly (ethylene glycol maleate citrate) (PEGMC), which has been shown to have excellent cyto-/tissue-compatibility and controlled degradability both *in vitro* and *in vivo* for tissue engineering and drug delivery applications [200]. The ability to be injected using minimally invasive methods and deliver therapeutics in a controlled manner has prompted the investigation of PEGMC as a new EMR injection solution. Unlike previous materials, the liquid to gel transformation of PEGMC can provide sustained mucosal lift without administration difficulties, and the controlled release of Rebamipide [320], which stimulates prostaglandin generation and improves the speed of ulcer healing, from the biodegradable gel can potentially aid in mucosal regeneration after resection. The purpose of this study is to evaluate the efficacy and safety of a PEGMC

based injectable drug eluting elastomeric polymer (iDEEP), which aims to address the limitations of previous solutions. As shown in Figure 3.40, the iDEEP system functions first by the endoscopic delivery of a water-soluble viscous liquid Part A polymer solution underneath the mucosal layers of the GI lesion site (Step 2). Since this Part A polymer solution is more viscous than saline solutions, improved submucosal lifts can be achieved similar to other EMR solutions, which rely on viscosity to provide the required safety-cushion (Step 3).

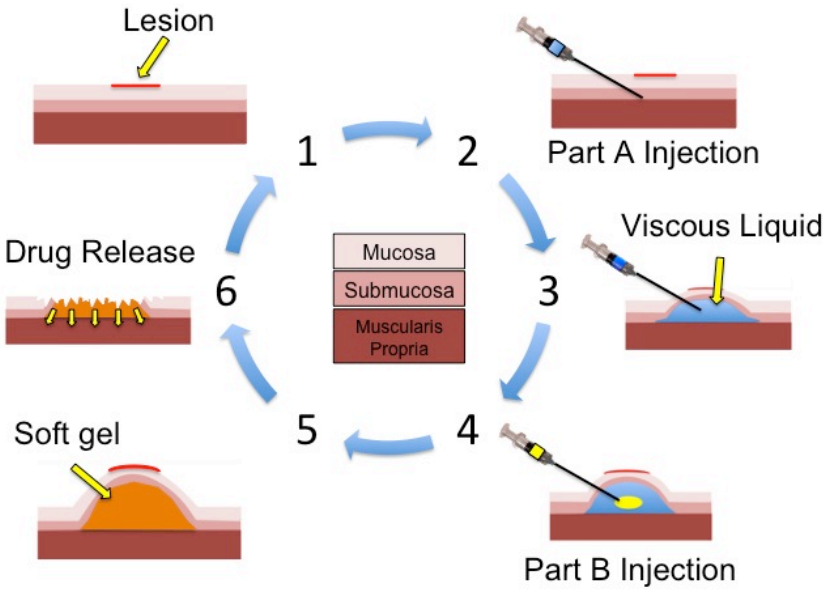

Figure 3.40 Schematic Representation of the iDEEP System for Endoscopic Mucosal Resection 1) Lesion confined to submucosal layer, 2) Injection of Part A solution, 3) Part A remains as a viscous liquid underneath submucosal layer, 4) Injection of Part B solution, 5) Formation of a soft gel, 6) After submucosal resection, remaining gel releases drug for submucosal regeneration

The injection of the Part A solution remains as a viscous liquid inside the body, and will not set unless combined with the Part B solution (Step 4). Unlike other *in situ* crosslinkable EMR solutions, this is advantageous in that the surgeon can specifically control the polymer solution's setting location and time. This two-component system will allow for better control over the location and timing of the polymer crosslinking without the use of special equipment. After injection of the Part B solution, a soft biodegradable gel is formed within 5 minutes to provide a

safety-cushion for the resection procedure (Step 5). After resection of the lesion, the remaining hydrogel can serve to prevent bleeding and deliver therapeutics to aid in mucosal regeneration (Step 6).

The rationale behind this approach is that 1) The development of a biodegradable citric acid based water soluble polymer, which has shown potential use in tissue engineering applications, can provide a biocompatible material for use in EMR; 2) Free radical crosslinking using redox initiators can provide an *in situ* crosslinkable material, which can be delivered as a liquid in a minimally invasive manner, and crosslinked into a set gel at the delivery site without the use of special equipment (i.e. UV light); 3) A two component system can be employed to control the timing and location of polymer crosslinking; 4) Water soluble polymer solutions can provide improved viscosity over clinically used saline solutions to improve submucosal lift; 5) The use of a crosslinked hydrogel can provide extended submucosal lift durations over liquid based solutions; 6) A biodegradable drug eluting polymer can potentially aid in mucosal regeneration after resection; and 7) A synthetic polymer formulation is cost-effective, easy to synthesize, and readily available unlike other EMR solutions.

3.6.2 Experimental

All chemicals were purchased from Sigma-Aldrich (St. Louis, MO, USA) and used as received. All materials were purchased from Fisher Scientific (Pittsburg, PA, USA) unless specified otherwise and used as received.

3.6.2.1 Poly (ethylene glycol maleate citrate) (PEGMC) Pre-Polymer Synthesis

PEGMC with different citric acid: maleic anhydride monomer ratios were synthesized as previously described [200]. Citric acid, poly (ethylene glycol) (MW 200), and maleic anhydride were reacted together in a three-neck 250 mL round bottom flask fitted with an inlet and outlet adapter. The contents were stirred using a magnetic pear shaped stir bar and allowed to melt at 160 °C under a continuous flow of nitrogen for 10 minutes. Once the constituents melted, the temperature was reduced to 140 °C for 2 hours. The pressure of the system was then reduced

to 50 mTorr for an additional 2 hours. The prepared PEGMC pre-polymer was dissolved in deionized water and dialyzed with a 500 Da molecular weight cut off membrane for 2 days followed by lyophilization to obtain purified pre-PEGMC.

3.6.2.2 iDEEP Component Preparation

To prepare the iDEEP Part A Component (iDEEP-A), PEGMC was dissolved in deionized water (20 wt. %), and combined with poly (ethylene glycol diacrylate) (12 wt. %), and tetramethylethylenediamine (0.5 wt. %). The iDEEP Part B Component (iDEEP-B) was prepared by dissolving ammonium persulfate redox initiator (0.25 wt. %) in deionized water. Combining the Part A and B solutions in a 2:1 ratio, respectively, produced iDEEP gels.

3.6.2.3 Injection Pressure Characterization

In order to assess the relative ease of injection of the iDEEP system solutions in real life conditions, the maximum pressures developed during injection were measured according the schematic shown in Figure 3.41.

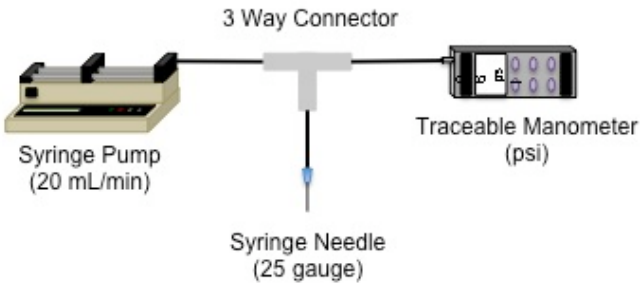

Figure 3.41 Injection Pressure Experimental Set Up

Briefly, 5 mL of a saline solution (0.9%), sodium hyaluronate (0.4%) (Thermo Fisher Scientific, Waltham, MA, US), and different concentrations of the iDEEP Part A component (10, 15, and 20 wt.-%) were injected using a 10 mL syringe (Thermo Fisher Scientific, Waltham, MA, US) connected via a 3-way luer-lock with a digital traceable manometer (Cole Parmer, Vernon Hills, IL, US) and a 25-gauge sclerotherapy needle. The injection rate was set at 20 mL/minute using a KD Scientific Model 200 syringe pump (KD Scientific, Holliston, MA, US), and the maximum pressure value was recorded at the time when a steady force of embolus of the syringe

produced a fluid jet of stable radius from the tip of the sclerotherapy needle. The maximum pressure was recorded in pressure per square inch (PSI), and the experiments were repeated 4 times for each solution.

3.6.2.4 Rebamipide Release

To determine the Rebamipide release rate, Rebamipide (1 mM) was mixed with various iDEEP-A solutions, and combined with the iDEEP-B to form crosslinked gels. The drug-loaded gels were then incubated in phosphate buffered saline (37 °C; pH 7.4), and Rebamipide release was determined using high performance liquid chromatography (HPLC) (Waters, Milford, MA).

3.6.2.5 Ex Vivo Evaluation

The upper third of porcine stomachs were used for all ex vivo studies due to the resemblance with the human stomach in thickness and histology. The gastric specimens were obtained immediately after sacrifice, cut into 5 × 5 cm squares, and fixed onto a corkboard. Using a 2.5 mL syringe and 25-gauge needle, 1 mL of each solution was injected tangentially into the submucosa through the mucosal surface. Mucosal elevation height was quantitatively determined from photographs using Image J Analysis software.

3.6.2.6 Preliminary In Vivo Evaluation

For the *in vivo* model, 4 EMR procedures were performed in the stomach of a porcine specimen using a 25-gauge catheter injection needle. All solutions were mixed with methylene blue (0.5/10 mL of solution) for visualization. An “en bloc” resection of the elevated mucosa was performed with a hook-knife and polypectomy snare, and recorded with endoscopic photographs.

3.6.2.7 Statistical Methods

All results are expressed as the mean ± standard deviation (n = 10). Statistical significance between two sets of data was calculated using a two-tail Student’s t-test, and non-parametric one-way ANOVA tests were performed where appropriate. Data was taken to be significant when a P value < .05 was obtained.

3.6.3 Results and Discussion

EMR is a minimally invasive endoscopic procedure now accepted worldwide as a treatment modality in the removal dysplastic and early malignant lesions limited to the superficial layers of the gastrointestinal tract [321, 322]. Unfortunately, the EMR procedure has been historically limited by the short submucosal lift durations of the available injection solutions, which have been constrained by two design avenues: the osmolarity or viscosity of a solution is responsible for the lifting properties the material [308]. The recent introduction of injectable materials, which utilize a liquid to gel transformation, has shown promise in providing extended submucosal lift durations. However, many of these gel-forming materials are plagued by administration difficulties, which further complicate the procedure. In review of the recent progress in the development of EMR solutions, the ideal injection solution should be cost-effective, widely available, easily injectable, biocompatible, biodegradable, able to provide prolonged submucosal lift durations, and able to aid in mucosal healing after the resection process in order to have clinical relevance [311, 315].

In this study, we have developed a novel injectable drug eluting elastomeric biodegradable polymer, which aims to meet all the requirements of an ideal EMR solution and overcome the limitations of previous solutions. As shown in Figure 3.40, iDEEP utilizes both viscosity and gel formation through redox initiated crosslinking to overcome the limitations of previous designs. Liquid to gel transformation occurred within 4 minutes of combining the iDEEP Part A and B Components (**Figure 3.42**). A water-soluble iDEEP-A, which is more viscous than saline, will remain a viscous liquid until combined with the water-soluble iDEEP-B to produce a soft biodegradable hydrogel. Dividing the system into two separate components offers a huge advantage over previous designs in that the surgeon can precisely control the gel setting location and time and avoid premature gelling inside the delivery tools. In addition, the utilization of a redox initiated crosslinking mechanism does not require the use of additional equipment such as UV light for the gel formation to occur.

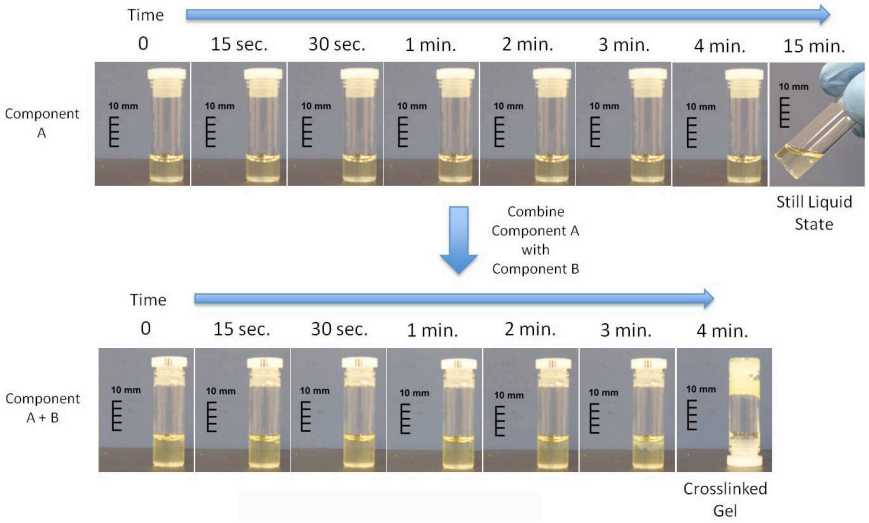

Figure 3.42 iDEEP Liquid to Gel Transformation

A higher viscosity liquid typically translates into a greater force required to inject the solution through small caliber delivery tools, which may produce unwanted administration difficulties. To ensure the iDEEP components were easily injectable, we have assessed the maximum pressures developed using real life conditions. No significant difference in the pressures developed during injection was observed between iDEEP-A (28.9 ± 0.3 PSI) and SH (29.5 ± 0.4 PSI, $P > .05$). Injection pressures of iDEEP-B were much lower (6.6 ± 0.1 PSI) and were found comparable to that of saline solutions (6.0 ± 0.1 PSI, $P > .05$). Injection of the iDEEP-A component through a 25-gauge endoscopic needle showed no difficulties in achieving a constant flow, and was found comparable to SH whereas iDEEP-B solutions were even easier to inject showing similar injection pressures to that of normal saline. The localized and controlled delivery of Rebamipide [315], a mucosal protective and ulcer healing drug shown to stimulate prostaglandin generation, may improve the speed of ulcer healing to aid in the management of EMR-induced damages. Rebamipide release studies from iDEEP showed an initial burst release at 4 hours for all iDEEP-A compositions. After the initial burst release, a controlled release for up to 2 weeks was observed, and could be controlled with the iDEEP-A

monomer ratios (**Figure 3.43**). The developed polymers are also capable of incorporating hemostatic and/or anti-neoplastic drugs to assist mucosal resection and treatment.

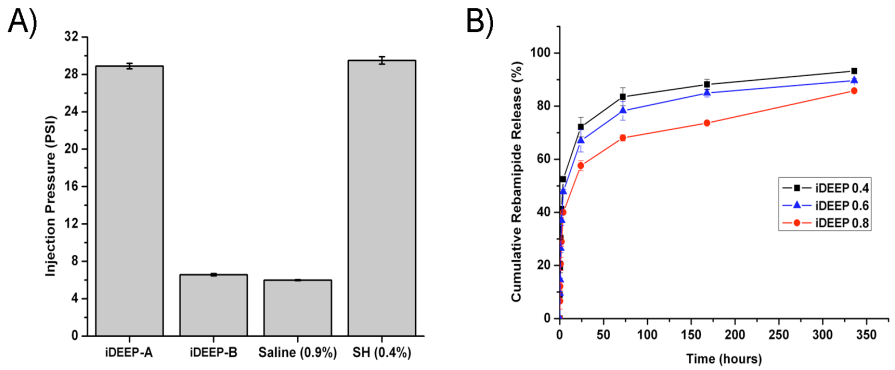

Figure 3.43 iDEEP Characterization Studies. A) Maximum injection pressures and B) *In vitro* Rebamipide release

In the *ex vivo* study (**Figure 3.44**), iDEEP displayed the highest submucosal elevation heights at all time points. After 30 minutes, iDEEP displayed extended lift durations (5.7 ± 0.5 mm) with higher submucosal elevations over saline (2.8 ± 0.2 mm, $P < .01$) and SH (4.2 ± 0.2 mm, $P < .05$). No significant changes in iDEEP cushion height were observed after 5 minutes due to gel formation. To minimize any discrepancies and limitations of an ex vivo study, all specimens were obtained within the first hour of the animal's death, and all tests were performed at constant temperature of 37 °C to minimize any tissue changes.

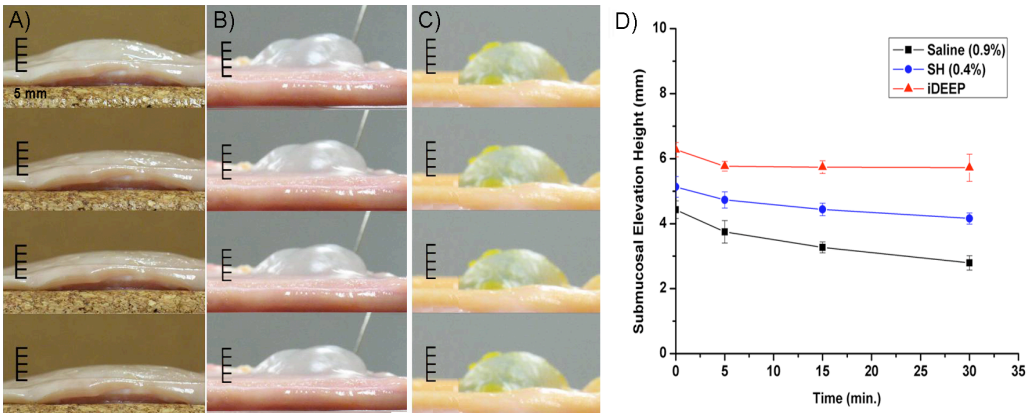

Figure 3.44 Photographic Images Depicting the Chronological Changes in the Submucosal Elevation of A) Saline (0.9%), B) Sodium hyaluronate (0.4%), C) iDEEP (30%), and D) Graphical representation of the chronological changes in submucosal elevation

To evaluate the efficacy of iDEEP, standard EMR procedures were performed in vivo using a live porcine stomach model. In the preliminary in vivo study, the iDEEP-A was easily injected into the porcine stomach to create submucosal elevation (**Figure 3.45A**). Using the same injection needle, the iDEEP-B was injected to produce a soft biodegradable gel underneath the mucosa (**Figure 3.45B**). No electrocautery settings changes were needed to perform the procedure. The iDEEP-A was easily injected using standard delivery tools, and was able to create an adequate submucosal cushion.

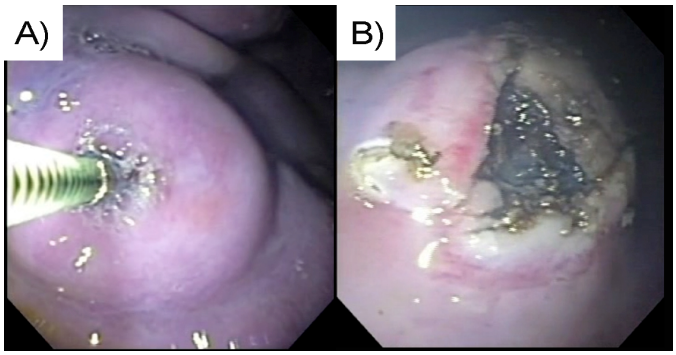

Figure 3.45 Endoscopic Views of A) Contained vertical submucosal elevation after injection of the iDEEP, and B) Mucosal defect post-iDEEP EMR resection

Using the same injection needle, the iDEEP-B solution was then injected into the same location without any clogging inside the delivery tool. After 5 minutes of iDEEP-B injection, the en bloc resection of the elevated mucosa revealed a soft biodegradable gel underneath the mucosa to provide protection for the underlying muscle layer from electrocautery damage. The presence of the iDEEP gel did not complicate the resection procedure or require any changes to the electrocautery settings. Although the iDEEP gel cannot be removed entirely following the EMR procedure, previous studies have shown complete biodegradation of the hydrogel, excellent tissue compatibility, and minimal inflammation [200]. We also believe that the remaining material left behind after the resection procedure can be used to delivery therapeutics, and promote regeneration of the damaged mucosa. Although mucosal regeneration was not

evaluated in this study, long term *in vivo* degradation and mucosal regeneration in porcine stomachs will be the focus of future studies.

3.6.4 Conclusion

In conclusion, iDEEP is a cost-effective, readily available, and easily injectable two-component solution, which allows for biodegradable gel formation under the submucosal space without complex administration difficulties and can potentially aid in mucosal regeneration through controlled therapeutic delivery. The iDEEP system displayed long lasting cushion elevations over other frequently used injection solutions, and performed well in EMR procedures in vivo. These results suggest that iDEEP may provide a significant step towards the realization of an ideal injection material for EMR. Further comparative long-term studies in living animals are needed to confirm the efficacy and submucosal regeneration of the iDEEP.

3.7 Conclusions

The potential application of citrate-based biomaterials has been presented through the development of novel tissue engineering scaffolding with particular interest in thin scaffold sheets, multiphasic small diameter vascular grafts, multichanneled nerve guides, and as a unique material for submucosal elevation in gastrointestinal endoscopy procedures. A new method was introduced for the generation of a new era of sodium chloride porogen, which was utilized in combination with micro-engineering approaches in the design and fabrication of novel anatomically correct tissue engineering scaffolding. The newly developed scaffolds were characterized to elucidate the structure-mechanical property relationship of each type of scaffold, and the preliminary *in vivo* performance was assessed through a peripheral nerve regeneration animal model. The newly developed scaffold designs should address many of the existing challenges in tissue engineering and advance the field as a whole.

CHAPTER 4

FUTURE DIRECTIONS

The biomaterials and scaffold designs discussed herein demonstrate the importance of developing new biomaterial with novel properties to introduce new therapeutic approaches and tackle unmet clinical problems. Citric acid has proven to be a unique multifunctional monomer, which imparts key pendant functionality to give citrate-based materials their advantageous properties over previous materials. Significant progress has already been made since the inception of the poly (diol citrates), and new citrate-based materials with unique properties are constantly being discovered. In order to improve upon and create the next generation of materials, functionalization of the biomaterials should be actively explored in order to create designer biomaterials, which can influence cell behavior to release specific growth factors to improve regeneration.

Although significant progress has been made in the areas of biodegradable elastomer research and the design of anatomically correct or biomimetic scaffolds, much is still unknown about the molecular mechanisms by which tissue regeneration occurs. From a biomaterial scientist standpoint, further collaboration with developmental biologists and other biological disciplines are needed to develop intelligent materials, which exploit nature's own mechanism of repair for proper tissue regeneration. It is highly unlikely that the implantation of a bare scaffold alone can lead to the successful functional recovery of damaged tissues. Further elucidation of the molecular mechanisms of tissue repair are needed to pinpoint the chemical cues necessary in developing an off-the-shelf implant, which utilizes a complex combination of the biomaterial and the orchestrated release of chemical cues to generate the optimum balance of cell recruitment and differentiation at the implant site for tissue regeneration.

Unfortunately, many of the previous limitations associated with tissue engineering still remain, and will continue to constrain the success of the field. The regeneration of thick, vascularized tissues composed of different cell types is a milestone that has been documented and still remains today. The inability to properly recreate the complex extracellular matrix and multi-cellular spatial architecture is still a major challenge. In addition to and more importantly, the inability to provide the requirement vascularization into the implanted construct will be a major limiting factor to the success of the implanted scaffold. Until these major obstacles are addressed, tissue engineering will not meet clinical expectations and widespread acceptance as expected. Further advances in the field will rely on multi-disciplinary approaches that combine medicine, chemistry, engineering and pathology to develop effective strategies to treat complex wounds and pathologies to bring tissue engineering closer to clinical relevance.

REFERENCES

1. J.P. Bruggeman, C.J. Bettinger and R. Langer, *J Biomed Mater Res A,* 2008, **95**, 92.
2. M.P. Lutolf and J.A. Hubbell, *Nat Biotechnol,* 2005, **23**, 47.
3. C.L. Nijst, J.P. Bruggeman, J.M. Karp, L. Ferreira, A. Zumbuehl, C.J. Bettinger and R. Langer, *Biomacromolecules,* 2007, **8**, 3067.
4. M. Hiles and J. Hodde, *Int Urogynecol J Pelvic Floor Dysfunct,* 2006, **17**, S39.
5. J.A. Hubbell, *Biotechnology (N Y),* 1995, **13**, 565.
6. J. Lee, M.J. Cuddihy and N.A. Kotov, *Tissue Eng Part B Rev,* 2008, **14**, 61.
7. N.A. Peppas and R. Langer, *Science,* 1994, **263**, 1715.
8. M. Brittberg, A. Lindahl, A. Nilsson, C. Ohlsson, O. Isaksson and L. Peterson, *N Engl J Med,* 1994, **331**, 889.
9. K.P. Ponder, S. Gupta, F. Leland, G. Darlington, M. Finegold, J. DeMayo, F.D. Ledley, J.R. Chowdhury and S.L. Woo, *Proc Natl Acad Sci U S A,* 1991, **88**, 1217.
10. J. Dey, H. Xu, J. Shen, P. Thevenot, S.R. Gondi, K.T. Nguyen, B.S. Sumerlin, L. Tang and J. Yang, *Biomaterials,* 2008, **29**, 4637.
11. L. Soletti, Y. Hong, J. Guan, J.J. Stankus, M.S. El-Kurdi, W.R. Wagner and D.A. Vorp, *Acta Biomater,* 2010, **6**, 110.
12. J.C. Middleton and A.J. Tipton, *Biomaterials,* 2000, **21**, 2335.
13. I. Vroman and L. Tighzert, *Materials,* 2009, **2**, 307.
14. N. Bursac, M. Papadaki, J.A. White, S.R. Eisenberg, G. Vunjak-Novakovic and L.E. Freed, *Tissue Engineering,* 2003, **9**, 1243.

15. N. Huang, P. Yang, Y.X. Leng, J.Y. Chen, H. Sun, J. Wang, G.J. Wang, P.D. Ding, T.F. Xi and Y. Leng, *Biomaterials,* 2003, **24**, 2177.

16. V. Maquet and R. Jerome, *Porous Materials for Tissue Engineering,* 1997, **250**, 15.

17. J.L. Ifkovits and J.A. Burdick, *Tissue Eng,* 2007, **13**, 2369.

18. A. Mahdavi, L. Ferreira, C. Sundback, J.W. Nichol, E.P. Chan, D.J. Carter, C.J. Bettinger, S. Patanavanich, L. Chignozha, E. Ben-Joseph, A. Galakatos, H. Pryor, I. Pomerantseva, P.T. Masiakos, W. Faquin, A. Zumbuehl, S. Hong, J. Borenstein, J. Vacanti, R. Langer and J.M. Karp, *Proc Natl Acad Sci U S A,* 2008, **105**, 2307.

19. M.A. Shaker, J.J. Dore and H.M. Younes, *J Biomater Sci Polym Ed,* 2010, **21**, 507.

20. R.T. Tran, Y. Zhang, D. Gyawali and J. Yang, *Recent Patents on Biomedical Engineering,* 2009, **2**, 216.

21. W. He, Z. Ma, T. Yong, W.E. Teo and S. Ramakrishna, *Biomaterials,* 2005, **26**, 7606.

22. W. He, T. Yong, W.E. Teo, Z. Ma and S. Ramakrishna, *Tissue Eng,* 2005, **11**, 1574.

23. R. Langer and J.P. Vacanti, *Science,* 1993, **260**, 920.

24. L.E. Niklason, J. Gao, W.M. Abbott, K.K. Hirschi, S. Houser, R. Marini and R. Langer, *Science,* 1999, **284**, 489.

25. J.P. Stegemann and R.M. Nerem, *Ann Biomed Eng,* 2003, **31**, 391.

26. E. Behravesh, S. Jo, K. Zygourakis and A.G. Mikos, *Biomacromolecules,* 2002, **3**, 374.

27. S.L. Chia, K. Gorna, S. Gogolewski and M. Alini, *Tissue Eng,* 2006, **12**, 1945.

28. E.J. Chong, T.T. Phan, I.J. Lim, Y.Z. Zhang, B.H. Bay, S. Ramakrishna and C.T. Lim, *Acta Biomater,* 2007, **3**, 321.

29. C. Danielsson, S. Ruault, M. Simonet, P. Neuenschwander and P. Frey, *Biomaterials,* 2006, **27**, 1410.

30. A. Hofmann, U. Ritz, S. Verrier, D. Eglin, M. Alini, S. Fuchs, C.J. Kirkpatrick and P.M. Rommens, *Biomaterials,* 2008, **29**, 4217.

31. R. Sodian, J.S. Sperling, D.P. Martin, A. Egozy, U. Stock, J.E. Mayer, Jr. and J.P. Vacanti, *Tissue Eng,* 2000, **6**, 183.

32. C.A. Sundback, J.Y. Shyu, Y. Wang, W.C. Faquin, R.S. Langer, J.P. Vacanti and T.A. Hadlock, *Biomaterials,* 2005, **26**, 5454.

33. R. Shi, D. Chen, Q. Liu, Y. Wu, X. Xu, L. Zhang and W. Tian, *Int J Mol Sci,* 2009, **10**, 4223.

34. J. Boretos and W. Pierce, *Science,* 1967, **158**, 1481.

35. S.A. Guelcher, *Tissue Engineering: Part B,* 2008, **14**, 3.

36. R. Zdrahala and I. Zdrahala, *Journal of Biomaterials Applications,* 1999, **14**, 67.

37. G. Skarja and K. Woodhouse, *Journal of Biomaterial Science, Polymer Edition,* 1998, **9**, 271.

38. G. Skarja and K. Woodhouse, *Journal of Applied Polymer Science,* 2000, **75**, 1522.

39. G. Skarja and K. Woodhouse, *Journal of Biomaterial Science, Polymer Edition,* 2001, **12**, 851.

40. J. Guan and W.R. Wagner, *Biomacromolecules,* 2005, **6**, 2833.

41. J. Guan, M. Sacks, E. Beckman and W.R. Wagner, *Journal of Biomedical Materials Research,* 2002, **61**, 493.

42. J. Kylma and J.V. Seppala, *Macromolecules,* 1997, **30**, 2876.

43. L. Tatai, T.G. Moore, R. Adhikari, F. Malherbe, R. Jayasekara, I. Griffiths and P.A. Gunatillake, *Biomaterials,* 2007, **28**, 5407.

44. G. Ciardelli, A. Rechichi, P. Cerrai, M. Tricoli, N. Barbani and P. Giusti, *Macromolecular Symposia,* 2004, **218**, 261.

45. D. Sarkar, J.C. Yang, A.S. Gupta and S.T. Lopina, *J Biomed Mater Res A,* 2008,

46. D. Sarkar, J.C. Yang and S.T. Lopina, *Journal of Applied Polymer Science,* 2008, **108**, 2345.

47. T.D. Hirt, P. Neuenschwander and U.W. Suter, *Macromol. Chem. Phys.,* 1996, **197**, 4253.

48. D. Cohn, T. Stern, M.F. Gonzalez and J. Epstein, *Journal of Biomedical Materials Research,* 2002, **59**, 273.

49. J. Guan, M. Sacks, E. Beckman and W.R. Wagner, *Biomaterials,* 2004, **25**, 85.

50. G.A. Abraham, A. Marcos-Fernandez and J.S. Roman, *J Biomed Mater Res A,* 2006, **76**, 729.

51. J. Guan, K.L. Fujimoto, M.S. Sacks and W.R. Wagner, *Biomaterials,* 2005, **26**, 3961.

52. K.L. Fujimoto, J. Guan, H. Oshima, T. Sakai and W.R. Wagner, *Ann Thorac Surg,* 2007, **83**, 648.

53. A. Nieponice, L. Soletti, J. Guan, B.M. Deasy, J. Huard, W.R. Wagner and D.A. Vorp, *Biomaterials,* 2008, **29**, 825.

54. M. Borkenhagen, R.C. Stoll, P. Neuenschwander, U.W. Suter and P. Aebischer, *Biomaterials,* 1998, **19**, 2155.

55. K.J. Zhu, R.W. Hendren, K. Jensen and C.G. Pitt, *Macromolecules,* 1991, **24**, 1736.

56. A.P. Pego, M.J. Van Luyn, L.A. Brouwer, P.B. van Wachem, A.A. Poot, D.W. Grijpma and J. Feijen, *J Biomed Mater Res A,* 2003, **67**, 1044.

57. A.P. Pego, A.A. Poot, D.W. Grijpma and J. Feijen, *J Biomater Sci Polym Ed,* 2001, **12**, 35.

58. A.P. Pego, A.A. Poot, D.W. Grijpma and J. Feijen, *J Mater Sci Mater Med,* 2003, **14**, 767.

59. A.P. Pego, A.A. Poot, D.W. Grijpma and J. Feijen, *J Control Release,* 2003, **87**, 69.

60. A.P. Pego, C.L. Vleggeert-Lankamp, M. Deenen, E.A. Lakke, D.W. Grijpma, A.A. Poot, E. Marani and J. Feijen, *J Biomed Mater Res A,* 2003, **67**, 876.

61. A.P. Pego, B. Siebum, M.J. Van Luyn, X.J. Gallego y Van Seijen, A.A. Poot, D.W. Grijpma and J. Feijen, *Tissue Eng,* 2003, **9**, 981.

62. A.P. Pego, D.W. Grijpma and J. Feijen, *Polymer,* 2003, **44**, 6495.

63. B. Buchholz, *Journal of Materials Science: Materials in Medicine,* 1993, **4**, 381.

64. C. Jie and K.J. Zhu, *Polymer International,* 1997, **42**, 373.

65. A.P. Pego, A.A. Poot, D.W. Grijpma and J. Feijen, *Macromolecular Bioscience,* 2002, **2**, 411.

66. Q. Chen, S.E. Harding, N.N. Ali, A.R. Lyon and A.R. Boccaccini, *Materials Science and Engineering R,* 2008, **59**, 1.

67. Q.Z. Chen, A. Bismarck, U. Hansen, S. Junaid, M.Q. Tran, S.E. Harding, N.N. Ali and A.R. Boccaccini, *Biomaterials,* 2008, **29**, 47.

68. T. Fabre, M. Schappacher, R. Bareille, B. Dupuy, A. Soum, J. Bertrand-Barat and C. Baquey, *Biomaterials,* 2001, **22**, 2951.

69. L. Nair and C. Laurencin, *Polym Degrad Stab,* 2007, **32**, 762.

70. S. Lee, *Biotechnology and Bioengineering,* 1996, **49**, 1.

71. Y. Poirier, C. Nawrath and C. Somerville, *Biotechnology (N Y),* 1995, **13**, 142.

72. P. Hocking and R. Marchessault, *Polym Bull,* 1993, **30**, 163.

73. J. Kemnitzer, S. McCarthy and R. Gross, *Macromolecules,* 1993, **26**, 1221.

74. J. Kemnitzer, S. McCarthy and R. Gross, *Macromolecules,* 1993, **16**, 6143.

75. Y. Hori and T. Hagiwara, *Int J Biol Macromol,* 1999, **25**, 237.

76. S. Williams, P. Martin, D. Horowitz and O. Peoples, *International Journal of Biological Macromolecules,* 1999, **25**, 111.

77. U.A. Stock and J.E. Mayer, Jr., *J Long Term Eff Med Implants,* 2001, **11**, 249.

78. U.A. Stock, M. Nagashima, P.N. Khalil, G.D. Nollert, T. Herden, J.S. Sperling, A. Moran, J. Lien, D.P. Martin, F.J. Schoen, J.P. Vacanti and J.E. Mayer, Jr., *J Thorac Cardiovasc Surg,* 2000, **119**, 732.

79. M. Nagata, T. Kiyotsukuri, H. Ibuki, N. Tsutsumi and W. Sakai, *Reactive Functional Polymers,* 1996, **30**, 165.

80. Y. Wang, G.A. Ameer, B.J. Sheppard and R. Langer, *Nat Biotechnol,* 2002, **20**, 602.

81. L. Lei, T. Ding, R.S. R, Q. Liu, L. Zhang, D. Chen and W. Tian, *Polymer Degradation and Stability,* 2007, **92**, 389.

82. Y. Wan, G. Feng, F.H. Shen, G. Balian, C.T. Laurencin and X. Li, *Macromol Biosci,* 2007, **7**, 1217.

83. H. Qiu, J. Yang, P. Kodali, J. Koh and G.A. Ameer, *Biomaterials,* 2006, **27**, 5845.

84. J. Yang, Webb, AR, Hageman, G, Ameer, GA., *Advance Materials,* 2004, **16**, 511.

85. J. Yang, Y. Zhang, S. Gautam, L. Liu, J. Dey, W. Chen, R.P. Mason, C.A. Serrano, K.A. Schug and L. Tang, *Proc Natl Acad Sci U S A,* 2009,

86. M.C. Serrano, L. Carbajal and G.A. Ameer, *Advanced Materials,* 2011, **23**, 2211.

87. R. Shi, J. Bi, Z. Zhang, A. Zhu, D. Chen, X. Zhou, L. Zhang and W. Tian, *Carbohydrate Polymers,* 2008, **74**, 763.

88. J. Yang, D. Motlagh, A.R. Webb and G.A. Ameer, *Tissue Eng,* 2005, **11**, 1876.

89. B.G. Amsden, *Expert Opin Drug Deliv,* 2008, **5**, 175.

90. R. Hoshi, S. Behl and G.A. Ameer, *Advanced Materials,* 2009, **21**, 188.

91. X.Q. Zhang, H. Tang, R. Hoshi, L. De Laporte, H. Qiu, X. Xu, L.D. Shea and G.A. Ameer, *Biomaterials,* 2009, **30**, 2632.

92. T. Ding, Q. Liu, R. Shi, M. Tian, J. Yang and L. Zhang, *Polymer Degradation and Stability,* 2006, **91**, 733.

93. D. Gyawali, R.T. Tran, K.J. Guleserian, L. Tang and J. Yang, *J Biomater Sci Polym Ed,* 2010, **21**, 1761.

94. E.J. Chung, M.J. Sugimoto and G.A. Ameer, *Acta Biomater,* 2011,

95. J. Yang, A.R. Webb, S.J. Pickerill, G. Hageman and G.A. Ameer, *Biomaterials,* 2006, **27**, 1889.

96. C. Laurencin, Y. Khan and S.F. El-Amin, *Expert Rev Med Devices,* 2006, **3**, 49.

97. X. Gao, L. Yang, J.A. Petros, F.F. Marshall, J.W. Simons and S. Nie, *Curr Opin Biotechnol,* 2005, **16**, 63.

98. M. Gaumet, R. Gurny and F. Delie, *Int J Pharm,* 2007, **342**, 222.

99. Y. Ogura and H. Kimura, *Surv Ophthalmol,* 1995, **39 Suppl 1**, S17.

100. M.N. Rhyner, A.M. Smith, X. Gao, H. Mao, L. Yang and S. Nie, *Nanomed,* 2006, **1**, 209.

101. J. Yang, J. Gunn, S.R. Dave, M. Zhang, Y.A. Wang and X. Gao, *Analyst,* 2008, **133**, 154.

102. E.R. Wright and V.P. Conticello, *Adv Drug Deliv Rev,* 2002, **54**, 1057.

103. S. Wang, W. Cui and J. Bei, *Anal Bioanal Chem,* 2005, **381**, 547.

104. Y.-Q. Wang and J.-Y. Cai, *Current Applied Physics,* 2007, **7S1**, e108.

105. B. Amsden, *Soft Matter,* 2007, **3**, 1335

106. L. Yu and J. Ding, *Chem Soc Rev,* 2008, **37**, 1473.

107. B. Guo, J. Yuan and Q. Gao, *Colloids Surf B Biointerfaces,* 2007, **58**, 151.

108. S. Harrisson and K.L. Wooley, *Chem Commun (Camb),* 2005, 3259.

109. S.H. Kim, C.Y. Won and C.C. Chu, *J Biomed Mater Res,* 1999, **46**, 160.

110. M. Lang and C.-C. Chu, *J Appl Polym Sci,* 2002, **86**, 2296.

111. T. Pompe, S. Zschoche, N. Herold, K. Salchert, M.F. Gouzy, C. Sperling and C. Werner, *Biomacromolecules,* 2003, **4**, 1072.

112. J.P. Fisher, T.A. Holland, D. Dean and A.G. Mikos, *Biomacromolecules,* 2003, **4**, 1335.

113. S. Tanodekaew, S. Channasanon and P. Uppanan, *J. Appl. Polym. Sci.,* 2006, **100**, 1914.

114. W. Zhu and J. Ding, *J Appl Polym Sci,* 2005, **99**, 2375.

115. D.A. Solovjov, E. Pluskota and E.F. Plow, *J Biol Chem,* 2005, **280**, 1336.

116. P.-J. Shi, Y.-G. Li and C.-Y. Pan, *European Polymer Journal,* 2004, **40**, 1283.

117. B.D. Ratner and S.J. Bryant, *Annu Rev Biomed Eng,* 2004, **6**, 41.

118. J. Yang, Y. Wan, J. Bei and S. Wang, *J Biomed Mater Res A,* 2003, **67**, 1139.

119. Z. Chen, S. Cheng and K. Xu, *Biomaterials,* 2009, **30**, 2219.

120. C.J. Bettinger, B. Orrick, A. Misra, R. Langer and J.T. Borenstein, *Biomaterials,* 2006, **27**, 2558.

121. Y.F. Poon, Y. Cao, Y. Zhu, Z.M. Judeh and M.B. Chan-Park, *Biomacromolecules,* 2009, **10**, 2043.

122. I. Levental, P. Georges and P. Janmey, *Soft Matter,* 2007, **3**, 299.

123. A. Jacinto, A. Martinez-Arias and P. Martin, *Nat. Cell Biol.,* 2001, **3**, E117.

124. R. Bashir, *Adv Drug Deliv Rev,* 2004, **56**, 1565.

125. A. Khademhosseini and R. Langer, *Biomaterials,* 2007, **28**, 5087.

126. A.K. Burkoth and K.S. Anseth, *Biomaterials,* 2000, **21**, 2395.

127. C.J. Bettinger, J.P. Bruggeman, J.T. Borenstein and R.S. Langer, *Biomaterials,* 2008, **29**, 2315.

128. T.R. Kyriakides, M.J. Foster, G.E. Keeney, A. Tsai, C.M. Giachelli, I. Clark-Lewis, B.J. Rollins and P. Bornstein, *Am J Pathol,* 2004, **165**, 2157.

129. J.M. Anderson, A. Rodriguez and D.T. Chang, *Semin Immunol,* 2008, **20**, 86.

130. S. Atzet, S. Curtin, P. Trinh, S. Bryant and B. Ratner, *Biomacromolecules,* 2008, **9**, 3370.

131. C. Alperin, P.W. Zandstra and K.A. Woodhouse, *Biomaterials,* 2005, **26**, 7377.

132. S.E. Dahms, H.J. Piechota, R. Dahiya, T.F. Lue and E.A. Tanagho, *Br J Urol,* 1998, **82**, 411.

133. M.C. Lee and R.C. Haut, *J Biomech,* 1992, **25**, 925.

134. J.A. Clark, J.C. Cheng and K.S. Leung, *Burns,* 1996, **22**, 443.

135. R. Tran, P. Thevenot, Y. Zhang, L. Tang and J. Yang, *Materials,* 2010, **3**, 1375.

136. C.C. Berry, G. Campbell, A. Spadiccino, M. Robertson and A.S. Curtis, *Biomaterials,* 2004, **25**, 5781.

137. S.A. Sell, M.P. Francis, K. Garg, M.J. McClure, D.G. Simpson and G.L. Bowlin, *Biomedical Materials,* 2008, **3**, 11.

138. X. Zong, H. Bien, C.Y. Chung, L. Yin, D. Fang, B.S. Hsiao, B. Chu and E. Entcheva, *Biomaterials,* 2005, **26**, 5330.

139. R. Jayakumar, Y.S. Lee and S. Nanjundan, *Journal of Applied Polymer Science,* 2003, **90**, 3488.

140. B. Chu, T. Gao, Y. Li, J. Wang, C.R. Desper and C.A. Byrne, *Macromolecules,* 1992, **25**, 5724.

141. J.T. Garrett and J. Runt, *Macromolecules,* 2000, **33**, 6353.

142. F. Li, J. Hou, W. Zhu, X. Zhang, M. Xu, X. Luo, D. Ma and K. Kim, *Journal of Applied Polymer Science,* 1996, **62**, 631.

143. K. Nakamae, T. Nishino, S. Asaoka and Sudaryanto, *International Journal of Adhesion and Adhesives,* 1996, **16**, 233.

144. K. Gorna and S. Gogolewski, *J Biomed Mater Res,* 2002, **60**, 592.

145. S.Y. Lee, J.C. Lee and B.K. Kim, *Polymer International,* 1997, **42**, 67.

146. D.S. Muggli, A.K. Burkoth and K.S. Anseth, *J Biomed Mater Res,* 1999, **46**, 271.

147. J. Yang, J. Bei and S. Wang, *Biomaterials,* 2002, **23**, 2607.

148. S.H. Kim, H.J. Ha, Y.K. Ko, S.J. Yoon, J.M. Rhee, M.S. Kim, H.B. Lee and G. Khang, *J Biomater Sci Polym Ed,* 2007, **18**, 609.

149. L.G. Cima, J.P. Vacanti, C. Vacanti, D. Ingber, D. Mooney and R. Langer, *J Biomech Eng,* 1991, **113**, 143.

150. J.N. Mansbridge, *Curr Opin Biotechnol,* 2009, **20**, 563.

151. R. Cancedda, P. Giannoni and M. Mastrogiacomo, *Biomaterials,* 2007, **28**, 4240.

152. M. Marcacci, M. Berruto, D. Brocchetta, A. Delcogliano, D. Ghinelli, A. Gobbi, E. Kon, L. Pederzini, D. Rosa, G.L. Sacchetti, G. Stefani and S. Zanasi, *Clin Orthop Relat Res,* 2005, 96.

153. S. Calve, R.G. Dennis, P.E. Kosnik, 2nd, K. Baar, K. Grosh and E.M. Arruda, *Tissue Eng,* 2004, **10**, 755.

154. G. Vunjak-Novakovic, G. Altman, R. Horan and D.L. Kaplan, *Annu Rev Biomed Eng,* 2004, **6**, 131.

155. K.M. Kulig and J.P. Vacanti, *Transpl Immunol,* 2004, **12**, 303.

156. H. Jawad, N.N. Ali, A.R. Lyon, Q.Z. Chen, S.E. Harding and A.R. Boccaccini, *J Tissue Eng Regen Med,* 2007, **1**, 327.

157. N. Koike, D. Fukumura, O. Gralla, P. Au, J.S. Schechner and R.K. Jain, *Nature,* 2004, **428**, 138.

158. R.A. Penkala and S.S. Kim, *Expert Rev Med Devices,* 2007, **4**, 65.

159. M.S. Stosich and J.J. Mao, *Plast Reconstr Surg,* 2007, **119**, 71.

160. H.C. Fiegel, P.M. Kaufmann, H. Bruns, D. Kluth, R.E. Horch, J.P. Vacanti and U. Kneser, *J Cell Mol Med,* 2008, **12**, 56.

161. W.R. Wagner and B.P. Griffith, *Science,* 2010, **329**, 520.

162. C.T. Chalfoun, G.A. Wirth and G.R. Evans, *J Cell Mol Med,* 2006, **10**, 309.

163. E. Sachlos and J.T. Czernuszka, *Eur Cell Mater,* 2003, **5**, 29.

164. C.E. Ayres, B.S. Jha, S.A. Sell, G.L. Bowlin and D.G. Simpson, *Wiley Interdiscip Rev Nanomed Nanobiotechnol,* 2010, **2**, 20.

165. S.J. Hollister, *Nat Mater,* 2005, **4**, 518.

166. W.J. Li, C.T. Laurencin, E.J. Caterson, R.S. Tuan and F.K. Ko, *J Biomed Mater Res,* 2002, **60**, 613.

167. R. Tran, P. Thevenot, D. Gyawali, J. Chiao, L. Tang and J. Yang, *Soft Matter,* 2010, **6**, 2449.

168. I.O. Smith, X.H. Liu, L.A. Smith and P.X. Ma, *Wiley Interdiscip Rev Nanomed Nanobiotechnol,* 2009, **1**, 226.

169. D.W. Hutmacher, T. Schantz, I. Zein, K.W. Ng, S.H. Teoh and K.C. Tan, *J Biomed Mater Res,* 2001, **55**, 203.

170. F.J. O'Brien, B.A. Harley, I.V. Yannas and L.J. Gibson, *Biomaterials,* 2005, **26**, 433.

171. J. Zeltinger, J.K. Sherwood, D.A. Graham, R. Mueller and L.G. Griffith, *Tissue Eng,* 2001, **7**, 557.

172. F.J. O'Brien, B.A. Harley, I.V. Yannas and L. Gibson, *Biomaterials,* 2004, **25**, 1077.

173. A. Galperin, T.J. Long and B.D. Ratner, *Biomacromolecules,* 2010,

174. W.L. Murphy, R.G. Dennis, J.L. Kileny and D.J. Mooney, *Tissue Eng,* 2002, **8**, 43.

175. J. Lee, H. Lee, J. Kim, S. Hyon and S. Kim, *J Appl Polym Sci,* 2003, **88**, 2224.

176. T.H. Young, C.W. Lin, L.P. Cheng and C.C. Hsieh, *Biomaterials,* 2001, **22**, 1771.

177. N. Krasteva, B. Seifert, W. Albrecht, T. Weigel, M. Schossig, G. Altankov and T. Groth, *Biomaterials,* 2004, **25**, 2467.

178. A.G. Coombes, S.C. Rizzi, M. Williamson, J.E. Barralet, S. Downes and W.A. Wallace, *Biomaterials,* 2004, **25**, 315.

179. P. Sarazin, X. Roy and B.D. Favis, *Biomaterials,* 2004, **25**, 5965.

180. P. Roychowdhury and V. Kumar, *J Biomed Mater Res A,* 2006, **76**, 300.

181. A. Salerno, M. Oliviero, E. Di Maio, S. Iannace and P.A. Netti, *J Mater Sci Mater Med,* 2009, **20**, 2043.

182. H. Haugen, V. Ried, M. Brunner, J. Will and E. Wintermantel, *J Mater Sci Mater Med,* 2004, **15**, 343.

183. X.H. Zhu, L.Y. Lee, J.S. Jackson, Y.W. Tong and C.H. Wang, *Biotechnol Bioeng,* 2008, **100**, 998.

184. E. Maio, G. Mensitieri, S. Iiannace, L. Nicolais, W. Li and R. Rlumerfeit, *Polymer Engineering & Science,* 2005, **45**, 432.

185. P.G. Jessop and B. Subramaniam, *Chem Rev,* 2007, **107**, 2666.

186. Q. Xu, X. Ren, Y. Chang, J. Wang, L. Yu and K. Dean, *J Appl Polym Sci,* 2004, **94**, 593.

187. J.J. Barry, H.S. Gidda, C.A. Scotchford and S.M. Howdle, *Biomaterials,* 2004, **25**, 3559.

188. Y.S. Nam, J.J. Yoon and T.G. Park, *J Biomed Mater Res,* 2000, **53**, 1.

189. W. Sun, A. Darling, B. Starly and J. Nam, *Biotechnol Appl Biochem,* 2004, **39**, 29.

190. S.M. Peltola, F.P. Melchels, D.W. Grijpma and M. Kellomaki, *Ann Med,* 2008, **40**, 268.

191. C.Z. Liu, Z.D. Xia, Z.W. Han, P.A. Hulley, J.T. Triffitt and J.T. Czernuszka, *J Biomed Mater Res B Appl Biomater,* 2008, **85**, 519.

192. M. Xu, Y. Li, H. Suo, Y. Yan, L. Liu, Q. Wang, Y. Ge and Y. Xu, *Biofabrication,* 2010, **2**, 025002.

193. T. Cao, K.H. Ho and S.H. Teoh, *Tissue Eng,* 2003, **9 Suppl 1**, S103.

194. W.Y. Yeong, N. Sudarmadji, H.Y. Yu, C.K. Chua, K.F. Leong, S.S. Venkatraman, Y.C. Boey and L.P. Tan, *Acta Biomater,* 2010, **6**, 2028.

195. W.Y. Yeong, C.K. Chua, K.F. Leong and M. Chandrasekaran, *Trends Biotechnol,* 2004, **22**, 643.

196. D.W. Hutmacher, *Biomaterials,* 2000, **21**, 2529.

197. C.M. Cheah, C.K. Chua, K.F. Leong, C.H. Cheong and M.W. Naing, *Tissue Eng,* 2004, **10**, 595.

198. T. Weigel, G. Schinkel and A. Lendlein, *Expert Rev Med Devices,* 2006, **3**, 835.

199. Z. Ma, M. Kotaki, R. Inai and S. Ramakrishna, *Tissue Eng,* 2005, **11**, 101.

200. D. Gyawali, P. Nair, Y. Zhang, R. Tran, M. Samchukov, M. Makarov, H. Kim and J. Yang, *Biomaterials,* 2010,

201. Y.S. Nam and T.G. Park, *J Biomed Mater Res,* 1999, **47**, 8.

202. C.J. Liao, C.F. Chen, J.H. Chen, S.F. Chiang, Y.J. Lin and K.Y. Chang, *J Biomed Mater Res,* 2002, **59**, 676.

203. Z. Ma, C. Gao, Y. Gong and J. Shen, *J Biomed Mater Res B Appl Biomater,* 2003, **67**, 610.

204. J.S. Capes, H.Y. Ando and R.E. Cameron, *J Mater Sci Mater Med,* 2005, **16**, 1069.

205. L. Draghi, S. Resta, M.G. Pirozzolo and M.C. Tanzi, *J Mater Sci Mater Med,* 2005, **16**, 1093.

206. I. Leubner, *Precision Crystallization*. 2010, Boca Raton, FL: CRC Press.

207. E. Pechkova, R. Gebhardt, C. Riekel and C. Nicolini, *Biophys J,* 2010, **99**, 1256.

208. H.M. Galindo, Y. Carvajal, E. Njagi, R.A. Ristau and S.L. Suib, *Langmuir,* 2010, **26**, 13677.

209. J. De Yoreo and P. Vekilov, *Principles of crystal nucleation and growth*. Biomineralization, ed. S. Weiner. Vol. 54. 2003, Washington, DC. 57.

210. J.A. Mathew, V. Kache, C. Liu, L. Tang and J. Yang, *Nano-featured highly interconnective macroporous elastic scaffolds for cardiovascular tissue engineering*, in *Engineering in Medicine and Biology Workshop, 2007 IEEE Dallas*. 2007: Dallas, TX. p. 43.

211. M. Grellier, L. Bordenave and J. Amedee, *Trends Biotechnol,* 2009, **27**, 562.

212. S. Tully-Dartez, H.E. Cardenas and P.F. Sit, *Tissue Eng Part C Methods,* 2010, **16**, 339.

213. A.C. Jones, C.H. Arns, D.W. Hutmacher, B.K. Milthorpe, A.P. Sheppard and M.A. Knackstedt, *Biomaterials,* 2009, **30**, 1440.

214. V. Guarino, A. Guaccio, P.A. Netti and L. Ambrosio, *J Mater Sci Mater Med,* 2010, **21**, 3109.

215. C.M. Puleo, H.C. Yeh and T.H. Wang, *Tissue Eng,* 2007, **13**, 2839.

216. B.J. Papenburg, J. Liu, G.A. Higuera, A.M. Barradas, J. de Boer, C.A. van Blitterswijk, M. Wessling and D. Stamatialis, *Biomaterials,* 2009, **30**, 6228.

217. B.J. Papenburg, L. Vogelaar, L.A. Bolhuis-Versteeg, R.G. Lammertink, D. Stamatialis and M. Wessling, *Biomaterials,* 2007, **28**, 1998.

218. M.F. Fillinger, L.N. Sampson, J.L. Cronenwett, R.J. Powell and R.J. Wagner, *J Surg Res,* 1997, **67**, 169.

219. P.F. Davies, *Lab Invest,* 1986, **55**, 5.

220. C. Williams and T.M. Wick, *Ann Biomed Eng,* 2005, **33**, 920.

221. E.V. Lyubimov and A.I. Gotlieb, *Cardiovasc Pathol,* 2004, **13**, 139.

222. N. Hisano, Y. Yatomi, K. Satoh, S. Akimoto, M. Mitsumata, M.A. Fujino and Y. Ozaki, *Blood,* 1999, **93**, 4293.

223. M.A. Brown, L. Zhang, V.W. Levering, J.H. Wu, L.L. Satterwhite, L. Brian, N.J. Freedman and G.A. Truskey, *Arterioscler Thromb Vasc Biol,* 2010,

224. W. Ryu, S.W. Min, K.E. Hammerick, M. Vyakarnam, R.S. Greco, F.B. Prinz and R.J. Fasching, *Biomaterials,* 2007, **28**, 1174.

225. S. Yang, K.F. Leong, Z. Du and C.K. Chua, *Tissue Eng,* 2001, **7**, 679.

226. M.I. Santos, S. Fuchs, M.E. Gomes, R.E. Unger, R.L. Reis and C.J. Kirkpatrick, *Biomaterials,* 2007, **28**, 240.

227. X. Liu and P.X. Ma, *Biomaterials,* 2009, **30**, 4094.

228. S.K. Misra, T.I. Ansari, S.P. Valappil, D. Mohn, S.E. Philip, W.J. Stark, I. Roy, J.C. Knowles, V. Salih and A.R. Boccaccini, *Biomaterials,* 2009,

229. L. Boldrin, A. Malerba, L. Vitiello, E. Cimetta, M. Piccoli, C. Messina, P.G. Gamba, N. Elvassore and P. De Coppi, *Cell Transplant,* 2008, **17**, 577.

230. A.R. Costa-Pinto, A.J. Salgado, V.M. Correlo, P. Sol, M. Bhattacharya, P. Charbord, R.L. Reis and N.M. Neves, *Tissue Eng Part A,* 2008, **14**, 1049.

231. C.A. Vacanti, L.J. Bonassar, M.P. Vacanti and J. Shufflebarger, *N Engl J Med,* 2001, **344**, 1511.

232. M. Poh, M. Boyer, A. Solan, S.L. Dahl, D. Pedrotty, S.S. Banik, J.A. McKee, R.Y. Klinger, C.M. Counter and L.E. Niklason, *Lancet,* 2005, **365**, 2122.

233. I. Vesely, *Circ Res,* 2005, **97**, 743.

234. A.S. Goldstein, T.M. Juarez, C.D. Helmke, M.C. Gustin and A.G. Mikos, *Biomaterials,* 2001, **22**, 1279.

235. S.L. Ishaug-Riley, G.M. Crane, A. Gurlek, M.J. Miller, A.W. Yasko, M.J. Yaszemski and A.G. Mikos, *J Biomed Mater Res,* 1997, **36**, 1.

236. I. Martin, R.F. Padera, G. Vunjak-Novakovic and L.E. Freed, *J Orthop Res,* 1998, **16**, 181.

237. N. L'Heureux, S. Paquet, R. Labbe, L. Germain and F.A. Auger, *Faseb Journal,* 1998, **12**, 47.

238. M. Yamato, M. Utsumi, A. Kushida, C. Konno, A. Kikuchi and T. Okano, *Tissue Eng,* 2001, **7**, 473.

239. K. Nishida, M. Yamato, Y. Hayashida, K. Watanabe, N. Maeda, H. Watanabe, K. Yamamoto, S. Nagai, A. Kikuchi, Y. Tano and T. Okano, *Transplantation,* 2004, **77**, 379.

240. Y. Shiroyanagi, M. Yamato, Y. Yamazaki, H. Toma and T. Okano, *BJU Int,* 2004, **93**, 1069.

241. M. Hasegawa, M. Yamato, A. Kikuchi, T. Okano and I. Ishikawa, *Tissue Eng,* 2005, **11**, 469.

242. J. Yang, M. Yamato, K. Nishida, T. Ohki, M. Kanzaki, H. Sekine, T. Shimizu and T. Okano, *J Control Release,* 2006, **116**, 193.

243. R.M. Nerem and D. Seliktar, *Annu Rev Biomed Eng,* 2001, **3**, 225.

244. J. Yang, G. Shi, J. Bei, S. Wang, Y. Cao, Q. Shang, G. Yang and W. Wang, *J Biomed Mater Res,* 2002, **62**, 438.

245. S.J. Lee, S.H. Oh, J. Liu, S. Soker, A. Atala and J.J. Yoo, *Biomaterials,* 2008, **29**, 1422.

246. G. Vunjak-Novakovic and L.E. Freed, *Adv Drug Deliv Rev,* 1998, **33**, 15.

247. B.S. Kim, J. Nikolovski, J. Bonadio, E. Smiley and D.J. Mooney, *Exp Cell Res,* 1999, **251**, 318.

248. D.J. Mooney, C.L. Mazzoni, C. Breuer, K. McNamara, D. Hern, J.P. Vacanti and R. Langer, *Biomaterials,* 1996, **17**, 115.

249. W.J. van der Giessen, A.M. Lincoff, R.S. Schwartz, H.M. van Beusekom, P.W. Serruys, D.R. Holmes, Jr., S.G. Ellis and E.J. Topol, *Circulation,* 1996, **94**, 1690.

250. M. Watanabe, T. Shin'oka, S. Tohyama, N. Hibino, T. Konuma, G. Matsumura, Y. Kosaka, T. Ishida, Y. Imai, M. Yamakawa, Y. Ikada and S. Morita, *Tissue Eng,* 2001, **7**, 429.

251. G. Zund, S.P. Hoerstrup, A. Schoeberlein, M. Lachat, G. Uhlschmid, P.R. Vogt and M. Turina, *Eur J Cardiothorac Surg,* 1998, **13**, 160.

252. B. Amsden, S. Wang and U. Wyss, *Biomacromolecules,* 2004, **5**, 1399.

253. H.M. Younes, E. Bravo-Grimaldo and B.G. Amsden, *Biomaterials,* 2004, **25**, 5261.

254. S.J. Lee, J. Liu, S.H. Oh, S. Soker, A. Atala and J.J. Yoo, *Biomaterials,* 2008, **29**, 2891.

255. T. Huynh, G. Abraham, J. Murray, K. Brockbank, P.O. Hagen and S. Sullivan, *Nat Biotechnol,* 1999, **17**, 1083.

256. M. Avci-Adali, G. Ziemer and H.P. Wendel, *Biotechnol Adv,* 2010, **28**, 119.

257. V.L. Roger, A.S. Go, D.M. Lloyd-Jones, R.J. Adams, J.D. Berry, T.M. Brown, M.R. Carnethon, S. Dai, G. de Simone, E.S. Ford, C.S. Fox, H.J. Fullerton, C. Gillespie, K.J. Greenlund, S.M. Hailpern, J.A. Heit, P.M. Ho, V.J. Howard, B.M. Kissela, S.J. Kittner, D.T. Lackland, J.H. Lichtman, L.D. Lisabeth, D.M. Makuc, G.M. Marcus, A. Marelli, D.B. Matchar, M.M. McDermott, J.B. Meigs, C.S. Moy, D. Mozaffarian, M.E. Mussolino, G. Nichol, N.P. Paynter, W.D. Rosamond, P.D. Sorlie, R.S. Stafford, T.N. Turan, M.B. Turner, N.D. Wong and J. Wylie-Rosett, *Circulation*, **123**, e18.

258. X. Wang, P. Lin, Q. Yao and C. Chen, *World J Surg,* 2007, **31**, 682.

259. F.J. Veith, C.M. Moss, S. Sprayregen and C. Montefusco, *Surgery,* 1979, **85**, 253.

260. S. Ravi and E.L. Chaikof, *Regen Med*, **5**, 107.

261. R.Y. Kannan, H.J. Salacinski, P.E. Butler, G. Hamilton and A.M. Seifalian, *J Biomed Mater Res B Appl Biomater,* 2005, **74**, 570.

262. L. Xue and H.P. Greisler, *J Vasc Surg,* 2003, **37**, 472.

263. O. Basaran, H. Karakayali, R. Emiroglu, S. Belli and M. Haberal, *Transplant Proc,* 2003, **35**, 2578.

264. S.W. Jordan and E.L. Chaikof, *J Vasc Surg,* 2007, **45 Suppl A**, A104.

265. C.B. Weinberg and E. Bell, *Science,* 1986, **231**, 397.

266. P.J. Schaner, N.D. Martin, T.N. Tulenko, I.M. Shapiro, N.A. Tarola, R.F. Leichter, R.A. Carabasi and P.J. Dimuzio, *J Vasc Surg,* 2004, **40**, 146.

267. C.E. Schmidt and J.M. Baier, *Biomaterials,* 2000, **21**, 2215.

268. B.K. Mann, A.S. Gobin, A.T. Tsai, R.H. Schmedlen and J.L. West, *Biomaterials,* 2001, **22**, 3045.

269. N. L'Heureux, S. Paquet, R. Labbe, L. Germain and F.A. Auger, *FASEB J,* 1998, **12**, 47.

270. Y. Zhu, C. Gao, X. Liu, T. He and J. Shen, *Tissue Eng,* 2004, **10**, 53.

271. S. Iwai, Y. Sawa, H. Ichikawa, S. Taketani, E. Uchimura, G. Chen, M. Hara, J. Miyake and H. Matsuda, *J Thorac Cardiovasc Surg,* 2004, **128**, 472.

272. S.P. Hoerstrup, G. Zund, R. Sodian, A.M. Schnell, J. Grunenfelder and M.I. Turina, *Eur J Cardiothorac Surg,* 2001, **20**, 164.

273. S. Nemcova, A.A. Noel, C.J. Jost, P. Gloviczki, V.M. Miller and K.G. Brockbank, *J Invest Surg,* 2001, **14**, 321.

274. J. Dey, H. Xu, K.T. Nguyen and J. Yang, *Journal of Biomedical Materials Research Part A,* 2010, **95A**, 361.

275. A.W. Martinez and E.L. Chaikof, *Wiley Interdiscip Rev Nanomed Nanobiotechnol,* 2011, **3**, 256.

276. J. Lu, D. Khang and T.J. Webster, *J Biomed Mater Res A,* 2010, **94**, 1042.

277. P. Wang, J. Hu and P.X. Ma, *Biomaterials,* 2009, **30**, 2735.

278. M. Centola, A. Rainer, C. Spadaccio, S. De Porcellinis, J.A. Genovese and M. Trombetta, *Biofabrication,* 2010, **2**, 014102.

279. D.J. Bryan, J.B. Tang, S.A. Doherty, D.D. Hile, D.J. Trantolo, D.L. Wise and I.C. Summerhayes, *J Neural Eng,* 2004, **1**, 91.

280. A. Bozkurt, G.A. Brook, S. Moellers, F. Lassner, B. Sellhaus, J. Weis, M. Woeltje, J. Tank, C. Beckmann, P. Fuchs, L.O. Damink, F. Schugner, I. Heschel and N. Pallua, *Tissue Eng,* 2007, **13**, 2971.

281. Y.C. Huang, Y.Y. Huang, C.C. Huang and H.C. Liu, *J Biomed Mater Res B Appl Biomater,* 2005, **74**, 659.

282. A. Bozkurt, R. Deumens, C. Beckmann, L. Olde Damink, F. Schugner, I. Heschel, B. Sellhaus, J. Weis, W. Jahnen-Dechent, G.A. Brook and N. Pallua, *Biomaterials,* 2009, **30**, 169.

283. P. Thomas, *Muscle Nerve,* 1989, **12**, 796.

284. V. Guenard, N. Kleitman, T.K. Morrissey, R.P. Bunge and P. Aebischer, *J Neurosci,* 1992, **12**, 3310.

285. W.B. Jacobs and M.G. Fehlings, *Neurosurgery,* 2003, **53**, 943.

286. L. Flynn, P.D. Dalton and M.S. Shoichet, *Biomaterials,* 2003, **24**, 4265.

287. A.J. Krych, G.E. Rooney, B. Chen, T.C. Schermerhorn, S. Ameenuddin, L. Gross, M.J. Moore, B.L. Currier, R.J. Spinner, J.A. Friedman, M.J. Yaszemski and A.J. Windebank, *Acta Biomater,* 2009, **5**, 2551.

288. M.D. Bender, J.M. Bennett, R.L. Waddell, J.S. Doctor and K.G. Marra, *Biomaterials,* 2004, **25**, 1269.

289. N. Dubey, P.C. Letourneau and R.T. Tranquillo, *Exp Neurol,* 1999, **158**, 338.

290. N. Rangappa, A. Romero, K.D. Nelson, R.C. Eberhart and G.M. Smith, *J Biomed Mater Res,* 2000, **51**, 625.

291. N. Terada, L.M. Bjursten, M. Papaloizos and G. Lundborg, *Restor Neurol Neurosci,* 1997, **11**, 65.

292. S. Wang, A.C. Wan, X. Xu, S. Gao, H.Q. Mao, K.W. Leong and H. Yu, *Biomaterials,* 2001, **22**, 1157.

293. T.R. Stevenson, V.A. Kadhiresan and J.A. Faulkner, *J Reconstr Microsurg,* 1994, **10**, 171.

294. C. Sundback, T. Hadlock, M. Cheney and J. Vacanti, *Biomaterials,* 2003, **24**, 819.

295. T. Hadlock, C. Sundback, D. Hunter, M. Cheney and J.P. Vacanti, *Tissue Eng,* 2000, **6**, 119.

296. A. Wang, Q. Ao, W. Cao, M. Yu, Q. He, L. Kong, L. Zhang, Y. Gong and X. Zhang, *J Biomed Mater Res A,* 2006, **79**, 36.

297. Q. Ao, A. Wang, W. Cao, L. Zhang, L. Kong, Q. He, Y. Gong and X. Zhang, *J Biomed Mater Res A,* 2006, **77**, 11.

298. Q. Lu, A. Simionescu and N. Vyavahare, *Acta Biomater,* 2005, **1**, 607.

299. C.A. Brayfield, K.G. Marra, J.P. Leonard, X. Tracy Cui and J.C. Gerlach, *Acta Biomater,* 2008, **4**, 244.

300. M. Zhang and I.V. Yannas, *Adv Biochem Eng Biotechnol,* 2005, **94**, 67.

301. X. Hu, J. Huang, Z. Ye, L. Xia, M. Li, B. Lv, X. Shen and Z. Luo, *Tissue Eng Part A,* 2009, **15**, 3297.

302. J. Li, T.A. Rickett and R. Shi, *Langmuir,* 2009, **25**, 1813.

303. J. Ferlay, H. Shin, F. Bray, D. Forman, C. Mathers and D. Parkin. *Cancer Incidence and Mortality Worldwide: IARC CancerBase No. 10* 2008 [cited; International Agency for Research on Cancer]. Available from: http://globocan.iarc.fr.

304. H. Inoue, N. Fukami, T. Yoshida and S.E. Kudo, *J Gastroenterol Hepatol,* 2002, **17**, 382.

305. V. Catalano, R. Labianca, G.D. Beretta, G. Gatta, F. de Braud and E. Van Cutsem, *Crit Rev Oncol Hematol,* 2009, **71**, 127.

306. C. Tselepis, I. Perry, C. Dawson, R. Hardy, S.J. Darnton, C. McConkey, R.C. Stuart, N. Wright, R. Harrison and J.A. Jankowski, *Oncogene,* 2002, **21**, 6071.

307. P. Hermanek and C. Wittekind, *World J Surg,* 1995, **19**, 491.

308. D. Polymeros, G. Kotsalidis, K. Triantafyllou, G. Karamanolis, J.G. Panagiotides and S.D. Ladas, *Dig Liver Dis*, **42**, 226.

309. N. Rosenberg, *AMA Arch Surg,* 1955, **70**, 120.

310. M. Fujishiro, N. Yahagi, K. Kashimura, Y. Mizushima, M. Oka, S. Enomoto, N. Kakushima, K. Kobayashi, T. Hashimoto, M. Iguchi, Y. Shimizu, M. Ichinose and M. Omata, *Endoscopy,* 2004, **36**, 579.

311. S.V. Kantsevoy, D.G. Adler, J.D. Conway, D.L. Diehl, F.A. Farraye, R. Kwon, P. Mamula, S. Rodriguez, R.J. Shah, L.M. Wong Kee Song and W.M. Tierney, *Gastrointest Endosc,* 2008, **68**, 11.

312. H. Yamamoto, T. Yube, N. Isoda, Y. Sato, Y. Sekine, T. Higashizawa, K. Ido, K. Kimura and N. Kanai, *Gastrointest Endosc,* 1999, **50**, 251.

313. S.H. Lee, W.Y. Cho, H.J. Kim, Y.H. Kim, I.K. Chung, H.S. Kim, S.H. Park and S.J. Kim, *Gastrointest Endosc,* 2004, **59**, 220.

314. T. Uraoka, T. Fujii, Y. Saito, T. Sumiyoshi, F. Emura, P. Bhandari, T. Matsuda, K.I. Fu and D. Saito, *Gastrointest Endosc,* 2005, **61**, 736.

315. J.J. Hyun, H.R. Chun, H.J. Chun, Y.T. Jeen, C.W. Baeck, S.K. Yu, Y.S. Kim, H.S. Lee, S.H. Um, S.W. Lee, J.H. Choi, C.D. Kim, H.S. Ryu and J.H. Hyun, *Scand J Gastroenterol,* 2006, **41**, 488.

316. Y. Matsui, M. Inomata, K. Izumi, K. Sonoda, N. Shiraishi and S. Kitano, *Gastrointest Endosc,* 2004, **60**, 539.

317. S.H. Eun, J.Y. Cho, I.S. Jung, B.M. Ko, S.J. Hong, C.B. Ryu, J.O. Kim, S.Y. Jin, J.S. Lee, M.S. Lee, C.S. Shim and B.S. Kim, *Gut Liver,* 2007, **1**, 27.

318. T. Hayashi, T. Matsuyama, K. Hanada, K. Nakanishi, M. Uenoyama, M. Fujita, M. Ishihara, M. Kikuchi, T. Ikeda and H. Tajiri, *J Biomed Mater Res B Appl Biomater,* 2004, **71**, 367.

319. G. Fernandez-Esparrach, S.N. Shaikh, A. Cohen, M.B. Ryan and C.C. Thompson, *Gastrointest Endosc,* 2009, **69**, 1135.

320. Y.J. Kim, J.H. Cheon, S.K. Lee, J.H. Kim and Y.C. Lee, *J Korean Med Sci,* 2010, **25**, 583.

321. J. Bures, M. Kopacova, J. Kvetina, J. Osterreicher, Z. Sinkorova, Z. Svoboda, I. Tacheci, S. Filip, S. Spelda, M. Kunes and S. Rejchrt, *Surg Endosc,* 2009, **23**, 2094.

322. S. Coda, S.Y. Lee and T. Gotoda, *Gut and Liver,* 2007, **1**, 12.

BIOGRAPHICAL INFORMATION

Born in Fort Worth, Texas as a first generation American, Minh-Tuan “Richard” Tran graduated from the High School of Medical Professions and became the first in his extended family to attend university. He was awarded Baylor University’s Presidential Scholarship, and earned his Bachelor of Science degree in Bioinformatics with minors in Mathematics and Engineering in 2004. During his undergraduate studies, Richard was a key member in chartering the first Asian-American Service Fraternity, headed an annual local Bone Marrow Donor Program, and managed an after school Literacy Program for at risk students in the Waco Independent School District.

In 2006, Richard was accepted into the Joint Graduate Program in Biomedical Engineering at The University of Texas at Arlington and the University of Texas Southwestern Medical Center. Under the guidance of Dr. Jian Yang, he began his doctoral work, which focused on biodegradable elastomer development for novel tissue engineering scaffolding, and earned a Ph.D. in Bioengineering in the fall of 2011. In addition to his graduate work, Richard served as the Lab Manager for the UTA Biomaterials Lab, Teacher’s Assistant for Nanobiomaterials and Polymers in Biomedical Engineering graduate courses, and instructor for the Biomaterials Outreach Program with Martin High School. In 2011, he was honored as a University Scholar by the University of Texas at Arlington, awarded the Alfred R. and Janet H. Potvin Outstanding Bioengineering Student Award, and received Honorable Mention at The University of Texas at Arlington’s World’s Best Technologies Poster Competition. In his spare time, Richard enjoys basketball, golf, camping, and agonizing over local sports teams.